NEW INSIGHTS INTO THE ROLE OF UNC-6/NETRIN IN GROWTH CONE PROTRUSION, POLARITY AND CYTOSKELETAL ORGANIZATION

By

Mahekta Gujar

Submitted to the graduate degree program in Molecular Biosciences and the Graduate Faculty of the University of Kansas in partial fulfillment of the requirements for the degree of Doctor of Philosophy.

_____
Chairperson – Dr. Erik Lundquist

_____
Dr. Brian Ackley

_____
Dr. Stuart Macdonald

_____
Dr. Berl Oakley

_____
Dr. Justin Blumenstiel

Date Defended: May 25, 2018

The Dissertation Committee for Mahekta Gujar
certifies that this is the approved version of the following dissertation:

NEW INSIGHTS INTO THE ROLE OF UNC-6/NETRIN IN GROWTH CONE PROTRUSION, POLARITY AND CYTOSKELETAL ORGANIZATION

_____
Chairperson – Dr. Erik Lundquist

Date approved: May 25, 2018

Abstract

The formation of complex neuronal circuits is crucial for the proper development of the central nervous system. The wiring structure of the nervous system underlies its function in sensation and movement, and higher order functions such as learning, memory, and cognition. Disruption of this wiring leads to a number of neurodevelopmental disorders such as developmental disability syndromes, autism, and schizophrenia. Axon guidance is an important aspect in this process of development, as neurons are not born with axons but must actively extend these wires in the developing nervous system to reach their appropriate synaptic targets. The developing axons are led by growth cones, dynamic actin-based structures that sense and respond to extracellular guidance cues that drive the forward motion of the axon. Growth cones contain a dynamic lamellipodial body ringed by filopodial protrusions, both important in guiding the axon to its target destination. Motility and guidance behaviors of the growth cone are regulated by its actin and microtubule (MT) cytoskeleton through the modulatory influence of axon guidance cues, such as UNC-6/Netrin and its guidance receptors UNC-40/DCC and UNC-5 that are present at the leading edge of the growth cone. Netrin is a secreted guidance cue that acts as both an axon attractant and repellant in different receptor contexts. Though the role of Netrin and its receptors in axon pathfinding has been extensively studied, very little is known about how Netrin regulates growth cone behavior and morphology *in vivo*.

Caenorhabditis elegans is a useful system to study axon pathfinding and growth cone development *in vivo* due to its simple, well-characterized nervous system, transparency and fully sequenced genome. The VD and DD motor neurons reside along the ventral nerve cord of the animal, and their axons normally extend straight dorsally to the dorsal nerve cord to form commissures. Though the DD axons develop during embryogenesis, the VD neurons develop post-embryonically in a well-described and stereotypical manner, making them great candidates to study *in vivo* growth cone development.

After a brief introduction to axon guidance and growth cone morphology in chapter I, chapter II describes a novel role for the *C. elegans* flavin-containing monooxygenase (FMOs) genes in Netrin-mediated axon guidance and growth cone protrusion. We show that the FMO genes are required for VD/DD motor axon guidance and to restrict growth cone filopodial protrusions downstream of the Netrin receptors UNC-40 and UNC-5 and the Rac GTPases CED-10 and MIG-2 in Netrin-mediated growth cone repulsion.

In chapter III we present new roles for UNC-6/Netrin in regulating the polarity and extent of growth cone protrusion through its receptors UNC-40 and UNC-5. We demonstrate that UNC-5 signaling regulates three aspects of growth cone morphology during growth away from UNC-6: (i) inhibition of growth cone protrusion (ii) dorsal leading-edge polarization of F-actin and (ii) restriction of MT entry into the growth cone, possibly via the cytoskeletal interacting protein UNC-33/CRMP. We also find that UNC-6 and UNC-40 can stimulate VD growth cone

protrusion at the dorsal leading-edge, independent of dorsal F-actin polarity and growth cone MT plus-end accumulation.

The characterization of the small GTPases RHO-1 and its guanine nucleotide exchange factor RHGF-1 in modulating growth cone protrusion and microtubule accumulation is detailed in chapter IV. We show that RHO-1 and RHGF-1 are required to prevent MT plus-ends from entering the growth cone as well as limiting excessive filopodial protrusions downstream of UNC-6/Netrin signaling.

Chapter V provides new insights into the building blocks of MTs, the tubulins and their importance in MT organization and stability with respect to growth cone morphology. We show that certain missense mutations in the *C. elegans* alpha and beta-tubulin genes, *tba-1* and *tbb-1,* have different effects on MT stability and in turn growth cone morphology. Mutations that lead to MT destabilitization inhibited growth cone protrusivity, while mutations that lead to the formation of hyperstable MTs caused excess protrusions. This reveals a causal relationship between MT organization and growth cone structure.

To address whether other guidance systems cooperate with UNC-6/Netrin to regulate protrusion and directed growth cone migration, chapter VI demonstrates the role of the guidance receptor SAX-3/Robo in dorsal axon guidance and VD growth cone protrusion. We show that *sax-3* is required for the guidance of dorsally-directed VD/DD axons and inhibits growth cone protrusion through the Rac GEF UNC-73/Trio.

In summary, the results contained here provide new insights into the mechanisms by which Netrin signaling regulates several aspects of growth cone protrusion during the process of axon pathfinding. By studying established and novel genes in repulsion and growth cone inhibition, and by defining their effects on the growth cone cytoskeleton, we are starting to understand how these signaling pathways shape the morphological characteristics of the growth cone during directed migration *in vivo*.

Acknowledgments

This journey through graduate school has probably been the most challenging yet enjoyable and gratifying experience I have encountered. Though I have made it this far, it would not have been possible without the help and support of so many people and here I would like to extend my deepest gratitude to everyone who has made this experience so amazing. First and foremost, a big thank you to one of the best, or more correctly THE best mentor a student could ask for, Dr. Erik Lundquist, who has provided me with the knowledge and guidance to be the scientist I am today. He has been a true inspiration for me throughout grad school. His enthusiasm and love for science has not only motivated me to be a good researcher but also taught me to enjoy every bit of it. Erik, I cannot thank you enough for all the talks (science or otherwise), all the help and encouragement you have provided.

Also, a very big thank you to all the amazing Lundquist lab members, without whom, lab would not have been so much fun. To Eric Struckhoff for all his assistance in the lab and absolutely entertaining conversations. To Dr. Lakshmi Sundararajan for making me so comfortable when I first joined the lab and for being such a wonderful friend. To Dr. Special Horse a.k.a Matt Josephson, who has been a great friend and colleague and I am so grateful to have had him there with me my first couple of years. To Matt Ochs and Snehal Mahadik for being such amazing and fun people to work with. A very special thank you to my awesome, sweet and extremely hardworking undergrad Aubrie Stricker.

I would like to acknowledge Dr. Brian Ackley and his lab for all the great times and helpful discussions during lab meeting. I would also like to express my gratitude to all my committee members for their guidance, encouragement and insightful suggestions during this entire process.

Most importantly, none of this would be possible without the help of my family to whom I am ever so grateful. My parents Maharookh and Rajesh whose unconditional love and unwavering faith in me has allowed me to pave this path for myself which has brought me this far. I owe everything I am today to them and no words can truly express how much I love and miss them. My brother Abhishek who has always been there for me and supported my every decision no matter what. My sweet Aditya whose love, patience and encouragement has been my source of strength even on the worst of days. Last but not the least to the apple of my eye, my fluff munchkin, who travelled across the world with me and made every day a little bit brighter by just being there with me.

Table of Contents

List of figures

Chapter I

Introduction

The complexity of the human nervous system is seen its ability to perform numerous complex tasks that underlies the basis of human behavior. Composed of a myriad of nerves and cells making intricate connections with one another, the formation of functional neuronal circuits is essential for the proper structure and organization of the nervous system. These functional circuits ultimately enables us to process and respond to our external environment, execute mental and physical tasks and express emotion and feeling. A number of neurodevelopmental disorders such as intellectual disabilities, autism spectrum disorders and schizophrenia have their roots in aberrant neural circuit formation (Tau and Peterson, 2010).

The formation of proper neuronal circuitry relies on several developmental processes including the proper pathfinding of neuronal axons to their appropriate synaptic partners to establish functional synaptic connections. The dynamic and motile structure present at the tip of a developing axon, known as the growth cone, is able to sense and respond to several molecular cues in the environment and is crucial for navigating the axon through developing tissues, often over long distances, to its target destination (Tessier-Lavigne and Goodman, 1996).

The ability of the growth cone to navigate axons by advancing, retracting and turning is due to its complex and dynamic morphology (Goldberg and Burmeister, 1986; Goodhill et al., 2015). The most prominent feature of growth cone structure is the dynamic filopodial and lamellipodial protrusions present at the leading edge of the growth cone. The veil-like lamellipodia is composed of a meshwork of actin filaments that are important for propelling the forward motion

of a developing neurite (Gallo and Letourneau, 2004). Within the lamellipodium are bundles of filamentous actin (F-actin) that form spike-like projections, which when they emanate beyond the lamellipodium frontier are called filopodia. Filopodia are essential for sensing environmental cues and subsequent steering of the growth cone (Davenport et al., 1993; Lewis and Bridgman, 1992).

Growth cone motility through persistent protrusion and retraction of filopodia and lamellipodia is thought to be regulated by the coordinated behaviors of the actin and microtubule (MT) cytoskeleton of the growth cone in response to guidance cues and downstream signaling cascades (Conde and Caceres, 2009; Dent and Gertler, 2003; Lowery and Van Vactor, 2009). The axon shaft and the central region of the growth cone is composed of bundled microtubules with their plus (+) ends (MT+) oriented towards the growth cone, whereas, the peripheral region of the growth cone contains highly dynamic actin that is relatively free of microtubules. Myosin-dependent retrograde flow that occurs in both filopodia and lamellipodia involves cycles of actin assembly at the leading edge of the growth cone, and disassembly of the actin filaments proximally, regulating the rate of axon outgrowth and preventing MTs from invading the peripheral domain of the growth cone (Zhou and Cohan, 2004). Though MTs have been thought to have a secondary role to actin filaments in growth cone guidance, recent studies have shown that a small population of dynamic microtubules can explore the periphery and penetrate the filopodia, where they could interact with signaling pathways linked to guidance cue receptors resulting in proper axonal elongation (Dent and

Gertler, 2003; Lowery and Van Vactor, 2009; Sabry et al., 1991; Tanaka et al., 1995).

Numerous molecules including guidance cues, their receptors and signaling transduction molecules have been determined to be involved in axon guidance, the extension of lamellipodia and filopodia, and therefore, the modulation of the actin and microtubule cytoskeleton. However, most work in identifying and analyzing these proteins *in vivo* has been done post-developmentally (i.e., after axon outgrowth has taken place) through end-point analysis (Hedgecock et al., 1987), or by studying developing growth cones *in vitro* (Burnette et al., 2007; Kalil and Dent, 2005; Ming et al., 1997). As a consequence, little is known about how these molecules regulate growth cone lamellipodial and filopodial protrusions and the growth cone cytoskeleton *in vivo* in live organisms. In the studies presented here, we used the nematode *Caenorhabditis elegans* as a model system for its simplicity and several advantages in studying neural development. *C. elegans* has a relatively simple nervous system, with 302 neurons in an adult hermaphrodite (White et al., 1986), the pattern of which has been completely mapped. One of the most important features of *C. elegans* is its transparent cuticle which allows for the observation of developing neurons within the live intact animal. With these features, along with a well-studied genome and the ease of genetic manipulation, *C. elegans* allows for *in vivo* studies that would not be available in many other organisms.

The D-type motor neurons are 19 of the 26 GABA-containing cells in *C.elegans*. The 6 DD (Dorsal D-type) and 13 VD (Ventral D-type) motor neurons

innervate the dorsal and ventral body wall muscles respectively and are required for the reciprocal relaxation of the body wall muscles during locomotion, resulting in the characteristic sinusoidal body movement of the animal. The cell bodies of the DD and VD neurons reside along the ventral nerve cord of the animal, and their axons first extend anteriorly and then straight dorsally to the dorsal nerve cord to form commissures, after which they bifurcate to send processes anteriorly and posteriorly. Though the DD axons are formed during embryogenesis itself, the VD axons develop post-embryonically during late L1 to early L2 larval stages. This development occurs in an anterior to posterior manner, with VD1 beginning to extend its axon nearly 16 hours post-hatching and VD13 growth cones having completed their extension by 19 hours post-hatching. The stereotypical developmental pattern of the VD neurons and the ability to utilize transgenes containing the green florescent protein (GFP) driven by the GABAergic specific promoter *unc-25,* makes it easy to observe the D-type motor neurons (Knobel et al., 1999) and more importantly the outgrowth of the VD axons during development (Norris and Lundquist, 2011) providing us with an excellent system to study genetic networks that regulate growth cone protrusion during axon outgrowth *in vivo*.

Several families of extracellular guidance cues and their neuronal receptors have been implicated in guiding axons to their appropriate synaptic target in the nervous system. Netrins were the first family of guidance cues shown to be genetically conserved all the way from invertebrate to vertebrate nervous system (Kennedy, 2000; Merz and Culotti, 2000). In *C. elegans* UNC-

6/Netrin is secreted from the ventral cells and along with its receptors UNC-40/DCC (deleted in colorectal cancer) and UNC-5 is necessary for the guidance of circumferential neurons (Ishii et al., 1992). The receptor UNC-40/DCC when present on the growth cones mediates an attractive response to UNC-6, driving the ventral guidance of circumferential axons, while the receptor UNC-5 mediates a repulsive response to UNC-6, driving the dorsal guidance of circumferential axons (Hedgecock et al., 1990b; Hong et al., 1999). In vertebrates both DCC and UNC-5 respond to netrin by the formation of receptor dimers. In the presence of only DCC, netrin binding causes the formation of DCC homodimers, leading to an attractive response by the growth cone. Whereas in neurons that express both DCC and UNC-5, netrin binding leads to the formation of UNC-5 alone or UNC-5-DCC heterodimers, both of which mediate a repulsive response (Hong et al., 1999; MacNeil et al., 2009).

The role of Netrin and its receptors in axon guidance has been well established, but how these genes control growth cone behavior and dynamics during outgrowth has not been well studied. Recent studies using live time lapse imaging of the VD growth cone in *C. elegans* recognized a link between growth cone protrusion and axon guidance controlled by UNC-6/netrin (Norris and Lundquist, 2011). This study revealed a correlation between axon attraction and stimulation of growth cone protrusion through UNC-40, and repulsive axon guidance and inhibition of growth cone protrusion through the UNC-40-UNC-5 receptors. Thus, a VD growth cone repelled from UNC-6 required a balance of pro- and anti-protrusive activities of the receptors UNC-40 and UNC-40-UNC-5,

respectively, in the same growth cone (Norris and Lundquist, 2011). Genetic analysis also identified several cytoskeletal signaling mechanisms in Netrin-stimulated growth cone protrusion, including the Rac GTPases, the Arp2/3 complex, UNC-34/Enabled and UNC-115/abLIM (Norris et al., 2009). In contrast, less is known about the pathways used by Netrin to inhibit growth cone protrusion that correlates with repulsion.

The work in this dissertation is centered on gaining insight into the molecular mechanisms by which UNC-6/Netrin mediates axon repulsion. By utilizing the dorsally directed VD motorneurons as described above, we describe novel cytoskeletal signaling mechanisms of Netrin-based growth cone inhibition and new roles for Netrin in regulating growth cone polarity and protrusion through the actin and MT cytoskeleton.

In *Drosophila*, the large, multidomain MICAL (Molecule Interacting with Cas-L) protein is expressed in axons and regulates actin disassembly and growth cone collapse in response to Semaphorin 1a (Sema-1a)-PlexA-mediated repulsive axon guidance, via direct redox interaction of F-actin (Terman et al., 2002). Vertebrate orthologs of MICAL (MICAL 1-3) are also neuronally expressed and interact with vertebrate plexins (Terman, 2002). Vertebrate MICAL-1, through its effects on F-actin assembly, has been implicated in the development of lamina-restricted hippocampal connections (Van Battum et al., 2014). The role of the MICAL-like flavin monooxygenase (FMOs) molecules in axon guidance has not been studied in *C.elegans*. Here we report a novel role of the *C. elegans* FMOs and the Eps-15 homology domain binding protein (EHBP-

1) in Netrin-mediated axon guidance and inhibition of growth cone protrusion. We show that the FMOs can genetically interact with the Netrin receptors UNC-40 and UNC-5, and act autonomously in the VD/DD neurons to regulate axon guidance and growth cone protrusion. Through genetic analyses we also present evidence that the FMO genes are required to restrict growth cone protrusion downstream of the Guanine nucleotide exchange factor (GEF) UNC-73/Trio and the Rac GTPases.

UNC-6/Netrin and its receptors UNC-40 and UNC-5 are clearly important for the dorsal migration of commissural axons i.e., away from UNC-6, but also are important in controlling the polarity of protrusion and the extent of protrusion in a developing growth cone (this report and (Norris and Lundquist, 2011)). UNC-5 limits growth cone protrusion through a pathway involving the Rac GEF UNC-73/Trio, the Rac GTPases and the cytoskeletal interacting molecules UNC-33/CRMP and UNC-44/Ankyrin (Norris et al 2014). To further examine how UNC-6/Netrin and its receptors regulate the polarity and the extent of growth cone protrusions, we analyzed the MT plus-end (MT+ -end) distribution and F-actin accumulation in the VD growth cones of *unc-6, unc-5 and unc-40* mutants. We find that UNC-5 signaling regulates three aspects of growth cone morphology during growth away from UNC-6/Netrin including, inhibition of growth cone protrusion, dorsal leading-edge polarization of F-actin and the restriction of MT entry into the growth cone. UNC-33 and UNC-44, similar to UNC-5, were also required for F-actin polarity and to restrict MT+-end accumulation in the growth cone. However, *unc-40; unc-5* and *ced-10; mig-2* displayed loss of F-actin

polarity and excess MT+ -end accumulation but not excess growth cone protrusion. This demonstrates that neither excess MT+ -ends nor loss of F-actin polarity alone are sufficient to drive excess protrusion. Our work establishes two distinct roles of UNC-6/Netrin in regulating growth cone protrusion. First it has a role in polarizing the growth cone, visualized by dorsal F-actin accumulation, resulting in protrusion restricted to the dorsal leading edge. Second it regulates extent of protrusion by stimulating protrusion at the dorsal leading edge and inhibiting it in the rest of the growth cone, based on the earlier establishment of polarity.

To further elucidate the signaling mechanisms by which guidance cues communicate with the growth cone cytoskeleton to regulate protrusion, we focused on the signal transduction machinery that interprets and transduces those cues, particularly the *C. elegans* small GTPase RHO-1 and its GEF, RHGF-1. RHO-1 is the sole *C. elegans* ortholog of mammalian RhoA. Rho signaling studies in *C. elegans* show that Rho is required throughout development to regulate many processes including neuronal morphogenesis, axon pathfinding and ventral hypodermal closure (Reiner and Lundquist, 2016; Zallen et al., 2000). The requirement for Rho signaling during development is not restricted to *C. elegans* and inactivation of RhoA in mice and *Drosophila* results in embryonic lethality showing that this requirement is evolutionarily conserved (Strutt et al., 1997; Wang and Zheng, 2007). Here we describe the role of *rho-1* and *rhgf-1* in controlling growth cone protrusion and MT+ -end distribution in the VD growth cone. We show that RHO-1 is required to limit the amount of growth

cone protrusion and also restrict the number of MT+ -ends that enter the VD growth cone periphery and it does so downstream of the PDZ/RhoGEF RHGF-1. Through epistasis studies we also present evidence that these molecules function through Netrin and its heterodimeric receptor UNC-5-UNC-40. We also find an interesting interaction between RHO-1 and the cytoskeletal interacting molecule UNC-33/CRMP in regulating growth cone morphology, where *rho-1* can suppress the excessive growth cone protrusions seen in *unc-33* mutants but cannot inhibit the excess MT+ -end accumulation in these growth cones. This suggests other mechanisms are involved in controlling the MT cytoskeleton and highlights the complexity of these molecules in development.

In an effort to identify how MT dynamics and stability affect growth cone morphology and in turn axon outgrowth we constructed and analyzed the effects of several missense mutations in the *C. elegans tba-1* and *tbb-1* genes. As the building blocks of MTs the alpha and beta-tubulin subunits are crucial determinants of MT stability, and several neurodevelopmental defects are associated with mutations in different tubulin isotypes (Zheng et al., 2017). We find that different mutated residues in *tba-1* and *tbb-1* caused distinct effects on growth cone morphology. For example, mutations that act in a dominant negative manner likely by forming poisonous alpha and beta-tubulin subunits are thought to block MT polymerization (Zheng et al., 2017), produced VD growth cones with a marked decrease in growth cone protrusion. In contrast, mutations that are likely to cause the formation of hyperstable MTs resulted in VD growth cones with longer filopodial protrusions. Our work provides evidence that suggests the

importance of MT stability in regulating growth morphology *in vivo*.

Our results so far have characterized the role of UNC-6/Netrin and its downstream effectors in different aspects of VD growth cone. However, several other guidance cues have important roles in axon guidance. A well characterized example is the guidance cue Slit and its receptor Roundabout (Robo) that are required for repulsion of axons from the midline (Kidd et al., 1998). In *C. elegans* SLT-1/Slit is expressed dorsally and mediates ventral guidance of axons via the SAX-3/Robo receptor. We find that *sax-3/Robo* mutants have defects in dorsally directed VD/DD axons. This role of SAX-3 seems to be independent of SLT-1, suggesting that SAX-3 mediates dorsal guidance using a cue distinct from SLT-1. We also find that SAX-3 regulates the polarity and the extent of growth cone protrusion similar to UNC-6/Netrin. Also, our genetic analyses places the Rac GEF UNC-73 downstream of SAX-3 in limiting growth cone protrusion. Whether SAX-3 functions in an UNC-6 dependent manner or if it participates in UNC-40/DCC-mediated repulsion of VD growth cones will be investigated in future studies.

In sum, our studies provide novel, fundamental insights into the mechanisms by which Netrin signaling regulates different aspects of growth cone morphology in repulsive guidance, and begins to bridge the gap in understanding how these mechanisms affect the development of the growth cone *in vivo*.

Chapter II

Flavin Monooxygenases Regulate *C. elegans* Axon Guidance and Growth Cone Protrusion with UNC-6/Netrin signaling and Rac GTPases

2.1 Abstract

The guidance cue UNC-6/Netrin regulates both attractive and repulsive axon guidance. Our previous work showed that in *C. elegans*, the attractive UNC-6/Netrin receptor UNC-40/DCC stimulates growth cone protrusion, and that the repulsive receptor, an UNC-5:UNC-40 heterodimer, inhibits growth cone protrusion. We have also shown that inhibition of growth cone protrusion downstream of the UNC-5:UNC-40 repulsive receptor involves Rac GTPases, the Rac GTP exchange factor UNC-73/Trio, and the cytoskeletal regulator UNC-33/CRMP, which mediates Semaphorin-induced growth cone collapse in other systems. The multidomain flavoprotein monooxygenase (FMO) MICAL (Molecule Interacting with CasL) also mediates growth cone collapse in response to Semaphorin by directly oxidizing F-actin, resulting in depolymerization. The *C. elegans* genome does not encode a multidomain MICAL-like molecule, but does encode five flavin monooxygenases (FMO-1, -2, -3, -4, and 5) and another molecule, EHBP-1, similar to the non-FMO portion of MICAL.

Here we show that FMO-1, FMO-4, FMO-5, and EHBP-1 may play a role in UNC-6/Netrin directed repulsive guidance mediated through UNC-40 and UNC-5 receptors. Mutations in *fmo-1, fmo-4, fmo-5,* and *ehbp-1* showed VD/DD axon guidance and branching defects, and variably enhanced *unc-40* and *unc-5* VD/DD axon guidance defects. Developing growth cones *in vivo* of *fmo-1, fmo-4, fmo-5,* and *ehbp-1* mutants displayed excessive filopodial protrusion, and transgenic expression of FMO-5 inhibited growth cone protrusion. Mutations suppressed growth cone inhibition caused by activated UNC-40 and UNC-5

signaling, and activated Rac GTPase CED-10 and MIG-2, suggesting that these molecules are required downstream of UNC-6/Netrin receptors and Rac GTPases. From these studies we conclude that FMO-1, FMO-4, FMO-5, and EHBP-1 represent new players downstream of UNC-6/Netrin receptors and Rac GTPases that inhibit growth cone filopodial protrusion in repulsive axon guidance.

2.2 Introduction

The formation of neural circuits during development depends on the guidance of growing axons to their proper synaptic targets. This process relies on the growth cone, a dynamic actin based structure present at the tip of a growing axon. Growth cones contain a dynamic lamellipodial body ringed by filopodial protrusions, both important in guiding the axon to its target destination (Gallo and Letourneau, 2004; Omotade et al., 2017; Pak et al., 2008; Zhou and Cohan, 2004). Guidance receptors present on the leading edge of the growth cone sense and respond to various extracellular guidance cues, which attract or repel axons enabling them to reach their proper target destination (Mortimer et al., 2008; Tessier-Lavigne and Goodman, 1996).

The secreted laminin-like guidance molecule UNC-6/Netrin mediates both axon attraction and axon repulsion and defines a dorsal-ventral guidance mechanism conserved from invertebrates to vertebrates (Ishii et al., 1992; Lai Wing Sun et al., 2011; Serafini et al., 1994). Attractive or repulsive responses to UNC-6/Netrin depend on the receptors expressed on the growth cone. Homodimers of the UNC-6/Netrin receptor UNC-40/DCC mediate attraction, and UNC-5:UNC-40 heterodimers or UNC-5 homodimers mediate repulsion (Hong et al., 1999; MacNeil et al., 2009; Moore et al., 2007).

In *C. elegans,* UNC-6/Netrin is secreted by the ventral cells and along with its receptors UNC-40 and UNC-5 is required for the dorsal ventral guidance of circumferential neurons and axons (Chan et al., 1996; Hedgecock et al., 1990b; Ishii et al., 1992). Previous studies of repelled VD growth cones in Netrin

signaling mutants revealed a correlation between attractive axon guidance and stimulation of growth cone protrusion, and repulsive axon guidance and inhibition of growth cone protrusion (Norris and Lundquist, 2011). For example, in *unc-5* mutants, growth cones were larger and more protrusive, and often displayed little or no directed movement. This is consistent with observation that increased growth cone size was associated with decreased neurite growth length (Ren and Suter, 2016). Conversely, constitutive activation of UNC-5:UNC-40 signaling in repelled VD growth cones led to smaller growth cones with severely reduced filopodial protrusion (Norris and Lundquist, 2011; Norris et al., 2014). Thus, directed growth cone repulsion away from UNC-6/Netrin requires a balance of pro- and anti-protrusive activities of the receptors UNC-40 and UNC-40:UNC-5, respectively, in the same growth cone (Norris and Lundquist, 2011).

Genetic analysis has identified a cytoskeletal signaling pathway involved in stimulation of growth cone protrusion in response to the attractive UNC-40 signaling that includes CDC-42, the Rac-specific guanine nucleotide exchange factor TIAM-1, the Rac-like GTPases CED-10 and MIG-2, as well as the cytoskeletal regulators Arp2/3 and activators WAVE-1 and WASP-1, UNC-34/Enabled, and UNC-115/abLIM (Demarco et al., 2012; Gitai et al., 2003; Norris et al., 2009; Shakir et al., 2006; Shakir et al., 2008; Struckhoff and Lundquist, 2003), consistent with findings in other systems (Lai Wing Sun et al., 2011). Mechanisms downstream of UNC-5 in axon repulsion are less well described, but the PH/MyTH4/FERM molecule MAX-1 and the SRC-1 tyrosine kinase have been implicated (Huang et al., 2002; Lee et al., 2005). We delineated a new

pathway downstream of UNC-5 required for its inhibitory effects on growth cone protrusion, involving the Rac GEF UNC-73/Trio, the Rac GTPases CED-10 and MIG-2, and the cytoskeletal-interacting molecule UNC-33/CRMP (Norris et al., 2014).

Collapsin response mediating proteins (CRMPs) were first identified as mediators of growth cone collapse in response to the Semaphorin family of guidance cues (Goshima et al., 1995), and we have shown that UNC-33/CRMP inhibits growth cone protrusion in response to Netrin signaling (Norris et al., 2014). This motivated us to consider other mediators of Semaphorin-induced growth cone collapse in Netrin signaling. In *Drosophila*, the large multidomain cytosolic protein MICAL (Molecule Interacting with CasL) is required for the repulsive motor axon guidance mediated by interaction of Semaphorin 1a and Plexin A (Ayoob et al., 2006; Terman et al., 2002). MICAL proteins are a class of flavoprotein monooxygenase enzymes that bind flavin adenine dinucleotide (FAD) and use the cofactor nicotinamide dinucleotide phosphate (NADPH) to facilitate oxidation-reduction (Redox) reactions (Terman et al., 2002). MICAL regulates actin disassembly and growth cone collapse in response to semaphorin via direct redox interaction with F-actin (Hung et al., 2011; Hung et al., 2010). MICAL molecules from *Drosophila* to vertebrates have a conserved domain organization: an N-terminal flavin-adenine dinucleotide (FAD)-binding monooxygenase domain, followed by a calponin homology (CH) domain, a LIM domain, a proline-rich domain, and a coiled-coil ERM α-like motif (Suzuki et al., 2002; Terman et al., 2002).

The *C. elegans* genome does not encode a MICAL-like molecule with the conserved domain organization described above. However, it does encode five flavin monooxygenase (*fmo*) genes similar to the Flavin monooxygenase domain of MICAL: *fmo-1, fmo-2, fmo-3, fmo-4 and fmo-5* (Petalcorin et al., 2005). Like MICAL, the *C. elegans* FMO molecules contain an N-terminal FAD binding domain and a C-terminal NADP or NADPH binding domain (Petalcorin et al., 2005; Terman et al., 2002). The *C. elegans* gene most similar to the non-FMO portion of MICAL is the Eps-15 homology domain binding protein EHBP-1 (Shi et al., 2010), which contains a CH domain as does MICAL.

In this work, we test the roles of the *C. elegans* FMOs and EHBP-1 in Netrin-mediated axon guidance and growth cone protrusion. We find that *fmo-1, fmo-4, fmo-5* and *ehbp-1* mutants display pathfinding defects of the dorsally-directed VD/DD motor neuron axons that are repelled by UNC-6/Netrin, and that they interact genetically with *unc-40* and *unc-5*. We also find that VD growth cones in these mutants display increased filopodial protrusion, similar to mutants in repulsive UNC-6/Netrin signaling (e.g. *unc-5* mutants), and that transgenic expression of FMO-5 inhibits growth cone protrusion, similar to constitutively-activated UNC-40 and UNC-5. We also show that FMO-1, FMO-4, FMO-5 and EHBP-1 are required for the growth cone inhibitory effects of activated UNC-5, UNC-40, and the Rac GTPases CED-10 and MIG-2. Together, these genetic analyses suggest that FMO-1, FMO-4, FMO-5, and EHBP-1 normally restrict growth cone protrusion, and that they might do so in UNC-6/Netrin-mediated growth cone repulsion.

2.3 Materials and Methods

Genetic methods

Experiments were performed at 20°C using standard *C. elegans* techniques (Brenner, 1974). Mutations used were LGI: *unc-40(n324)*, *unc-73(rh40)*; LGII: *juIs76[Punc-25::gfp]*; LGIII: *fmo-3(gk184651)*; LGIV: *fmo-1(ok405)*, *fmo-2(ok2147)*, *lqIs128[Punc-25::myr::unc-40]*, *unc-5(op468* and *e152)*, *unc-33(e204*); LGV: *fmo-4(ok294)*, *fmo-5(tm2438)*, *ehbp-1(ok2140M+)*; LGX: *lqIs182[Punc-25::mig-2(G16V)]*. Chromosomal locations not determined: *lqIs129[Punc-25::myr::unc-40], lqIs296[Punc-25::myr::unc-5], lqIs204[Punc-25::ced-10(G12V)], lhIs6[Punc-25::mCherry], lqIs311[fmo-5 genomic]* by integration of *lqEx1047*. Extrachromosomal arrays were generated using standard gonadal injection (Mello and Fire, 1995) and include: *lqEx901* and *lqEx931[Pehbp-1::gfp, Pgcy-32::yfp]; lqEx1014, lqEx1015*, *lqEx1016, lqEx1045, lqEx1046 and lqEx1047[Pfmo-5::fmo-5, Pgcy-32::yfp]; lqEx949, lqEx950, lqEx951, lqEx1053, lqEx1054* and *lqEx1055[Punc-25::fmo-1, Pgcy-32::yfp]; lqEx1098, lqEx1099, lqEx1100, lqEx1101* and *lqEx1102[Punc-25::fmo-4, Pgcy-32::yfp]; lqEx952, lqEx953, lqEx954, lqEx1061, lqEx1062, lqEx1063, lqEx1078, lqEx1079* and *lqEx1080[Punc-25::fmo-5, Pgcy-32::yfp]; lqEx1146, lqEx1147, lqEx1148* and *lqEx1149[Pdpy-7::fmo-5, Pgcy-32::yfp]; lqEx1113* and *lqEx1114[Pfmo-5::fmo-5::GFP, Pstr-1::gfp]; whEx28[Pfmo-4::gfp, pRF4/rol-6]*. Multiple (≥3) extrachromosomal transgenic lines of *Pfmo-5::fmo-5* for overexpression data of *fmo-5* were analyzed with similar effect, and one was chosen for integration and further analysis. Genotypes containing M+ indicate

that homozygous animals from a heterozygous mother were scored. The *ehbp-1(ok2140M+)* strain was balanced with the *nT1* balancer, since *ehbp-1(ok2140)* homozygous animals are sterile. RNAi was performed by feeding as previously described (Kamath et al., 2003).

Transgene construction

Details about transgene construction are available by request. *Punc-25::fmo-1*, *Punc-25::fmo-4* and *Punc-25::fmo-5* were made using the entire genomic regions of *fmo-1*, *fmo-4* and *fmo-5* respectively. Expression analysis for *fmo-5* was done by amplifying the entire genomic region of *fmo-5* along with its endogenous promoter (1.2kb upstream) and fusing it to *gfp* followed by the 3' UTR of *fmo-5*.

Analysis of axon guidance defects

VD neurons were visualized with a *Punc-25::gfp* transgene, *juIs76* (Jin et al., 1999), which is expressed in GABAergic neurons including the six DDs and 13 VDs, 18 of which extend commissures on the right side of the animal. The commissure on the left side (VD1) was not scored. In *wild-type*, an average of 16 of these 18 VD/DD commissures are apparent on the right side, due to fasciculation of some of the commissural processes (Figure 2.2C). In some mutant backgrounds, fewer than 16 commissures were observed (e.g. *unc-5*). In these cases, only observable axons emanating from the ventral nerve cord were scored for axon guidance defects. VD/DD axon defects scored include axon

guidance (termination before reaching the dorsal nerve cord or wandering at an angle greater than 45° before reaching the dorsal nerve cord) and ectopic branching (ectopic neurite branches present on the commissural processes). In the case of double mutant analysis with *unc-40 and unc-5* only lateral midline crossing (axons that fail to extend dorsally past the lateral midline) were considered (Figure 2.4, 2.5 and 2.6). Fisher's exact test was used to determine statistical significance between proportions of defective axons. In double mutant comparisons, the predicted additive effect of the mutants was calculated by the formula P1+P2-(P1*P2), where P1and P2 are the phenotypic proportions of the single mutants. The predicted additive effect of single mutants was used in statistical comparison to the observed double mutant effect.

Growth cone imaging

VD growth cones were imaged as previously described (Norris et al., 2009; Norris and Lundquist, 2011). Briefly, animals at 16 h post-hatching at 20°C were placed on a 2% agarose pad and paralyzed with 5mM sodium azide in M9 buffer, which was allowed to evaporate for 4 min before placing a coverslip over the sample. Some genotypes were slower to develop than others, so the 16 h time point was adjusted for each genotype. Growth cones were imaged with a Qimaging Rolera mGi camera on a Leica DM5500 microscope. Projections less than 0.5 µm in width emanating from the growth cone were scored as filopodia. Filopodia length and growth cone area were measured using ImageJ software. Filopodia length was determined by drawing a line from the base where the

filopodium originates on the edge of the peripheral membrane to the tip of the filopodium. Growth cone area was determined by tracing the periphery of the growth cone, not including filopodial projections. Significance of difference was determined a two-sided *t*-test with unequal variance.

2.4 Results

fmo-1,4,5 and *ehbp-1* affect VD/DD axon pathfinding.

The *C. elegans* genome lacks an apparent homolog of MICAL. However, it contains five flavin monooxygenase genes (*fmo-1,2,3,4,*5) (Figure 2.1A) (Petalcorin et al., 2005). The *C. elegans* molecule most similar to the non-FMO portion of MICAL is EHBP-1, the homolog of the mammalian EH domain binding protein 1 (Ehbp1) protein (Shi et al., 2010). We analyzed existing mutations in *fmo* genes and *ehbp-1* (Figure 2.1B) for VD/DD axon guidance defects. *fmo-1(ok405)* was a 1,301-bp deletion that removed part of exon 3 and all of exons 4, 5 and 6. *fmo-2(ok2147)* was a 1070-bp deletion that removed part of exon 4 and 5. *fmo-4(ok294)* was a 1490-bp deletion that removed all of exons 2, 3, 4 and 5. *fmo-5(tm2438)* is a 296-bp deletion which removes part of intron 3 and exon 4. These deletions all affected one or both predicted enzymatic domains of the FMO molecules**.** *fmo-3(gk184651)* was a G to A substitution in the 3' splice site of intron 6 and may not be a null mutation. *ehbp-1(ok2140)* is a 1,369-bp deletion that removed all of exon 5 and 6. Genotypes involving *ehbp-1(ok2140)* have wild-type maternal *ehbp-1* activity, as homozygotes are sterile and must be maintained as heterozygotes balanced by *nT1*.

The 19 D-class motor neurons cell bodies reside in the ventral nerve cord. They extend axons anteriorly and then dorsally to form a commissure, which normally extend straight dorsally to the dorsal nerve cord (Figure 2.2 and Figure 2.3B). On the right side of wild-type animals, an average of 16 commissures were observed, due to the fasciculation of some processes as a single

commissure (Figure 2.2C and Materials and Methods). *fmo-1, 4,* and *5* and *ehbp-1* mutants showed significant defects in VD/DD axon pathfinding, including ectopic axon branching and wandering (~3-5%; see Materials and Methods and Figure 2.3A, C and D), although most crossed the lateral midline despite wandering. *fmo-2* and *fmo-3* mutations showed no significant defects compared to *wild-type* (Figure 2.3A). We used RNAi directed against *ehbp-1*, which has the potential to eliminate any maternally-supplied mRNAs, but not translated proteins. *ehbp-1(RNAi)* resembled *ehbp-1 M+* mutants (Figure 2.3A), suggesting that maternal mRNAs are not involved in VD/DD axon guidance.

Most double mutants showed no strong synergistic defects compared to the predicted additive effects of the single mutants (Figure 2.3A). However, the *fmo-2; fmo-3* and the *fmo-2; fmo-4* double mutants showed significantly more defects compared to the predicted additive effects of the single mutants. The *fmo-4; ehbp-1* double mutant displayed significantly reduced defects than either mutation alone. The *fmo-1; fmo-4 fmo-5* triple mutant also showed no synergistic defects as compared to single mutants alone (Figure 2.3A). Lack of extensive phenotypic synergy suggests that the FMOs do not act redundantly, but rather that they might have discrete and complex roles in axon guidance, as evidenced by *fmo-4; ehbp-1* mutual suppression.

Axon pathfinding defects of *unc-40* and *unc-5* are increased by *fmo-1*, *fmo-4* and *fmo-5* mutations.

In *unc-40(n324)* strong loss-of-function mutants, most axons (92%) extended past the lateral midline despite wandering (see Materials and Methods and Figures 2.4A and B). *fmo-1, fmo-4, fmo-5,* and *ehbp-1* displayed < 1% failing to extend past the lateral midline (Figure 2.4A). *fmo-1, fmo-4,* and *fmo-5* mutations significantly enhanced the VD/DD lateral midline crossing defects of *unc-40(n324)* (Figure 2.4A and C). *ehbp-1* did not enhance *unc-40* (Figure 2.4A).

unc-5(e53) strong loss-of-function mutants display a nearly complete failure of VD axons to reach the dorsal nerve cord (Hedgecock et al., 1990b; Norris and Lundquist, 2011). *unc-5(e152)* is a hypomorphic allele (Killeen et al., 2002) and displayed 22% failure of axons to cross the lateral midline (Figure 2.5A). The *unc-5(op468)* allele (Merz et al., 2001) also displayed a weaker lateral midline crossing phenotype (10%), indicating that it is also a hypomorphic allele (Figure 2.5B). *fmo-1, fmo-4* and *fmo*-5 significantly enhanced the VD/DD axon guidance defects of both *unc-5(e152)* and *unc-5(op468)*, but *ehbp-1* did not (Figure 2.5). While *fmo* mutations alone caused few midline crossing defects compared to *unc-40* and *unc-5*, they enhanced the midline crossing defects of *unc-40* and *unc-5* hypomorphic mutants. These results indicate that FMO-1,4, and 5 might act with UNC-40 and UNC-5 in VD/DD axon pathfinding.

***fmo-1*, *fmo-4* and *fmo-5* act cell-autonomously in the VD/DD neurons**.

Expression of the *fmo-1*, *fmo-4,* and *fmo-5* coding regions were driven in VD/DD motor neurons using the *unc-25* promoter. *Punc-25::fmo* transgenes significantly rescued lateral midline crossing defects in *fmo; unc-5(op468)* and *fmo; unc-5(e152)* (Figure 2.6). These data suggest that the axon defects observed in *fmo* mutants are due to mutation of the *fmo* genes themselves, and that *fmo-1, 4,* and *5* can act cell-autonomously in the VD/DD neurons in axon guidance.

Previous studies showed that *fmo-1* and *fmo-5* promoter regions were active in intestinal cells and the excretory gland cell, whereas the *fmo-4* promoter was active in hypodermal cells, duct and pore cells (Hirani et al., 2016; Petalcorin et al., 2005). *ehbp-1* is expressed in all somatic cells including neurons (Shi et al., 2010). Furthermore, cell-specific transcriptome profiling indicated that *fmo-1, fmo-4* and *fmo-5* were expressed in embryonic and adult neurons, including motor neurons (Fox et al., 2005; Kaletsky et al., 2016; McKay et al., 2003). We fused the upstream promoter regions of *fmo-1, fmo-4,* and *fmo-5* to *gfp*. We could observe no *fmo-1::gfp* expression in transgenic animals, in contrast to previous studies using a *LacZ* reporter (Petalcorin et al., 2005). However, transcriptome profiling indicates neuronal expression of *fmo-1 (Kaletsky et al., 2016).* Our *fmo-1::gfp* transgene might be missing regulatory regions required for expression*. fmo-4::gfp* was expressed strongly in hypodermal cells, excluding the seam cells and vulval cells, consistent with previous studies (Petalcorin et al., 2005) (Figure 2.6D). We also observed *fmo-4::gfp* expression in cells in the

ventral nerve cord (Figure 2.6 D and D'). *Pfmo-5::fmo-5::gfp* was expressed strongly in the intestine as previously reported (Petalcorin et al., 2005) (Figure 2.6E). We also observed expression along the ventral nerve cord (Figure 2.6E and E'). In sum, previous expression studies combined with those described here suggest that *fmo-1,4,5* and *ehbp-1* are expressed in neurons, and that *fmo-1,4,* and *5* can act cell-autonomously in the VD/DD motor neurons in axon guidance.

fmo-1, fmo-4 **and** ***fmo-5*** **mutants display increased growth cone filopodial protrusion.**

The growth cones of dorsally-directed VD commissural axons are apparent in early L2 larvae (Figure 2.2B). We imaged VD growth cones at 16 hours post-hatching, when the VD growth cones have begun their dorsal migrations, as described previously (Norris and Lundquist, 2011). *fmo-1*, *fmo-4,* and *fmo-5* mutant growth cones displayed longer filopodial protrusions compared to wild type (e.g. 0.96 µm in wild type compared with 1.55 µm in *fmo-5(tm2438)*; $p < 0.001$) (Figure 2.7). This effect was not significant in *ehbp-1(ok2140)* (Figure 2.7). Growth cone area was not significantly different in any mutant. These results suggest that *fmo-1, fmo-4* and *fmo-5* normally limit growth cone filopodial protrusion length. This is consistent with ectopic axon branches observed in post-development VD/DD neurons in these mutants (Figure 2.3), as other mutants with increased growth cone filopodial protrusions (e.g. *unc-5, unc-73, unc-33*) also display ectopic branches, likely due to failure of filopodial retraction and

subsequent consolidation into a neurite (Norris and Lundquist, 2011; Norris et al., 2014).

Expression of the *fmo-5* coding region driven in VD/DD motor neurons using the *unc-25* promoter also significantly rescued axon guidance defects as well as the long filopodial protrusions seen in *fmo-5(tm2438)* (Figure 2.8). We expressed the *fmo-5* coding region in the hypodermis using the *dpy-7* promoter (Gilleard et al., 1997) and observed no significant rescue of axon guidance defects or filopodial protrusions (Figure 2.8). These data confirm that *fmo-5* can act cell-autonomously in the VD/DD neurons in axon guidance and growth cone filopodial protrusion.

fmo-1, fmo-4, fmo-5 **and** ***ehbp-1*** **mutations suppress activated** ***myr::unc-40*** **and** ***myr::unc-5*** **and activated Rac GTPases*.***

Previous studies showed that UNC-6/netrin signaling via the heterodimeric UNC-5:UNC-40 receptor leads inhibition of growth cone protrusion important in UNC-6/Netrin's role in repulsive axon guidance (Norris and Lundquist, 2011; Norris et al., 2014). Constitutive activation of this pathway using expression of myristoylated versions of the cytoplasmic domains of UNC-40 and UNC-5 (*myr::unc-40* and *myr::unc-5*) results in small growth cones with few if any filopodial protrusions (i.e. protrusion is constitutively inhibited by MYR::UNC-40 and MYR::UNC-5) (Gitai et al., 2003; Norris and Lundquist, 2011; Norris et al., 2014). Loss of *fmo-1*, *fmo-4, fmo-5* and *ehbp-1* significantly suppressed inhibition of filopodial protrusion and growth cone size caused by *myr::unc-40* (Figure 2.9)

and *myr::unc-5* (Figure 2.10). Notably, *ehbp-1* did not enhance loss-of-function mutations in *unc-5* or *unc-40* (Figure 2.4), suggesting that *myr::unc-5* and *myr::unc-40* are sensitized backgrounds in which interactions can be determined that are not apparent in loss-of-function backgrounds.

Expression of activated CED-10(G12V) and MIG-2(G16V) in the VD neurons results in reduced growth cone protrusion similar to MYR::UNC-40 and MYR::UNC-5 (Norris et al., 2014). We found that *fmo-1, fmo-4* and *fmo-5* suppressed filopodial protrusion deficits caused by *ced-10(G12V)* and *mig-2(G16V)* (Figure 2.11). *ehbp-1* suppressed *mig-2(G16V)*, but *ehbp-1(ok2140M+); ced-10(G12V)* double mutants were inviable and could not be scored. Furthermore, *fmo-4* and *fmo-5,* but not *fmo-1*, significantly suppressed growth cone size reduction caused by CED-10(G12V) and MIG-2(G16V). *ehbp-1* also suppressed growth cone size reduction of MIG-2(G16V). Taken together, these data indicate that functional FMO-1, FMO-4, FMO-5, and EHBP-1 are required for the full effect of MYR::UNC-40, MYR::UNC-5, CED-10(G12V), and MIG-2(G16V) on growth cone protrusion inhibition, including filopodial protrusion and growth cone size.

FMO-5 can inhibit growth cone protrusion.

fmo-5 loss-of-function mutant growth cones displayed excessively-protrusive filopodia (Figure 2.7) and suppressed activated UNC-5:UNC-40 and Rac signaling (Figures 2.9-2.11). Transgenic expression of wild-type FMO-5 driven by its endogenous promoter rescued the axon guidance defects and long

filopodial protrusions seen in *fmo-5(tm2438)* mutant VD growth cones (Figure 2.12A-E). In a wild-type background, *fmo-5* transgenic expression resulted in growth cones with smaller area and shortened filopodia (Figure 2.13A, B and E), indicating that wild-type FMO-5 activity can inhibit growth cone protrusion. This inhibition was not observed in the *fmo-5(tm2438)* background, possibly due to the decreased levels of FMO-5 compared to the wild-type background.

Mutations in *unc-5, unc-73*, and *unc-33* result in excessively large growth cones with increased filopodial length (Figure 2.13A and B) (Norris and Lundquist, 2011; Norris et al., 2014). Transgenic *fmo-5* expression significantly reduced growth cone size and filopodial protrusion in *unc-5(e152)*, *unc-73(rh40),* and *unc-33(e204)* (Figure 2.13A, B, F, G, and H). However, *fmo-5* expression only partially inhibited filopodial protrusion in *unc*-5 and *unc-33* (i.e. to wild-type levels, higher than *fmo-5* transgenic expression alone) (Figure 2.13A). These data indicate that FMO-5 activity does not rely on UNC-5, UNC-73, or UNC-33 and that it might act downstream of them. However, the hybrid interaction of *fmo-5* transgenic expression with *unc-33(e204)* could also indicate that FMO-5 and UNC-33 represent distinct, compensatory pathways downstream of UNC-5 and the Rac GTPases to inhibit filopodial protrusion. *unc-33; fmo-5* double mutants did not show any significant increase in filopodial length (Figure 2.13A and B), which would be expected if they act in parallel pathways.

In contrast to *unc*-5 mutants, *unc-40* single mutants display shortened filopodial protrusions and a relatively normal growth cone size (Figure 2.13A and B) (Norris and Lundquist, 2011). This is likely due to the dual role of UNC-40 in

both stimulating protrusion as a homodimer and inhibiting protrusion as a heterodimer with UNC-5. *fmo-5* transgenic expression had no effect on filopodial protrusions in *unc-40*, but did reduce growth cone size, consistent with a role of FMO-5 in inhibiting protrusion.

Finally, we also found that transgenic *fmo-5* expression in *fmo-1(ok405)* suppressed growth cone area and filopodial length of *fmo-1(ok405)* mutants (Figure 2.13A, B and H), indicating that *fmo-5* activity can partially compensate for loss of *fmo-1.*

2.5 Discussion

Results here implicate the *C. elegans* flavoprotein monooxygenase molecules FMO-1, FMO-4 and FMO-5 in inhibition of growth cone protrusion via UNC-6/Netrin receptor signaling in repulsive axon guidance (Figure 2.14). The MICAL molecule found in vertebrates and *Drosophila* is a flavoprotein monooxygenase required for semaphorin-plexin mediated repulsive motor axon guidance (Pasterkamp et al., 2006; Terman et al., 2002). Here we focus on UNC-6/Netrin signaling and have not analyzed the role of the FMOs in semaphorin signaling in *C. elegans*. MICAL is a multi-domain molecule that also includes a calponin homology (CH) domain, a LIM domain and multiple CC domains. No molecule encoded in the *C. elegans* genome has a similar multi-domain organization. However, the Eps-15 homology (EH) domain binding protein EHBP-1 is similar to the non-FMO portion of MICAL and contains a CH domain (Shi et al., 2010). We show here that EHBP-1 also is also involved in inhibition of growth cone protrusion and axon guidance. Thus, while *C. elegans* does not have a multidomain MICAL-like molecule, it is possible that the functional equivalents are the FMOs and EHBP-1.

FMO-1, FMO-4, FMO-5 and EHBP-1 regulate axon guidance and growth cone filopodial protrusion. *fmo-1, fmo-4, fmo-5,* and *ehbp-1* mutants display defects in dorsal guidance of the VD/DD motor axons that are repelled from UNC-6/Netrin (Figure 2.3). Double and triple mutant analysis did not uncover significant redundancy, suggesting that these molecules might have discrete and

complex roles in axon guidance. Consistent with this idea, *fmo-4* and *ehbp-1* mutually suppress VD/DD axon guidance defects. Furthermore, transgenic expression of FMO-5 rescued excess growth cone and filopodial protrusions of *fmo-1* mutants. This suggests that FMO-5 can partially compensate for loss of FMO-1, and that the function of FMO-5 does not depend on FMO-1. Combined with lack of phenotypic synergy, these data suggest that the FMOs act in a common pathway, where loss of one abolishes pathway function, and that FMO-5 might act downstream of FMO-1 in this pathway. *fmo-2* and *fmo-3* mutations displayed no significant defects alone, suggesting that they are not involved in axon guidance. *fmo-2* did significantly enhance *fmo-4*. Possibly, *fmo-2* and *fmo-3* might have roles in axon guidance that were not revealed by the mutations used.

Drosophila and vertebrate MICAL regulate actin cytoskeletal dynamics in both neuronal and non-neuronal processes through direct redox activity of the monooxygenase domain (Beuchle et al., 2007; Bron et al., 2007; Giridharan and Caplan, 2014; Hung et al., 2011; Kirilly et al., 2009; Schmidt et al., 2008; Terman et al., 2002). In *Drosophila*, loss of MICAL showed abnormally shaped bristles with disorganized and larger F-actin bundles, whereas, overexpression of MICAL caused a rearrangement of F-actin into a complex meshwork of short actin filaments (Hung et al., 2010). Here we show that loss of *fmo-1, fmo-4,* and *fmo-5* resulted in longer filopodial protrusions in the VD motor neurons (Figure 2.7), suggesting that their normal role is to limit growth cone filopodial protrusion. Indeed, transgenic expression of wild-type FMO-5 resulted in VD growth cones

with a marked decrease in growth cone filopodial protrusion (Figure 2.13). Growth cone size was not affected in any loss-of-function mutation, but growth cone size was reduced by transgenic expression of wild-type FMO-5 (Figure 2.13), suggesting a role of the FMO-5 in both filopodial protrusion and growth cone lamellipodial protrusion.

Previous studies have shown that *Drosophila* MICAL may require both its FMO and CH domain to induce cell morphological changes; however, mammalian MICAL in non-neuronal cell lines requires only its FAD domain suggesting a difference in the mechanism of action in these MICALs (Giridharan et al., 2012; Hung et al., 2010). These data suggest that in some cases, the FMO domain is sufficient for the function of MICAL. Thus, single domain FMOs as in *C. elegans* could function despite lacking the multi-domain structure of MICAL. Loss of the *C. elegans* MICAL-like molecule EHBP-1, which contains a CH domain and is similar to the non-FMO portion of MICAL (Figure 2.1), also resulted in VD/DD axon guidance defects, but did not significantly affect growth cone filopodial protrusion. EHBP-1 might act with the FMOs in axon guidance. Phenotypic differences could be due to EHBP-1-dependent and independent events, or to the wild-type maternal contribution in *ehbp-1* homozygous mutants derived from a heterozygous mother. It is also possible that EHBP-1 affects axon guidance independently of the FMOs. EHBP-1 is involved in Rab-dependent endosomal vesicle trafficking by bridging interaction of endosomal Rabs with the actin cytoskeleton (Shi et al., 2010; Wang et al., 2016). MICAL has also been implicated in Rab-dependent endosomal biogenesis and trafficking (Giridharan et

al., 2013; Rahajeng et al., 2012; Sharma et al., 2009), suggesting that FMO/EHBP-1 and MICALs might share common functions, although it remains to be determined if FMOs in *C. elegans* regulate endosomal trafficking.

MICAL has been shown to directly oxidize cysteine residues in F-actin, leading to actin depolymerization and growth cone collapse (Hung et al., 2011; Hung et al., 2013; Hung and Terman, 2011; Hung et al., 2010). We speculate that FMO-1, FMO-4, and FMO-5 might act by a similar mechanism to inhibit growth cone filopodial protrusion. Previous studies have shown that the single calponin homology (CH) domain containing protein CHDP-1 promotes the formation of cell protrusions in *C. elegans* by directly binding to Rac1/CED-10 through its CH domain (Guan et al. 2016). The role of EHBP-1 however, is less clear, but previous studies have shown that *Drosophila* MICAL might require both its FMO and CH domain to induce cell morphological changes (Hung et al., 2010). Thus, in axon guidance, FMO-1, FMO-4, and FMO-5 might require the CH domain provided by EHBP-1 in some instances. Mammalian MICAL requires only the FMO domain (Giridharan et al., 2012), suggesting that in some cases the CH domain is not required and the FMO domain can act alone. Future studies will be directed at answering these questions.

FMOs can act autonomously in the VD/DD neurons. Expression of full length *fmo-1, fmo-4* and *fmo-5* coding regions under the control of the *unc-25* promoter specific for GABA-ergic neuron expression (including the VD/DD neurons) rescued VD/DD axon guidance defects (Figure 2.6 and 2.8). Furthermore, the

promoters of *fmo-4* and *fmo-5* were active in ventral nerve cord cells (Figure 2.6). Expression of full length *fmo-5* coding region under the control of the *unc-25* promoter rescued axon guidance defects as well as the long filopodial protrusions seen in *fmo-5(tm2438)*, whereas expression from the hypodermal *dpy-7* promoter did not (Figure 2.8). Cell-specific transcriptome profiling indicated that *fmo-1, fmo-4* and *fmo-5* were expressed in embryonic and adult neurons, including motor neurons (Fox et al., 2005; Kaletsky et al., 2016; McKay et al., 2003). Together, these results suggest that the FMOs can act cell-autonomously in the VD/DD neurons in axon guidance and growth cone filopodial protrusion.

FMO-1, FMO-4 and FMO-5 mediate UNC-6/Netrin receptor signaling in growth cone inhibition of protrusion. Our findings suggest that the FMOs act with the UNC-40 and UNC-5 receptors to mediate UNC-6/netrin repulsive axon guidance and inhibition of growth cone protrusion. *fmo-1, fmo-4,* and *fmo-5* mutations enhanced axon pathfinding defects in *unc-40* and hypomorphic *unc-5* mutants (Figures 2.4 and 2.5). The axon guidance defects of the *fmos* were weaker than those of *unc-40* and *unc-5* mutants (e.g. the *fmos* displayed few lateral midline crossing defects despite axon wandering). We speculate that the FMOs are but one of several pathways mediating the effects of UNC-40 and UNC-5 in axon pathfinding. *ehbp-1* did not enhance *unc-40* or *unc-5*, suggesting discrete roles of these molecules or wild-type maternal *ehbp-1* contribution. *fmo-1, fmo-4, fmo-5*, and *ehbp-1* mutations each suppressed the effects of activated MYR::UNC-40 and MYR::UNC-5 on inhibition of growth cone protrusion (Figure

2.10). In this case, both filopodial protrusion and growth cone area was restored, consistent with a role of these molecules in inhibiting both growth cone filopodial and lamellipodial protrusion. We also find the *fmo-5* transgenic expression suppressed *unc-5(e152)* growth cone area and filopodial protrusions (Figure 2.13). That the FMOs and EHBP-1 were required for the effects of the constitutively active MYR::UNC-40 and MYR::UNC-5 suggest that they act downstream of these molecules in growth cone inhibition of protrusion. While the loss-of-function and gain-of-function data are consistent with acting downstream of UNC-40 and UNC-5, it is possible that the FMOs define a parallel pathway in growth cone protrusion.

Interestingly, mutations in these genes have very distinct penetrances (e.g. the axon guidance and protrusion defects of *unc-5* are much stronger than those of the *fmo* mutants). One explanation for this is that these molecules act in networks rather than simple linear pathways. The FMOs might be one of many mechanisms acting downstream of UNC-5, and multiple pathways might converge on UNC-33 (e.g. UNC-5 and UNC-33 are major “nodes” in this network). Further loss- and gain-of-function studies will be required to understand this signaling network.

FMOs and EHBP-1 act downstream of Rac GTPase signaling in inhibition of growth cone protrusion. Similar to activated MYR::UNC-40 and MYR::UNC-5, constitutively-activated Rac GTPases CED-10(G12V) and MIG-2(G16V) inhibit VD growth cone protrusion. We show that *fmo-1, fmo-4, fmo-5* and *ehbp-1*

mutations suppressed activated CED-10(G12V) and MIG-2(G16V) (e.g. double mutant growth cones displayed longer filopodial protrusions similar to *fmo-1, fmo-4, fmo-5* and *ehbp-1* single mutants) (Figure 2.11). Furthermore, loss of the Rac GTP exchange factor UNC-73/Trio had no effect on the inhibited growth cone phenotype of FMO-5 transgenic expression (i.e. the growth cones resembled those of *fmo-5* over expression alone) (Figure 2.13). UNC-73/Trio acts with the Rac GTPases CED-10 and MIG-2 in growth cone protrusion inhibition, and *unc-73* mutants display excessive growth cone protrusion (Norris et al., 2014). That FMO-5 transgenic expression could inhibit protrusion in the absence of the Rac activator UNC-73/Trio suggests that FMO-5 acts downstream of UNC-73/Trio, consistent with the FMOs and EHBP-1 acting downstream of the Rac GTPases.

FMO-5 interacts with UNC-33/CRMP. Previous studies have shown that the *C. elegans* CRMP-like molecule UNC-33 is required in a pathway downstream of Rac GTPases for inhibition of growth cone protrusion in response to UNC-6/Netrin (Norris et al., 2014). *unc-33* loss-of-function mutants with FMO-5 transgenic expression displayed a mutually-suppressed phenotype. The excessively-long filopodial protrusions of *unc-33* mutants were reduced to wild-type levels, but were significantly longer than in animals with FMO-5 transgenic expression, and the growth cone area was reduced to resemble FMO-5 transgenic expression alone (Figure 2.13). This hybrid phenotype makes it difficult to determine if FMO-5 and UNC-33 act in the same pathway, in parallel pathways, or both.

One proposed mechanism of cytoskeletal regulation by MICAL is the production of the reactive oxygen species (ROS) H_2O_2 by the FAD domain in the presence of NADPH (Nadella et al., 2005). Upon activation by Sema3A, MICALs generate H_2O_2, which can, via thioredoxin, promote phosphorylation of CRMP2 via glycogen synthase kinase-3, leading to growth cone collapse (Morinaka et al., 2011). Thus, the FMOs have the potential to inhibit growth cone protrusion through direct oxidation of F-actin resulting in depolymerization, and through redox regulation of the activity of UNC-33/CRMP (i.e. to act both in the UNC-33 pathway and in parallel to it).

In summary, we present evidence of a novel role of the *C. elegans* flavin-containing monooxygenase molecules (FMOs) in inhibition of growth cone protrusion downstream of UNC-6/Netrin signaling. The FMOs acted downstream of the UNC-6/Netrin receptors UNC-5 and UNC-40, and downstream of the Rac GTPases CED-10 and MIG-2 (Figure 2.14). Future studies will determine if the FMOs regulate UNC-33/CRMP, if they cause actin depolymerization, or both, to inhibit growth cone protrusion.

Figure 2.1

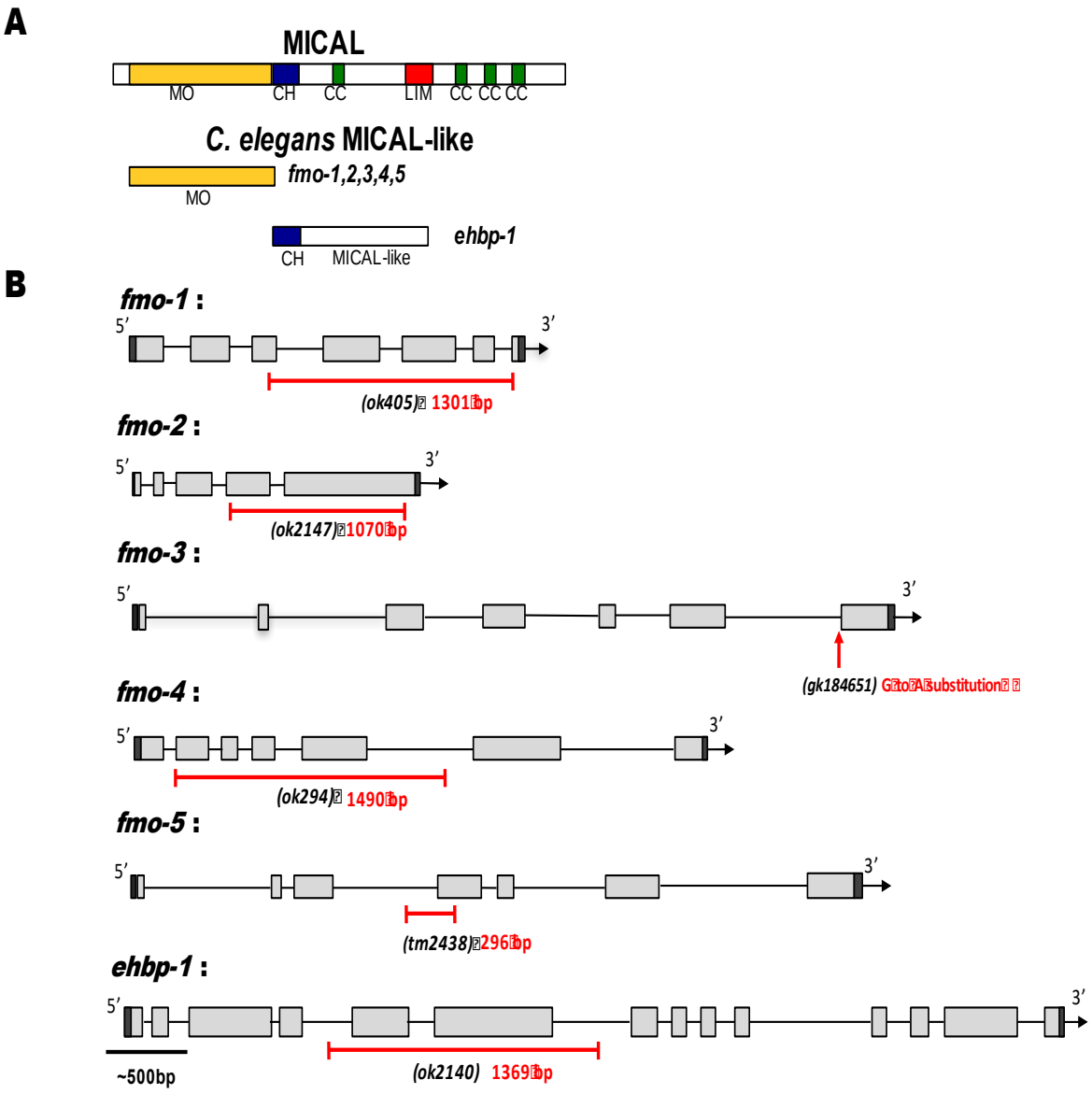
A
MICAL
MO
CH
CC
LIM
CC CC CC
C. elegans MICAL-like
fmo-1,2,3,4,5
MO
ehbp-1
CH
MICAL-like
B
fmo-1 :
5′
3′
(ok405) 1301bp
fmo-2 :
5′
3′
(ok2147) 1070bp
fmo-3 :
5′
3′
(gk184651) G to A substitution
fmo-4 :
5′
3′
(ok294) 1490bp
fmo-5 :
5′
3′
(tm2438) 296bp
ehbp-1 :
5′
3′
~500bp
(ok2140) 1369bp

Figure 2.1. *fmo* genes and *ehbp-1.* (A) Diagram of Drosophila MICAL, the *C. elegans* flavin monooxygenases (FMOs), and *C. elegans* EHBP-1. MO, flavin monooxygenase domain; CH-calponin homology domain, CC, coiled-coiled domain; LIM, LIM domain. **(B)** The structures of the *fmo-1*, *fmo-2*, *fmo-3*, *fmo-4*, *fmo-5* and *ehbp-1* genes are shown. Filled boxes represent exons. The extent of deletions in *fmo-1*, *fmo-2*, *fmo-4*, *fmo-5* and *ehbp-1* are shown below the structure, indicated by a red line. The red arrow points to the region of the splice site mutation in *fmo-3*. Scale bar indicates 500bp.

Figure 2.2.

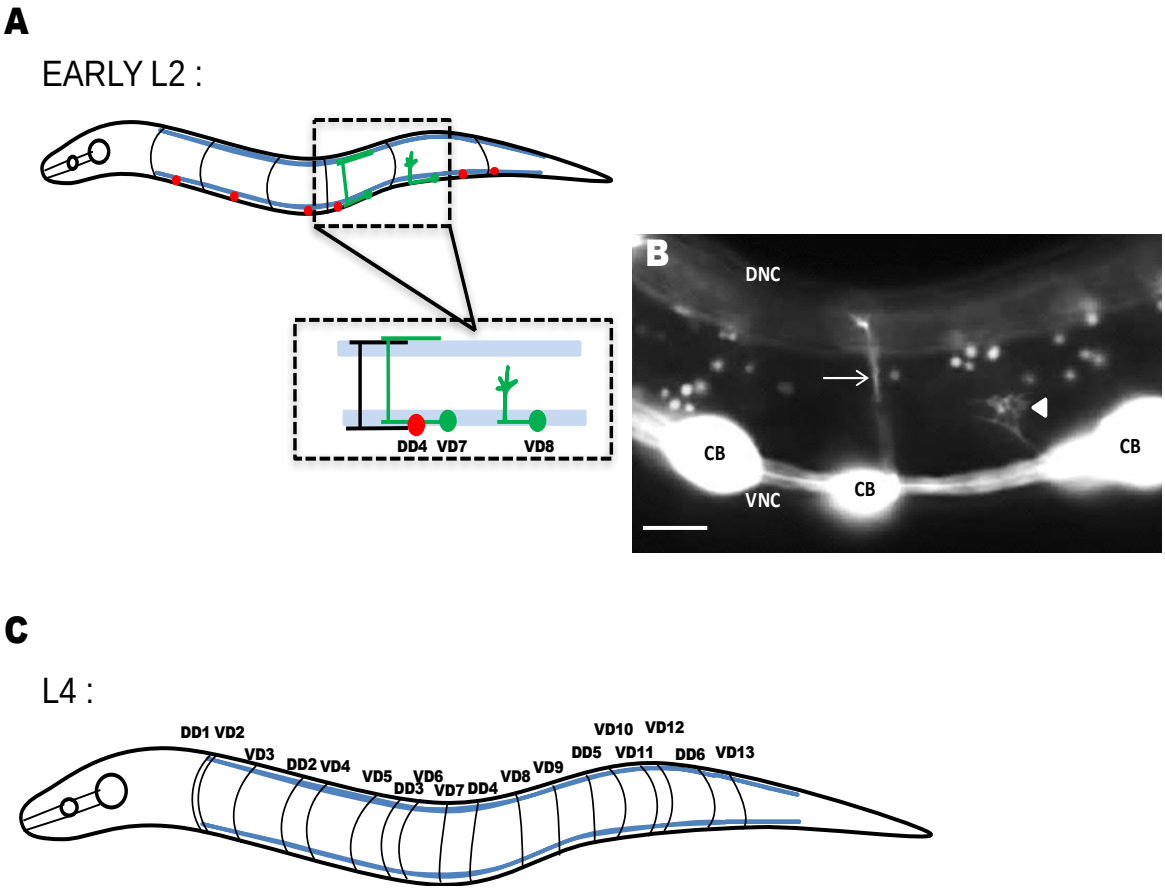
A
EARLY L2 :
DD4 VD7 VD8
B
DNC
CB
CB
CB
VNC
C
L4 :
DD1 VD2
VD3
DD2 VD4
VD5
DD3
VD6
VD7
DD4
VD8
VD9
VD10
VD12
DD5
VD11
DD6
VD13

Figure 2.2. VD/DD motor neurons and axons in *C. elegans*. (A) Diagram of an early L2 larval *C. elegans* hermaphrodite highlighting the position and structure of the DD motor neurons (red) and axons (black). Anterior is to the left, and dorsal is up. The blue lines represent the ventral and dorsal muscle quadrants. In the early L2 larval stage, the VD neurons (green) extend axons anteriorly in the ventral nerve cord after which the axons turn dorsally and migrate to the dorsal nerve cord to form commissures. Only two of the 13 VD neurons are shown. While migrating towards the dorsal nerve cord, VD growth cones display an extended, protrusive morphology with highly dynamic filopodial protrusions (VD8). VD7 shows the final structure of the VD neurite. **(B)** Fluorescent micrograph of an early L2 larval wild-type commissure indicated by an arrow, and a VD growth cone indicated by an arrowhead. CB, cell body; DNC, dorsal nerve cord; and VNC, ventral nerve cord. Scale bar represents 5μm. **(C)** Diagram of an L4 hermaphrodite after all the VD axon outgrowth is complete. The 18 commissures on the right side of the animal are shown (black lines), and axon guidance defects of these commissures were scored. One commissure (VD1) extends on the right side and was not scored. Of the 18 commissures on the right side, two (DD1 and VD2) extend as a single fascicle. Others pairs occasionally extended as single fascicles as well, resulting in an average of 16 observable commissures per *wild-type* animal.

Figure 2.3.

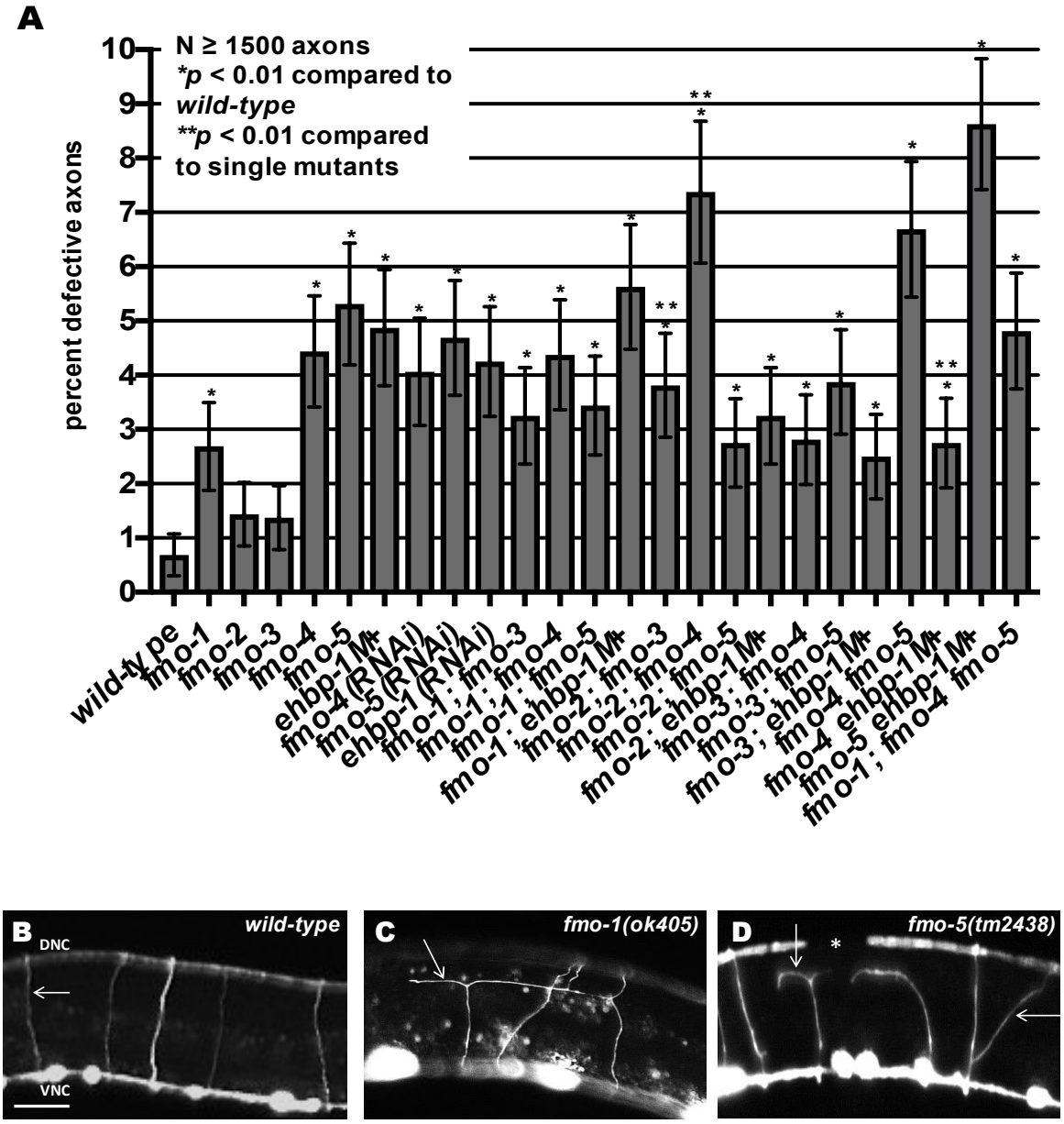
A
N ≥ 1500 axons
*p < 0.01 compared to wild-type
**p < 0.01 compared to single mutants
percent defective axons
0
1
2
3
4
5
6
7
8
9
10
wild-type
fmo-1
fmo-2
fmo-3
fmo-4
fmo-5
ehbp-1M+
fmo-4(RNAi)
fmo-5(RNAi)
ehbp-1(RNAi)
fmo-1 ; fmo-3
fmo-1 ; fmo-4
fmo-1 ; fmo-5
fmo-1 ; ehbp-1M+
fmo-2 ; fmo-3
fmo-2 ; fmo-4
fmo-2 ; fmo-5
fmo-2 ; ehbp-1M+
fmo-3 ; fmo-4
fmo-3 ; fmo-5
fmo-3 ; ehbp-1M+
fmo-4 ; fmo-5
fmo-4 ; ehbp-1M+
fmo-5 ; ehbp-1M+
fmo-1 ; fmo-4
fmo-1 ; fmo-5

B
DNC
VNC
wild-type
C
fmo-1(ok405)
D
fmo-5(tm2438)

Figure 2.3. Mutations in *fmo-1, fmo-4, fmo-5* and *ehbp-1* cause axon pathfinding defects. (A) Percentage of VD/DD axons with pathfinding defects (see Materials and Methods) in single mutants, double mutants and triple mutant harboring the *juIs76[Punc-25::gfp]* transgene. Single asterisks (*) indicate the significant difference between wild-type and the mutant phenotype ($p < 0.01$); Double asterisks (**) indicate significant difference between double mutants and the predicted additive effect of single mutants ($p < 0.01$) determined by Fischer's exact test. Error bars represent 2x standard error of proportion. **(B-D)** Representative fluorescent micrograph of L4 VD/DD axons. Anterior is to the left, and dorsal is up. The scale bar represents 5μm. DNC, dorsal nerve cord; and VNC, ventral nerve cord. (B) A *wild-type* commissure is indicated by an arrow. (C) An *fmo-1(ok405)* commissure branched and failed to reach to dorsal nerve cord (arrow). (D) *fmo-5(tm2438)* VD/DD axons branched and wandered (arrows). A gap in the dorsal nerve cord (asterisk) indicates that commissural processes failed to reach the dorsal nerve cord. determined by Fischer's exact test. At least 1500 axons were scored per genotype. M+ indicates that the animal has wild-type maternal *ehbp-1(+)* activity.

Figure 2.4.

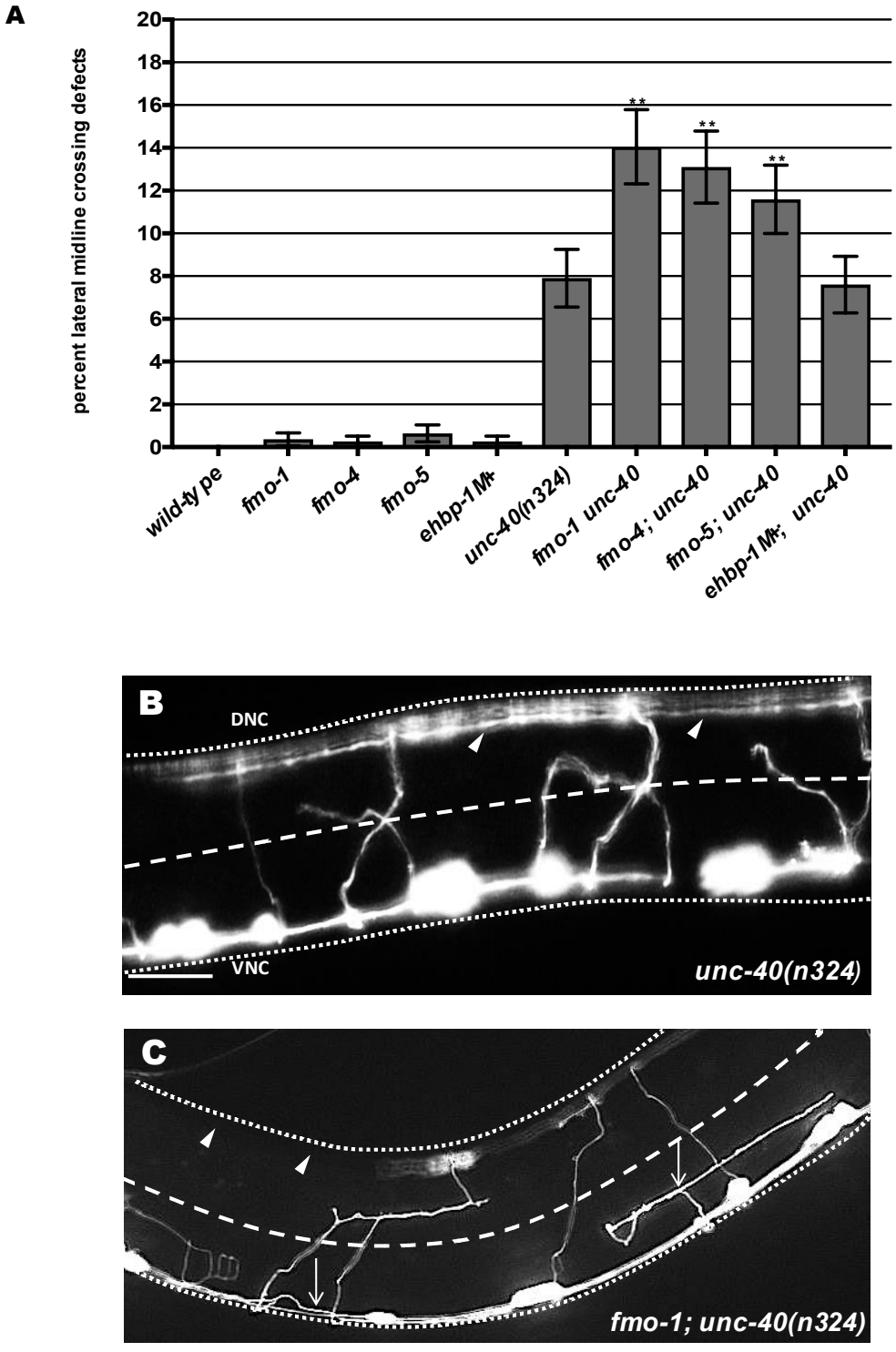
A
percent lateral midline crossing defects
20
18
16
14
12
10
8
6
4
2
0
**
**
**
wild-type
fmo-1
fmo-4
fmo-5
ehbp-1Mr
unc-40(n324)
fmo-1 unc-40
fmo-4; unc-40
fmo-5; unc-40
ehbp-1Mr; unc-40
B
DNC
VNC
unc-40(n324)
C
fmo-1; unc-40(n324)

Figure 2.4. Axon pathfinding defects in *unc-40(n324)* are enhanced by loss of *fmo-1*, *fmo-4* and *fmo-5*. (A) Percentage of VD/DD axons that failed cross the lateral midline of L4 hermaphrodites. Error bars represent 2x standard error of the proportion; double asterisks (**) indicates a significant difference between *unc-40(n324)* alone and the double mutants ($p < 0.001$) determined by Fisher's exact test. Only axon commissures visibly emanating from the ventral nerve cord were scored. **(B,C)** Representative images showing VD/DD axons (arrows) after their complete outgrowth in L4 animals. The lateral midline of the animal is indicated by the dashed white line. The dorsal nerve cord and ventral nerve cord are indicated by a dotted white line. Dorsal is up, anterior is to the left. Scale bar represents 5μm. (B) In *unc-40(n324)*, many axons extend past the lateral midline, as evidenced by axons in the dorsal nerve cord (arrowheads). (C) In *fmo-1(ok405); unc-40(n324)*, an increased number of axons did not cross the midline resulting in extensive regions of dorsal nerve cord without axons (arrowheads). Arrowhead indicates large gaps in the dorsal nerve cord.

Figure 2.5.

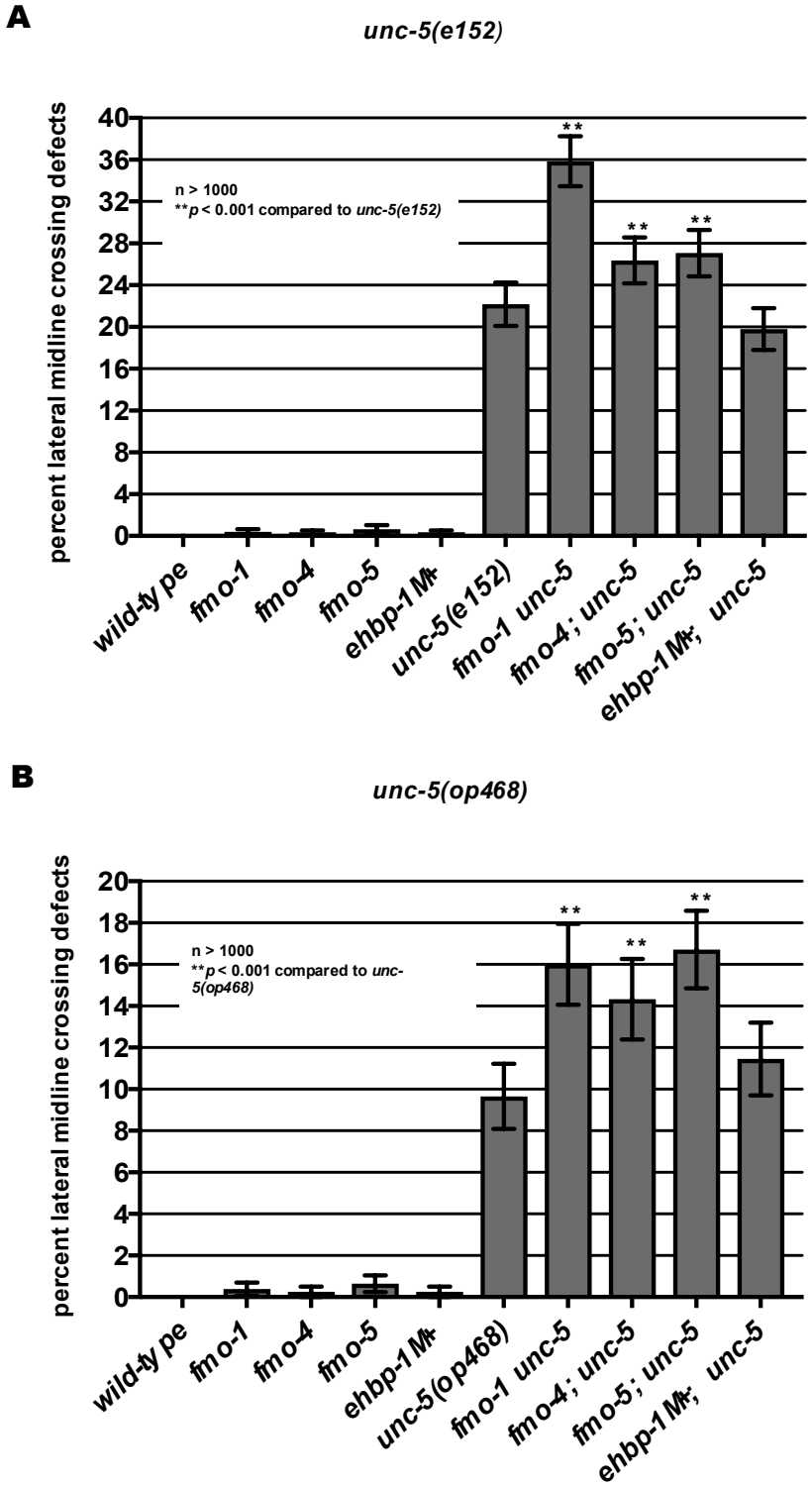
A
unc-5(e152)
percent lateral midline crossing defects
n > 1000
**p < 0.001 compared to unc-5(e152)
wild-type
fmo-1
fmo-4
fmo-5
ehbp-1Mt
unc-5(e152)
fmo-1 unc-5
fmo-4; unc-5
fmo-5; unc-5
ehbp-1Mt; unc-5
B
unc-5(op468)
percent lateral midline crossing defects
n > 1000
**p < 0.001 compared to unc-5(op468)
wild-type
fmo-1
fmo-4
fmo-5
ehbp-1Mt
unc-5(op468)
fmo-1 unc-5
fmo-4; unc-5
fmo-5; unc-5
ehbp-1Mt; unc-5

Figure 2.5.

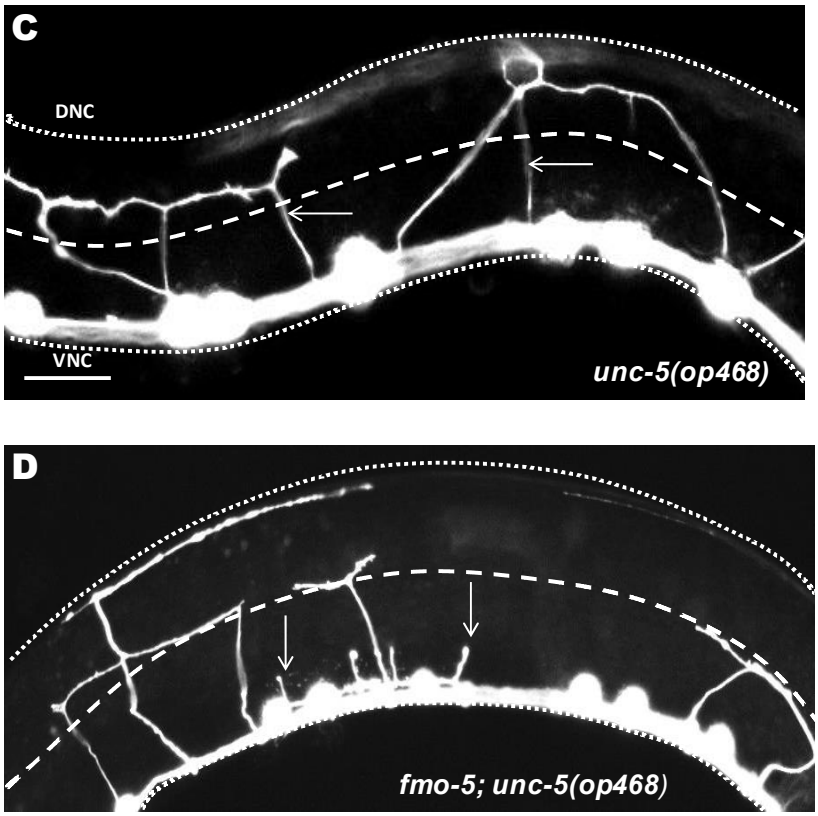

Figure 2.5. Axon pathfinding defects of hypomorphic *unc-5* mutants are enhanced by loss of *fmo-1* and *fmo-4*. (A) and (B) Quantification of VD/DD axons that failed to cross the lateral midline of L4 hermaphrodites in hypomorphic *unc-5(e152)* and *unc-5(op468)* mutants alone and in double mutant animals. Error bars represent 2x standard error of the proportion; double asterisks (**) indicates a significant difference between *unc-5(e152)* or *unc-5(op468)* alone and the double mutants ($p < 0.001$) determined by Fisher's exact test. Only visible commissural processes emanating from the ventral nerve cord were scored. **(C,D)** Fluorescence micrographs of VD/DD axons (arrows) in L4 hermaphrodites. The lateral midline of the animal is indicated by the dashed white line. The dorsal nerve cord and ventral nerve cord are indicated by dotted white lines. Dorsal is up, anterior is to the left. Scale bar represents 5μm. (C) In the weak loss of function *unc-5(op468)* mutants, axons crossing the lateral midline are indicated (arrows). (D) In *fmo-5(tm2438); unc-5(op468)*, some axons cross the lateral midline, but many terminate before crossing the lateral midline (arrows).

Figure 2.6.

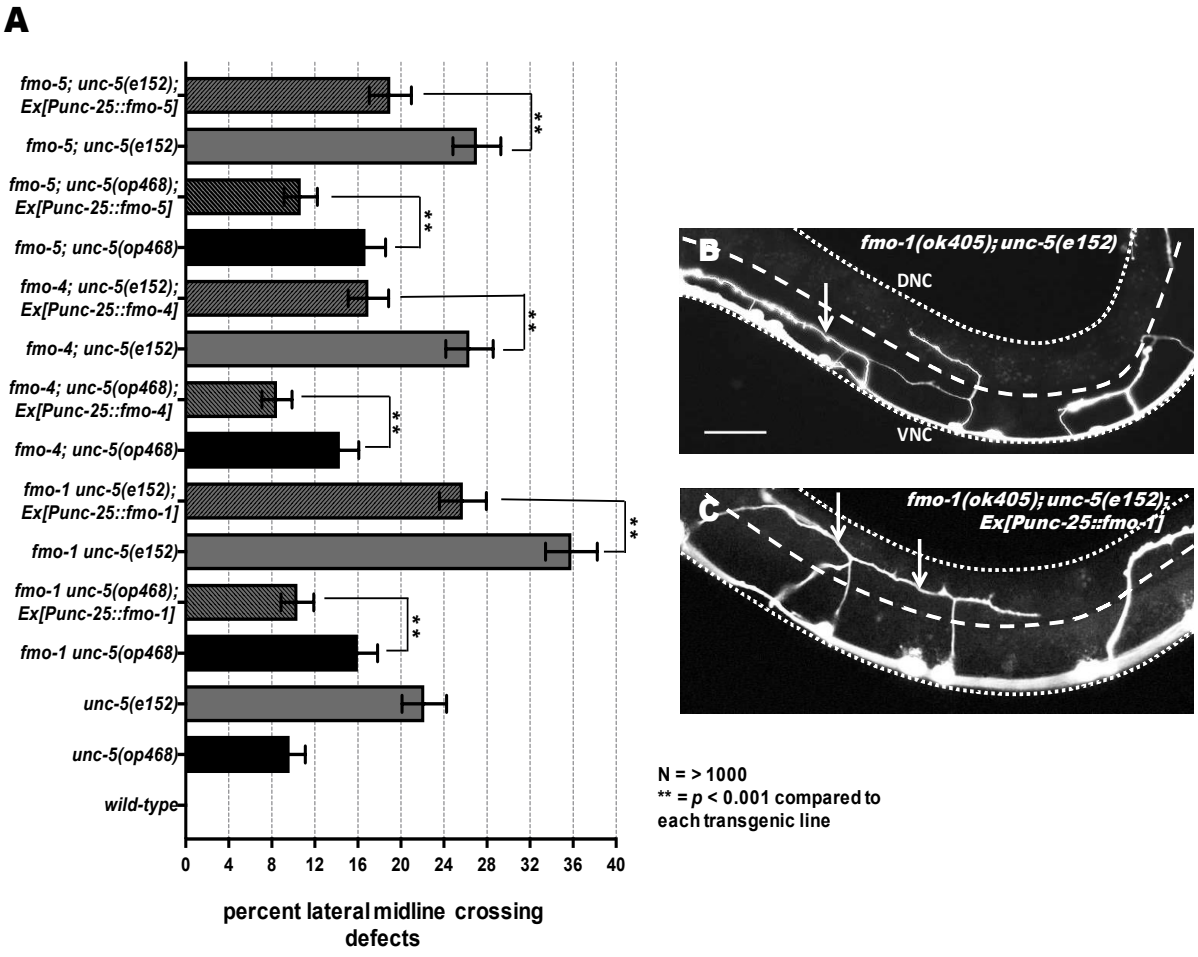
A
fmo-5; unc-5(e152); Ex[Punc-25::fmo-5]
fmo-5; unc-5(e152)
fmo-5; unc-5(op468); Ex[Punc-25::fmo-5]
fmo-5; unc-5(op468)
fmo-4; unc-5(e152); Ex[Punc-25::fmo-4]
fmo-4; unc-5(e152)
fmo-4; unc-5(op468); Ex[Punc-25::fmo-4]
fmo-4; unc-5(op468)
fmo-1 unc-5(e152); Ex[Punc-25::fmo-1]
fmo-1 unc-5(e152)
fmo-1 unc-5(op468); Ex[Punc-25::fmo-1]
fmo-1 unc-5(op468)
unc-5(e152)
unc-5(op468)
wild-type
0 4 8 12 16 20 24 28 32 36 40
percent lateral midline crossing defects
B
fmo-1(ok405); unc-5(e152)
DNC
VNC
C
fmo-1(ok405); unc-5(e152); Ex[Punc-25::fmo-1]
N = > 1000
** = p < 0.001 compared to each transgenic line

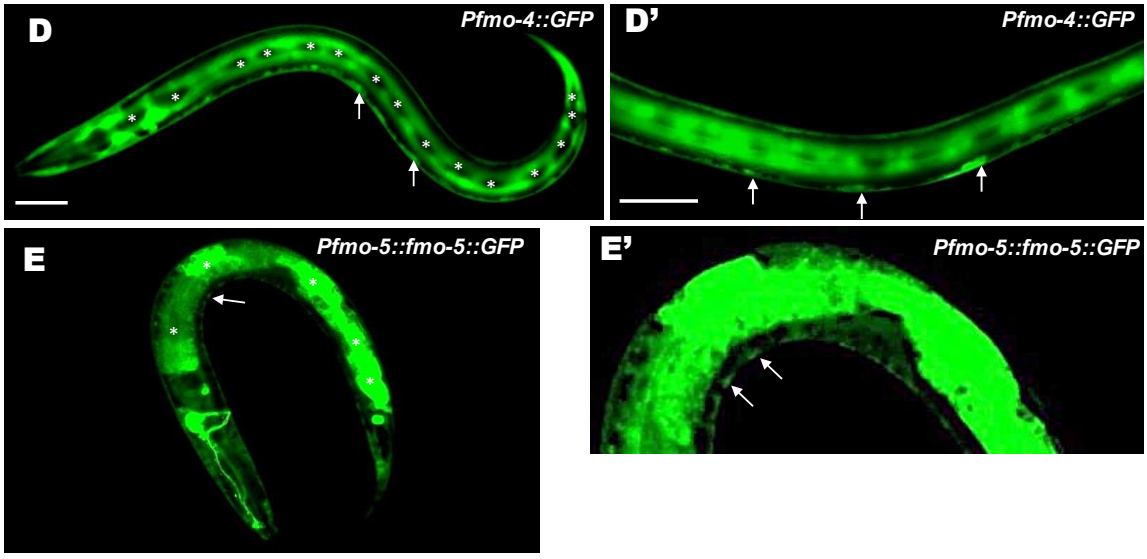
D
Pfmo-4::GFP
D'
Pfmo-4::GFP
E
Pfmo-5::fmo-5::GFP
E'
Pfmo-5::fmo-5::GFP

Figure 2.6. Expression of *fmo-1, fmo-4 and fmo-5* in VD/DD neurons rescues axon pathfinding defects. (A) The percentages of VD/DD axons failing to cross the lateral mid-line are as described in Figure 2.5A. *unc-5* double mutant genotypes are indicated, and the *Punc-25::fmo-1, Punc-25::fmo-4,* and *Punc-25::fmo-5* transgenes are bracketed. Data for transgenic strains are the combined results from three independently-derived transgenes with similar effects. Double asterisks (**) indicate a significant difference between the double mutant and the transgenic strain (p <0.001; Fisher's exact test). Error bars represent 2x standard error of the proportion. **(B, C)** Micrographs of mutant and rescued animals. Dorsal is up, anterior to the left. Scale bar represents 5μm. The lateral midline of the animal is indicated by the dashed white line. The dorsal nerve cord and ventral nerve cord are indicated by dotted white lines. (B) *fmo-1(ok405) unc-5(e152)* axons often fail to cross the lateral midline (arrow). (C) *fmo-1(ok405) unc-5(e152*); Ex(*Punc-25::fmo-1*) axons crossed the lateral midline (arrows). **(D-E and D'-E')** Images are micrographs of L2 animals with transgenic expression of *Pfmo-4::gfp* and *Pfmo-5::fmo-5::gfp*. Dorsal is up and anterior is left. Scale bar: 5μm. (D) *fmo-4::gfp* is broadly expressed, including in hypodermis and in cells along the ventral nerve cord that resemble motor neurons. Expression is not evident in the lateral hypodermal seam cells (asterisks). (D') Enlarged image of *fmo-4::gfp* expression in ventral nerve cord cells (arrows). (E). *fmo-5::gfp* is expressed strongly in the gut (asterisks), as well as in cells along the ventral nerve cord. (arrow) (E') Enlarged image of *fmo-5::gfp* expression in ventral nerve cord cells (arrows).

Figure 2.7.

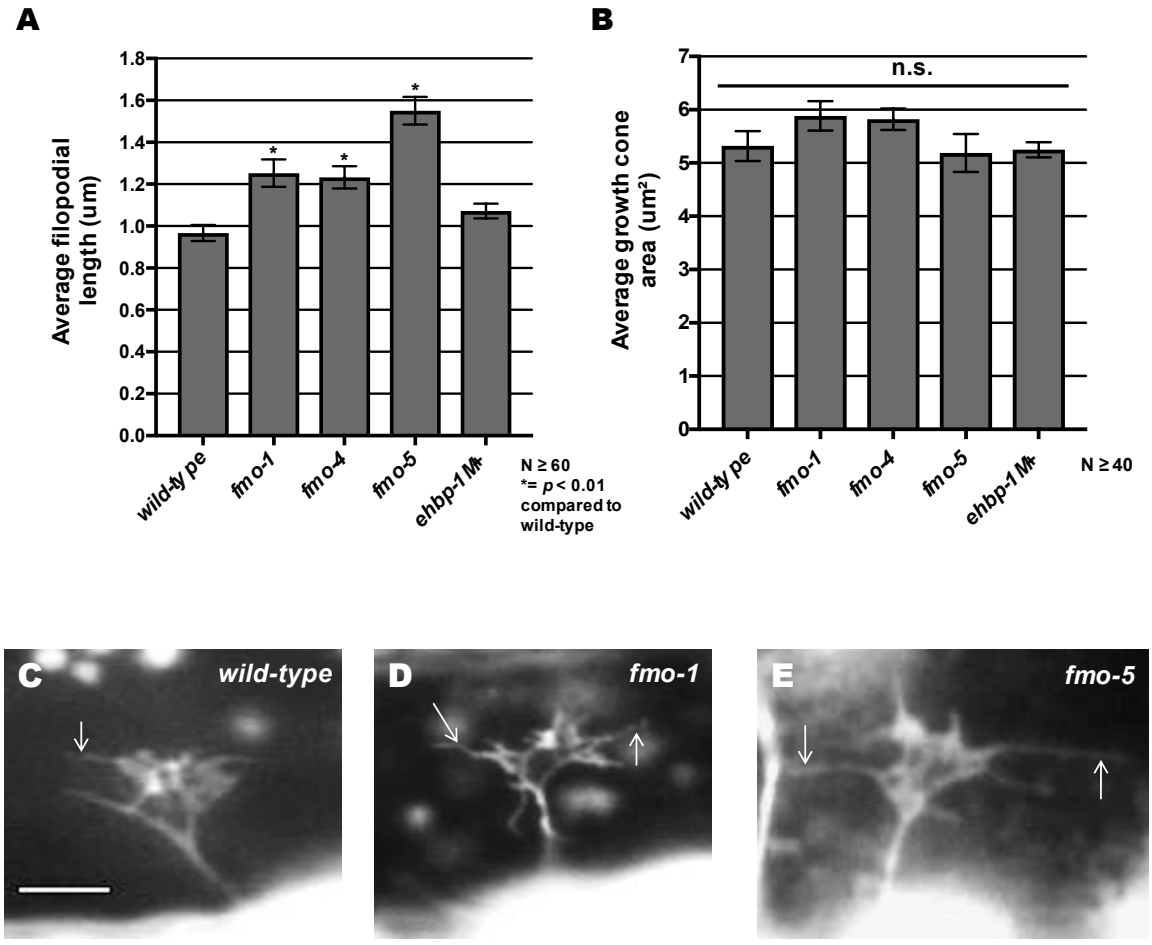
A
Average filopodial length (um)
1.8
1.6
1.4
1.2
1.0
0.8
0.6
0.4
0.2
0.0
*
*
*
wild-type
fmo-1
fmo-4
fmo-5
ehbp-1 M-
N ≥ 60
*= p < 0.01 compared to wild-type
B
Average growth cone area (um²)
7
6
5
4
3
2
1
0
n.s.
wild-type
fmo-1
fmo-4
fmo-5
ehbp-1 M-
N ≥ 40
C
wild-type
D
fmo-1
E
fmo-5

Figure 2.7. Mutations in *fmo-1, fmo-4* and *fmo-5* increase VD growth cone filopodial length. (A,B) Quantification of VD growth cone filopodial length and growth cone area in wild-type and mutant animals. (A) Average filopodial length, in μm. (B) Growth cone area in μm^2. Error bars represent 2x standard error of the mean; asterisks indicate the significant difference between wild-type and the mutant phenotype (*$p < 0.01$) determined by two-sided *t*-test with unequal variance. n.s., not significant. **(C-E)** Fluorescence micrographs of VD growth cones; (C) A wild-type VD growth cone. (D) *fmo-1(ok405)* and (E) *fmo-5(tm2438)* growth cones showing increased filopodial protrusion in the form of longer filopodia. Arrows indicate representative filopodia. Scale bar: 5μm.

Figure 2.8.

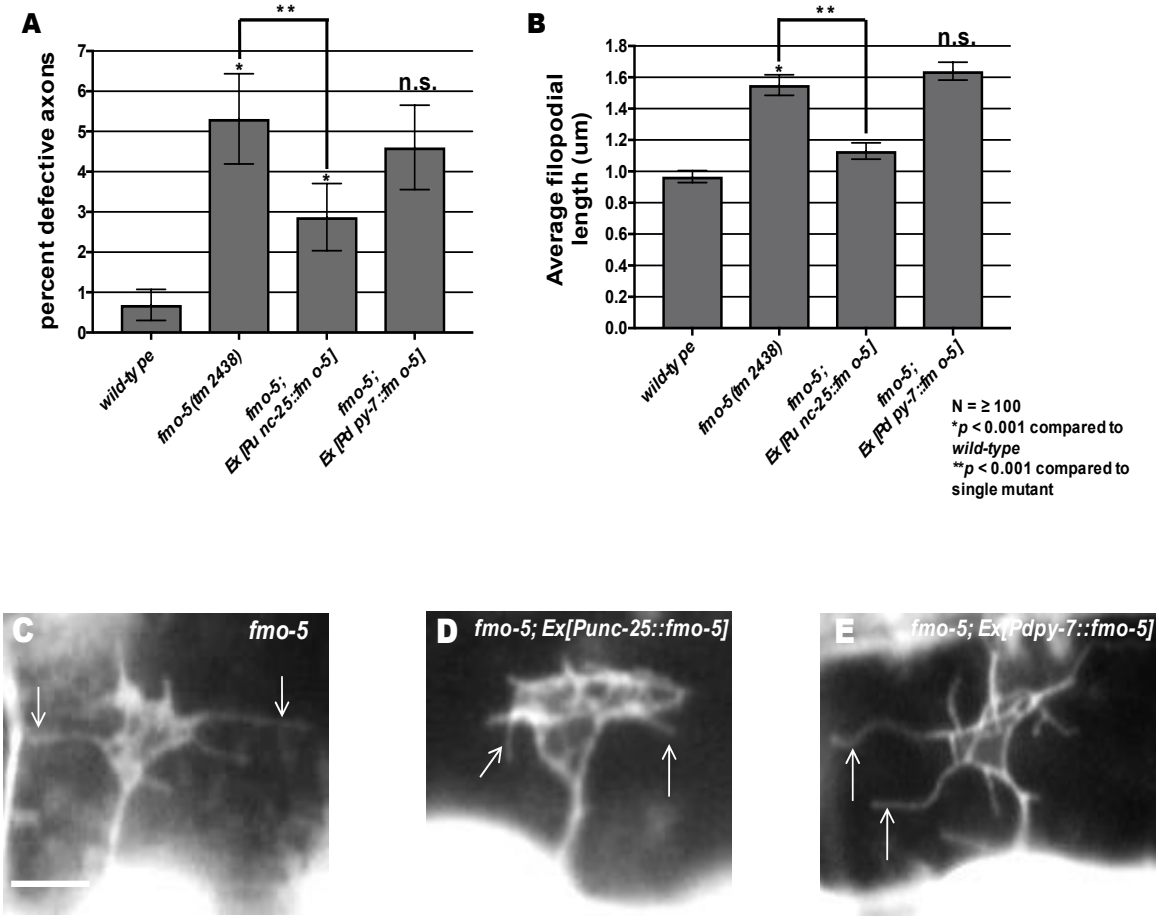
A
percent defective axons
**
*
*
n.s.
wild-type
fmo-5(tm2438)
fmo-5; Ex[Punc-25::fmo-5]
fmo-5; Ex[Pdpy-7::fmo-5]
B
Average filopodial length (um)
**
*
n.s.
wild-type
fmo-5(tm2438)
fmo-5; Ex[Punc-25::fmo-5]
fmo-5; Ex[Pdpy-7::fmo-5]
N = ≥ 100
*p < 0.001 compared to wild-type
**p < 0.001 compared to single mutant
C
fmo-5
D
fmo-5; Ex[Punc-25::fmo-5]
E
fmo-5; Ex[Pdpy-7::fmo-5]

Figure 2.8. Expression of *fmo-5* in VD/DD neurons rescues axon pathfinding defects and growth cone filopodial protrusion. (A) Rescue of *fmo-5(tm2438)* VD/DD axons by transgenes expressing *fmo-5* under the *unc-25* promoter (*Ex[Punc-25(fmo-5)]*). Data for transgenic arrays are the combined results from three independently-derived arrays with similar effects. Single asterisks (*) indicate a significant difference between wild type and the mutant ($p < 0.001$); Double asterisks (**) indicates a significant difference between the mutant and rescuing transgene ($p < 0.001$) determined by two-sided *t*-test with unequal variance. (**B**) Rescue of *fmo-5(tm2438)* VD growth cone filopodial length by transgenes expressing *fmo-5* under the *unc-25* promoter (*Ex[Punc-25(fmo-5)]*). Average lengths of filopodial protrusions are shown (μm). Error bars represent 2x standard error of the mean. Data for transgenic arrays are the combined results from three independently-derived arrays with similar effects. Single asterisks (*) indicate a significant difference between wild type and the mutant ($p < 0.001$); Double asterisks (**) indicates a significant difference between the mutant and rescuing transgene ($p < 0.001$) determined by two-sided *t*-test with unequal variance. n.s., not significant. **(C-E)** Fluorescence micrographs of VD growth cones in *fmo-5(tm2438)*, *fmo-5(tm2438); Ex[Punc-25::fmo-5]* and *fmo-5(tm2438); Ex[Pdpy-7::fmo-5]* which showed no rescue. Arrows indicate representative filopodia. Scale bar: 5μm.

Figure 2.9.

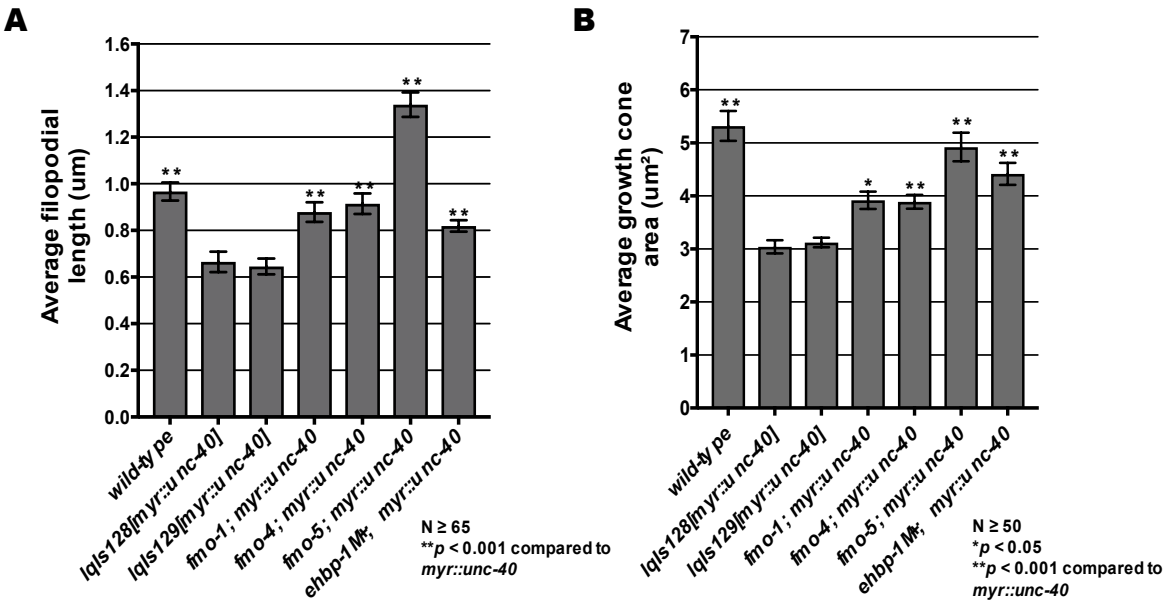
A
Average filopodial length (um)
1.6
1.4
1.2
1.0
0.8
0.6
0.4
0.2
0.0
**
wild-type
lqIs128[myr::unc-40]
lqIs129[myr::unc-40]
fmo-1; myr::unc-40
fmo-4; myr::unc-40
fmo-5; myr::unc-40
ehbp-1Mt; myr::unc-40
N ≥ 65
**p < 0.001 compared to myr::unc-40
B
Average growth cone area (um²)
7
6
5
4
3
2
1
0
*
N ≥ 50
*p < 0.05
**p < 0.001 compared to myr::unc-40

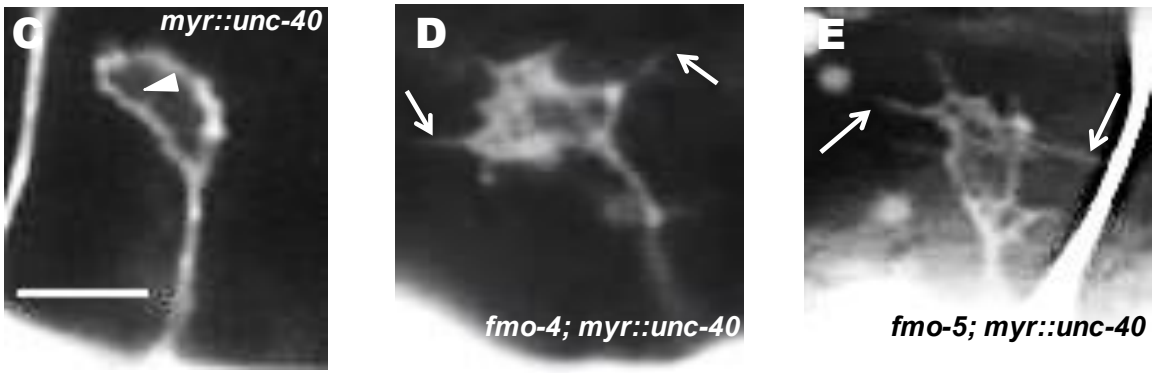
C
myr::unc-40
D
fmo-4; myr::unc-40
E
fmo-5; myr::unc-40

Figure 2.9. FMO-1, FMO-4, FMO-5, and EHBP-1 are required for MYR::UNC-40-mediated inhibition of VD growth cone protrusion. (A,B) Quantification of VD growth cone filopodial length and growth cone area in *wild-type*, *myr::unc-40 (lqIs128* and *lqIs129)* and double mutants. (A) Average filopodial length, in μm. (B) Growth cone area in μm^2. Error bars represent 2x standard error of the mean. Asterisks indicate significant difference between *myr::unc-40*, *wild-type* and the double mutants (*$p < 0.05$, ** $p < 0.001$) determined by two-sided *t*-test with unequal variance. **(C-E)** Fluorescent micrographs of mutant VD growth cones; (C) Image of a *myr::unc-40* growth cone in an early L2 animal. The arrowhead points to a growth cone with little or no filopodial protrusion. (D, E) Images of *fmo-4(ok294); myr::unc-40* and *fmo-5(tm2438); myr::unc-40* growth cones. Filopodial protrusions are indicated (arrows). Scale bar: 5μm. *fmo-1(ok405); myr::unc-40* double mutants were built and compared with *lqIs129[myr::unc-40]* due to the linkage of the *lqIs128* transgene.

Figure 2.10.

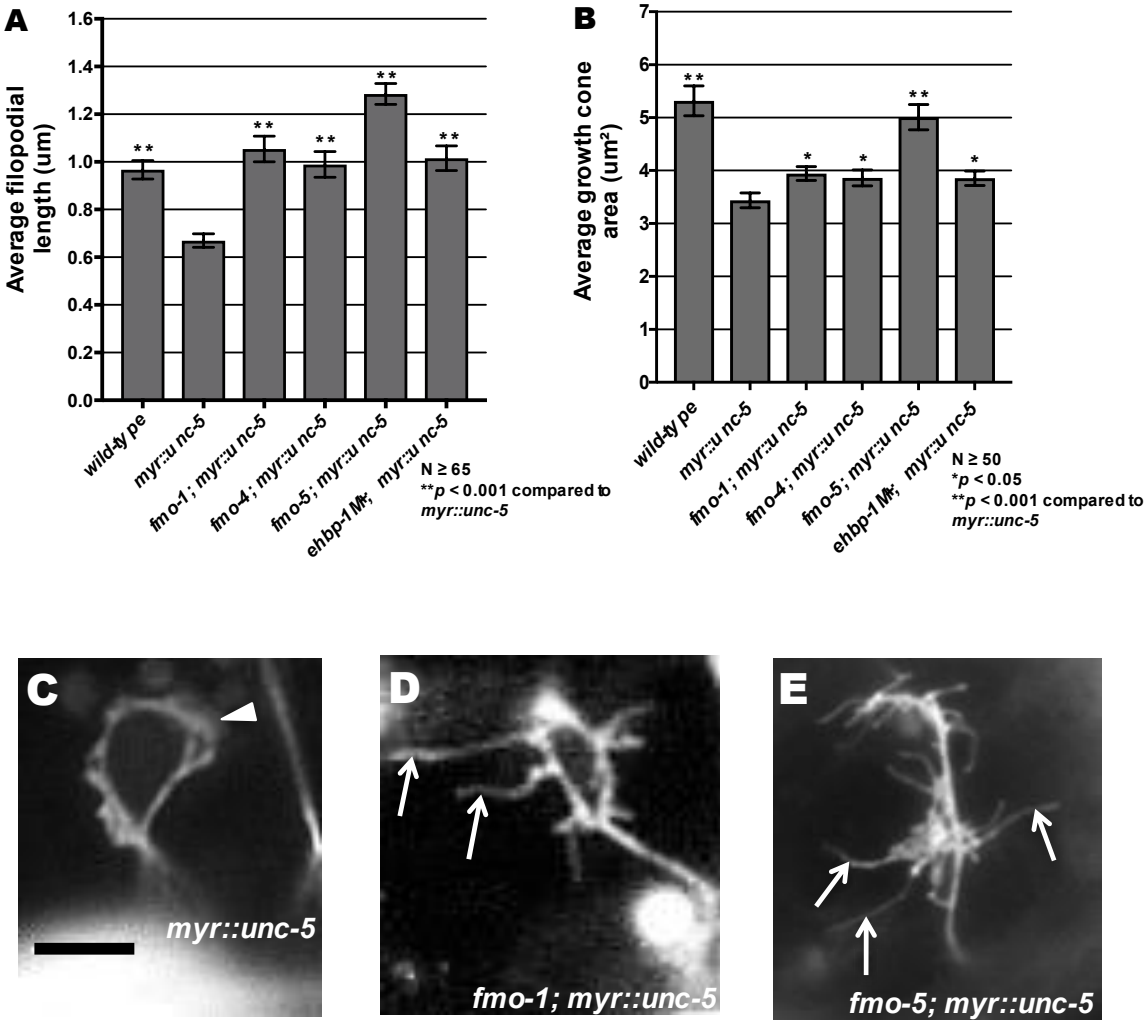
A
Average filopodial length (um)
1.6
1.4
1.2
1.0
0.8
0.6
0.4
0.2
0.0
**
wild-type
myr::unc-5
fmo-1; myr::unc-5
fmo-4; myr::unc-5
fmo-5; myr::unc-5
ehbp-1Mut; myr::unc-5
N ≥ 65
**p < 0.001 compared to myr::unc-5
B
Average growth cone area (um²)
7
6
5
4
3
2
1
0
**
*
wild-type
myr::unc-5
fmo-1; myr::unc-5
fmo-4; myr::unc-5
fmo-5; myr::unc-5
ehbp-1Mut; myr::unc-5
N ≥ 50
*p < 0.05
**p < 0.001 compared to myr::unc-5
C
myr::unc-5
D
fmo-1; myr::unc-5
E
fmo-5; myr::unc-5

Figure 2.10. FMO-1, FMO-4, FMO-5, and EHBP-1 are required for MYR::UNC-5-mediated inhibition of VD growth cone protrusion. (A,B) Quantification of VD growth cone filopodial length and growth cone area in *wild-type*, *myr::unc-5,* and double mutants. (A) Average filopodial length, in μm. (B) Growth cone area in μm^2. Error bars represent 2x standard error of the mean. Asterisks indicate significant difference between *myr::unc-5* and the double mutants (**p* < 0.05, ***p* < 0.001) determined by two-sided *t*-test with unequal variance. **(C-E)** Representative fluorescent micrographs of mutant VD growth cones; (C) Image of a *myr::unc-5* growth cone in an early L2 animal. The arrowhead points to a growth cone with limited protrusion. (D, E) Images of *fmo-1(ok405); myr::unc-5* and *fmo-5(tm2438); myr::unc-5* growth cones. Arrows point to filopodial protrusions. Scale bar: 5μm.

Figure 2.11.

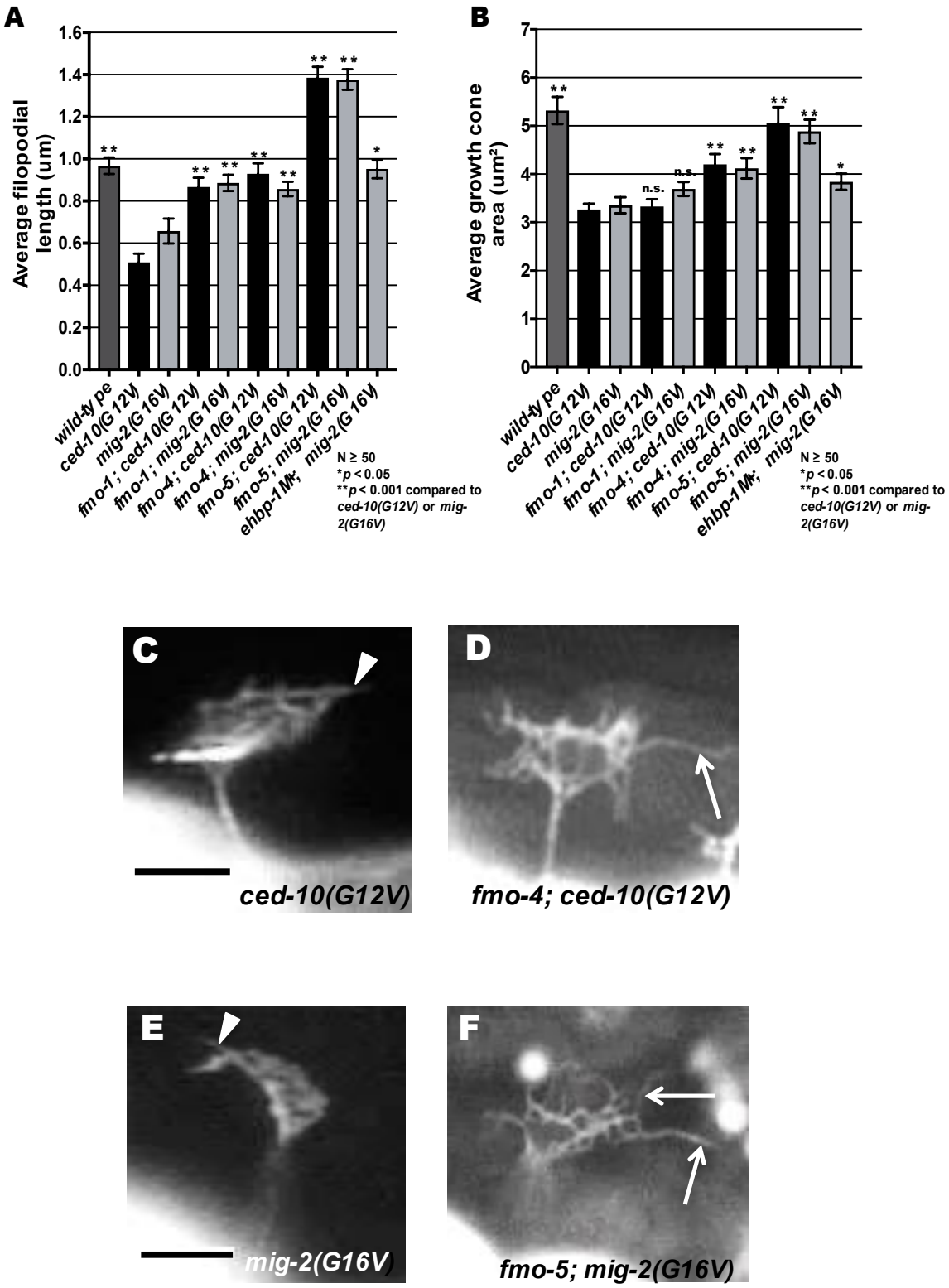
A
Average filopodial length (um)
1.6
1.4
1.2
1.0
0.8
0.6
0.4
0.2
0.0
wild-ty pe
ced-10(G12V)
mig-2(G16V)
fmo-1; ced-10(G12V)
fmo-1; mig-2(G16V)
fmo-4; ced-10(G12V)
fmo-4; mig-2(G16V)
fmo-5; ced-10(G12V)
fmo-5; mig-2(G16V)
ehbp-1Mt; mig-2(G16V)
N ≥ 50
*p < 0.05
**p < 0.001 compared to ced-10(G12V) or mig-2(G16V)
B
Average growth cone area (um²)
7
6
5
4
3
2
1
0
n.s.
n.s.
wild-ty pe
ced-10(G12V)
mig-2(G16V)
fmo-1; ced-10(G12V)
fmo-1; mig-2(G16V)
fmo-4; ced-10(G12V)
fmo-4; mig-2(G16V)
fmo-5; ced-10(G12V)
fmo-5; mig-2(G16V)
ehbp-1Mt; mig-2(G16V)
N ≥ 50
*p < 0.05
**p < 0.001 compared to ced-10(G12V) or mig-2(G16V)
C
ced-10(G12V)
D
fmo-4; ced-10(G12V)
E
mig-2(G16V)
F
fmo-5; mig-2(G16V)

Figure 2.11. FMO-1, FMO-4 and EHBP-1 are required for Rac GTPase-mediated inhibition of VD growth cone protrusion. (A,B) Quantification of VD growth cone filopodial length and growth cone area in *wild-type*, activated *ced-12(G12V)* and *mig-2(G16V),* and double mutants. (A) Average filopodial length, in μm. (B) Growth cone area in μm^2. Error bars represent 2x standard error of the mean. Asterisks indicate significant difference between *ced-10(G12V) mig-2(G16V)* and their respective double mutants (*$p < 0.05$, **$p < 0.001$) determined by two-sided *t*-test with unequal variance. n.s., not significant. **(C-F)** Representative fluorescent micrographs of mutant VD growth cones. (C,D) Images of *ced-10(G12V)* and *fmo-4(ok294); ced-10(G12V)* growth cones. The arrowhead in (C) points to a growth cone with limited protrusion, and the arrow in (D) indicates a filopodial protrusion. (E,F) Images of *mig-2(G16V)* and *fmo-5(tm2438); mig-2(G16V)* growth cones. The arrowhead in (E) points to a growth cone with limited protrusion, and the arrow in (F) indicates a filopodial protrusion. Scale bar: 5μm.

Figure 2.12.

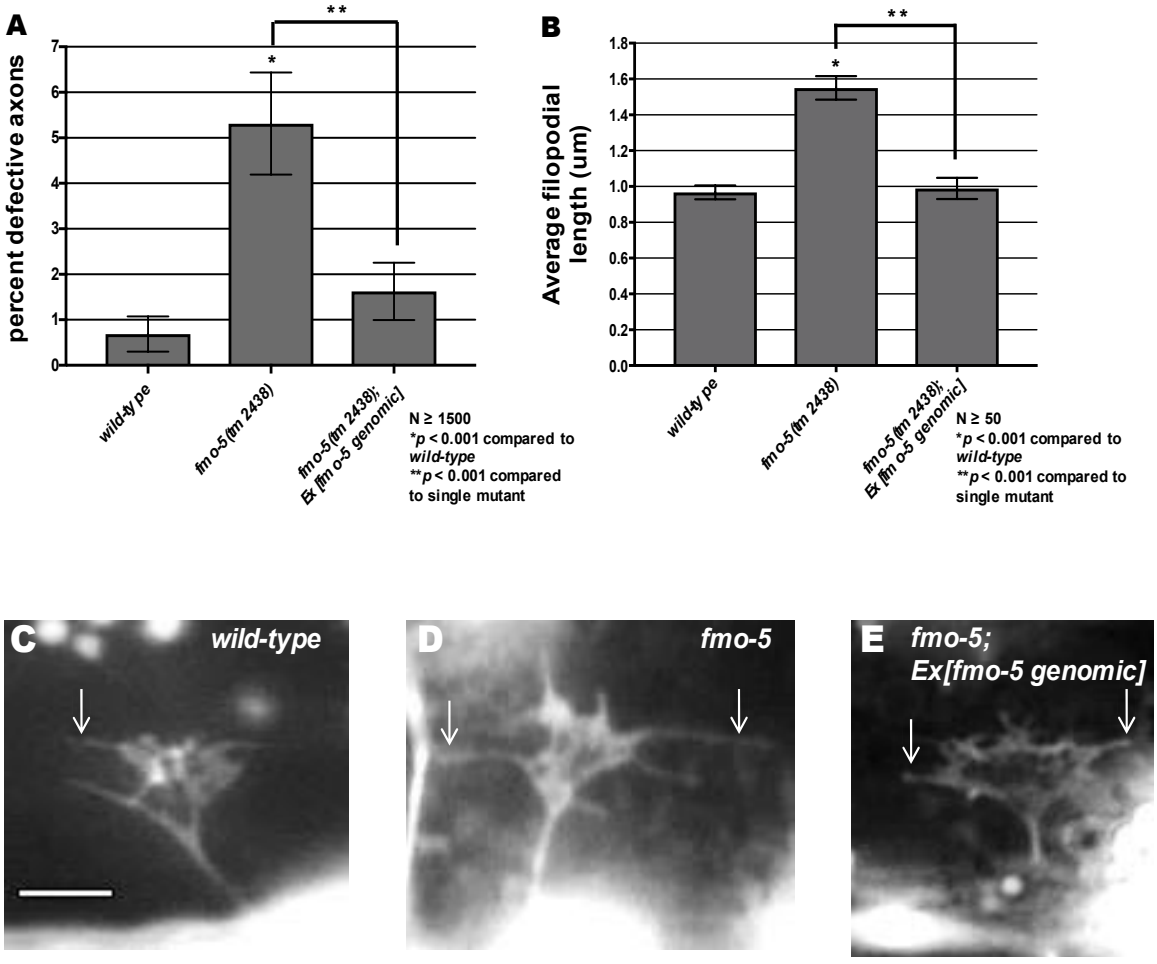
A
percent defective axons
0
1
2
3
4
5
6
7
*
**
wild-type
fmo-5(tm 2438)
fmo-5(tm 2438); Ex [fmo-5 genomic]
N ≥ 1500
*p < 0.001 compared to wild-type
**p < 0.001 compared to single mutant
B
Average filopodial length (um)
0.0
0.2
0.4
0.6
0.8
1.0
1.2
1.4
1.6
1.8
*
**
wild-type
fmo-5(tm 2438)
fmo-5(tm 2438); Ex [fmo-5 genomic]
N ≥ 50
*p < 0.001 compared to wild-type
**p < 0.001 compared to single mutant
C
wild-type
D
fmo-5
E
fmo-5;
Ex[fmo-5 genomic]

Figure 2.12. FMO-5 can inhibit growth cone filopodial protrusion. (A) Rescue of *fmo-5(tm2438)* VD/DD axons by transgenes containing genomic *fmo-5* (*Ex[fmo-5 genomic]*). Data for transgenic arrays are the combined results from three independently-derived arrays with similar effects. Single asterisks (*) indicate a significant difference between wild type and the mutant ($p < 0.001$); Double asterisks (**) indicates a significant difference between the mutant and rescuing transgene ($p < 0.001$) determined by two-sided *t*-test with unequal variance. **(B)** Rescue of *fmo-5(tm2438)* VD growth cone filopodial protrusions by transgenes containing genomic *fmo-5* (*Ex[fmo-5 genomic]*). Data for transgenic arrays are the combined results from three independently-derived arrays with similar effects. Average lengths of filopodial protrusions are shown (μm). Error bars represent 2x standard error of the mean. Single asterisks (*) indicate a significant difference between wild type and the mutant ($p < 0.001$); Double asterisks (**) indicates a significant difference between the mutant and rescuing transgene ($p < 0.001$) determined by two-sided *t*-test with unequal variance **(C-E)** Fluorescence micrographs of VD growth cones in *wild-type*, *fmo-5(tm2438)*, and *fmo-5(tm2438); Ex[fmo-5 genomic]*. Arrows indicate representative filopodia. Scale bar: 5μm.

Figure 2.13.

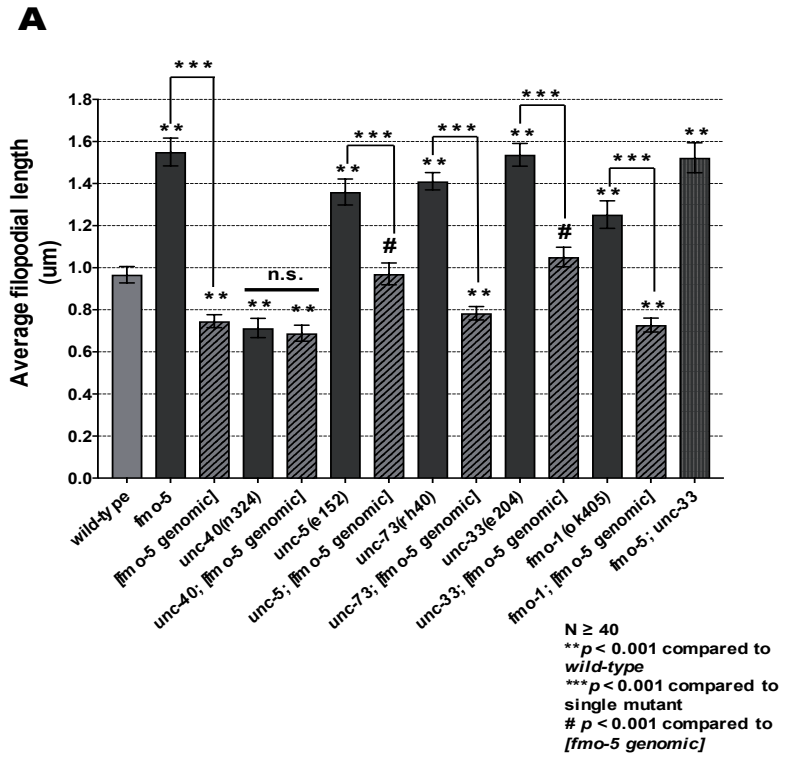
A
Average filopodial length (um)
1.8
1.6
1.4
1.2
1.0
0.8
0.6
0.4
0.2
0.0
n.s.
wild-type
fmo-5
[fmo-5 genomic]
unc-40(n324)
unc-40; [fmo-5 genomic]
unc-5(e152)
unc-5; [fmo-5 genomic]
unc-73(rh40)
unc-73; [fmo-5 genomic]
unc-33(e204)
unc-33; [fmo-5 genomic]
fmo-1(ok405)
fmo-1; [fmo-5 genomic]
fmo-5; unc-33
N ≥ 40
**p < 0.001 compared to wild-type
***p < 0.001 compared to single mutant
# p < 0.001 compared to [fmo-5 genomic]

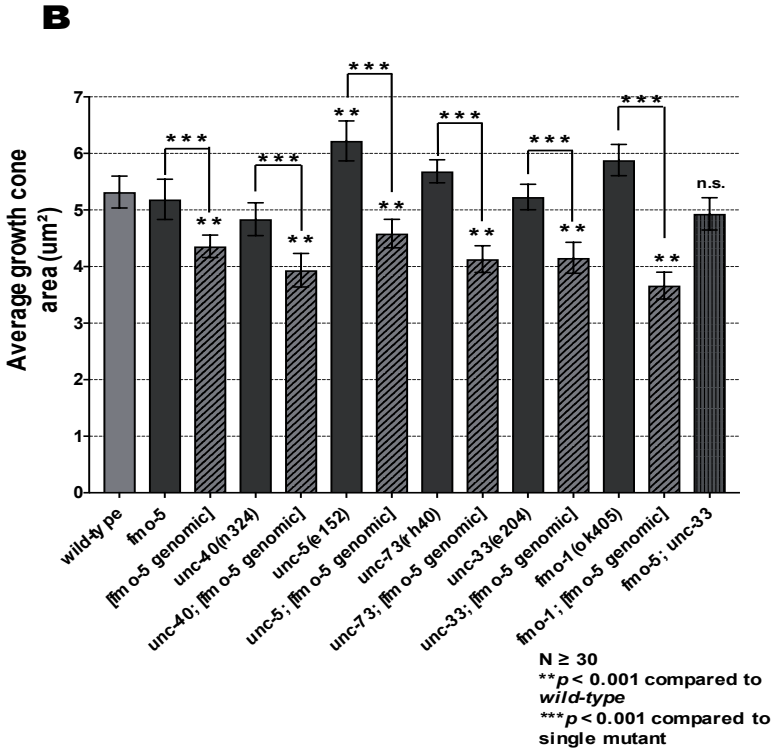
B
Average growth cone area (um²)
7
6
5
4
3
2
1
0
n.s.
wild-type
fmo-5
[fmo-5 genomic]
unc-40(n324)
unc-40; [fmo-5 genomic]
unc-5(e152)
unc-5; [fmo-5 genomic]
unc-73(rh40)
unc-73; [fmo-5 genomic]
unc-33(e204)
unc-33; [fmo-5 genomic]
fmo-1(ok405)
fmo-1; [fmo-5 genomic]
fmo-5; unc-33
N ≥ 30
**p < 0.001 compared to wild-type
***p < 0.001 compared to single mutant

Figure 2.13.

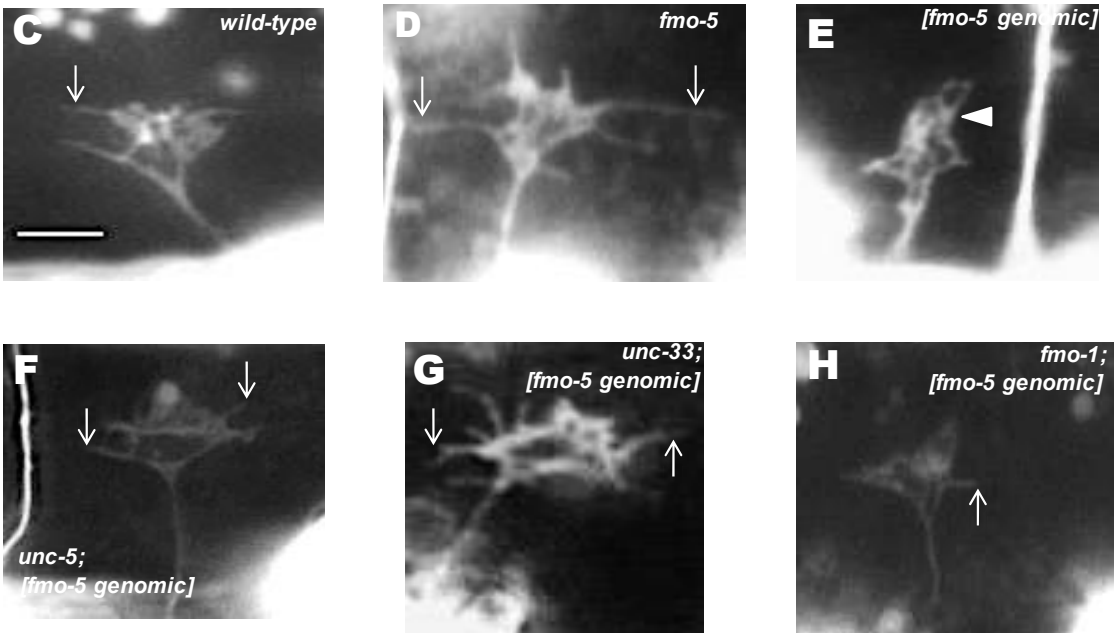
C
wild-type
D
fmo-5
E
[fmo-5 genomic]
F
unc-5;
[fmo-5 genomic]
G
unc-33;
[fmo-5 genomic]
H
fmo-1;
[fmo-5 genomic]

Figure 2.13. FMO-5 activity can partially compensate for UNC-5, UNC-73/Trio, and UNC-33/CRMP. (A,B) Quantification of VD growth cone filopodial length and growth cone area in indicated genotypes. Error bars represent 2x standard error of the mean. Asterisks indicate significant difference between wild-type and mutants (** $p < 0.001$) and *** indicate a significant difference between each single mutant compared to the double mutant. Pound signs (#) indicate a significant difference between [*fmo-5 genomic*] and double mutant (#$p < 0.001$) determined by two-sided *t*-test with unequal variance. n.s., not significant. **(C-H)** Fluorescence micrographs of VD growth cones from *wild-type*, *fmo-5(tm2438), [fmo-5 genomic]*, *unc-5; [fmo-5 genomic]*, *unc-33; [fmo-5 genomic]*and *fmo-1; [fmo-5 genomic]*. The arrowhead points to a growth cone with limited protrusion. Arrows indicate representative filopodia. Scale bar: 5μm.

Figure 2.14.

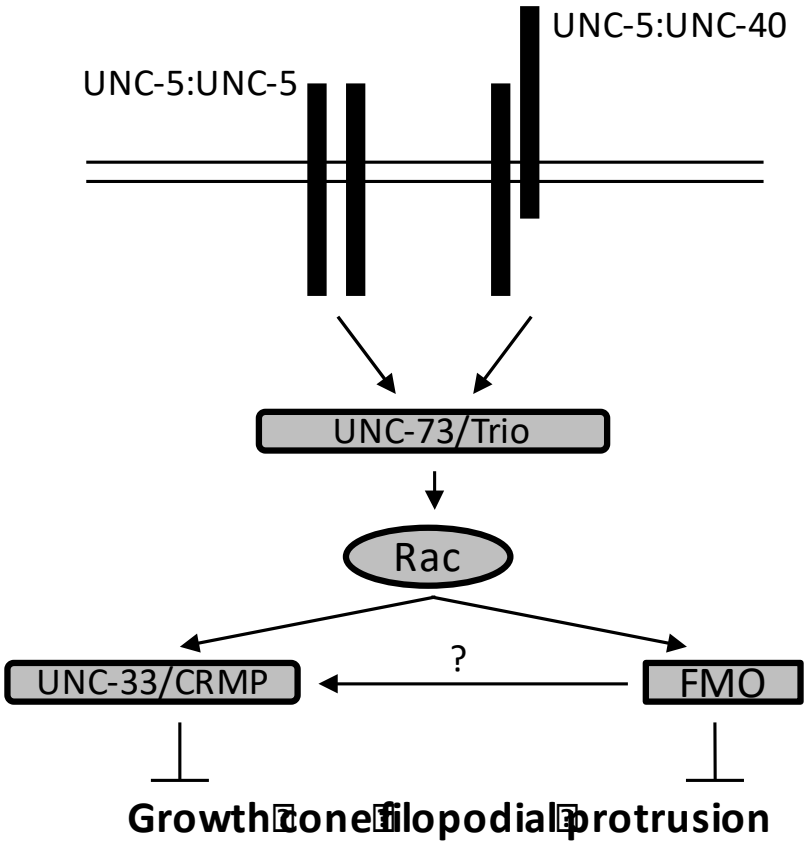
UNC-5:UNC-40
UNC-5:UNC-5
UNC-73/Trio
Rac
?
UNC-33/CRMP
FMO
Growth cone filopodial protrusion

Figure 2.14. Genetic model of inhibition of growth cone protrusion. UNC-5 homodimers and/or UNC-5:UNC-40 heterodimers act through the Rac GTP exchange factor UNC-73/Trio and the Rac GTPases, which then utilize the flavin monooxygenases and UNC-33/CRMP to inhibit protrusion. The FMOs might inhibit protrusion directly, by possibly directly oxidizing F-actin, or by promoting phosphorylation of UNC-33/CRMP.

Chapter III

UNC-6/Netrin and its Receptors UNC-5 and UNC-40/DCC Control Growth Cone Polarity, Microtubule Accumulation, and Protrusion

3.1 Abstract

Many axon guidance ligands and their receptors have been identified, but it is still unclear how these ligand-receptor interactions regulate events in the growth cone, such as protrusion and cytoskeletal arrangement, during directed outgrowth *in vivo*. In this work, we dissect the multiple and complex effects of UNC-6/Netrin on the growth cone. Previous studies showed that in *C. elegans*, the UNC-6/Netrin receptor UNC-5 regulates growth cone polarity, as evidenced by loss of asymmetric dorsal F-actin localization and protrusion in *unc-5* mutants. UNC-5 and another UNC-6/Netrin receptor UNC-40/DCC also regulate the extent of protrusion, with UNC-40/DCC driving protrusion and UNC-5 inhibiting protrusion. In this work, we analyze the roles of UNC-6/Netrin, UNC-40/DCC, and UNC-5 in coordinating growth cone F-actin localization, microtubule organization, and protrusion that results in directed outgrowth away from UNC-6/Netrin. We find that a previously-described pathway involving the UNC-73/Trio Rac GEF and UNC-33/CRMP that acts downstream of UNC-5, regulates growth cone dorsal asymmetric F-actin accumulation and protrusion. *unc-5* and *unc-33* mutants also display excess EBP-2::GFP puncta, suggesting that MT + end accumulation is important in growth cone polarity and/or protrusion. *unc-73* Rac GEF mutants did not display excess EBP-2::GFP puncta despite larger and more protrusive growth cones, indicating a MT-independent mechanism to polarize the growth cone and to inhibit protrusion, possibly via actin. Finally, we show that UNC-6/Netrin and UNC-40/DCC are required for excess protrusion in *unc-5* mutants, but not for loss of F-actin asymmetry or MT + end accumulation, indicating that

UNC-6/Netrin and UNC-40/DCC are required for protrusion downstream of F-actin asymmetry and MT + end entry. Our data suggest a model in which UNC-6/Netrin polarizes the growth cone via UNC-5, and then regulates a balance of pro- and anti-protrusive forces driven by UNC-40 and UNC-5, respectively, that result in directed protrusion and outgrowth.

3.2 Introduction

Neural circuits and networks are formed by intricate interactions of axonal growth cones with the extracellular environment (Mortimer et al., 2008; Tessier-Lavigne and Goodman, 1996). Many extracellular molecules that guide growth cone migrations have been identified, but the effects of these guidance molecules on growth cone morphology during outgrowth *in vivo* are incompletely understood.

The secreted UNC-6/Netrin guidance cue and its receptors UNC-5 and UNC-40/DCC guide cell and growth cone migrations in a manner conserved from invertebrates to mammals. In *C. elegans*, UNC-6/Netrin is expressed in cells along the ventral midline, including neurons with axons that extend down the lengths of the ventral nerve cord (Asakura et al., 2007; Wadsworth et al., 1996). UNC-6 controls both ventral migrations (towards UNC-6) and dorsal migrations (away from UNC-6), and *unc-6* mutants have defects in both ventral and dorsal guidance (Hedgecock et al., 1990b; Norris and Lundquist, 2011). Ventral versus dorsal responses to UNC-6/Netrin are mediated by expression of UNC-40 and UNC-5 on growth cones. Classically, UNC-40 was thought to mediate ventral growth toward UNC-6 (Chan et al., 1996), and UNC-5 was thought to mediate dorsal growth away from UNC-6 (Leung-Hagesteijn, 1992), although UNC-40 also acts in dorsal growth along with UNC-5, likely as a heterodimer (Hong et al., 1999; MacNeil et al., 2009; Norris and Lundquist, 2011; Norris et al., 2014). Recent studies indicate that UNC-5 can act also act in ventral migrations (Levy-Strumpf and Culotti, 2014; Limerick et al., 2018; Yang et al., 2014), and might

serve to focus UNC-40 localization ventrally in the cell body toward the UNC-6/Netrin source. Thus, the roles of UNC-40 and UNC-5 in ventral and dorsal growth are more complex than initially appreciated.

The growth cones of the VD motor neuron processes migrate dorsally in a commissural route to the dorsal nerve cord (Knobel et al., 1999; Norris and Lundquist, 2011). The VD cell bodies reside in the ventral nerve cord, and extend processes anteriorly, which then turn and begin dorsal commissural migration away from UNC-6. Mutations in *unc-6, unc-5,* and *unc-40* disrupt the dorsal guidance of the VD axons (Hedgecock et al., 1990b). Commissural VD growth cones display robust and dynamic lamellipodial and filopodial protrusion localized to the dorsal leading edge, away from the UNC-6/Netrin source, resulting in directed dorsal migration (Knobel et al., 1999; Norris and Lundquist, 2011). F-actin also accumulated at the dorsal leading edge, near the site of protrusion (Norris and Lundquist, 2011). Previous studies showed that UNC-6/Netrin, UNC-5, and UNC-40/DCC control lamellipodial and filopodial protrusion of VD growth cones (Norris and Lundquist, 2011; Norris et al., 2014). *unc-5* mutant VD growth cones showed excess protrusion, with larger lamellipodial growth cone bodies and longer and longer-lasting filopodial protrusions. Furthermore, the protrusions were no longer focused to the dorsal leading edge but occurred all around the growth cone. Finally, F-actin was no longer restricted to the dorsal leading edge but was found throughout the periphery of the growth cone in *unc-5* mutants. Thus, these large, unfocused *unc-5* mutant growth cones moved very little,

consistent with findings in cultured growth cones that large, more protrusive growth cones exhibited reduced rates of movement (Ren and Suter, 2016).

While the effect of *unc-5* mutation on VD growth cones was severe, loss of *unc-40* had no significant effect on extent or polarity of protrusion (Norris and Lundquist, 2011). However, constitutive activation of UNC-40 signaling (MYR::UNC-40) in VD growth cones led to small growth cones with little or no protrusion, similar to constitutive activation of UNC-5 (MYR::UNC-5) (Norris and Lundquist, 2011; Norris et al., 2014). Functional UNC-5 was required for the inhibitory effects of MYR::UNC-40. This suggests that MYR::UNC-40 acts as a heterodimer with UNC-5 to inhibit protrusion, and in *unc-40* mutants, UNC-5 alone was sufficient to inhibit protrusion. *unc-6(ev400)* null mutants had no effect on extent of VD growth cone protrusion, but did affect polarity of protrusion as well as F-actin polarity, both lost in *unc-6* mutants (Norris and Lundquist, 2011). Thus, UNC-6/Netrin affects VD growth cone polarity (F-actin and protrusion), but it is unclear if the effects on extent of protrusion by UNC-5 and UNC-40 involve UNC-6/Netrin.

These results suggest that in the same VD growth cone, UNC-40 can both drive protrusion and inhibit protrusion along with UNC-5. That the normal VD growth cone has polarized protrusion to the dorsal leading edge and reduced protrusion ventrally near the axon shaft suggests that the activities of UNC-40 and UNC-40-UNC-5 might be asymmetric across the growth cone. The *unc-6(e78)* mutation, which specifically affects interaction with UNC-5, causes excess growth cone protrusion and abolished polarity similar to *unc-5* mutants (Norris

and Lundquist, 2011), suggesting that UNC-6/Netrin inhibits protrusion through UNC-5. The involvement of UNC-6/Netrin in pro-protrusive UNC-40 activity is unclear.

UNC-5 affects three aspects of growth cone morphology during outgrowth *in vivo*: polarity of protrusion to the dorsal leading edge, F-actin asymmetric accumulation to the dorsal leading edge, and inhibition of growth cone protrusion (Norris and Lundquist, 2011; Norris et al., 2014). Growth cone motility and guidance is dependent on the actin and microtubule cytoskeleton (Dent and Gertler, 2003). The axon shaft and the central region of the growth cone is composed of bundled microtubules with their plus (+) ends (MT+) oriented towards the growth cone. The peripheral region of the growth cone contains highly dynamic actin that is relatively free of microtubules. The actin filaments at the leading edge of the growth cone form a branched lamellipodial meshwork and filopodial bundles in the essential in sensing guidance cues and driving the forward motion of the axon (Dent et al., 2011; Forscher and Smith, 1988; Gallo and Letourneau, 2004; Omotade et al., 2017; Pak et al., 2008).

Our previous results show an effect of UNC-5 on F-actin polarity and protrusive events driven by F-actin. We recently showed that a family of genes encoding flavin monooxygenases (FMOs) are required for inhibition of protrusion mediated by UNC-5 (Gujar et al., 2017). In Drosophila and mammals, the FMO-containing MICAL molecule causes actin depolymerization and collapse through direct oxidation of actin (Hung et al., 2011; Hung et al., 2010; Terman et al., 2002). We previously described a second signaling pathway downstream of

UNC-5 required to inhibit protrusion that includes the UNC-73/Trio Rac GEF, the Rac GTPases CED-10 and MIG-2, and the UNC-33/CRMP cytoskeletal molecule (Norris et al., 2014), which can interact with MTs in other systems (Fukata et al., 2002). In cultured growth cones, most stable microtubules remain in the central domain. A small population of dynamic microtubules can explore the periphery and penetrate the filopodia, where they interact with extracellular cues resulting in proper axonal elongation and guidance (Dent and Gertler, 2003; Lowery and Van Vactor, 2009; Sabry et al., 1991; Tanaka et al., 1995). Thus, motility of the growth cone is achieved through proper regulation and coordination between microtubules and the actin cytoskeleton (Buck and Zheng, 2002; Dent and Kalil, 2001; Zhou and Cohan, 2004; Zhou et al., 2002). MTs have been implicated in Unc5 signaling (Huang et al., 2018; Shao et al., 2017), but the role of MTs in UNC-5-mediated VD growth cone outgrowth *in vivo* remains unclear.

That UNC-5 and UNC-40 cooperate to guide migrations of axons that grow toward UNC-6/Netrin indicates that the roles of these molecules are more complex than discrete “attractive” and “repulsive” functions. The signaling pathways used by UNC-40 are well-described, but the intracellular pathways used by UNC-5 remain unclear. In this work, we analyze three aspects of growth cone behavior to understand the roles of these molecules in growth away from UNC-6/Netrin: growth cone protrusion; F-actin asymmetric accumulation; and EBP-2::GFP distribution, which has been used previously to monitor MT + ends in *C. elegans* embryos and neurons (Kozlowski et al., 2007; Srayko et al., 2005; Yan et al., 2013). We find that UNC-6/Netrin is required for the excess protrusion

in *unc-5* mutant growth cones, similar to UNC-40, and that UNC-6/Netrin, along with UNC-5, polarizes growth cone F-actin accumulation and protrusion to the dorsal leading edge, resulting in focused dorsal protrusion of the growth cone. We find that EBP-2::GFP puncta are found in excess in *unc-5, unc-6,* and *unc-33* mutant growth cones, suggesting that UNC-6/Netrin and UNC-5 signaling can block MT + end accumulation in growth cones, which correlates with inhibited growth cone protrusion, and suggests a pro-protrusive role for MTs in the growth cone. Finally, we show that UNC-6/Netrin and UNC-40 stimulate VD growth cone protrusion downstream of dorsal F-actin polarity and growth cone EBP-2::GFP accumulation. An implication of our results is that in a growth cone growing away from an UNC-6/Netrin source, UNC-6/Netrin both stimulates protrusion dorsally, away from the source, and inhibits protrusion ventrally, near the source, resulting in directed outgrowth.

3.3 Materials and Methods

Genetic methods

Experiments were performed at 20°C using standard *C. elegans* techniques. Mutations used were LGI: *unc-40(n324* and *e1430)*, *unc-73(rh40, e936, ev802* and *ce362)*; LGII: *juIs76[Punc-25::gfp]*. LGIV: *unc-5(e53, e553, e791* and *e152)*, *unc-33(e204* and *e1193*), *unc-44(e362, e1197* and *e1260*), *ced-10(n1993)*; LGX: *unc-6(ev400), unc-6(e78), mig-2(mu28), lqIs182* [*Punc-25::mig-2(G16V)*]*, lqIs170* [*rgef-1::vab-10ABD::gfp*]. Chromosomal locations not determined: *lqIs279* and *lqIs280* [*Punc-25::ebp-2::gfp*], *lqIs296* [*Punc-25::myr::unc-5*]*, lhIs6* [*Punc-25::mCherry*]. The presence of mutations in single and double mutant strains was confirmed by phenotype, PCR genotyping, and sequencing. Extrachromosomal arrays were generated using standard gonadal injection (Mello and Fire, 1995) and include: *lqEx999* and *lqEx1000* [*Punc-25::myr::unc-40; Pgcy-32::yfp*], *lqEx1017* and *lqEx1018* [*Punc-25::ced-10(G12V); Pgcy-32::yfp*]. Multiple (≥3) extrachromosomal transgenic lines of transgenes described here were analyzed with similar effect, and one was chosen for integration and further analysis. The *mig-2(mu28); ced-10(n1993M+)* strain was balanced with the nT1 balancer. The *Punc-25::ebp-2::gfp* plasmid was constructed using standard recombinant DNA techniques. The sequences of all plasmids and all oligonucleotides used in their construction are available upon request.

Growth cone imaging

VD growth cones were imaged and quantified as previously described (Norris and Lundquist, 2011). Briefly, animals at ~16 h post-hatching at 20°C were placed on a 2% agarose pad and paralyzed with 5mM sodium azide in M9 buffer, which was allowed to evaporate for 4 min before placing a coverslip over the sample. Some genotypes were slower to develop than others, so the 16 h time point was adjusted for each genotype. Growth cones were imaged with a Qimaging Rolera mGi camera on a Leica DM5500 microscope. Images were analyzed in ImageJ, and statistical analyses done with Graphpad Prism software. As described in (Norris and Lundquist, 2011; Norris et al., 2014), growth cone area was determined by tracing the perimeter of the growth cone body, not including filopodia. Average filopodial length was determined using a line tool to trace the length of the filopodium. Unless otherwise indicated, ≥25 growth cones were analyzed for each genotype. These data were gathered in ImageJ and entered into Graphpad Prism for analysis. A two-sided *t*-test with unequal variance was used to determine significance of difference between genotypes.

VAB-10ABD::GFP imaging

The F-actin binding domain of VAB-10/spectraplakin fused to GFP has been used to monitor F-actin in *C. elegans* (Bosher et al., 2003; Patel et al., 2008). We used it to image F-actin in the VD growth cones as previously described (Norris and Lundquist, 2011). To control for variability in growth cone size and shape, and as a reference for asymmetric localization of VAB-

10ABD::GFP, a soluble mCherry volume marker was included in the strain. Growth cones images were captured as described above. ImageJ was used image analysis to determine asymmetric VAB-10ABD::GFP localization. For each growth cone, five line scans were made from dorsal to ventral (see results). For each line, pixel intensity was plotted as a function of distance from the dorsal leading edge of the growth cone. The average intensity (arbitrary units) and standard error for each growth cone was determined. For dorsal versus ventral comparisons, the pixel intensities for VAB-10ABD::GFP were normalized to the volumetric mCherry fluorescence in line scans from the dorsal half and the ventral half of each growth cone. This normalized ratio was determined for multiple growth cones, and the average and standard error for multiple growth cones was determined. Statistical comparisons between genotypes were done using a two-tailed *t*-test with unequal variance on these average normalized ratios of multiple growth cones of each genotype.

EBP-2::GFP imaging

EBP-2::GFP has previously been used to monitor microtubule plus ends in other *C. elegans* cells including neurons (Kozlowski et al., 2007; Srayko et al., 2005; Yan et al., 2013). We constructed a transgene consisting of the *unc-25* promoter driving expression of *ebp-2::gfp* in the VD/DD neurons. In growth cones, a faint fluorescence was observed throughout the growth cone, resembling a soluble GFP and allowing for the growth cone perimeter to be defined. In addition to this faint, uniform fluorescence, brighter puncta of EBP-

2::GFP were observed that resembled the EBP-1::GFP puncta described in other cells and neurons. For each growth cone, the perimeter and filopodia were defined, and the EBP-2::GFP puncta in the growth cone were counted. For each genotype, the puncta number for many growth cones (≥25 unless otherwise noted) was determined. Puncta number displayed high variability within and between genotypes, so box-and-whiskers plots (Graphpad Prism) were used to accurately depict this variation. The grey boxes represent the upper and lower quartiles of the data set, and the “whiskers” represent the high and low values. Dots represent major outliers. Significance of difference was determined by a two-sided *t*-test with unequal variance.

3.4 Results

Functional UNC-6 is required for excess growth cone protrusion of *unc-5* mutants.

Previous studies have shown that *unc-5* mutants displayed increased VD growth cone protrusiveness with larger growth cone area and longer filopodial protrusions as compared to wild-type (Norris and Lundquist, 2011). However, *unc-5; unc-40* double mutants were found to have near wild-type levels of VD growth cone protrusion, suggesting that a functional UNC-40 was required for the over protrusive growth cone phenotype observed in *unc-5* loss of function mutants alone (Norris and Lundquist, 2011). *unc-6(ev400)* also suppressed the excess growth cone protrusion (growth cone size and filopodial length) of *unc-5* mutants (Figure 3.1A-E), suggesting that excess protrusion in *unc-5* mutants also requires functional UNC-6.

VD Growth cone F-actin and EBP-2::GFP organization.

The F-actin binding domain of the spectraplakin VAB-10 was previously used to monitor F-actin in the VD growth cone in *C. elegans* (Norris and Lundquist, 2011). In wild-type VD growth cones F-actin preferentially localized to the leading edge of the growth cone (~1.23 fold more accumulation in the dorsal half or the growth vs the ventral half) (Figure 3.2 and (Norris and Lundquist, 2011)). Most growth cone filopodial protrusion occurs at the dorsal leading edge of the VD growth cone, correlating with F-actin accumulation.

The MT+-end binding protein EBP-2 fused to GFP has been used previously to monitor MT+ ends in embryos and neuronal processes in *C. elegans* (Kozlowski et al., 2007; Kurup et al., 2015; Maniar et al., 2012; Srayko et al., 2005; Yan et al., 2013). We expressed *ebp-2::gfp* in the VD/DD neurons using the *unc-25* promoter. Puncta of EBP-2::GFP fluorescence were distributed along the length of commissural axons (arrows in Figure 3.2H) and in growth cones (arrowheads in Figure 3.2H and arrows in Figure 3.2J-L). In wild-type VD growth cones, an average of 2 EBP-2::GFP puncta were observed in the growth cone itself (Figure 3.2I). These were present at the growth cone base (arrowheads in Figure 3.2H) as well as in the growth cone periphery (Figure 3.2J). These data show that in wild-type, EBP-2::GFP puncta were abundant in the axon as previously observed, but relatively rare in the growth cone.

UNC-5 and UNC-6 affect VD growth cone F-actin dorsal asymmetry and EBP-2::GFP accumulation.

In *unc-6* and *unc-5* mutants, VAB-10ABD::GFP dorsal asymmetry in the VD growth cone was abolished (Figure 3.3A and D and (Norris and Lundquist, 2011)). VAB-10ABD::GFP was observed at the growth cone periphery, but often in lateral and even ventral positions (Figure 3.3D). This loss of VAB-10ABD::GFP asymmetry was accompanied by a corresponding loss of dorsal asymmetry of filopodial protrusion, which occurred all around the growth cone in *unc-5* and *unc-6* mutants (Norris and Lundquist, 2011). *unc-40* null mutants displayed relatively normal VD growth cone protrusion compared to wild-type and also

showed no effect on VAB-10ABD::GFP distribution (Figure 3.3A and C and (Norris and Lundquist, 2011). These results suggest that UNC-6 and UNC-5 normally control distribution of F-actin to the dorsal leading edge of the VD growth cone, and thus restrict filopodial protrusion to the dorsal leading edge.

unc-5 and *unc-6* mutants displayed significantly increased numbers of EBP-2::GFP puncta in VD growth cones and filopodial protrusions (Figure 3.2I and L). In some mutant growth cones, more than eight puncta were observed, whereas wild-type never showed more than five. *unc-40* mutants displayed no significant increase in EBP-2::GFP puncta accumulation (Figure 3.2I and K). Sizes of EBP-2::GFP puncta in *C. elegans* neurons were previously found to be on the order of the smaller puncta we observe in wild type (~100nm) (Figure 3.2J) (Maniar et al., 2012). In *unc-5* and *unc-6* mutants, we observed larger puncta (~0.5-1μm) (Figure 3.2L). We do not understand the nature of the distinct puncta sizes, but the same integrated transgene was used to analyze wild-type and mutants. This suggests that puncta size and number are an effect of the mutant and not transgene variation. In sum, these studies suggest that UNC-5 and UNC-6 are required for the dorsal bias of F-actin accumulation in VD growth cones, and might be required to restrict MT + end entry into VD growth cones as represented by increased numbers of EBP-2::GFP puncta in mutant growth cones.

EBP-2::GFP puncta accumulation and loss of growth cone F-actin polarity in *unc-5* mutants is not dependent on functional UNC-6 or UNC-40.

We found that in *unc-5(e53)*; *unc-40(n324)* and *unc-5(e53); unc-6(ev400)* double mutants, VAB-10ABD::GFP distribution resembled that of *unc-5* mutants alone (i.e. was randomized in the growth cone) (Figure 3.4A-D). Likewise, EBP-2::GFP accumulation resembled *unc-5*, with increased EBP-2::GFP puncta compared to wild-type or *unc-40* alone (Figure 3.4E-H). Thus, while UNC-6 and UNC-40 activities were required for the excess growth cone protrusion observed in *unc-5* mutants, they were not required for randomized F-actin or for increased EBP-2::GFP accumulation. These results suggest that UNC-6 and UNC-40 have a role in protrusion that is independent of UNC-5-mediated F-actin dorsal accumulation and EBP-2::GFP accumulation. Consistent with this idea, *unc-6(ev400)* null mutants alone displayed loss of F-actin polarity and increased EBP-2::GFP puncta (Figures 3.3 and 3.4), but not increased protrusion (Figure 3.1) (Norris and Lundquist, 2011), suggesting that UNC-6 is required for both UNC-40-mediated protrusion and UNC-5-mediated inhibition of protrusion.

UNC-73 Rac GEF activity controls growth cone F-actin polarity.

Previous studies showed that the Rac GTP exchange factor activity of UNC-73 was required to inhibit growth cone protrusion downstream of UNC-5 (Norris et al., 2014). *unc-73(rh40),* which specifically eliminates the Rac GEF activity of the molecule (Figure 3.5A) (Steven et al., 1998), resulted in excessive filopodial protrusion (Figure 3.5B, C, and E, and (Norris et al., 2014)). *unc-*

73(rh40) mutants displayed a loss of VAB-10ABD::GFP dorsal symmetry in the VD growth cone similar to *unc-5* and *unc-6* mutants (Figure 3.6A and C). However, *unc-73(rh40)* mutants did not show significantly increased EBP-2::GFP puncta distribution compared to wild-type (Figure 3.6E and G). Thus, despite having excessively protrusive growth cones, *unc-73(rh40)* mutants did not display increased EBP-2::GFP puncta number. This indicates that the increased numbers of EBP-2::GFP puncta observed in *unc-5* and *unc-6* mutants was not simply due to larger growth cone size. This result also indicates that excess growth cone protrusion can occur in the absence of increased numbers of EBP-2::GFP puncta.

The C- terminal GEF domain of UNC-73 controls the Rho GTPase (Figure 3.5A) (Spencer et al., 2001) and has been shown to affect motility and normal synaptic neurotransmission (Hu et al., 2011; Steven et al., 2005). *unc-73(ce362)* is a missense mutation in the Rho GEF domain (Figure 3.5A) (Hu et al., 2011; McMullan et al., 2012; Williams et al., 2007) and *unc-73(ev802)* is a 1,972 bp deletion which completely deletes the Rho GEF domain (Figure 3.5A) (Williams et al., 2007). *unc-73(ce362)* and *unc-73(ev802)* displayed reduced growth cone body size, and increased filopodial length (Figure 3.5B, C, F, and G) Neither *unc-73(ce362)* nor *unc-73(ev802)* had an effect on growth cone F-actin dorsal accumulation (Figure 3.6A and D), but both showed a significant increase in growth cone EBP-2::GFP puncta (Figure 3.6E and H). Thus, Rho GEF activity of UNC-73/Trio might have distinct effects on growth cone morphology compared to Rac GEF activity.

The Rac GTPases CED-10 and MIG-2 affect F-actin polarity but not EBP-2::GFP puncta accumulation in VD growth cones.

The Rac GTPases CED-10/Rac and MIG-2/RhoG have been shown to redundantly control axon guidance (Lundquist et al., 2001; Struckhoff and Lundquist, 2003). CED-10 and MIG-2 act with UNC-40 to stimulate protrusion in axons attracted to UNC-6/Netrin (Demarco et al., 2012), and to inhibit growth cone protrusion with UNC-5-UNC-40 in the repelled VD growth cones (Norris et al., 2014). The Rac GEF TIAM-1 acts with CED-10 and MIG-2 to stimulate protrusion (Demarco et al., 2012), and the Rac GEF UNC-73/Trio acts in the anti-protrusive pathway (Norris et al., 2014).

The VD growth cones of *mig-2; ced-10* double mutants resembled wild-type, except that the filopodial protrusions had a longer maximal length and were longer lasting (Norris et al., 2014). This subtle phenotype might represent the fact that the molecules have roles in both pro- and anti-protrusive pathways. *mig-2(mu28)* and *ced-10(n1993)* single mutants and *ced-10; mig-2* double mutants all showed significant F-actin polarity defects (Figure 3.7A-D), consistent with the idea that the GEF domain of Trio affects actin organization through Rac activation. However, VD/DD axon guidance defects in *mig-2* and *ced-10* single mutants were much less severe than the *mig-2; ced-10* double mutants and *unc-73(rh40)* (Norris et al., 2014). *unc-73(rh40)* and *mig-2; ced-10* double mutants might have additional effects on axon guidance compared to *mig-2* and *ced-10* double mutants not observed in these studies. Similar to *unc-5; unc-40* double

mutants, loss of asymmetry of F-actin did not result in excess protrusion in *mig-2* and *ced-10* single mutants.

ced-10 and *mig-2* single mutants had no significant effect on EBP-2 distribution in the VD growth cone (Figure 3.7E and H). However, *ced-10; mig-2* double mutants showed a significant increase in EBP-2 puncta distribution in the VD growth cone and filopodial protrusions as compared to wild-type and the single mutants alone (Figure 3.7E and I). This result suggests that the Rac GTPases CED-10 and MIG-2 act redundantly in limiting EBP-2 puncta distribution in the VD growth cone. This also indicates that MIG-2 and CED-10 have a role in limiting EBP-2::GFP puncta that is independent of UNC-73/Trio Rac GEF activity.

UNC-33/CRMP and UNC-44/ankyrin are required for F-actin polarity and restricting EBP-2::GFP from the VD growth cone.

Previous studies showed that UNC-33/CRMP and UNC-44/ankyrin act downstream of UNC-5 and Rac GTPases to limit growth cone protrusion (Norris et al., 2014). *unc-33* and *unc-44* mutants randomized F-actin polarity similar to *unc-5* and *unc-73(rh40)* (Figure 3.8A-D). *unc-33* and *unc-44* also displayed a significant increase in EBP-2::GFP puncta in the growth cone and protrusions (Figure 3.8E-H). Thus, UNC-33 and UNC-44 are both required for dorsal F-actin asymmetry as well as restriction of EBP-2::GFP growth cone puncta. That *unc-33* and *unc-44* phenotypes are similar to *unc-5* is consistent with the previous genetic interactions placing UNC-33 and UNC-44 in the UNC-5 pathway.

Constitutive activation of UNC-40, UNC-5, CED-10 and MIG-2 affects F-actin polarity and EBP-2 distribution.

The heterodimeric receptor UNC-5-UNC-40 is required for inhibition of growth cone protrusion in UNC-6/netrin repulsive axon guidance (Norris and Lundquist, 2011; Norris et al., 2014). Constitutive activation of UNC-40 and UNC-5 by addition of an N-terminal myristoylation signal to their cytoplasmic domain (Gitai et al., 2003; Norris and Lundquist, 2011) causes a significant decrease in VD growth cone protrusiveness, with a reduction in growth cone area and filopodial protrusions (Demarco et al., 2012; Norris et al., 2014). The Rac GTPases CED-10 and MIG-2 have been shown to act in both stimulation and inhibition of growth cone protrusion (Demarco et al., 2012; Norris et al., 2014). The constitutively activated Rac GTPases CED-10(G12V) and MIG-2(G16V) also cause an inhibited VD growth cone phenotype similar to *myr::unc-40* and *myr::unc-5* (Norris et al., 2014).

We assayed VAB-10ABD::GFP and EBP-2::GFP distribution in the VD growth cones of these various activated molecules. All four (MYR::UNC-5, MYR::UNC-40, CED-10(G12V), and MIG-2(G16V) showed peripheral accumulation around the entire growth cone, with the dorsal bias lost (Figure 3.9A-D). Furthermore, we observed significantly fewer EBP-2::GFP puncta compared to wild type in each case (Figure 3.9E-H). Thus, constitutive activation of UNC-5, UNC-40, CED-10, and MIG-2 might lead to F-actin accumulation

around the entire periphery of the growth cone, as opposed to dorsal bias, and might restrict MT + ends from accumulating in the growth cone.

3.5 Discussion

Netrins are thought to regulate dorsal-ventral axon guidance through a conserved mechanism involving ventral expression of Netrin coupled with expression of UNC-40/DCC receptors on attracted axons and UNC-5 receptors on repelled axons. Recent studies have highlighted the previously-underappreciated complexity of UNC-6/Netrin function in axon guidance. In *C. elegans,* UNC-5 acts in axons that grow toward Netrin to focus UNC-40 activity (Levy-Strumpf and Culotti, 2014; Limerick et al., 2018; Yang et al., 2014), and both UNC-40 and UNC-5 act in the same growth cone to mediate protrusion in directed guidance away from UNC-6/Netrin (Norris and Lundquist, 2011; Norris et al., 2014). In this work, we analyze three aspects of VD growth cone morphology (growth cone protrusion, F-actin accumulation, and EBP-2::GFP accumulation) to probe the roles of UNC-6/Netrin, UNC-40/DCC, and UNC-5 in growth away from UNC-6/Netrin. We find that UNC-6/Netrin signaling coordinates these growth cone features to result in directed growth away from it.

Previous studies suggested that UNC-6/Netrin and the receptor UNC-5-UNC-40 inhibit growth cone protrusion and are required to polarize F-actin to the dorsal protrusive leading edge in repelled VD growth cones in *C. elegans* (Norris and Lundquist, 2011; Norris et al., 2014). Furthermore, previous studies defined a new signaling pathway downstream of UNC-5-UNC-40 in repulsive axon guidance and inhibition of growth cone protrusion. This pathway consists of the Rac GTP exchange factor UNC-73/Trio, the Rac GTPases CED-10 and MIG-2, and the cytoskeletal interacting molecules UNC-44/ankyrin and UNC-33/CRMP

(Norris et al., 2014). Loss of function in these molecules led to excess growth cone protrusion, and activation led to constitutively-inhibited growth cone protrusion. Using VAB-10ABD::GFP to visualize F-actin and EBP-2::GFP to visualize MT + ends, we endeavored in this work to define the effects of members of this pathway on the cytoskeleton of the VD growth cone. We found that mutations in *unc-5, unc-6, unc-33,* and *unc-44* led to excessively protrusive growth cones with randomized F-actin distribution and increased numbers of EBP-2::GFP puncta in the growth cones. *unc-40* mutation suppressed the excess protrusion of *unc-5* mutants but not the F-actin randomization nor the excess EBP-2::GFP puncta, suggesting that UNC-40 might have a stimulatory role in protrusion independent of UNC-5. We found that Rac GEF activity was required to inhibit protrusion and for F-actin dorsal bias, but was not required to restrict EBP-2::GFP puncta, suggesting a mechanism distinct from EBP-2::GFP puncta increase that stimulates growth cone protrusion. Finally, we found a complex involvement of the Rac GTPases in protrusion, F-actin bias, and EBP-2::GFP puncta that is consistent with these molecules having both pro- and anti-protrusive roles in the growth cone.

UNC-5 and UNC-6/Netrin might inhibit MT+ - end accumulation in the VD growth cone. Loss of *unc-5* and *unc-6* caused significant mislocalization of F-actin and significantly increased the average number of EBP-2::GFP puncta distribution in VD growth cones (Figure 3.2 and 3.3), which have been used to track MT + ends in *C. elegans* neurons and embryos (Kozlowski et al., 2007;

Kurup et al., 2015; Maniar et al., 2012; Srayko et al., 2005; Yan et al., 2013). UNC-6 and UNC-5 might inhibit growth cone protrusion by preventing F-actin formation in the ventral/lateral regions of the growth cone to restrict protrusion to the dorsal leading edge, and by preventing accumulation of MT + ends in the growth cone. In cultured growth cones, MTs are involved in both DCC and UNC5C-mediated axon outgrowth, and DCC and UNC5C physically associate with MTs in a Netrin-dependent manner in cultured cells (Huang et al., 2018; Qu et al., 2013; Shao et al., 2017). Our results suggest a link between UNC-6/Netrin signaling and VD growth cone MTs *in vivo*.

MTs in the growth cone might be pro-protrusive. Our data show a correlation between MT + ends in growth cones and excess growth cone protrusion. This is consistent with *in vitro* studies of growth cones in which MT + end entry into the growth cone is tightly regulated, is intimately associated with F-actin, and is essential for protrusion and outgrowth (Coles and Bradke, 2015; Dent et al., 2011; Lowery and Van Vactor, 2009; Vitriol and Zheng, 2012). Possibly, MT entry into growth cones serves as a conduit for transport of vesicles, organelles, and pro-protrusive factors involved in actin polymerization that drive filopodial protrusion in *C. elegans,* such as Arp2/3, UNC-115/abLIM, and UNC-34/Enabled (Norris et al., 2009; Shakir et al., 2006; Shakir et al., 2008). This is consistent with results from cultured growth cones showing that MT stabilization results in growth cone turning in the direction of stabilization, and MT destabilization results in growth cone turning away from MT destabilization (Buck and Zheng, 2002).

Also, MTs are involved in both DCC and UNC5C-mediated axon guidance (Huang et al., 2018; Qu et al., 2013; Shao et al., 2017), and physically associate with UNC5C, which is decoupled by Netrin and associated with growth away from Netrin (Shao et al., 2017). We have no evidence that UNC-5 or UNC-40 physically associate with MTs, but these data are consistent with MTs having a pro-protrusive role (i.e. protrusion depends on UNC-40 and MTs, and inhibiting protrusion via UNC-5 results in fewer growth cone MTs).

UNC-40 might have a pro-protrusive role downstream of EBP-2::GFP puncta and F-actin polarity. *unc-40* alone showed wild-type levels of protrusion (Norris and Lundquist, 2011), and here we find that *unc-40* did not affect F-actin polarity or EBP-2::GFP puncta accumulation. Previous work showed that a functional UNC-40 is required for the large protrusive growth cones seen in *unc-5* single mutants (Norris and Lundquist, 2011). However, *unc-5; unc-40* double mutants, despite have smaller growth cones, showed loss of F-actin polarity and excess EBP-2::GFP puncta similar to *unc-5* alone (Figure 3.4). Thus, UNC-40 might have a role in protrusion that is downstream of F-actin polarity and EBP-2::GFP puncta. In migrating embryonic cells and anchor cell invasion, UNC-40 affects over all F-actin levels but not F-actin polarity (Bernadskaya et al., 2012; Wang et al., 2014). Something similar might be occurring in the growth cone, where UNC-40 has a role in actin polymerization but not polarity, which might be determined by UNC-5 or the UNC-5-UNC-40 heterodimer. This is similar to recent results in neurons with axons that grow ventrally toward the UNC-6/Netrin

source, which require UNC-5 for ventral guidance (Kulkarni et al., 2013; Levy-Strumpf and Culotti, 2014). In this case, UNC-40 drives protrusion and is polarized ventrally in the cell body by UNC-6/Netrin. UNC-5 further refines this UNC-40 localization of protrusion and prevents lateral and ectopic protrusions (Kulkarni et al., 2013; Limerick et al., 2018; Yang et al., 2014). Our results suggest that F-actin and EBP-2::GFP accumulation, controlled by UNC-5, are pro-protrusive, and that UNC-40 might act downstream of these events to drive growth cone protrusion.

The Rac GEF domain of UNC-73 inhibits protrusion independently of restricting MT + ends. Rac GTPases CED-10 and MIG-2 and the UNC-73/Trio Rac GEF have been shown to play central roles in axon guidance (Lundquist, 2003; Lundquist et al., 2001; Steven et al., 1998; Struckhoff and Lundquist, 2003). Rac GTPases CED-10 and MIG-2 are required to both stimulate and inhibit protrusion, with distinct GEFs regulate each of these activities. TIAM-1 stimulates protrusion (Demarco et al., 2012), and UNC-73 limiting protrusion (Norris et al., 2014). The *unc-73(rh40)* mutation eliminates the Rac GEF activity of UNC-73 but does not affect Rho GEF activity (Steven et al., 1998). *unc-73(rh40)* mutants displayed F-actin polarity defects (Figure 3.6) consistent with the idea that UNC-73 regulates actin dynamics during cell growth and growth cone migrations (Bateman et al., 2000; Lundquist et al., 2001; Steven et al., 1998; Wu et al., 2002). We found that *unc-73(rh40)* had no effect on EBP-2::GFP accumulation in VD growth cones despite having larger, more protrusive growth

cones (Figure 3.6). Despite the large, overly-protrusive growth cones, *unc-73(rh40)* mutants did not display excess EBP-2::GFP puncta as observed in *unc-6, unc-5*, and *unc-33* mutants. This indicates that the excess EBP-2::GFP puncta in *unc-5, unc-6,* and *unc-33* mutants are not due increased growth cone size and protrusion. Furthermore, this suggests that the UNC-73 Rac GEF activity might inhibit protrusion by a mechanism distinct from restricting MT + end entry, possibly by affecting actin polymerization directly. Such a mechanism could involve the flavin monooxygenase (FMOs) FMO-1, FMO-4 and FMO-5, which were recently shown to act downstream of UNC-5 and activated Rac GTPases to inhibit VD growth cone protrusion (Gujar et al., 2017). In *Drosophila*, the FMO-containing MICAL molecule causes actin depolymerization by directly oxidizing actin (Hung et al., 2011; Hung et al., 2010). The *C. elegans* genome does not encode a single MICAL-like molecule containing an FMO plus additional functional domains. In *C. elegans* the FMOs might play an analogous role to MICAL in actin regulation and growth cone inhibition.

Mutations in the Rho-specific GEF domain of *unc-73* led to a complex phenotype. Growth cones were slightly smaller with slightly increased filopodial length. F-actin polarity was unaffected, but excess EBP-2::GFP puncta were observed. This phenotype could reflect the role of RHO-1 in the growth cone, or could reflect that these mutations are not specific to the Rho GEF domain and might affect overall function of the molecule. In any event, these mutations display a distinct phenotype compared to *unc-73(rh40)*, which is specific to the Rac GEF activity of UNC-73.

The Rac GTPases CED-10 and MIG-2 affect F-actin polarity and EBP-2::GFP accumulation. The Rac GEF activity of UNC-73/Trio was required for F-actin polarity but not EBP-2::GFP restriction. However, the *mig-2; ced-10* Rac double mutant displayed both F-actin polarity defects and excess EBP-2::GFP puncta (Figure 3.7), suggesting that Rac GTPases have an UNC-73/Trio Rac GEF activity-independent role in EBP-2::GFP restriction and thus possibly MT + end restriction from the growth come. Possibly another Rac GEF regulates MIG-2 and CED-10 in MT + end restriction. Despite unpolarized F-actin and excess MT + ends, the growth cones in *mig-2; ced-10* double mutants have only subtly-increased filopodial protrusions, much weaker than *unc-73(rh40)*. This might be due to MIG-2 and CED-10 being required in both pro- and anti-protrusive activities, resulting in an intermediate effect on growth cone protrusion in the double mutant.

ced-10 and *mig-2* single mutants displayed F-actin polarity defects alone, but did not display excess EBP-2::GFP puncta accumulation. Thus, CED-10 and MIG-2 are individually required for F-actin polarity and act redundantly in MT + end restriction. Despite F-actin polarity defects, protrusion of the *ced-10* and *mig-2* growth cones resembles wild-type. This could again be explained by their roles in both pro- and anti-protrusive activities.

UNC-33/CRMP and UNC-44/Ankyrin are required to exclude MT+ -ends from the VD growth cone. Our previous work showed that the collapsin-response-

mediating protein UNC-33/CRMP and UNC-44/ankyrin are required for inhibition of protrusion by UNC-5-UNC-40 and Rac GTPases. Here we show that UNC-33 and UNC-44, similar to UNC-5, are required for F-actin polarity and to restrict MT + end accumulation in the growth cone. CRMPs were first identified as molecules required for growth cone collapse induced by semaphorin-3A through Plexin-A and Neuropilin-1 receptors (Goshima et al., 1995; Takahashi et al., 1999). CRMP4 knockdown in cultured mammalian neurons led to increased filopodial protrusion and axon branching (Alabed et al., 2007), consistent with our findings of UNC-33/CRMP as an inhibitor of protrusion. However, hippocampal neurons from a CRMP4 knock-out mouse exhibited decreased axon extension and growth cone size (Khazaei et al., 2014).

CRMPs have various roles in actin and MT organization and function (Khazaei et al., 2014). CRMP2 promotes microtubule assembly *in vitro* by interacting with tubulin heterodimers and microtubules to regulate axonal growth and branching (Fukata et al., 2002). CRMP2 also binds to the kinesin-1 light chain subunit and acts as an adaptor for the transport of tubulin heterodimers as well as the actin regulators Sra-1 and WAVE into axonal growth cones (Kawano et al., 2005; Kimura et al., 2005). Furthermore, CRMP4 physically associates with *in vitro* F-actin (Rosslenbroich et al., 2005). In cultured DRG neurons, CRMP1 colocalizes to the actin cytoskeleton (Higurashi et al., 2012), and drives actin elongation in lamellipodia formation in cultured epithelial cells (Yu-Kemp et al., 2017). These studies indicate that CRMPs can have both positive and negative effects on neuronal protrusion, and most of the biochemical evidence

indicates that CRMPs promote actin assembly and MT function. Our results suggest that UNC-33/CRMP has a negative effect on growth cone protrusion and MT entry into growth cones, consistent with the original finding of CRMPs as anti-protrusive factors (Goshima et al., 1995; Takahashi et al., 1999). The role of UNC-44/ankyrin might be to properly localize UNC-33/CRMP as previously described (Maniar et al., 2012). Loss of dorsal F-actin asymmetry and excess protrusion could be a secondary consequence of excess MT accumulation in the growth cone, or could represent independent roles of UNC-33/CRMP.

We have identified three aspects of VD growth cone morphology affected by *unc-5* mutants: excess protrusion; dorsal F-actin accumulation; and restriction of MT + ends from the growth cone. Neither excess MT + ends nor loss of dorsal F-actin polarity alone were sufficient to drive excess protrusion, as *unc-40; unc-5* and *ced-10; mig-2* double mutants display loss of F-actin polarity and excess MT + ends but not excess growth cone protrusion. Thus, an additional mechanism, possibly involving UNC-40, CED-10, MIG-2, and actin nucleators such as Arp2/3, UNC-115/abLIM, and UNC-34/Ena are required to drive protrusion downstream of F-actin polarity and MT + end entry.

Possibly, a dynamic interaction between MTs and actin, mediated by UNC-33/CRMP, controls MT accumulation in the growth cone during repulsive axon guidance mediated by UNC-6/Netrin. The interactions between actin and microtubules in growth cones *in vitro* is well-documented and complex (Coles and Bradke, 2015; Dent et al., 2011), including the idea that actin retrograde flow removes MTs from the growth cone periphery due to physical linkage to actin

undergoing retrograde flow (Lee and Suter, 2008; Lin and Forscher, 1995; Schaefer et al., 2008; Short et al., 2016; Turney et al., 2016). An intriguing interpretation of our results, based upon those in cultured neurons, is that the UNC-6/Netrin signaling pathway we have described inhibits protrusion by maintaining MT attachment to actin, possibly via UNC-33/CRMP, and thus restriction of MTs from the growth cone. Growth cone dorsal advance could occur by regulated MT entry and interaction with the dorsal leading edge of the growth cone, possibly by interacting with polarized dorsal F-actin. Furthermore, we show that a pro-protrusive function of UNC-40/DCC and the Rac GTPases might act independently of UNC-5 to drive growth cone protrusion, normally at the dorsal leading edge.

In conclusion, our results suggest that UNC-6/Netrin signaling coordinates growth cone F-actin accumulation, EBP-2::GFP accumulation, and protrusion to direct growth away from it. UNC-6/Netrin and UNC-5 have a role in polarizing the growth cone, visualized by dorsal F-actin accumulation, resulting in protrusion restricted to the dorsal leading edge (Figure 3.10). Furthermore, UNC-6/Netrin and UNC-40 stimulate protrusion at the dorsal leading edge, based on the establishment of polarity via UNC-5 (Figure 3.10). This is similar to results in neurons with axons that grow ventrally toward UNC-6/Netrin (e.g. HSN), wherein UNC-6/Netrin and UNC-5 regulate where UNC-40-mediated protrusion can occur in the neuron, in this case ventrally toward the site of UNC-6/Netrin (Kulkarni et al., 2013; Limerick et al., 2018; Yang et al., 2014). These results in axons that grow toward UNC-6/Netrin, along with our results in growth cones that grow

away from UNC-6/Netrin, suggest a model of UNC-6/Netrin function involving growth cone polarization coupled with regulation of growth cone protrusion based on this polarity. Recent studies in the vertebrate spinal cord have shown that expression of Netrin-1 in the floorplate is dispensable for commissural axon ventral guidance, (Dominici et al., 2017; Varadarajan and Butler, 2017; Varadarajan et al., 2017; Yamauchi et al., 2017) and that contact-mediated interactions with ventricular cells expressing Netrin-1 are more important, consistent with a possible contact-mediated polarity role of Netrin. In any case, several outstanding questions about the polarization/protrusion model presented here remain. For example, how does UNC-6/Netrin result in polarized protrusive activities in the growth cone? Asymmetric localization of UNC-40 and/or UNC-5 is an attractive idea, but UNC-40::GFP shows uniform association of the growth cone margin in VD growth cones and no asymmetric distribution (Norris et al., 2014). Also, once established, how is polarized protrusive activity maintained as the growth cone extends dorsally away from the UNC-6/Netrin source? Answers to these questions will be the subject of future study.

Figure 3.1.

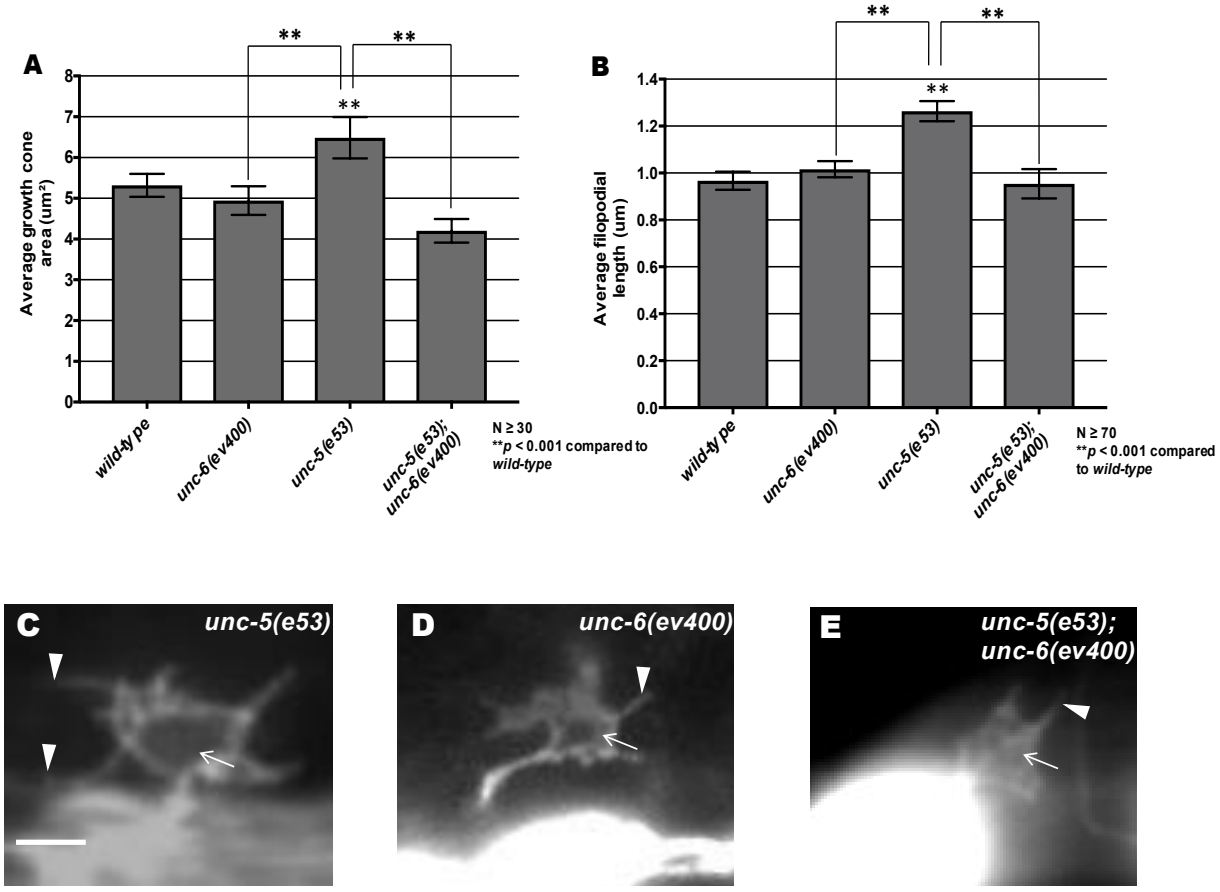
A
Average growth cone area (um²)
**
**
**
wild-type
unc-6(ev400)
unc-5(e53)
unc-5(e53); unc-6(ev400)
N ≥ 30
**p < 0.001 compared to wild-type
B
Average filopodial length (um)
**
**
**
wild-type
unc-6(ev400)
unc-5(e53)
unc-5(e53); unc-6(ev400)
N ≥ 70
**p < 0.001 compared to wild-type
C
unc-5(e53)
D
unc-6(ev400)
E
unc-5(e53); unc-6(ev400)

Figure 3.1. UNC-6 regulates growth cone protrusion. (A-B) Graphs of the average growth cone area and filopodial length in wild-type and mutants, as described in (Norris and Lundquist, 2011) (See Methods). **(C-E)** Fluorescence micrographs of VD growth cones with *Punc-25::gfp* expression from the transgene *juIs76*. Arrows point to the growth cone body, and arrowheads to filopodial protrusions. Scale bar: 5μm.

Figure 3.2.

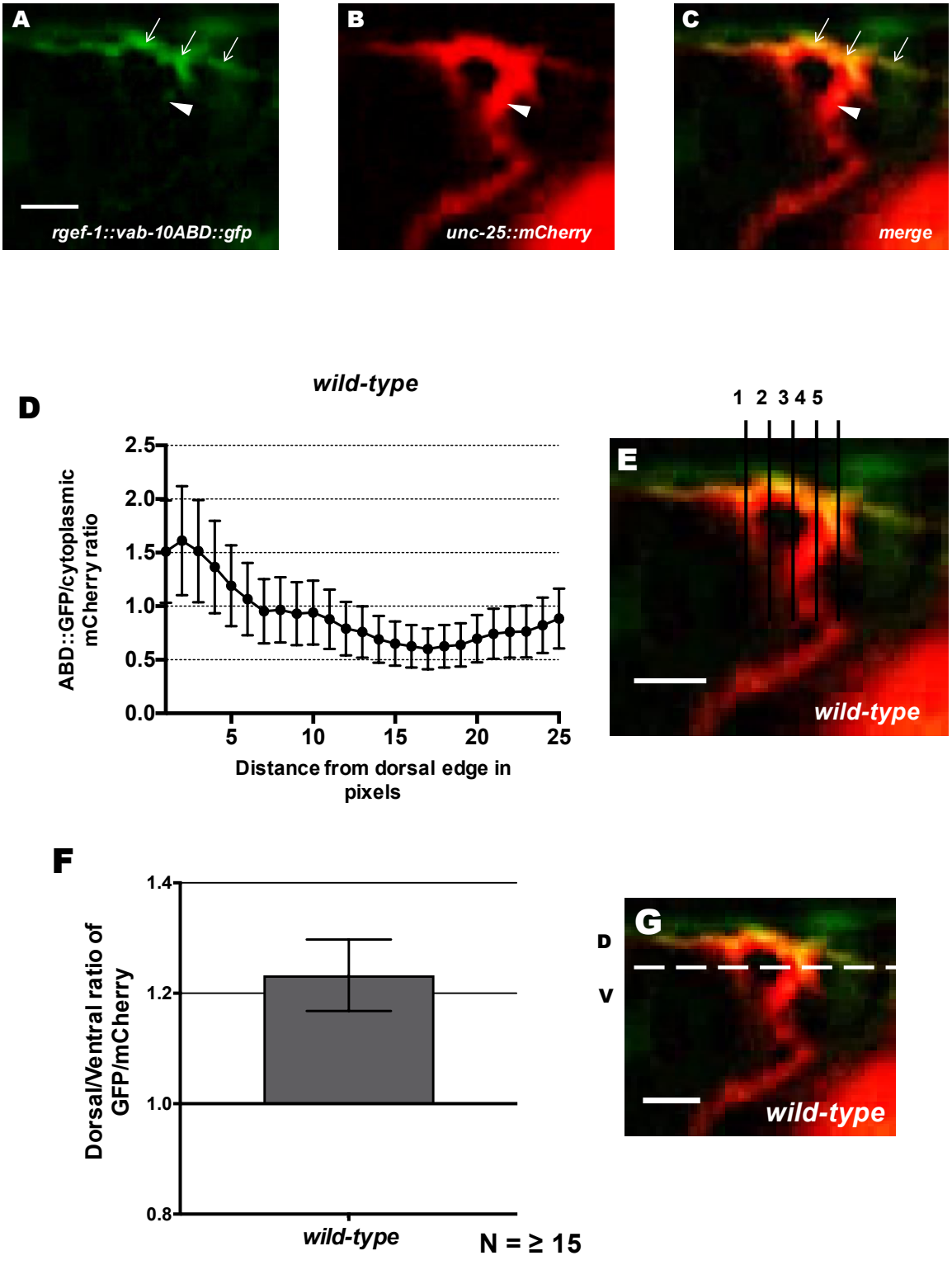
A
rgef-1::vab-10ABD::gfp
B
unc-25::mCherry
C
merge
D
wild-type
ABD::GFP/cytoplasmic mCherry ratio
2.5
2.0
1.5
1.0
0.5
0.0
5
10
15
20
25
Distance from dorsal edge in pixels
1 2 3 4 5
E
wild-type
F
Dorsal/Ventral ratio of GFP/mCherry
1.4
1.2
1.0
0.8
wild-type
N = ≥ 15
G
D
V
wild-type

Figure 3.2.

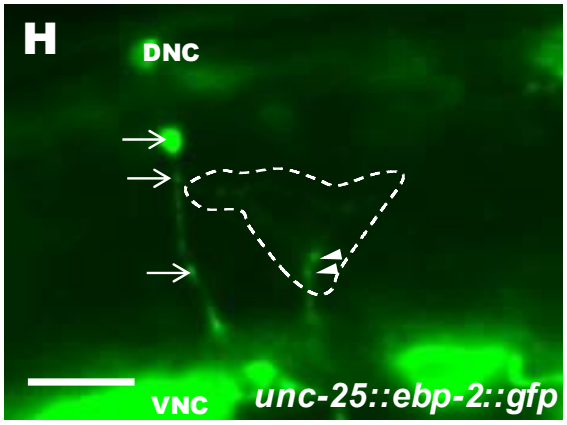
H
DNC
VNC
unc-25::ebp-2::gfp

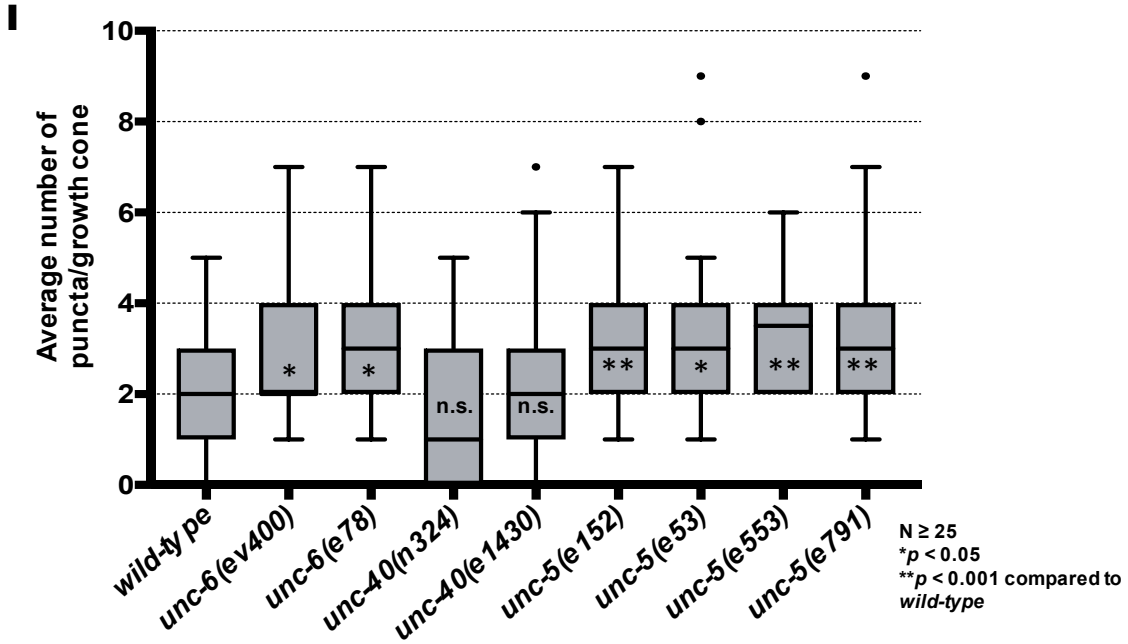
I
Average number of puncta/growth cone
10
8
6
4
2
0
*
*
n.s.
n.s.
**
*
**
**
wild-ty pe
unc-6(ev400)
unc-6(e78)
unc-40(n324)
unc-40(e1430)
unc-5(e152)
unc-5(e53)
unc-5(e553)
unc-5(e791)
N ≥ 25
*p < 0.05
**p < 0.001 compared to wild-type

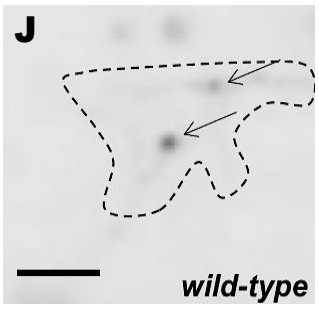
J
wild-type

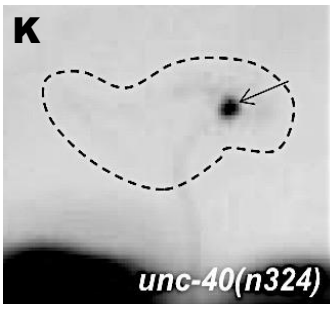
K
unc-40(n324)

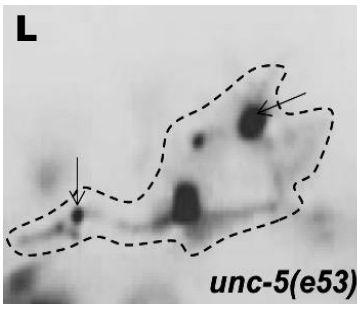
L
unc-5(e53)

Figure 3.2. Dorsally-polarized F-actin and EBP-2::GFP accumulation. (A) VAB-10ABD::GFP accumulation at the dorsal edge of a wild-type VD growth cone (arrows). Ventral region of the growth cone with little VAB-10ABD::GFP accumulation (arrow heads). **(B)** mCherry growth cone volume marker. **(C)** Merge. Dorsal is up and anterior is left. Scale bar: 5μm in A-C. **(D-G).** A representative line plot of a wild-type VD growth cone as previously described (Norris and Lundquist, 2011). **(D)** A graph representing the pixel intensity ratio (arbitrary units) of GFP/mCherry (y-axis) against the distance from the dorsal growth cone edge. **(E)** For each growth cone, five lines were drawn as shown and the pixel intensity ratios were averaged (error bars represent standard deviation). **(F)** The average dorsal-to-ventral ratio of GFP/mCherry in wild-type from multiple growth cones (≥15). Error bars represent the standard error of the mean of the ratios from different growth cones. **(G)** Growth cones were divided into dorsal and ventral halves, and the average intensity ratio of VAB-10ABD::GFP/mCherry was determined for each half and represented in (F). The scale bars in (E) and (G) represent 5μm. **(H)** A wild-type VD growth cone with *Punc-25::ebp-2::*gfp expression from the *lqIs279* transgene. The extent of the growth cone body is highlighted by a dashed line. Arrows point to EBP-2::GFP puncta in the axons of a DD neuron. Arrowheads point to puncta in the VD growth cone. VNC is the ventral nerve cord, and DNC is the dorsal nerve cord. Scale bar: 5μm. **(I)** Box-and-whiskers plot of the number of EBP-2::GFP puncta in the growth cones of different genotypes (≥25 growth cones for each genotype). The grey boxes represent the upper and lower quartiles, and error bars represent

the upper and lower extreme values. Dots represent outliers. *p* values were assigned using the two-sided *t*-test with unequal variance. **(J-L)** Growth cones of different genotypes, with EBP-2::GFP puncta indicated with arrows. Dashed lines indicate the growth cone perimeter. Dorsal is up and anterior is left. Scale bar: 5μm.

Figure 3.3.

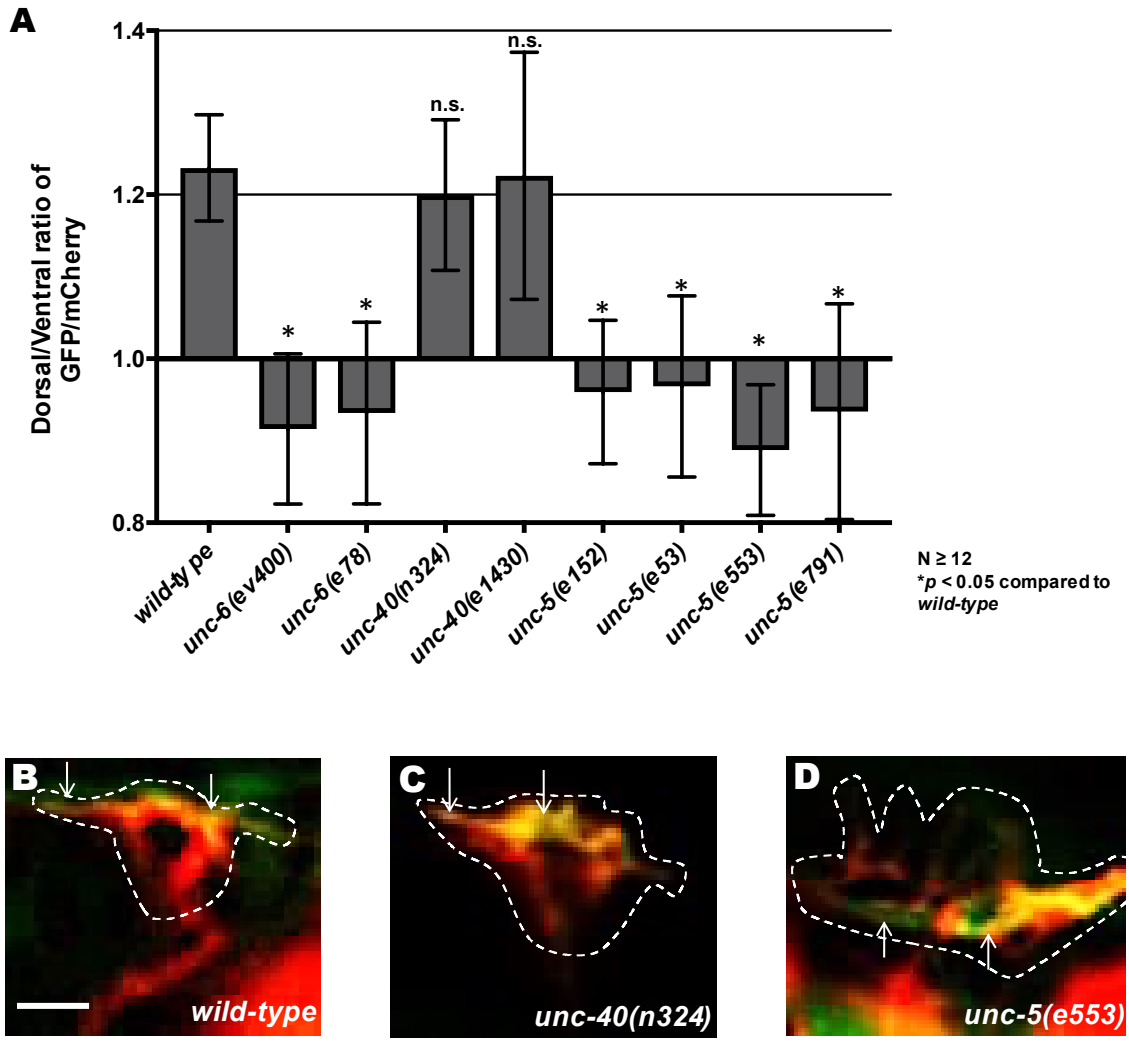
A
Dorsal/Ventral ratio of GFP/mCherry
1.4
1.2
1.0
0.8
n.s.
n.s.
*
wild-type
unc-6(ev400)
unc-6(e78)
unc-40(n324)
unc-40(e1430)
unc-5(e152)
unc-5(e53)
unc-5(e553)
unc-5(e791)
N ≥ 12
*p < 0.05 compared to wild-type
B
wild-type
C
unc-40(n324)
D
unc-5(e553)

Figure 3.3. Dorsal F-actin polarity is lost in *unc-5* and *unc-6* mutants. (A) The average dorsal-to-ventral ratio of GFP/mCherry from multiple growth cones (≥12) from different genotypes as described in Figure 1. Asterisks (*) indicate the significance of difference between wild-type and the mutant phenotype (*$p < 0.05$) (two-tailed *t*-test with unequal variance between the ratios of multiple growth cones of each genotype). Error bars represent the standard error of the mean **(B-D)** Representative merged images of VD growth cones with cytoplasmic mCherry in red (a volumetric marker) and the VAB-10ABD::GFP in green. Areas of overlap are yellow. Dashed lines indicate the perimeter of the growth cone. Scale bar: 5 μm.

Figure 3.4.

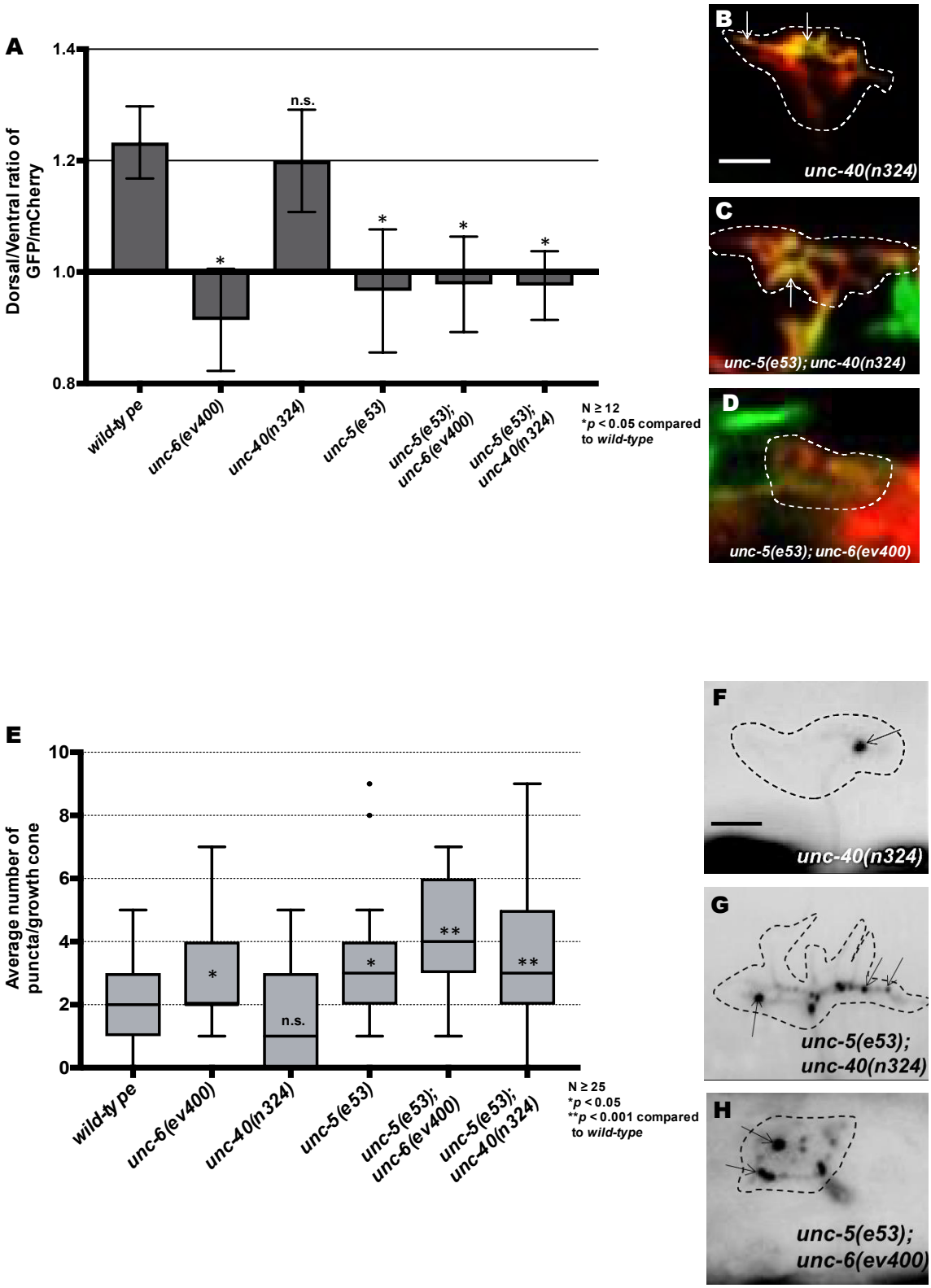
A
Dorsal/Ventral ratio of GFP/mCherry
1.4
1.2
1.0
0.8
n.s.
*
*
*
*
wild-ty pe
unc-6(ev400)
unc-40(n324)
unc-5(e53)
unc-5(e53); unc-6(ev400)
unc-5(e53); unc-40(n324)
N ≥ 12
*p < 0.05 compared to wild-type
B
unc-40(n324)
C
unc-5(e53); unc-40(n324)
D
unc-5(e53); unc-6(ev400)
E
Average number of puncta/growth cone
10
8
6
4
2
0
*
n.s.
*
**
**
wild-ty pe
unc-6(ev400)
unc-40(n324)
unc-5(e53)
unc-5(e53); unc-6(ev400)
unc-5(e53); unc-40(n324)
N ≥ 25
*p < 0.05
**p < 0.001 compared to wild-type
F
unc-40(n324)
G
unc-5(e53); unc-40(n324)
H
unc-5(e53); unc-6(ev400)

Figure 3.4. EBP-2::GFP puncta accumulation and loss of growth cone F-actin polarity in *unc-5* mutants is not dependent on functional UNC-6 or UNC-40. (A) The average dorsal-to-ventral ratio of GFP/mCherry from multiple growth cones in wild-type and mutant animals as described in Figure 3. **(B-D)** Representative images of VD growth cones with cytoplasmic mCherry in red (a volumetric marker) and the VAB-10ABD::GFP in green as described in Figure 1. Scale bar: 5 μm. **(E)** Quantification of average number of EBP-2::GFP puncta in wild-type and mutant animals as described in Figure 2. **(F-H)** Fluorescence micrographs of EBP-2::GFP expression in VD growth cones. Arrows point to EBP-2::GFP puncta Scale bar: 5μm

Figure 3.5.

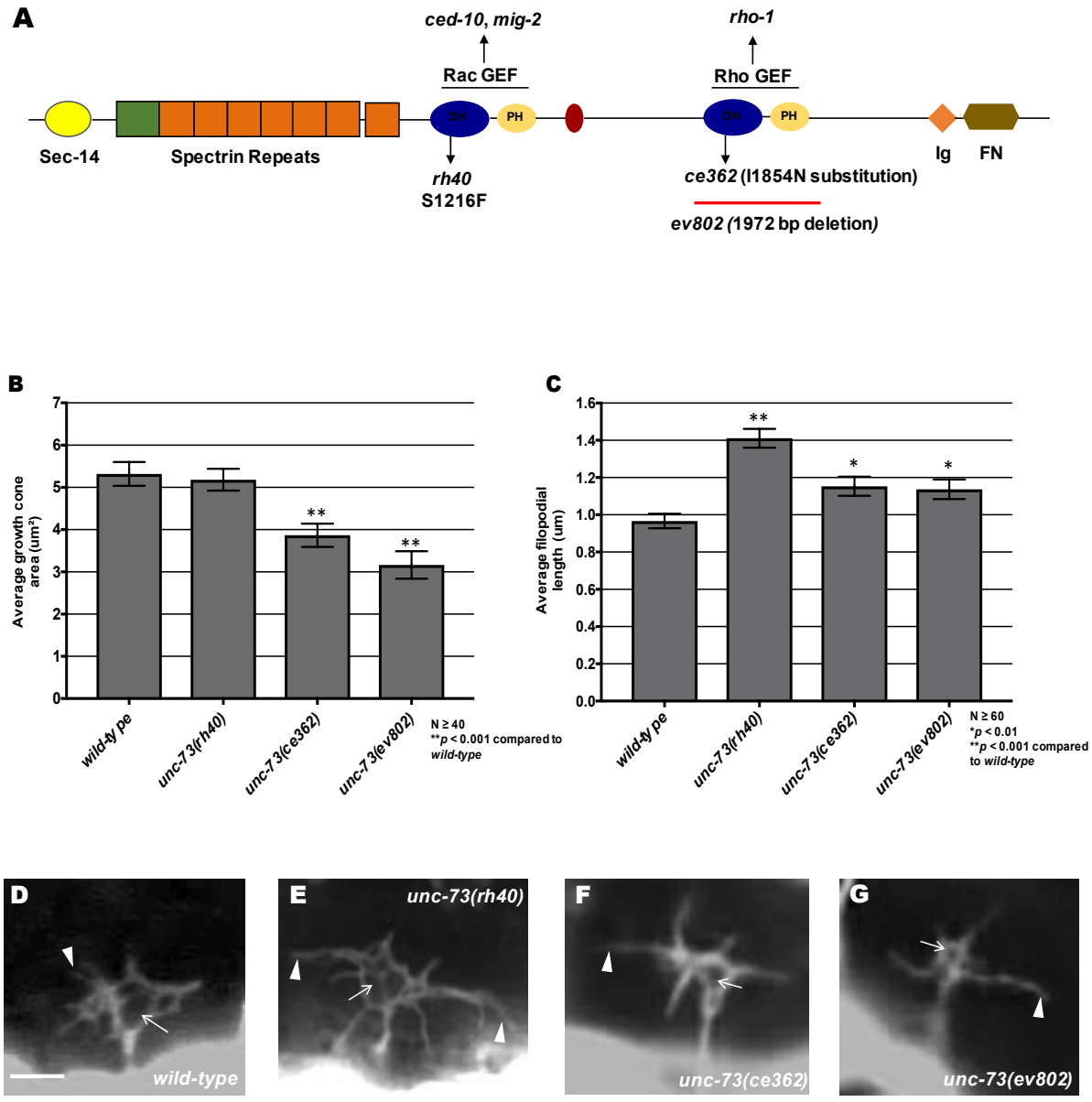
A
ced-10, mig-2
Rac GEF
rho-1
Rho GEF
DH
PH
DH
PH
Sec-14
Spectrin Repeats
Ig
FN
rh40
S1216F
ce362 (I1854N substitution)
ev802 (1972 bp deletion)
B
Average growth cone area (um²)
wild-ty pe
unc-73(rh40)
unc-73(ce362)
unc-73(ev802)
N ≥ 40
**p < 0.001 compared to wild-type
C
Average filopodial length (um)
wild-ty pe
unc-73(rh40)
unc-73(ce362)
unc-73(ev802)
N ≥ 60
*p < 0.01
**p < 0.001 compared to wild-type
D
wild-type
E
unc-73(rh40)
F
unc-73(ce362)
G
unc-73(ev802)

Figure 3.5. UNC-73/Trio alleles have distinct effects on VD growth cone protrusion. (A) A diagram of the full-length UNC-73/Trio molecule. The *rh40, ce362,* and *ev802* mutations are indicated. **(B)** Graphs of the average growth cone area and filopodial length in wild-type and *unc-73* mutants, as described in (Norris and Lundquist, 2011) (See Methods). Significance was determined by a two-sided *t*-test with unequal variance. **(D-G)** Fluorescence micrographs of VD growth cones with *Punc-25::gfp* expression from the transgene *juIs76*. Arrows point to the growth cone body, and arrowheads to filopodial protrusions. Scale bar: 5μm.

Figure 3.6.

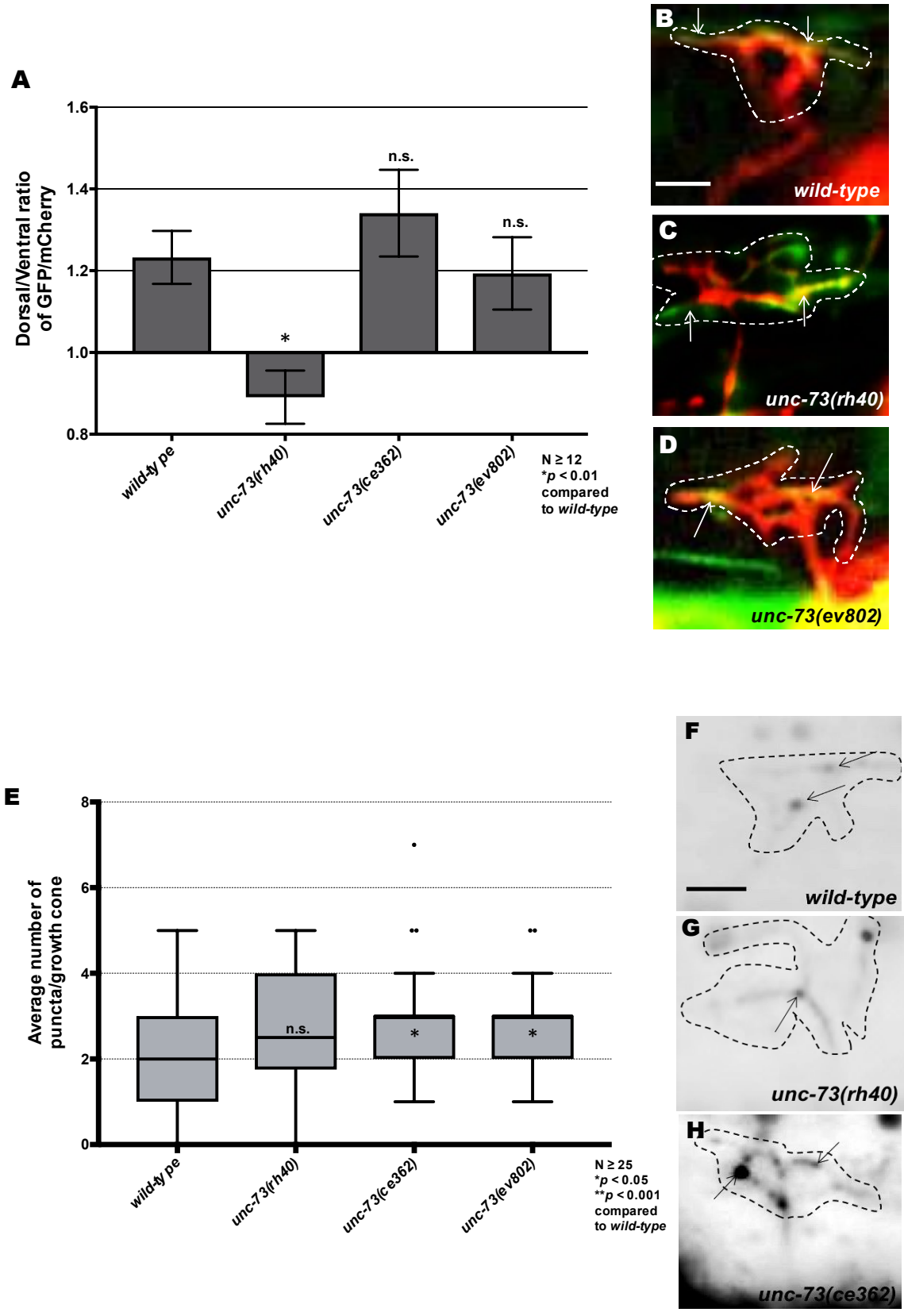
A
Dorsal/Ventral ratio of GFP/mCherry
1.6
1.4
1.2
1.0
0.8
n.s.
n.s.
*
wild-type
unc-73(rh40)
unc-73(ce362)
unc-73(ev802)
N ≥ 12
*p < 0.01
compared
to wild-type
B
wild-type
C
unc-73(rh40)
D
unc-73(ev802)
E
Average number of puncta/growth cone
8
6
4
2
0
n.s.
*
*
wild-type
unc-73(rh40)
unc-73(ce362)
unc-73(ev802)
N ≥ 25
*p < 0.05
**p < 0.001
compared
to wild-type
F
wild-type
G
unc-73(rh40)
H
unc-73(ce362)

Figure 3.6. The Rac GEF activity of UNC-73/Trio affects F-actin polarity but not EBP-2::GFP puncta accumulation. (A) The average dorsal-to-ventral ratio of GFP/mCherry from multiple growth cones in wild-type and mutant animals as described in Figures 1 and 3. **(C-E)** Representative merged images of VD growth cones with cytoplasmic mCherry in red (a volumetric marker) and the VAB-10ABD::GFP in green, as in Figure 1. Areas of overlap are yellow (arrows). Scale bar: 5 μm. **(F)** Quantification of average number of EBP-2::GFP puncta in wild-type and mutant animals as described in Figure 2. **(G-J)** Fluorescence micrographs of VD growth cones showing EBP-2::GFP puncta (arrows). Scale bar: 5μm.

Figure 3.7

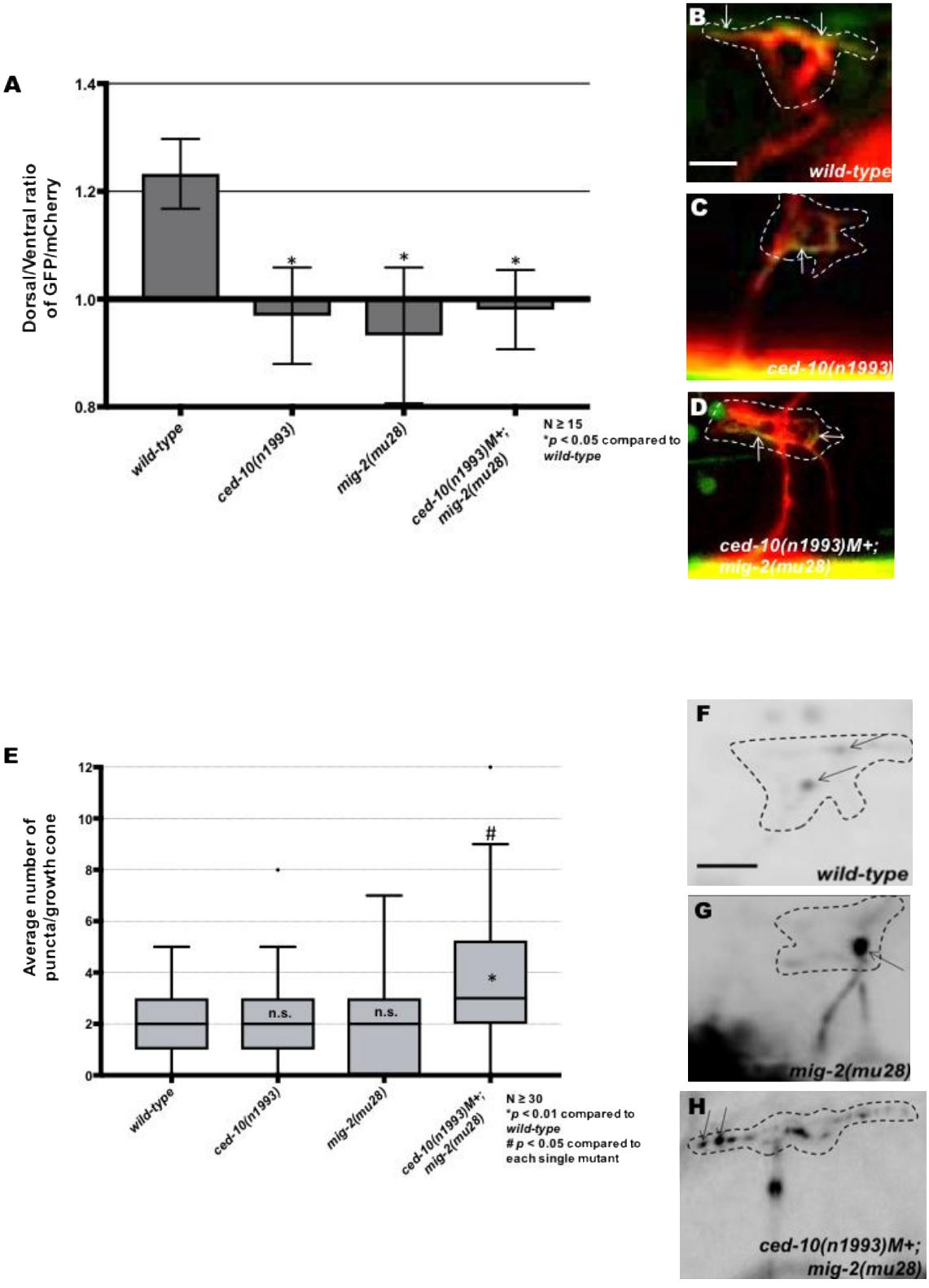
A
Dorsal/Ventral ratio of GFP/mCherry
1.4
1.2
1.0
0.8
*
*
*
wild-type
ced-10(n1993)
mig-2(mu28)
ced-10(n1993)M+; mig-2(mu28)
N ≥ 15
*p < 0.05 compared to wild-type
B
wild-type
C
ced-10(n1993)
D
ced-10(n1993)M+; mig-2(mu28)
E
Average number of puncta/growth cone
12
10
8
6
4
2
0
n.s.
n.s.
*
#
wild-type
ced-10(n1993)
mig-2(mu28)
ced-10(n1993)M+; mig-2(mu28)
N ≥ 30
*p < 0.01 compared to wild-type
# p < 0.05 compared to each single mutant
F
wild-type
G
mig-2(mu28)
H
ced-10(n1993)M+; mig-2(mu28)

Figure 3.7. The Rac GTPases CED-10 and MIG-2 individually affect F-actin polarity and are redundant for EBP-2::GFP puncta accumulation. (A) The average dorsal-to-ventral ratio of GFP/mCherry from multiple growth cones in wild-type and mutant animals as described in Figures 3.1 and 3.3. **(B-D)** Representative merged images of VD growth cones with cytoplasmic mCherry in red (a volumetric marker) and the VAB-10ABD::GFP in green as in Figure 3.1. Scale bar: 5 μm. **(E)** Quantification of average number of EBP-2::GFP puncta in wild-type and mutant animals as described in Figure 2. **(F-H)** Fluorescence micrographs of VD growth cones with EBP-2::GFP puncta indicated arrows. Scale bar: 5μm.

Figure 3.8.

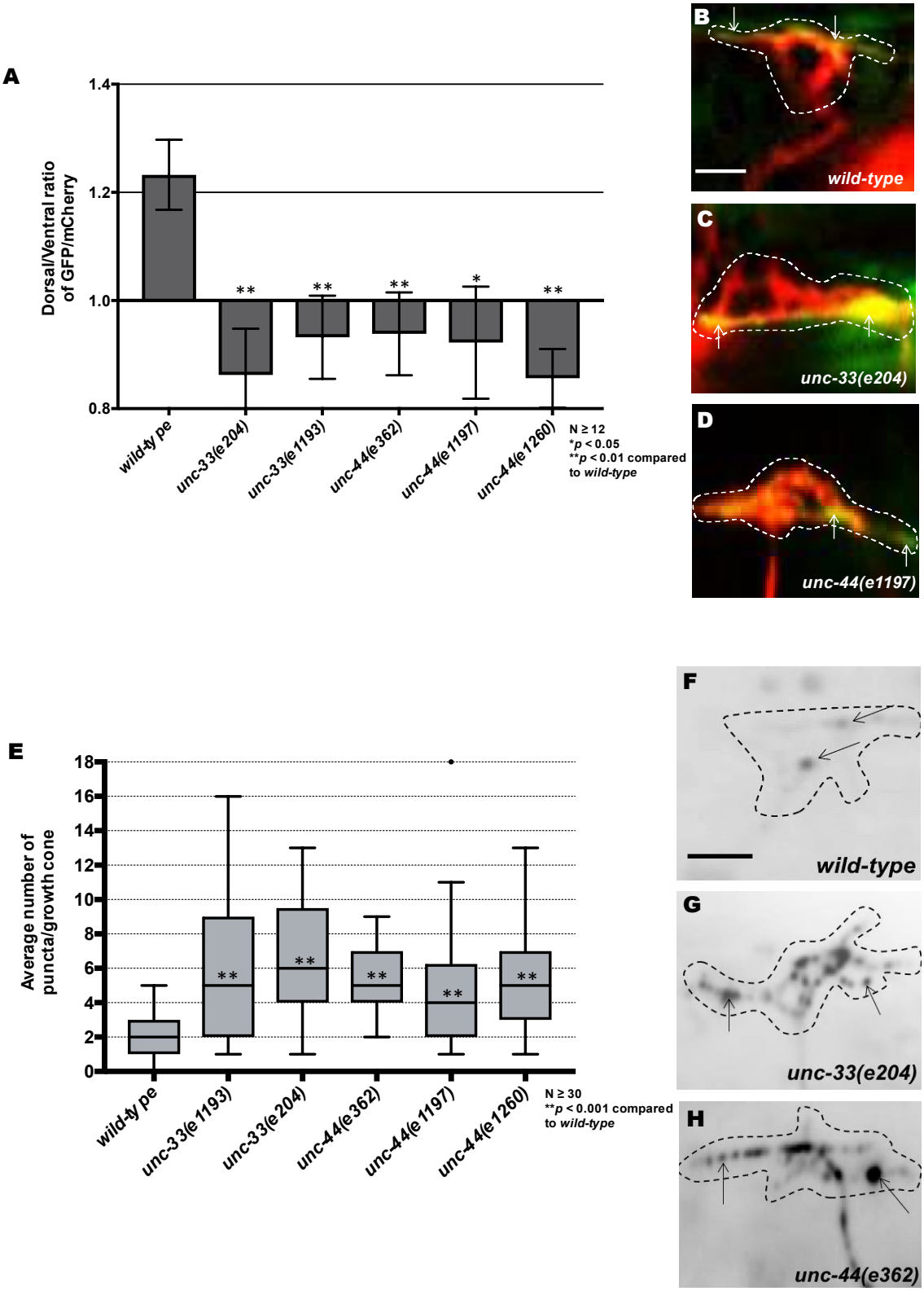
A
Dorsal/Ventral ratio of GFP/mCherry
1.4
1.2
1.0
0.8
**
**
**
*
**
wild-type
unc-33(e204)
unc-33(e1193)
unc-44(e362)
unc-44(e1197)
unc-44(e1260)
N ≥ 12
*p < 0.05
**p < 0.01 compared to wild-type
B
wild-type
C
unc-33(e204)
D
unc-44(e1197)
E
Average number of puncta/growth cone
18
16
14
12
10
8
6
4
2
0
wild-type
unc-33(e1193)
unc-33(e204)
unc-44(e362)
unc-44(e1197)
unc-44(e1260)
N ≥ 30
**p < 0.001 compared to wild-type
F
wild-type
G
unc-33(e204)
H
unc-44(e362)

Figure 3.8. *unc-33* and *unc-44* mutants disrupt F-actin polarity and affect EBP-2::GFP puncta accumulation. (A) The average dorsal-to-ventral ratio of GFP/mCherry from multiple growth cones in wild-type and mutant animals as described in Figure 3. **(B-D)** Representative merged images of VD growth cones with cytoplasmic mCherry in red (a volumetric marker) and the VAB-10ABD::GFP in green, as in Figure 1. Scale bar: 5 μm. **(E)** Quantification of average number of EBP-2::GFP puncta in wild-type and mutant animals as in Figure 2. **(F-H)** Fluorescence micrographs of VD growth cones with EBP-2::GFP puncta indicate by arrows. Scale bar: 5μm.

Figure 3.9.

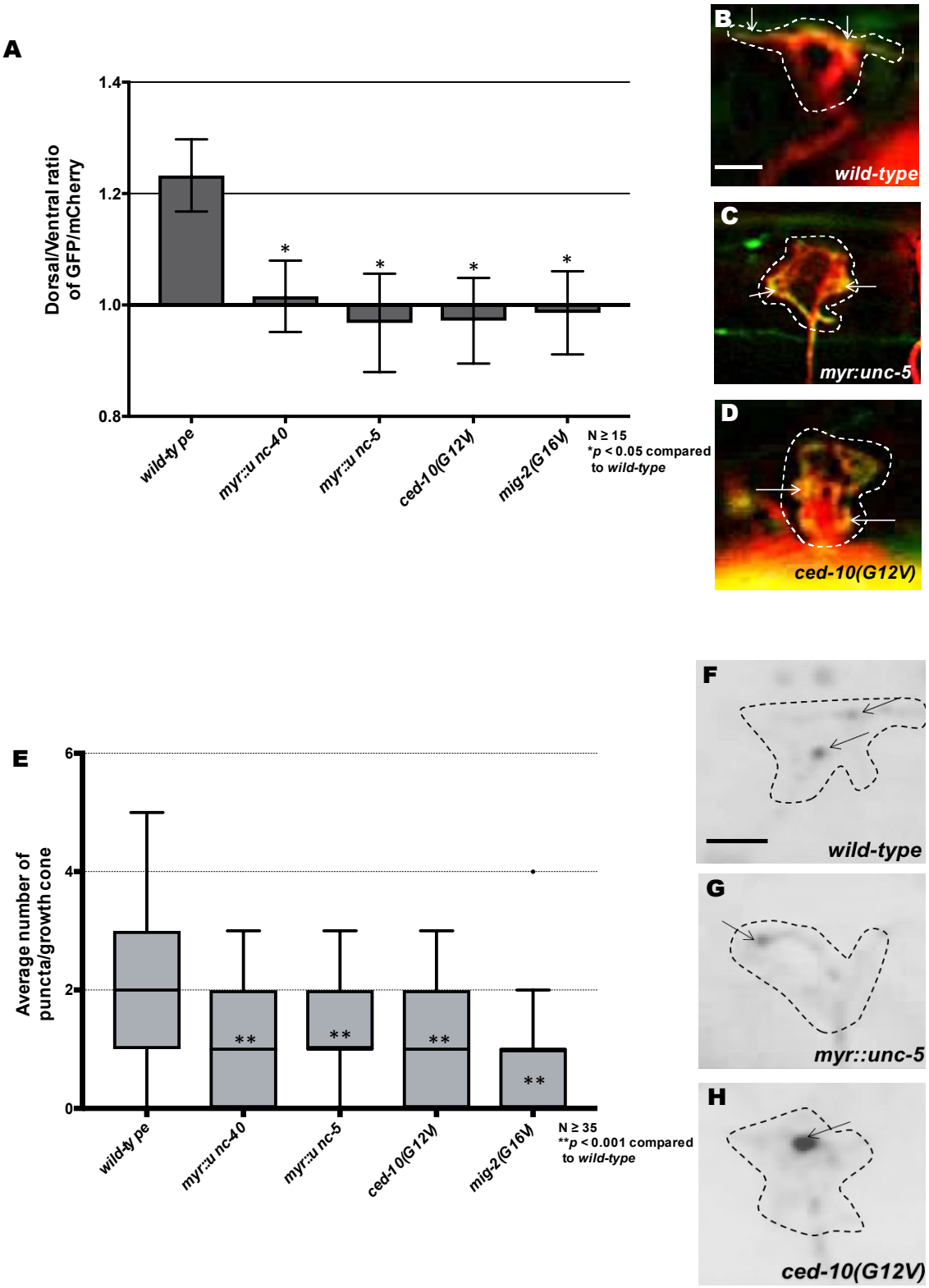
A
Dorsal/Ventral ratio of GFP/mCherry
1.4
1.2
1.0
0.8
wild-type
myr::unc-40
myr::unc-5
ced-10(G12V)
mig-2(G16V)
N ≥ 15
*p < 0.05 compared to wild-type
B
wild-type
C
myr:unc-5
D
ced-10(G12V)
E
Average number of puncta/growth cone
6
4
2
0
wild-type
myr::unc-40
myr::unc-5
ced-10(G12V)
mig-2(G16V)
N ≥ 35
**p < 0.001 compared to wild-type
F
wild-type
G
myr::unc-5
H
ced-10(G12V)

Figure 3.9. Constitutive activation of UNC-40, UNC-5, CED-10 and MIG-2 affects F-actin polarity and EBP-2 distribution. (A) The average dorsal-to-ventral ratio of GFP/mCherry from multiple growth cones in wild-type and mutant animals as described in Figure 3. **(B-D)** Representative merged images of VD growth cones with cytoplasmic mCherry in red (a volumetric marker) and the VAB-10ABD::GFP in green. Scale bar: 5 μm. **(E)** Quantification of average number of EBP-2::GFP puncta in wild-type and mutant animals as described in Figure 2. **(F-H)** Fluorescence micrographs of VD growth cones with EBP-2::GFP puncta indicated by arrows. Scale bar: 5μm.

Figure 3.10.

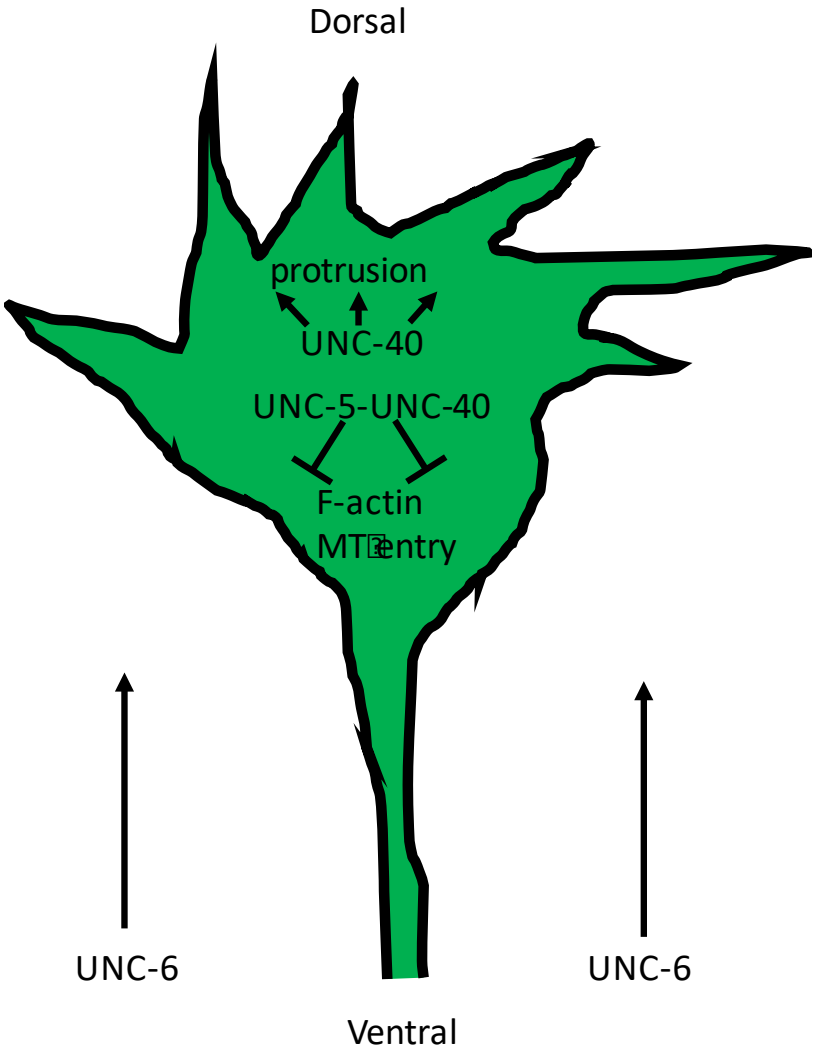
Dorsal
protrusion
UNC-40
UNC-5-UNC-40
F-actin
MT entry
UNC-6
UNC-6
Ventral

Figure 3.10. A model of the roles of UNC-5 and UNC-40 in growth cone outgrowth. Our results indicate that UNC-6/Netrin controls multiple, complex aspects of growth cone behavior and morphology during growth away from it. UNC-6 polarizes the growth cone via UNC-5, including F-actin accumulation and protrusion localized to the dorsal leading edge away from the UNC-6 source. UNC-6 also regulates the extent of growth cone protrusion. It inhibits protrusion via UNC-5, possibly by restricting MT + end accumulation in the growth cone. Protrusion can be inhibited independently of MT + ends, possibly via an actin-based mechanism involving the flavin monooxygenases (FMOs). UNC-6/Netrin can also drive growth cone protrusion via UNC-40/DCC. These anti- and pro-protrusive activities of UNC- 6/Netrin might act asymmetrically in the growth cone, possible established by the earlier role of UNC-6/Netrin in polarizing the growth cone.

Chapter IV

The Small GTPase RHO-1 and its Regulator RHGF-1/PDZRhoGEF Regulate *C. elegans* Growth Cone Protrusion and Microtubule Accumulation

4.1 Abstract

During development, axons emerge from neuronal cell bodies, elongate, and navigate towards target regions guided by a range of environmental cues through interactions with distinct receptors that are present at the tip of a growing axon—the growth cone. Growth cone motility that causes the growing axon to extend, turn or retract is dependent on the actin and microtubule cytoskeleton. The Rho family of small GTPases have central roles in axon guidance with their ability to coordinate multiple signal transduction pathways that drive the dynamic assembly, disassembly, and reorganization of the actin and microtubule cytoskeletons. Several guanine nucleotide exchange factors (GEFs) are required for the activation of the GTPases. The activated conformation then interacts with specific cytoskeletal effectors to propagate downstream signaling events that influence growth cone morphology. Our previous work has shown that in *C. elegans* the Rac-like GTPases CED-10/Rac and MIG-2/RhoG can both stimulate and inhibit growth cone protrusion in UNC-6/Netrin receptor signaling through distinct GEFs; TIAM-1 and UNC-73/Trio respectively. In this work we analyze the roles of the *C. elegans* Rho GTPases RHO-1 and the RhoGEF RHGF-1 in growth cone protrusion, F-actin localization and microtubule organization. We find that these molecules are required for the normal limitation of filopodial protrusion and microtubule plus-end distribution in developing growth cones. Epistasis studies using activated RHO-1 indicated that RHGF-1 acts upstream of RHO-1 in inhibition of growth cone protrusion as well as restricting MT+ - ends in the growth cone. RHGF-1 is required for inhibition of growth cone

protrusion caused by activated MYR::UNC-40 and MYR::UNC-5 signaling and RHO-1 interacts with the cytoskeletal interacting protein UNC-33/CRMP to control microtubule distribution in the developing growth cone.

4.2 Introduction

The connectivity of neuronal circuits is established through properly guided axons which form functional synaptic connections. The growing axon is guided to its proper synaptic targets with help of highly motile, actin based structures present at the tip of the growing neurites known as growth cones. Growth cone motility and their ability to respond to various environmental guidance cues allows the axon to extend, retract, turn and branch. This is regulated by the reorganization and dynamics of the actin and microtubule cytoskeleton of the growth cone (Dent and Gertler, 2003).

The growth cone is a fan shaped structure comprising of two domains; the central domain and the peripheral domain. The central domain (C-domain) is rich in microtubules and is continuous with the axon shaft. The peripheral domain (P-domain) is dominated by actin filaments that form the veil-like lamellopodia and the finger-like filopodial protrusions, both of which are important for the proper growth of an axon to its target destination(Goldberg and Burmeister, 1986; Zhou and Cohan, 2004). Steady state myosin-dependent retrograde flow of actin occurs in both the lamellipodia and filopodia, allowing for cycles of assembly and disassembly of actin filaments proximally(Craig et al., 2012; Van Goor et al., 2012). Retrograde actin flow is thought to regulate axon outgrowth and prevents microtubules from invading the P-domain of the growth cone (Burnette et al., 2007). Filopodial protrusions are important for sensing extracellular guidance cues and steering the growth cone. Actin filaments present at the leading edge of the growth cones are direct targets for these guidance cues (Bear et al., 2001;

Luo, 2002). Attractive guidance cues promote actin polymerization at the proximal end of the growth cone driving the forward motion of the axon. Repulsive guidance cues trigger actin depolymerization causing the growth cone to retract and move away from the repulsive source (Guan and Rao, 2003).

The laminin-like UNC-6/Netrin guidance cue and its receptors UNC-40/DCC and UNC-5 control both attraction and repulsion in the dorsal-ventral axis(Chan et al., 1996; Hong et al., 1999; Leonardo et al., 1997; Montell, 1999; Moore et al., 2007; Shekarabi and Kennedy, 2002). The receptor UNC-40 in its homodimeric state is expressed in the growth cones and mediates an attractive response to UNC-6, while UNC-5:UNC-40 heterodimers or UNC-5 homodimers mediate a repulsive response to UNC-6 (Hong et al., 1999; MacNeil et al., 2009). In *C.elegans* UNC-6 is secreted by the ventral cells and along with UNC-40 and UNC-5 mediates the dorsal-ventral circumferential migrations of growth cones and axons ((Chan et al., 1996; Hedgecock et al., 1990a; Ishii et al., 1992; Leung-Hagesteijn et al., 1992). The VD growth cones repelled from UNC-6 display dorsally directed, dynamic lamellipodial and filopodial protrusions ((Knobel et al., 1999; Norris and Lundquist, 2011; Norris et al., 2014).

Previous studies have shown that UNC-40/DCC mediated attractive guidance drives neuronal lamellipodial and filopodial protrusions and this involves several cytoskeletal signaling molecules such as, Cdc42, the Rac-specific guanine nucleotide exchange factor (GEF) TIAM-1, Rac-like GTPases CED-10/Rac and MIG-2/RhoG and actin cytoskeletal regulators Arp2/3, UNC-34/Enabled and UNC-115/abLIM (Demarco et al., 2012; Gitai et al., 2003; Norris

et al., 2009; Shakir et al., 2008; Struckhoff and Lundquist, 2003). UNC-5 is required for its inhibitory effects on growth cone protrusion. Loss of *unc-5* cause an over-protrusive VD growth cone phenotype, with significantly longer filopodial protrusions and larger growth cone area compared to wild-type growth cones. Furthermore, filopodial protrusions are no longer biased dorsally and can occur all around the growth cone, including ventrally (Norris et al., 2009). UNC-5 mediated inhibition involves the Rac GEF UNC-73/trio, Rac GTPases CED-10/Rac and MIG-2/RhoG and the cytoskeletal interacting proteins UNC-33/CRMP and UNC-44/Ankyrin. In addition to limiting growth cone protrusion UNC-6 and UNC-5 control F-actin polarity in *C. elegans* VD growth cones (Norris and Lundquist, 2011). Using the VAB-10 actin binding domain expressed in the VD neurons we see that F-actin accumulates dorsally at the leading edge of the growth cone (Bosher et al., 2003; Norris and Lundquist, 2011). In *unc-6* and *unc-5* mutants this asymmetry is lost, consistent with the loss of polarity in growth cone protrusion in these mutants (Norris and Lundquist, 2011)

The Rho family of small GTPases are key regulators of the actin and microtubule cytoskeleton and mediate several neuronal developmental processes such as neuronal migration, dendritic development, axon growth and guidance(Govek et al., 2005; Luo et al., 1994; Threadgill et al., 1997; Zipkin et al., 1997). During axon growth Rac induces the formation of the actin-rich lamellopodia and Cdc42 induces the formation of the finger-like filopodial extensions, whereas Rho promotes the formation of stress fibres through actin-myosin contraction (Guan and Rao, 2003). The GTPases are likely to function as

the key mediators that link guidance signals to cytoskeletal rearrangements, where attractive guidance cues activate Cdc42 and Rac, but inhibit RhoA and repulsive cues are thought to activate Rho and inhibit Rac and Cdc42 (Guan and Rao, 2003). *C. elegans* has one Rho (*rho-1*), one Cdc42 (*cdc-42*), two canonical Racs similar to vertebrate Rac1 (*ced-10* and *rac-2*), and one Mtl Rac (*mig-2*) with similarity to both Rac and Cdc42 (Reiner and Lundquist, 2016). Functionally, MIG-2 is similar to mammalian RhoG (deBakker et al., 2004). In *C. elegans* the Rac GTPases CED-10 and MIG-2 redundantly control axon guidance and have been shown to mediate neuronal protrusion downstream of UNC-40/DCC in UNC-6/Netrin mediated attraction (Demarco et al., 2012; Struckhoff and Lundquist, 2003) as well as limit VD growth cone protrusion in response to UNC-6 mediated repulsion (Norris et al., 2014). RNAi of the single RhoA orthlog in *C. elegans* (*rho-1*) results in early embryonic arrest, with a failure in cytokinesis (JANTSCH-PLUNGER *et al.* 2000; (Bringmann and Hyman, 2005; Morita et al., 2005; Motegi and Sugimoto, 2006; Spencer et al., 2001). Embryos that arrest later in development also display severe defects in tissue morphogenesis, probably due to defects in Rho-mediated actin-myosin cytoskeletal defects (Schonegg and Hyman, 2006). RHO-1 is expressed throughout the nervous system (Chen and Lim, 1994) has been shown to control neuronal cell shape and neurite outgrowth in the ASE sensory neurons (Zallen et al., 2000) as well as neurotransmitter release at neuromuscular junctions (Hiley et al., 2006; McMullan et al., 2006).

The Rho GTPases are activated by specific guanine nucleotide exchange factors (GEFs) which stimulate the exchange of GTP for GDP (Schmidt and Hall, 2002). In mammals, the RhoGEF LARG protein specifically interacts with G12α via its regulator of G protein signaling (RGS) domain to activate Rho (Suzuki et al., 2003). *C. elegans* RHGF-1, is the homolog of mammalian LARG and is a multidomain protein that contains a PDZ, RGS (regulator of G signaling), C1 (diacylglycerol binding), DH (Dbl homology) and PH (plekstrin homology) domain (Alam et al., 2016; Chen et al., 2014; Hiley et al., 2006). The GTP exchange activity of RHGF-1 resides in the DH domain (Hiley et al., 2006; Yau et al., 2003). RHGF-1 is expressed in many neurons including the ventral nerve cord motor neurons (Chen et al., 2014; Yau et al., 2003) and has been shown to be important for neurotransmitter release and axon regeneration (Hiley et al., 2006; Lin et al., 2012). Previous work has also shown that RHGF-1 is normally associated with microtubules, making it an ideal sensor for microtubule integrity (Chen et al., 2014)

In this work, we tested the roles of *C. elegans* RHO-1 and its regulator RHGF-1 in growth cone protrusion, F- actin and microtubule plus end (MT+ -end) distribution in the VD growth cone. We find that in the VD growth cone, *rho-1* and *rhgf-1* mutants display increased filopodial protrusion and increased EBP-2 puncta distribution and that *rho-1* functions downstream of *rhgf-1* in both these processes. We also find that RHGF-1 may be required for the growth cone inhibitory effects and EBP-2 distribution of activated MYR::UNC-5 and MYR::UNC-40. We also show that RHO-1 may function in the UNC-5 pathway

and interacts with UNC-33/CRMP to mediate inhibition of growth cone protrusion and limit the number of MT+ -ends from entering the growth cone periphery.

4.3 Materials and methods

Genetic methods

Experiments were performed at 20°C using standard *C. elegans* techniques (Brenner, 1974). Mutations used were LGIV: *unc-5(e53* and *e152)*, *unc-33(e204*), *unc-44(e362*); *lqIs128* [*Punc-25::myr::unc-40*] LGX: *rhgf-1(gk217, ok880 and gk292502), lqIs170* [*rgef-1::vab-10ABD::gfp*]. Chromosomal locations not determined: *lqIs279* [*Punc-25::ebp-2::gfp*] by integration of *lqEx809, lhIs6* [*Punc-25::mCherry*], *lqIs296* [*Punc-25::myr::unc-5*]*, lqIs312* [*Punc-25::rho-1(G14V)*] by integration of *lqEx1043, lqIs314* [*Punc-25::rho-1(T19N)*] by integration of *lqEx1070*. Extrachromosomal arrays were generated using standard gonadal injection (Mello and Fire, 1995) and include: *lqEx999* and *lqEx1000* [*Punc-25::myr::unc-40; Pgcy-32::yfp*], *lqEx1119, lqEx1120, lqEx1121, lqEx1122, lqEx1178, lqEx1179 and lqEx1180* [*Punc-25::rho-1 CRISPR; Pgcy-32::yfp*], *lqEx1131, lqEx1132, lqEx1133* and *lqEx1134* [*Punc-25::rho-1 RNAi; Pgcy-32::yfp*], *OX347* [*Prgef-1::vab-10ABD::gfp; ttx-3::rfp*]. Multiple (≥3) extrachromosomal transgenic lines of *Punc-25::ebp-2::gfp*, *Punc-25::rho-1(G14V)* and *Punc-25::rho-1(T19N)* were analyzed with similar effect, and one was chosen for integration and further analysis.

Growth cone imaging

VD growth cones were imaged and quantified as previously described (Norris and Lundquist, 2011). Briefly, animals at ~16 h post-hatching at 20°C were placed on a 2% agarose pad and paralyzed with 5mM sodium azide in M9

buffer, which was allowed to evaporate for 4 min before placing a coverslip over the sample. Some genotypes were slower to develop than others, so the 16 h time point was adjusted for each genotype. Growth cones were imaged with a Qimaging Rolera mGi camera on a Leica DM5500 microscope. Images were analyzed in ImageJ, and statistical analyses done with Graphpad Prism software. As described in (Norris and Lundquist, 2011; Norris et al., 2014), growth cone area was determined by tracing the perimeter of the growth cone body, not including filopodia. Average filopodial length was determined using a line tool to trace the length of the filopodium. Unless otherwise indicated, ≥25 growth cones were analyzed for each genotype. These data were gathered in ImageJ and entered into Graphpad Prism for analysis. A two-sided *t*-test with unequal variance was used to determine significance of difference between genotypes.

VAB-10ABD::GFP imaging

The F-actin binding domain of VAB-10/spectraplakin fused to GFP has been used to monitor F-actin in *C. elegans* (Bosher et al., 2003; Patel et al., 2008). We used it to image F-actin in the VD growth cones as previously described (Norris and Lundquist, 2011). To control for variability in growth cone size and shape, and as a reference for asymmetric localization of VAB-10ABD::GFP, a soluble mCherry volume marker was included in the strain. Growth cones images were captured as described above. ImageJ was used image analysis to determine asymmetric VAB-10ABD::GFP localization. For each growth cone, five line scans were made from dorsal to ventral (see results). For

each line, pixel intensity was plotted as a function of distance from the dorsal leading edge of the growth cone. The average intensity (arbitrary units) and standard error for each growth cone was determined. For dorsal versus ventral comparisons, the pixel intensities for VAB-10ABD::GFP were normalized to the volumetric mCherry fluorescence in line scans from the dorsal half and the ventral half of each growth cone. This normalized ratio was determined for multiple growth cones, and the average and standard error for multiple growth cones was determined. Statistical comparisons between genotypes were done using a two-tailed *t*-test with unequal variance on these average normalized ratios of multiple growth cones of each genotype.

EBP-2::GFP imaging

EBP-2::GFP has previously been used to monitor microtubule plus ends in other *C. elegans* cells including neurons (Kozlowski et al., 2007; Srayko et al., 2005; Yan et al., 2013). We constructed a transgene consisting of the *unc-25* promoter driving expression of *ebp-2::gfp* in the VD/DD neurons. In growth cones, a faint fluorescence was observed throughout the growth cone, resembling a soluble GFP and allowing for the growth cone perimeter to be defined. In addition to this faint, uniform fluorescence, brighter puncta of EBP-2::GFP were observed that resembled the EBP-1::GFP puncta described in other cells and neurons. For each growth cone, the perimeter and filopodia were defined, and the EBP-2::GFP puncta in the growth cone were counted. For each genotype, the puncta number for many growth cones (≥25 unless otherwise

noted) was determined. Puncta number displayed high variability within and between genotypes, so box-and-whiskers plots (Graphpad Prism) were used to accurately depict this variation. The grey boxes represent the upper and lower quartiles of the data set, and the “whiskers” represent the high and low values. Dots represent major outliers. Significance of difference was determined by a two-sided *t*-test with unequal variance.

Transgenic RNA-mediated gene interference (RNAi)

We used a cell-specific transgenic RNAi approach as described previously (Esposito et al., 2007). Fragments of the *rho-1* coding region was amplified by PCR and inserted behind the *unc-25* promoter in a plasmid (primer and plasmid sequences available upon request). A “sense” and “antisense” orientation relative to the *unc-25* promoter was isolated. An equimolar mixture of the sense and antisense plasmids was used to construct transgenic animals. These transgenic animals were predicted to express both sense and antisense RNAs driven by the *unc-25* promoter in the VD/DD motor neurons, which was expected to trigger a double-stranded RNA response in these cells (RNAi).

Cell-specific CRISPR-Cas9

Three sgRNA sequences against exon 2 of *rho-1* were designed according to established criteria, and placed downstream of the U6 promoter. An equimolar mixture of the sgRNA plasmids was used to construct transgenic animals. Cas9 was driven by the *unc-25* promoter to ensure loss of *rho-1* only in the VD/DD motor neurons. Multiple (≥3) extrachromosomal transgenic lines were

analyzed with similar effect, and one was chosen for integration and further analysis

4.4 Results

RHO-1 is required for inhibition of growth cone filopodial protrusion

The single Rho homolog in *C. elegans* is *rho-1*. Loss of *rho-1* leads to embryonic lethality, with a failure in cytokinesis (Jantsch-Plunger et al., 2000). Previous work has also shown that perturbation of RHO-1 signaling in adults results in dysfunction in numerous neuronal and non-neuronal functions and leads to death (McMullan and Nurrish, 2011). To understand the role of RHO-1 in VD growth cone morphology we constructed the constitutively activated as well as the dominant negative versions of RHO-1. In the constitutively active RHO-1(G14V), RHO-1 is locked in the active GTP bound state, whereas, in the dominant negative RHO-1(T19N), RHO-1 is locked in the inactive GDP bound form. Expression of both the mutants was driven in the VD/DD motor neurons using the *unc-25* promoter. We find that expression *of rho-1(G14V)* significantly reduced the VD growth cone area and shortened filopodial protrusions as compared to wild-type (Figure 4.1A-B, D). In contrast, transgenic *rho-1(T19N)* expression displayed significantly longer filopodial protrusions as compared to wild-type VD growth cones (0.96 µm in wild type compared with 1.29 µm in *rho-1(T19N)*; $p < 0.001$) (Figure 4.1A-B, E). Growth cone area was not affected by *rho-1(T19N)* mutants. These results indicate that wild-type RHO-1 activity may be required to inhibit growth cone protrusion.

To further confirm these observations, we used transgenic RNAi approach to knock down *rho-1* in the VD/DD motor neurons as previously described (see Materials and Methods) (Esposito et al., 2007). Plasmids were generated to

drive expression of sense and antisense RNA complementary to the *rho-1* under the control of the *unc-25* promoter. Animals were made transgenic with a mix of the sense and antisense plasmids, and the resulting transgenes were used in analysis. *rho-1(RNAi)* mutants caused an increase in growth cone protrusiveness in VD growth cones. The average length of filopodial protrusions was significantly increased in these mutants, growth cone area was also significantly increased as compared to wild-type (Figure 4.1A-B, F).

Cell- specific knockout of *rho-1* using the CRISPR–Cas9 mediated genome editing was also done. Three sgRNA sequences targeting exon 2 of *rho-1* were designed and placed downstream of the U6 promoter. Cas9 was driven by the *unc-25* promoter to ensure loss of *rho-1* only in the VD/DD motor neurons. *rho-1(CRISPR)* also showed a significant increase in the average filopodial length, similar to *rho-1(T19N)* and *rho-1(RNAi)* expression. These data suggest that RHO-1 may be required for inhibition of VD growth cone protrusion.

RHO-1 is required to limit EBP-2::GFP puncta accumulation in the VD growth cones.

The Rho family of small GTPases, such as Rho, Rac, and Cdc42, regulate cytoskeletal reorganization in different ways (Jaffe and Hall, 2005; Kaibuchi et al., 1999). The functions of these GTPases have been primarily investigated with regard to their effects on actin filaments. Rho regulates stress fiber formation, actin depolymerization and growth cone retraction through actin-myosin contraction, whereas Rac and Cdc42 promote actin polymerization in

lamellipodia and filopodia, respectively, and promote protrusive activities (Hall, 2005).

To observe neuronal microtubules, we used the microtubule end-binding protein EBP-2 (EB1), which shows preferential association with plus ends of growing microtubules. EBP-2 has been used previously to monitor microtubule plus ends (MT+) in embryos and neuronal processes in *C. elegans* (Kozlowski et al., 2007; Kurup et al., 2015; Maniar et al., 2011; Srayko et al., 2005; Yan et al., 2013). We expressed EBP-2::GFP specifically in the VD/DD motor neurons using the *unc-25* promoter. In wild-type animals, we see very few EBP-2::GFP puncta in the periphery of the growth cone and in the filopodial protrusions (an average of 2 puncta per growth cone, Figure 4.2A-B), consistent with the idea that microtubules are rare in the growth cone periphery due retrograde flow of actin (Burnette et al., 2007; Craig et al., 2012). *rho-1(G14V)* showed a significant reduction in the average number of EBP-2 puncta in the growth cone periphery as compared to wild-type (2 puncta per growth cone compared with 0.92 in *rho-1(G14V)*; $p < 0.001$) (Figure 4.2A-C). This significant reduction is possibly due to the small, inhibited growth cone area and filopodial protrusions observed in *rho-1(G14V)*, suggesting that EBP-2 distribution in the growth cone is more of a pro-protrusive effect than an anti-protrusive one. Transgenic *rho-1(T19N)*, *rho-1(RNAi)* and *rho-1(CRISPR)* expression all significantly increased the average number of EBP-2::GFP puncta in the VD growth cone periphery (e.g. 2 puncta per growth cone compared with 3.6 in *rho-1(RNAi)*; $p < 0.001$).

Previous work has shown the F-actin binding domain (ABD) of the spectraplakin VAB-10, has been used to monitor F-actin in the VD growth cone in *C.elegans* (Norris and Lundquist, 2011). By expressing VAB-10ABD::GFP under a pan-neuronal promoter, *rgef-1* and using *unc-25::mCherry* as a volumetric marker, we see that in wild-type VD growth cones F-actin preferentially localizes to the leading edge of the growth cone (~1.23 fold more accumulation at the leading edge (dorsal half) of the growth vs the ventral half) (Figure 4.2E-F). *rho-1(G14V)* mutants showed significant mislocalization of VAB-10ABD::GFP as compared to wild-type (Figure 4.2E-G). F-actin was seen to accumulate all around the growth cone with loss in dorsal bias, possibly due to the inhibited growth cone phenotype observed in these mutants. *rho-1(T19N)*, *rho-1(RNAi)* and *rho-1(CRISPR)* expression had no effect on F-actin distribution in the VD growth cones (Figure 4.2E and H). These results suggest RHO-1 is controls EBP-2 and F-actin distribution in the growth cone.

The RhoGEF RHGF-1 is required for inhibition of growth cone filopodial protrusion

Guanine nucleotide exchange factors (GEFs) facilitate the exchange of GDP for GTP, resulting in Rho activation. Previous studies in cell lines have shown that leukemia-associated RhoGEF (LARG) and PDZ RhoGEFs stimulate the nucleotide exchange of RhoA (Fukuhara et al., 2000; Fukuhara et al., 1999). RHGF-1/PDZ RhoGEF is a multidomain protein that contains a PDZ, RGS (regulator of G signaling), C1 (diacylglycerol binding), DH (Dbl homology) and PH

(plekstrin homology) domains (Figure 4.3A). The GTP exchange activity of RHGF-1 resides in the DH domain (Hiley et al., 2006; Yau et al., 2003). Previous work has shown that RHGF-1 participates in neurotransmitter release and is expressed in the ventral nerve cord motor neurons (Hiley et al., 2006; Lin et al., 2012; Yau et al., 2003).

We analyzed several mutations in *rhgf-1* to check for effects on VD growth cone morphology. *rhgf-1(ok880)* is a 1170bp in frame deletion which removes a large part of the DH domain and is predicted to have no RhoGEF activity (Hiley et al., 2006). *rhgf-1(gk217)* is a 247bp in frame deletion which removes the C1 domain and *rhgf-1(gk292502)* produces a premature stop just before the C1 domain (Figure 4.4A). *rhgf-1* mutant animals all displayed longer filopodial protrusions compared to wild-type (e.g. 0.96 µm in wild-type compared with 1.46 µm in *rhgf-1(ok880)*; $p < 0.001$) (Figure 4.3B, D-F). Growth cone area was also significantly increased in these mutants (Figure 4.3C). These data indicate that RHGF-1 is normally required to limit the extent of growth cone protrusion.

RHGF-1 is required to exclude EBP-2 puncta from the growth cone periphery

In *Drosophila* the RHGF-1 homolog DRhoGEF2 is a key regulator of morphogenesis and associates with the tips of growing microtubules and exhibits plus end tracking (Rogers et al., 2004). Previous work in *C. elegans* has also shown RHGF-1 to be associated with microtubules (Chen et al., 2014). Loss of *rhgf-1* significantly increased the average number of EBP-2::GFP puncta in the

VD growth cone periphery as compared to wild-type (e.g. 2 puncta per growth cone compared with 4 in *rhgf-1(gk292502)*; $p < 0.001$) (Figure 4.4A-C). We find that *rhgf-1* mutants showed no change in VAB-10ABD::GFP distribution in the growth cones similar to those seen in *rho-1* mutants (Figure 4.4D-F). These results indicate that RHGF-1 may be required to inhibit growth protrusion by excluding MT+ -ends from entering the growth cone periphery.

Activated RHO-1 is epistatic to *rhgf-1* loss

Previous studies have shown RHGF-1 acts as GEF for RHO-1 in D type motor neuron axon regeneration as well as in neurotransmitter release in a subset of cholinergic neurons downstream of GPA-12 (Hiley et al., 2006; Alam et al., 2016). Furthermore, it has been shown that *rhgf-1* acts on *rho-1/Rho*, *ced-10/Rac* and *mig-2/RhoG* to mediate PLM branch defects in tubulin mutants (Chen et al., 2014). To confirm whether RHGF-1 acts as a GEF for RHO-1 in inhibition of VD growth cone protrusion and in limiting the number of MT+ -ends from entering the VD growth cone we performed epistasis experiments. When *rho-1(G14V)* is introduced into a *rhgf-1* loss of function background, the growth cones resembled those of activated RHO-1 expression alone, with a significant reduction in filopodial length and growth cone area as compared to *rhgf-1* mutants alone (Figure 4.5A-E). Similarly, double mutants of *rhgf-1* and *rho-1(G14V)* showed a significant decrease in the average number of EBP-2 puncta in the growth cone similar to *rho-1(G14V)* alone (Figure 4.6A-D). VAB-10ABD::GFP distribution in these double mutant growth cones also resembled

activated *rho-1(G14V)* with F-actin distributed randomly all across the growth cone (Figure 4.6E-H). That activated RHO-1 was epistatic to *rhgf-1* could mean that RHO-1 acts downstream of RHGF-1 in limiting growth protrusion and EBP-2 accumulation in VD growth cones.

rhgf-1 **mutants suppress activated** ***myr::unc-40*** **and** ***myr::unc-5***

Previous studies showed that UNC-6/netrin signaling via the heterodimeric UNC-40/UNC-5 receptor is required for inhibition of growth cone protrusion in UNC-6/Netrin repulsive axon guidance (Norris and Lundquist, 2011; Norris et al., 2014). Constitutive activation of UNC-40 and UNC-5 using myristoylated versions of the cytoplasmic domains of UNC-40 and UNC-5 (*myr::unc-40* and *myr::unc-5*) in the VD neurons result in small growth cones with few or no filopodial protrusions (Gitai et al., 2003; Norris and Lundquist, 2011; Norris et al., 2014). Loss of *rhgf-1* significantly suppressed inhibition of filopodial protrusion and growth cone size caused by *myr::unc-40* and *myr::unc-5* (Figure 4.7A-E), i.e. double mutants showed increased growth cone protrusiveness as indicated by average filopodial length and growth cone size.

myr::unc-40 and *myr::unc-5* growth cones show a significant decrease in the average number of EBP-2::GFP puncta in the VD growth cones as compared to wild-type due to their inhibited growth cone phenotype (Figure 4.8A-C). F-actin distribution is significantly mislocalized throughout the growth cone in these mutants similar to activated *rho-1(G14V)* (Figure 4.8E-G). Double mutants of *rhgf-1* with *myr::unc-40* and *myr::unc-5* resembled *rhgf-1* mutants, with a

significant increase in MT+ -end distribution in the growth cone periphery and filopodial protrusions (Figure 4.8A-D). We also find a significant change in F-actin distribution in the double mutants, where F-actin is now preferentially localized to the leading edge of the growth cone and was polarized throughout the growth cone (Figure 4.8E-H). Taken together, these data suggest that RHGF-1 may be required for the full effect of MYR::UNC-40 and MYR::UNC-5 on growth cone protrusion inhibition and to limit MT+ -end distribution in the VD growth cone.

Over-protrusive growth cone phenotype of *unc-5* mutants are not suppressed by activated RHO-1(G14V)

Previously, we have shown that loss of the repulsive cue UNC-5 in the VD growth cones results in excessively large growth cones with an increase in filopodial length (Norris and Lundquist, 2011). UNC-5 is also required to polarize F-actin in the VD growth cone away from the UNC-6/Netrin source and towards the protrusive dorsal edge (Norris and Lundquist, 2011). Here we show that *unc-5* mutant animals show a significant increase in EBP-2 puncta in the growth cone periphery as compared to wild-type, suggesting that UNC-5 is required to limit EBP-2 puncta in the growth cone (Figure 4.10A-B).

rho-1(G14V) expression did not suppress the large growth cone area and long filopodial protrusions seen in *unc-5* mutants (i.e. double mutants resembled *unc-5* alone) (Figure 4.9). We observed no significant change in EBP-2::GFP and VAB-10ABD::GFP distribution in the VD growth cones as compared to *unc-5* mutants alone (Figure 4.10). Since RHGF-1 seemed to be required for

MYR::UNC-40 and MYR::UNC-5 inhibition of growth cone protrusion, this data suggests that RHO-1 may be required for UNC-40-UNC-5 repulsive signaling in the VD growth cone. However, it is also possible that RHO-1 may not function directly downstream UNC-5 in this process.

UNC-33/CRMP requires RHO-1 in excluding EBP-2 puncta from the growth cone

The Collapsin-response mediator protein (CRMP) UNC-33 and the Ankyrin-like molecule UNC-44 are required for inhibition of growth cone protrusion in response to UNC-6/Netrin repulsive signaling (Norris and Lundquist, 2011). Loss of *unc-33* and *unc-44* results in growth cones with longer filopodial protrusions similar to *unc-5* mutants (Norris et al., 2014). *unc-33* and *unc-44* cause a significant increase in the number of EBP-2 puncta that enter the growth cone periphery and filopodial protrusions as compared to wild-type (Figure 4.12A). We also find F-actin was distribution randomized in these mutants (Figure 4.12E), suggesting that UNC-33 and UNC-44 are required for proper EBP-2 and F-actin distribution in the VD growth cone.

Double mutants of *unc-33* and *rho-1(G14V)* resembled those of activated *rho-1(G14V)* mutants alone, with a significant decrease in growth cone area and filopodial protrusions (Figure 4.11). That RHO-1(G14V) could suppress *unc-33* suggests that RHO-1 may work independently of UNC-33 in a parallel pathway. Interestingly, we find that the inhibited growth cone phenotype seen in *unc-33*

and *rho-1(G14V)* double mutants still showed a significant increase in MT+ -end distribution in the growth cone periphery compared to wild-type (Figure 4.12A-D). By contrast, double mutants of *unc-44* with *rho-1(G14V)* resembled *unc-44* mutants, with excessive growth cone filopodial as evidenced with increased filopodial length and growth cone area, as well as an increase in EBP-2 puncta distribution (Figure 4.11A-B, 4.12A).

Double mutants of *unc-33* and *unc-44* with *rho-1(G14V)* showed no significant change in F-actin distribution as compared to single mutants alone (Figure 4.12E-H). Taken together, these data suggest that RHO-1 may function upstream of UNC-44 in controlling growth protrusion and restricting MT+ -end entry in the growth cone and that UNC-33 may require RHO-1 for limiting EBP-2 accumulation in the VD growth cone.

4.5 Discussion

Our results here show that the small GTPases RHO-1 and the Rho Guanine nucleotide Exchange factor RHGF-1 mediate inhibition of growth cone filopodial protrusion and are required for limiting the number of MT+ -ends that enter the growth cone periphery. Activated RHO-1 was epistatic to *rhgf-1* loss of function (i.e. growth cones in double mutants displayed inhibited filopodial protrusions and a significant reduction in EBP-2 puncta distribution similar to activated *rho-1* alone), consistent with the known role of RHGF-1 as an upstream Rho activator.

This work also shows that RHO-1 may not function directly downstream of the repulsive netrin receptor UNC-5 to limit filopodial protrusion and EBP-2 accumulation in the VD growth cone, but are likely to work in parallel pathways. However, we see that RHO-1 requires the cytoskeleton associated molecule UNC-33/CRMP for both these processes in the VD growth cone and possibly act in parallel pathways.

RHO-1 regulates growth cone filopodial protrusion and EBP-2 distribution

The Rho family of GTPases have essential functions in development including cytoskeletal organization, cell polarity, cell migration and cell membrane protrusion. In *C. elegans* loss of *rho-1* leads to embryonic lethality and previous work has shown that even conditional perturbation of *rho-1* signaling activity in adults leads to disruption of several neuronal and non-neuronal processes

resulting in death (McMullan and Nurrish, 2011), suggesting that RHO-1 is important for several biological processes throughout the life of the organism.

Here, we show that RHO-1 is required for limiting the number of MTs from entering the growth cone peripheral region possibly by inhibiting filopodial protrusion. Expression of the dominant negative form of RHO-1(T19N) in the VD neurons resulted in longer filopodial protrusions along with an increase in the average number of MT+ -ends entering the growth cone periphery (Figure 4.1 and 4.2A). Similarly, loss of *rho-1* specifically in the VD neurons by RNA mediated interference and CRISPR Cas9 genome editing showed increased protrusiveness with a significant increase in EBP-2 puncta (Figure 4.1 and 4.2A). Notably, none of these mutations showed and change in F-actin distribution in the VD growth cones (Figure 4.1E).

Expression of activated RHO-1(G14V) resulted in VD growth cones with a marked decrease in growth cone filopodial protrusions and EBP-2 puncta distribution (Figure 4.1 and 4.2). Taken together, these data suggest a role for RHO-1 in both filopodial protrusion and MT distribution in the growth cone.

Previous work has identified roles of the Rho GTPases in regulation of both microtubules and actin (Wittmann and Waterman-Storer, 2001). RhoA has been shown to regulate formation of contractile actin structures such as stress fibres and promote stabilization of microtubules (Cook et al., 1998; Etienne-Manneville and Hall, 2002) through actomyosin contraction. One of the principal targets of RhoA activity is RhoA kinase (ROCK) which activates contractility by phosphorylating the regulatory myosin light chain (MLC). This heightened myosin

II activity may increase actin retrograde flow preventing MTs from entering the growth cone periphery, thereby reducing leading edge protrusion resulting in growth cone collapse and retraction (Gallo, 2004; Zhang et al., 2003). We speculate that loss of *rho-1* in the VD neurons prevents ROCK and non-muscle myosin activation thus leading to decreased actin retrograde flow, increased protrusion and a higher number of MTs entering the P-domain of the growth cone. Further studies will be directed at answering these questions.

RHO-1 acts downstream of RHGF-1 signaling in inhibition of growth cone protrusion and exclusion of EBP-2 puncta

Our findings suggest that the RGS RhoGEF (Regulator of G-protein signaling Rho guanine nucleotide exchange factor) RHGF-1 acts with the small GTPase RHO-1 to mediate inhibition of growth cone protrusion and to exclude MTs from the growth cone periphery. Loss of *rhgf-1* resulted in longer filopodial protrusion in the VD motor neurons and significantly increased the distribution of EBP-2 puncta in the growth cone periphery as well as filopodial protrusions (Figure 4.3 and 4.4). This suggests that RHGF-1 normally limits MT accumulation in the VD growth cone by limiting growth cone filopodial protrusion. Furthermore, *rhgf-1* mutants had no effect on F-actin distribution in the VD growth cone similar to that seen in *rho-1* mutations (Figure 4.4).

We also find that activated *rho-1* was epistatic to *rhgf-1* loss of function. Growth cones in these double mutants displayed inhibited protrusion and reduction in MT distribution similar to activated *rho-1* alone, suggesting that

RHGF-1 acts as an upstream RHO-1 regulator in this process (Figure 4.5 and 4.6).

Previous studies in *Drosophila* S2 cells have shown that the RHGF-1 homolog, DRhoGEF2, induces contractile cell shape changes by regulating myosin II dynamics via Rho1 pathway. Furthermore, DRhoGEF2 associates with tips of growing MTs and travels to the cell cortex (Rogers et al., 2004). In *C.elegans* RHGF-1 is normally associated with and inhibited by microtubules. RHGF-1 functions through Rho and ROCK to activate the MAPKKK DLK-1 during MT disruption, triggering synaptic branch retraction and overgrowth of PLM neurites ultimately leading to neuronal remodeling (Chen et al., 2014). We speculate that RHO-1 and RHGF-1 may function in the central domain of the VD growth cone and loss of *rhgf-1* prevents *rho-1* activation leading to a significant increase in MTs invading the growth cone periphery.

RHGF-1 is likely to act downstream of MYR::UNC-5 and MYR::UNC-40

We show that *rhgf-1* mutations suppressed activated *myr::unc-40* and *myr::unc-5* (e.g. double mutant growth cones displayed longer filopodial protrusions and an increase in EBP-2::GFP puncta similar to *rhgf-1*single mutants) (Figure 4.7 and 4.8). That RHGF-1 is required for the effects of constitutively active MYR::UNC-40 and MYR::UNC-5 suggest that they act downstream of these molecules in growth cone inhibition of protrusion as well as to limit the number of MT+ -ends from entering the growth cone periphery.

However, it is possible that RHGF-1 defines a parallel pathway in growth cone inhibition and exclusion of MTs from the growth cone P-domain.

RHO-1 may function downstream of an UNC-40-UNC-5 repulsive guidance response

Receptors to several attractive or repulsive guidance cues signal through complex pathways through the Rho family of small GTPases to direct changes in growth cone cytoskeletal organization (Govek et al., 2005; Luo, 2002). Rho activity is thought to be induced by repulsive cues (Guan and Rao, 2003). Loss of the repulsive netrin receptor *unc-5* has been shown to cause excessively large growth cones with increased filopodial length (Norris and Lundquist, 2011). We also find that *unc-5* mutants display excess MT+ -end accumulation in the growth cones. We find that activated *rho-1* did not rescue the over-protrusive growth cone phenotype seen in *unc-5* mutants and the growth cones in the double mutants resembled those seen in *unc-5* mutant animals alone in the case of both MT+ -end distribution and protrusiveness (Figure 4.9 and 4.10).

We have previously showed that this over-protrusive phenotype of *unc-5* is likely due to increased UNC-40 homodimerization in the growth cone, leading to over-stimulation of growth cone protrusion (Norris et al. 2009). We showed here that while an ectopically expressed *rho-1(G14V)* construct rescued the over-protrusive phenotypes observed in an *rhgf-1* loss of function, it failed to rescue the over-protrusive phenotypes observed in an *unc-5* loss of function, suggesting that the RHO-1 may not be required for an UNC- 40/UNC-40 attractive growth

cone response. Taken together, these results suggest that *rhgf-1* and *rho-1* may act downstream of an UNC-40/UNC-5 repulsive signal, but not downstream of an UNC-40/UNC-40 attractive signal.

RHO-1 interacts with UNC-33/CRMP

Previous studies have shown that the *C. elegans* UNC-33/CRMP is required in a pathway downstream of Rac GTPases for inhibition of growth cone protrusion in response to UNC-6/Netrin (Norris et al., 2014) (Norris et al., 2014). In cultured mammalian neurons, CRMP interacts with F-actin and with tubulin dimers to further promote microtubule assembly (Fukata et al., 2002; Rosslenbroich et al., 2005). Here we show, *unc-33* loss-of-function mutants show large protrusive growth cones with excess EBP-2 distribution in the growth cones. However, loss of *unc-33* with activated *rho-1* expression displayed a suppressed growth cone phenotype. The growth cone area and excessively-long filopodial protrusions of *unc-33* mutants were reduced to resemble *rho-1(G14V)* expression alone (Figure 4.11). Interestingly, we find that the inhibited growth cone phenotype in *unc-33; rho-1(G14V)* mutants still show a significantly higher number of EBP-2 puncta than wild-type animals, but significantly lower than *unc-33* mutants alone (Figure 4.12). This phenotype suggests a complex interaction between RHO-1 and UNC-33 in controlling growth cone protrusion and MT+ -end distribution in the VD growth cone. UNC-44/Ankyrin may function downstream of RHO-1 and may be required to properly localize UNC-33/CRMP to the axons as previously described (MANIAR *et al.* 2011). However, how RHO-1 would interact

with UNC-33/CRMP to affect growth cone morphology and MT distribution is difficult to determine. Previous work in cell lines has shown that expression of CRMP2 can alter Rho-GTPase-driven neurite morphology. Co-expression of Crmp-2 with activated Rho can promote cell spreading and neurite growth and this function of Crmp-2 is regulated by Rho Kinase (Hall et al., 2001). Furthermore, CRMP-2 has been shown to be phosphorylated by Rho Kinase II (Arimura et al., 2000; Arimura et al., 2005) which disrupts the association of mature full-length CRMP-2 with tubulin heterodimers so that tubulin cannot be transported to the plus ends of microtubules for assembly (FUKATA *et al.* 2002) causing neurite retraction and growth cone collapse (Arimura and Kaibuchi, 2007). This reduced binding capacity to tubulin by phosphorylated CRMP-2, can be reversed by inhibiting RhoA activity (Petratos et al., 2008). Thus, RHO-1 may regulate growth cone protrusion and MT distribution through the phosphorylation activity of UNC-33/CRMP possibly through the same pathway or in parallel to it.

In conclusion, our results suggest a novel role of the *C. elegans* small GTPase RHO-1 and its upstream regulator PDZ/RhoGEF RHGF-1 in inhibition of growth protrusion and restriction of MT+ -ends from the growth cone. RHGF-1 is required to inhibit protrusion by activated MYR::UNC-40 and MYR::UNC-5 suggesting that RHGF-1 is required for inhibition of growth cone protrusion by UNC-6/Netrin receptor signaling possibly by restricting MT+ -ends from entering the growth cone periphery and that RHO-1 is may function downstream of an UNC-40-UNC-5 repulsive signal.

Figure 4.1.

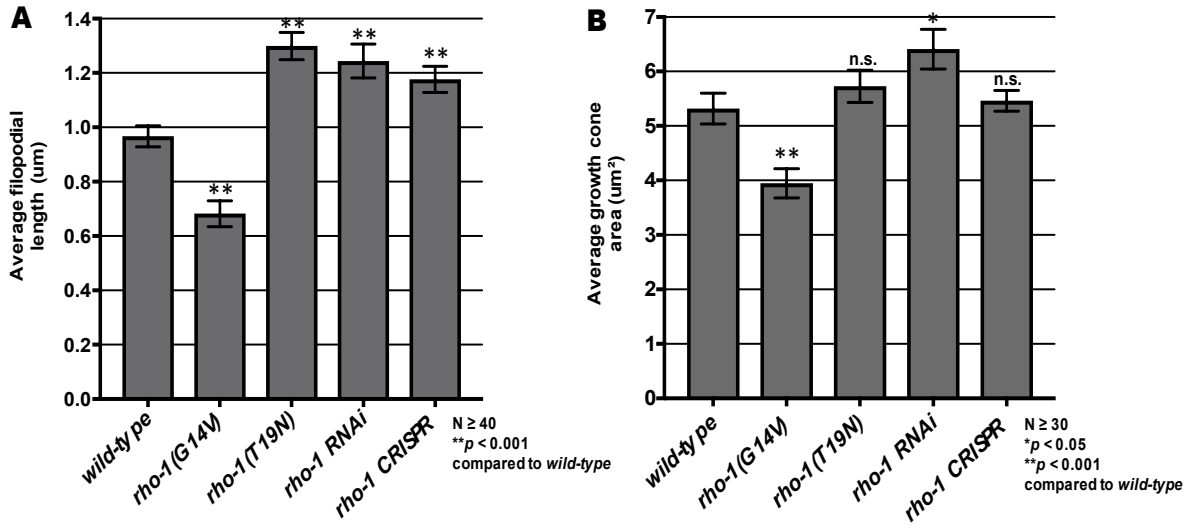
A
Average filopodial length (um)
1.4
1.2
1.0
0.8
0.6
0.4
0.2
0.0
**
**
**
**
wild-type
rho-1(G14V)
rho-1(T19N)
rho-1 RNAi
rho-1 CRISPR
N ≥ 40
**p < 0.001
compared to wild-type
B
Average growth cone area (um²)
7
6
5
4
3
2
1
0
**
n.s.
*
n.s.
wild-type
rho-1(G14V)
rho-1(T19N)
rho-1 RNAi
rho-1 CRISPR
N ≥ 30
*p < 0.05
**p < 0.001
compared to wild-type

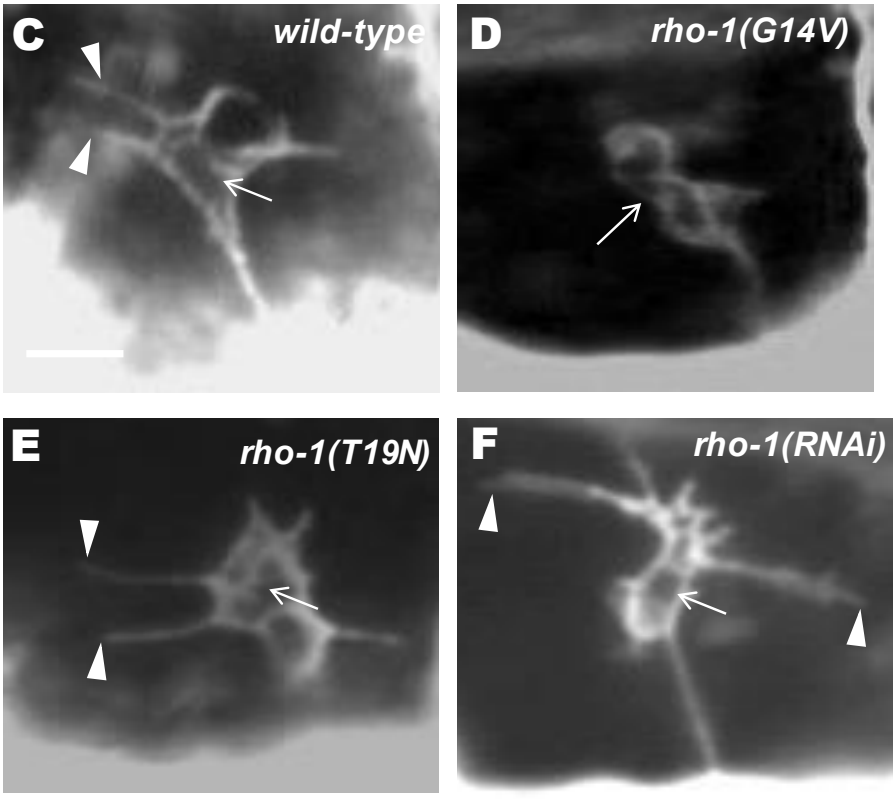
C
wild-type
D
rho-1(G14V)
E
rho-1(T19N)
F
rho-1(RNAi)

Figure 4.1. RHO-1 is required for inhibition of VD growth cone protrusion. **(A,B)** Quantification of VD growth cone filopodial length and growth cone area in wild-type and *rho-1* mutant animals. (A) Average filopodial length, in μm. (B) Growth cone area in μm^2. Error bars represent 2x standard error of the mean; asterisks indicate the significant difference between wild-type and the mutant phenotype (*$p < 0.05$, **$p < 0.001$) determined by two-sided *t*-test with unequal variance. n.s., not significant. **(C-E)** Fluorescence micrographs of mutant VD growth cones; (C) A wild-type VD growth cone. (D) *rho-1(G14V)* showing small and inhibited VD growth cone phenotype (E) *rho-1(T19N)* and (F) *rho-1(RNAi)* *g*rowth cones showing increased filopodial protrusion in the form of longer filopodia. Arrows point to the growth cone and arrow heads indicate representative filopodia. Scale bar: 5μm.

Figure 4.2.

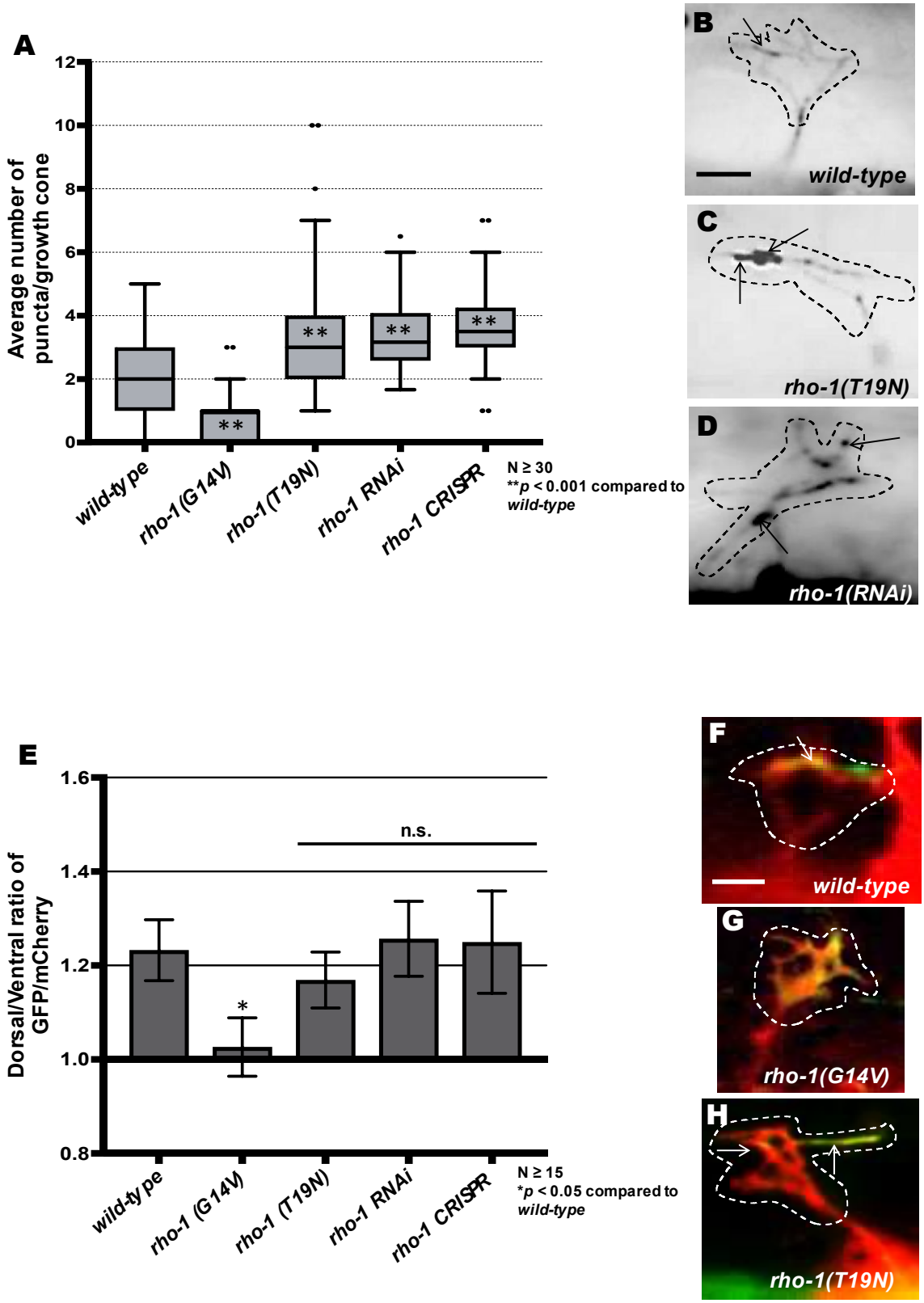
A
Average number of puncta/growth cone
12
10
8
6
4
2
0
**
**
**
**
wild-type
rho-1(G14V)
rho-1(T19N)
rho-1 RNAi
rho-1 CRISPR
N ≥ 30
**p < 0.001 compared to wild-type
B
wild-type
C
rho-1(T19N)
D
rho-1(RNAi)
E
Dorsal/Ventral ratio of GFP/mCherry
1.6
1.4
1.2
1.0
0.8
n.s.
*
wild-type
rho-1 (G14V)
rho-1 (T19N)
rho-1 RNAi
rho-1 CRISPR
N ≥ 15
*p < 0.05 compared to wild-type
F
wild-type
G
rho-1(G14V)
H
rho-1(T19N)

Figure 4.2. RHO-1 is required for EBP-2::GFP puncta distribution in the VD growth cone. **(A)** Box-and-whiskers plot of the number of EBP-2::GFP puncta in the growth cones of different genotypes (≥25 growth cones for each genotype). The grey boxes represent the upper and lower quartiles, and error bars represent the upper and lower extreme values. Dots represent outliers. Asterisks (*) indicate the significant difference between wild-type and the mutant phenotype (**$p < 0.001$) determined by two-sided *t*-test with unequal variance. n.s., not significant. **(B-D)** Fluorescence micrographs of EBP-2 distribution in the VD growth cones; (B) A wild-type VD growth cone and (C) *rho-1(T19N)* and (D) *rho-1(RNAi) g*rowth cones showing increased puncta in the growth cone and filopodial protrusions. Arrows indicate representative EBP-2::GFP puncta. Dashed lines indicate the growth cone perimeter. Dorsal is up and anterior is left. Scale bar: 5μm. **(E)** The average dorsal-to-ventral ratio of GFP/mCherry from multiple growth cones in wild-type and mutant animals as described previously (Norris and Lundquist, 2011) (see methods) **(F-H)** Representative images of VD growth cones with cytoplasmic mCherry in red (a volumetric marker) and the VAB-10ABD::GFP in green. Areas of overlap are yellow (arrows). Error bars represent 2x standard error of the mean. Asterisks (*) indicate the significant difference between wild-type and the mutant phenotype (*$p < 0.05$) determined by two-sided *t*-test with unequal variance. Dashed lines indicate the growth cone periphery. Dorsal is up and anterior is left. Scale bar: 5 μm. (F) A wild-type VD growth cone, (G) *rho-1(G14V)* and (H) *rho-1(T19N)* VD growth cones.

Figure 4.3.

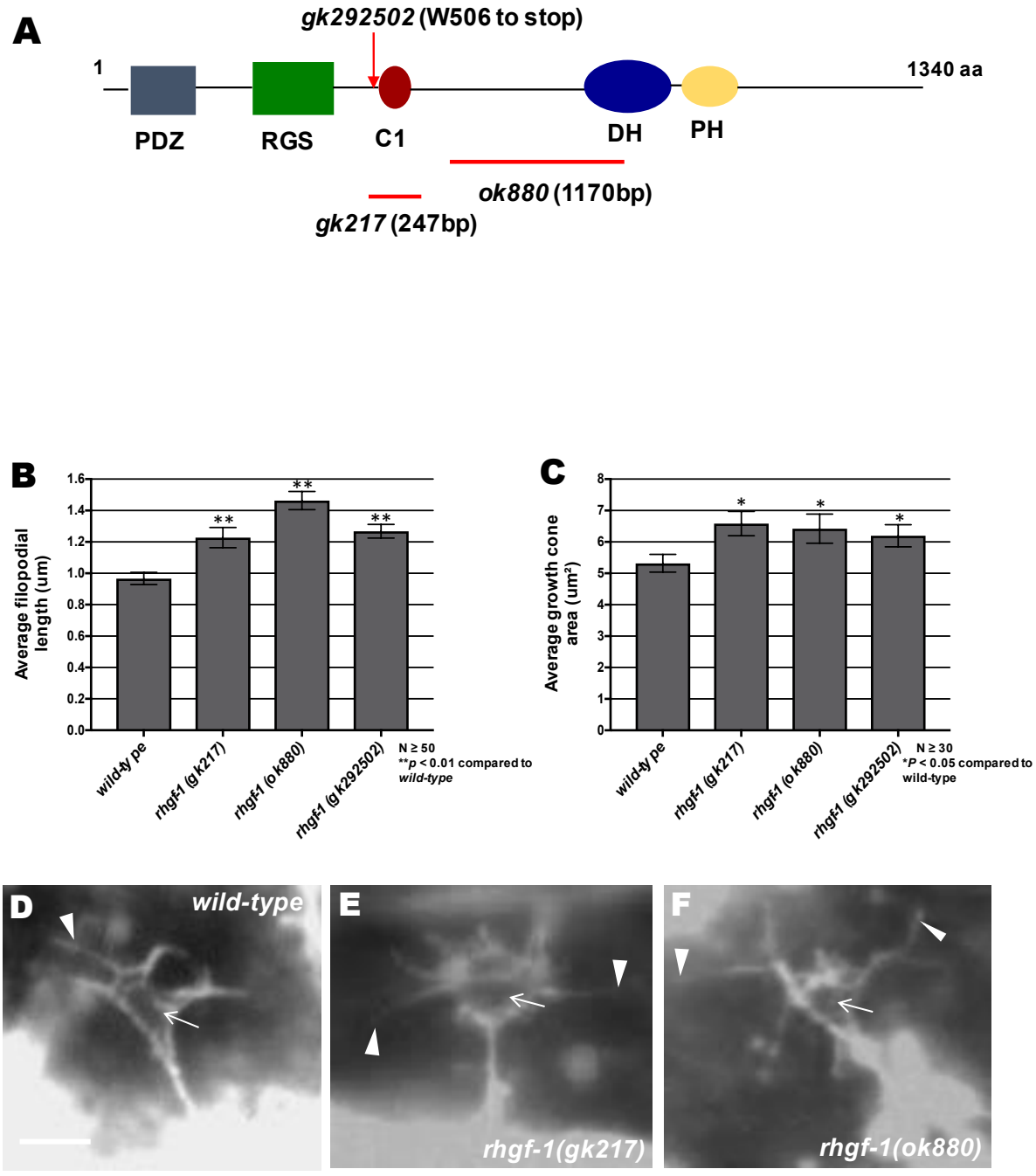
A
gk292502 (W506 to stop)
1
1340 aa
PDZ
RGS
C1
DH
PH
ok880 (1170bp)
gk217 (247bp)
B
Average filopodial length (um)
wild-ty pe
rhgf-1 (gk217)
rhgf-1 (ok880)
rhgf-1 (gk292502)
N ≥ 50
**p < 0.01 compared to wild-type
C
Average growth cone area (um²)
N ≥ 30
*P < 0.05 compared to wild-type
D
wild-type
E
rhgf-1(gk217)
F
rhgf-1(ok880)

Figure 4.3. Mutations in *rhgf-1* increase VD growth cone filopodial length. **(A)** A schematic diagram of the 1,340-amino acid residue RHGF-1 molecule. PDZ= PDZ domain, RGS= Regulator of G protein signaling domain, C1= Ester/diacylglycerol binding domain, DH= Dbl homology domain, PH= Plekstrin homology domain. Extent of deletions of ok880 and *gk217*are indicated by the red lines. The red arrow points to the premature stop site in *gk292502.* **(B,C)** Quantification of VD growth cone filopodial length and growth cone area in wild-type and mutant animals. (B) Average filopodial length, in μm. (C) Growth cone area in μm^2. Error bars represent 2x standard error of the mean; asterisks indicate the significant difference between wild-type and the mutant phenotype (*$p < 0.05$, **$p < 0.001$) determined by two-sided *t*-test with unequal variance. n.s., not significant. **(D-F)** Fluorescence micrographs of mutant VD growth cones; (D) A wild-type VD growth cone. (E) *rhgf-1(gk217)* and (F) *rhgf-1(ok880) g*rowth cones showing increased filopodial protrusion in the form of longer filopodia. Arrows point to the growth cone and arrow heads indicate representative filopodia. Scale bar: 5μm.

Figure 4.4.

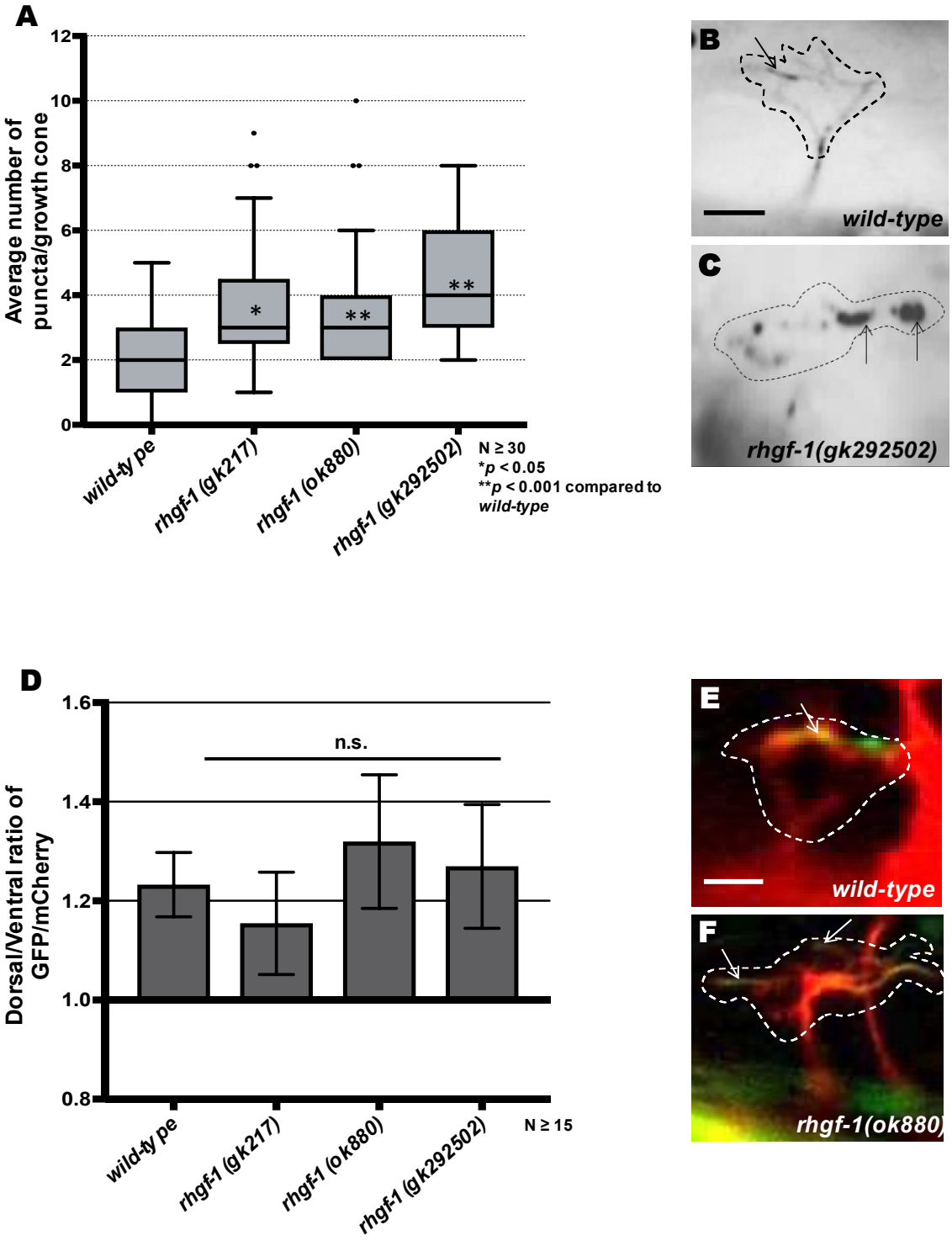
A
Average number of puncta/growth cone
12
10
8
6
4
2
0
*
**
**
wild-ty pe
rhgf-1 (gk217)
rhgf-1 (ok880)
rhgf-1 (gk292502)
N ≥ 30
*p < 0.05
**p < 0.001 compared to wild-type
B
wild-type
C
rhgf-1(gk292502)
D
Dorsal/Ventral ratio of GFP/mCherry
1.6
1.4
1.2
1.0
0.8
n.s.
wild-ty pe
rhgf-1 (gk217)
rhgf-1 (ok880)
rhgf-1 (gk292502)
N ≥ 15
E
wild-type
F
rhgf-1(ok880)

Figure 4.4. RHGF-1 is required for EBP-2::GFP puncta distribution in the VD growth cone. **(A)** Quantification of the number of EBP-2::GFP puncta in wild-type and *rhgf-1* mutant growth cones as described in Figure 4.2A. Asterisks (*) indicate the significant difference between wild-type and the mutant phenotype (*$p < 0.05$,**$p < 0.001$) determined by two-sided *t*-test with unequal variance. n.s., not significant. **(B-C)** Fluorescence micrographs of EBP-2 distribution in the VD growth cones; (B) A wild-type VD growth cone (C) *rhgf-1(gk292502) g*rowth cones showing increased puncta in the growth cone and filopodial protrusions. Arrows indicate representative EBP-2::GFP puncta. Dashed lines indicate the growth cone perimeter. Dorsal is up and anterior is left. Scale bar: 5μm. **(D)** The average dorsal-to-ventral ratio of VAB-10ABD::GFP/mCherry from multiple growth cones in wild-type and mutant animals **(E-F)** Representative images of VD growth cones with cytoplasmic mCherry in red (a volumetric marker) and the VAB-10ABD::GFP in green. Areas of overlap are yellow (arrows). Error bars represent 2x standard error of the mean; n.s., not significant. Dashed lines indicate the growth cone periphery. Dorsal is up and anterior is left. Scale bar: 5 μm. (E) A wild-type growth cone and (F) *rhgf-1(ok880)* growth cones with VAB-10ABD::GFP expression in the dorsal leading edge of the growth cone.

Figure 4.5.

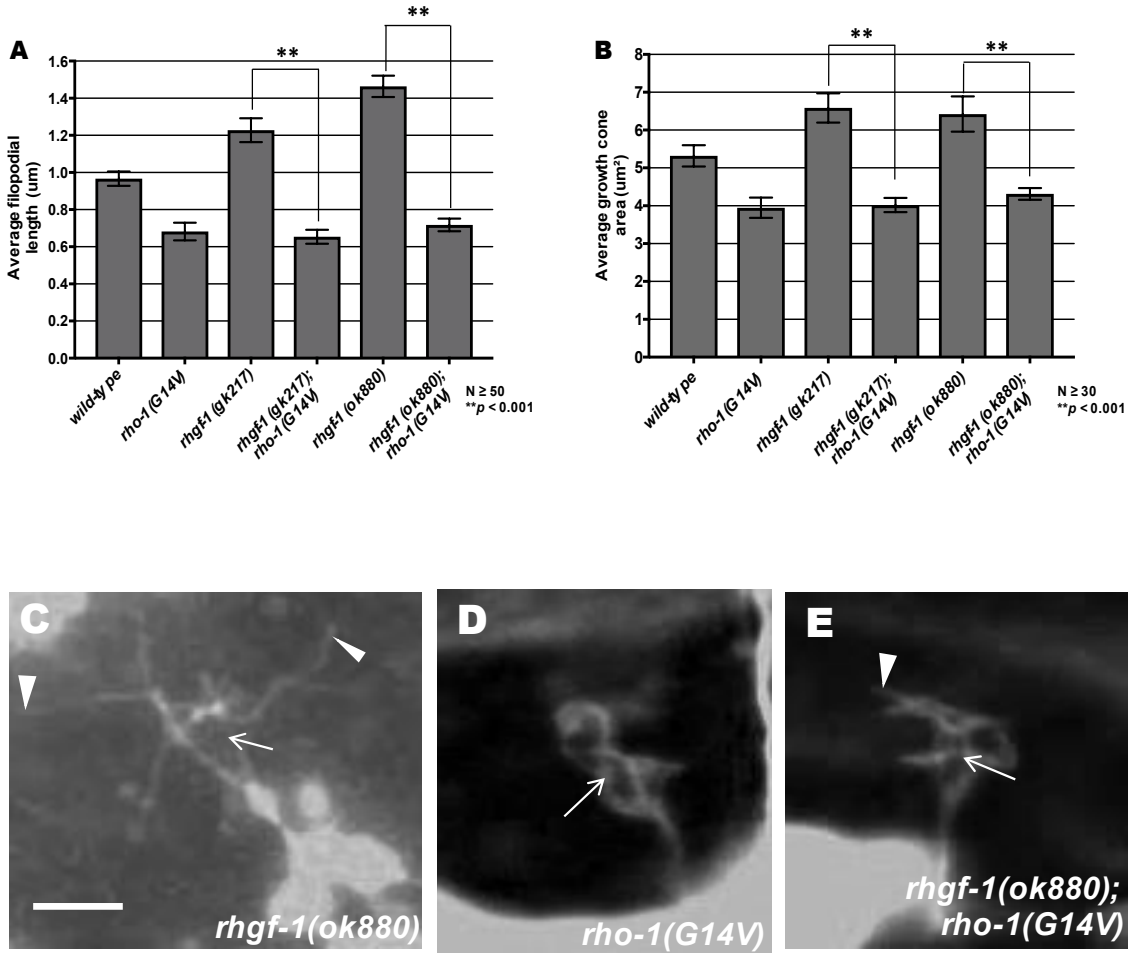
A
Average filopodial length (um)
1.6
1.4
1.2
1.0
0.8
0.6
0.4
0.2
0.0
**
**
wild-ty pe
rho-1 (G14V)
rhgf-1 (gk217)
rhgf-1 (gk217); rho-1(G14V)
rhgf-1 (ok880)
rhgf-1 (ok880); rho-1(G14V)
N ≥ 50
**p < 0.001
B
Average growth cone area (um²)
8
7
6
5
4
3
2
1
0
**
**
wild-ty pe
rho-1(G14V)
rhgf-1 (gk217)
rhgf-1 (gk217); rho-1(G14V)
rhgf-1 (ok880)
rhgf-1 (ok880); rho-1(G14V)
N ≥ 30
**p < 0.001
C
rhgf-1(ok880)
D
rho-1(G14V)
E
rhgf-1(ok880); rho-1(G14V)

Figure 4.5. RHGF-1 requires RHO-1 to limit growth cone protrusion. (A,B) Quantification of VD growth cone filopodial length and growth cone area in single and double mutant animals. (A) Average filopodial length, in μm. (B) Growth cone area in μm^2. Error bars represent 2x standard error of the mean; asterisks indicate the significant difference between *rhgf-1* single mutants and the double mutant phenotype (**$p < 0.001$) determined by two-sided *t*-test with unequal variance. **(C-E)** Fluorescence micrographs of mutant VD growth cones; (C) *rhgf-1(ok880)* growth cone (D) *rho-1(G14V)* growth cone (E) *rhgf-1(ok880); rho-1(G14V) g*rowth cone. Arrows point to the growth cone and arrow heads indicate representative filopodia. Scale bar: 5μm.

Figure 4.6

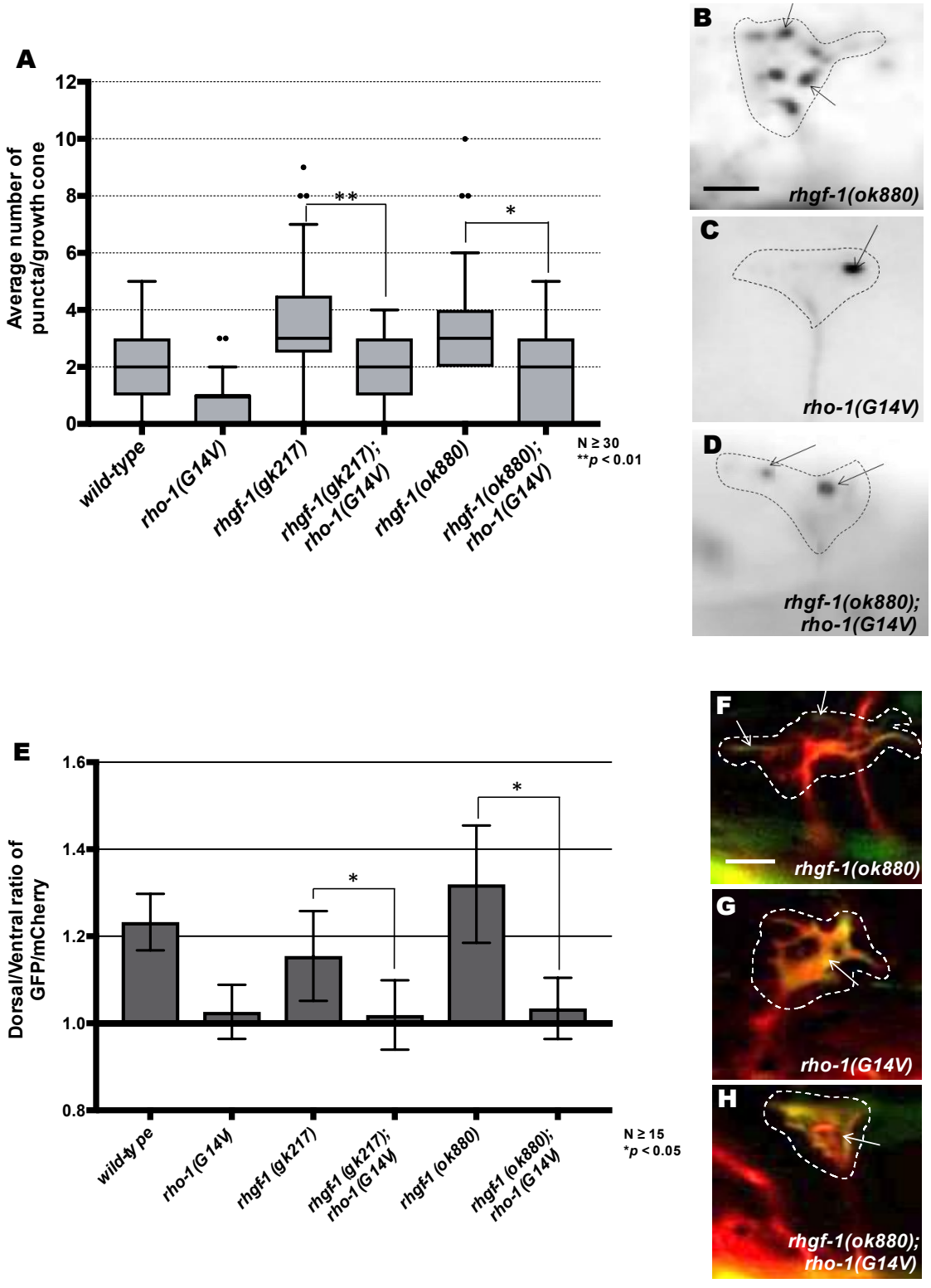
A
Average number of puncta/growth cone
12
10
8
6
4
2
0
**
*
wild-type
rho-1(G14V)
rhgf-1(gk217)
rhgf-1(gk217); rho-1(G14V)
rhgf-1(ok880)
rhgf-1(ok880); rho-1(G14V)
N ≥ 30
**p < 0.01
B
rhgf-1(ok880)
C
rho-1(G14V)
D
rhgf-1(ok880); rho-1(G14V)
E
Dorsal/Ventral ratio of GFP/mCherry
1.6
1.4
1.2
1.0
0.8
*
*
wild-type
rho-1(G14V)
rhgF1 (gk217)
rhgf-1 (gk217); rho-1(G14V)
rhgF1 (ok880)
rhgf-1 (ok880); rho-1(G14V)
N ≥ 15
*p < 0.05
F
rhgf-1(ok880)
G
rho-1(G14V)
H
rhgf-1(ok880); rho-1(G14V)

Figure 4.6. Activated RHO-1 is epistatic to RHGF-1 loss. (A) Quantification of the number of EBP-2::GFP puncta in wild-type and mutant animals as described in Figure 4.2A. Asterisks (*) indicate the significant difference between *rhgf-1* single mutants and the double mutant phenotype (**$p < 0.01$) determined by two-sided *t*-test with unequal variance. **(B-D)** Fluorescence micrographs of EBP-2 distribution in the VD growth cones; (B) *rhgf-1(ok880)* growth cone (C) *rho-1(G14V)* and (D) *rhgf-1(ok880); rho-1(G14V) g*rowth cones with decreased *ebp-2* puncta. Arrows indicate representative EBP-2::GFP puncta. Dashed lines indicate the growth cone periphery. Dorsal is up and anterior is left. Scale bar: 5 µm. **(E)** The average dorsal-to-ventral ratio of GFP/mCherry from multiple growth cones in single and double mutant animals. **(F-H)** Representative images of VD growth cones with cytoplasmic mCherry in red (a volumetric marker) and the VAB-10ABD::GFP in green. Areas of overlap are yellow (arrows). Error bars represent 2x standard error of the mean. Asterisks (*) indicate the significant difference between single and double mutant phenotype (*$p < 0.05$) determined by two-sided *t*-test with unequal variance (F) *rhgf-1(ok880)* growth cone, (G) *rho-1(G14V)* growth cone, (H) *rhgf-1(ok880); rho-1(G14V)* double mutant VD growth cones with cytoplasmic mCherry and VAB-10ABD::GFP expression. Dashed lines indicate the growth cone periphery. Dorsal is up and anterior is left. Scale bar: 5 µm.

Figure 4.7.

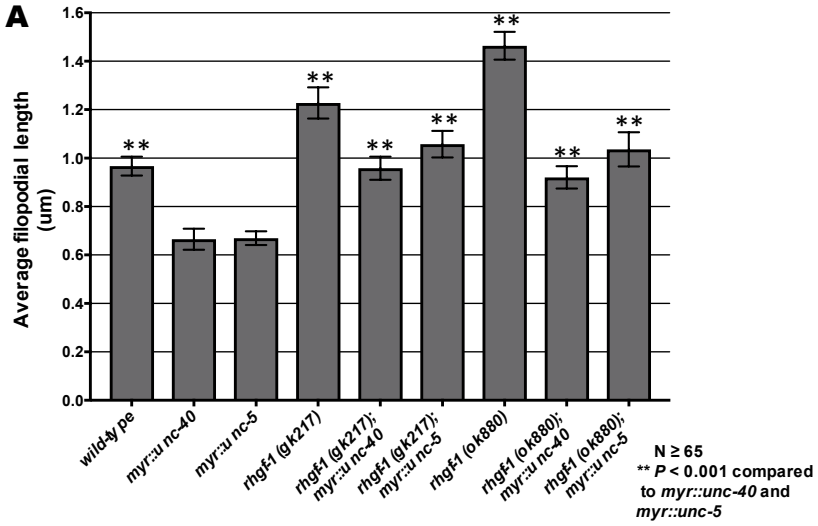
A
Average filopodial length (um)
1.6
1.4
1.2
1.0
0.8
0.6
0.4
0.2
0.0
**
wild-type
myr::unc-40
myr::unc-5
rhgf-1 (gk217)
rhgf-1 (gk217); myr::unc-40
rhgf-1 (gk217); myr::unc-5
rhgf-1 (ok880)
rhgf-1 (ok880); myr::unc-40
rhgf-1 (ok880); myr::unc-5
N ≥ 65
** P < 0.001 compared to myr::unc-40 and myr::unc-5

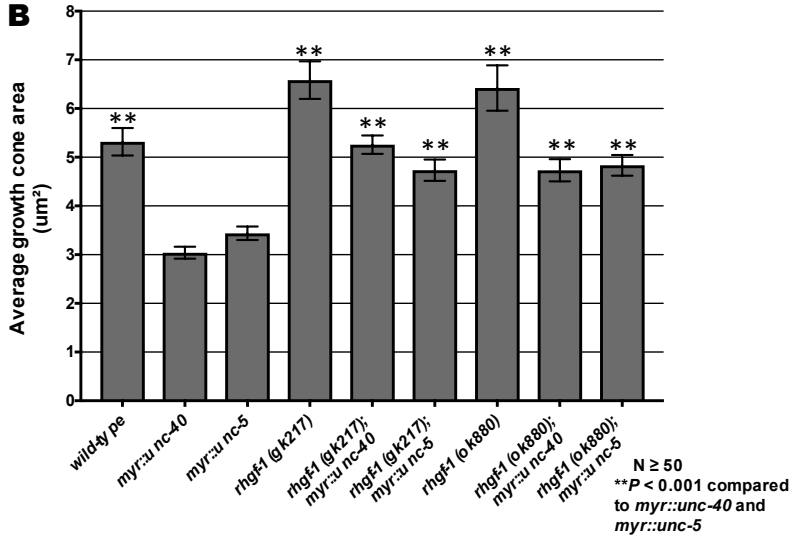
B
Average growth cone area (um²)
8
7
6
5
4
3
2
1
0
**
wild-type
myr::unc-40
myr::unc-5
rhgf-1 (gk217)
rhgf-1 (gk217); myr::unc-40
rhgf-1 (gk217); myr::unc-5
rhgf-1 (ok880)
rhgf-1 (ok880); myr::unc-40
rhgf-1 (ok880); myr::unc-5
N ≥ 50
**P < 0.001 compared to myr::unc-40 and myr::unc-5

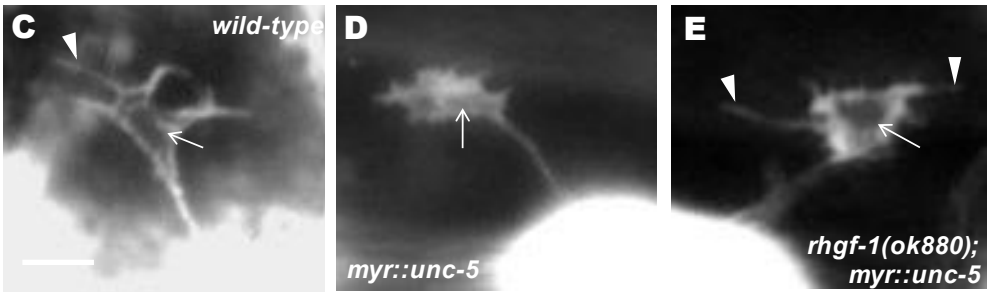
C
wild-type
D
myr::unc-5
E
rhgf-1(ok880); myr::unc-5

Figure 4.7. MYR::UNC-40 and MYR::UNC-5 - mediated inhibition of VD growth cone protrusion requires RHGF-1. (A,B) Quantification of VD growth cone filopodial length and growth cone area in single and double mutant animals. (A) Average filopodial length, in μm. (B) Growth cone area in μm^2. Error bars represent 2x standard error of the mean; asterisks indicate the significant difference between *myr::unc-40*, single and double mutants (**$p < 0.001$) determined by two-sided *t*-test with unequal variance. **(C-E)** Fluorescence micrographs of mutant VD growth cones; (C) A wild-type VD growth cone (D) *myr::unc-40* growth cone. (E) *rhgf-1(ok880); myr::unc-40 g*rowth cone. Arrows point to the growth cone and arrow heads indicate representative filopodia. Scale bar: 5μm.

Figure 4.8.

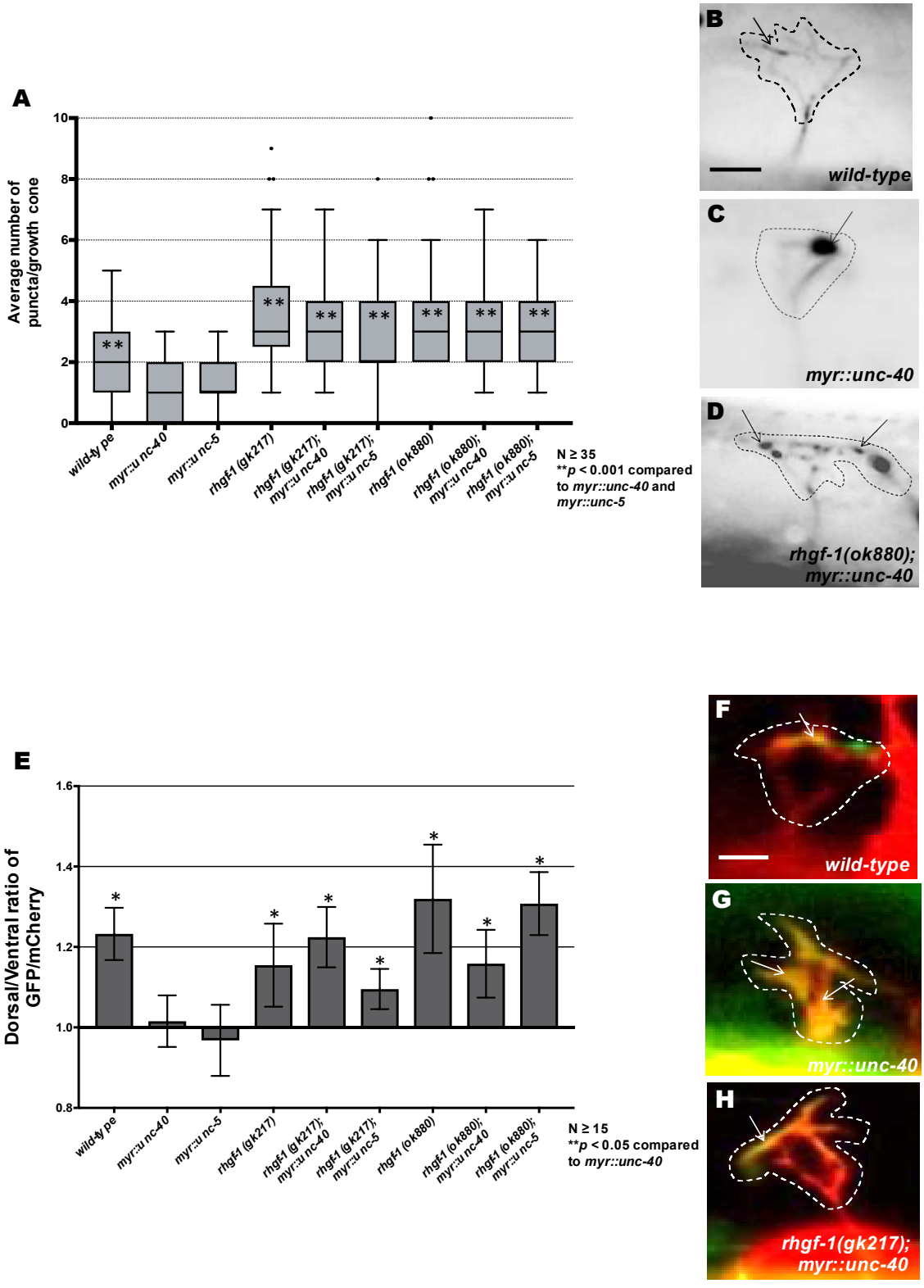
A
Average number of puncta/growth cone
10
8
6
4
2
0
**
wild-type
myr::unc-40
myr::unc-5
rhgf-1 (gk217)
rhgf-1 (gk217); myr::unc-40
rhgf-1 (gk217); myr::unc-5
rhgf-1 (ok880)
rhgf-1 (ok880); myr::unc-40
rhgf-1 (ok880); myr::unc-5
N ≥ 35
**p < 0.001 compared to myr::unc-40 and myr::unc-5
B
wild-type
C
myr::unc-40
D
rhgf-1(ok880); myr::unc-40
E
Dorsal/Ventral ratio of GFP/mCherry
1.6
1.4
1.2
1.0
0.8
*
wild-type
myr::unc-40
myr::unc-5
rhgf-1 (gk217)
rhgf-1 (gk217); myr::unc-40
rhgf-1 (gk217); myr::unc-5
rhgf-1 (ok880)
rhgf-1 (ok880); myr::unc-40
rhgf-1 (ok880); myr::unc-5
N ≥ 15
**p < 0.05 compared to myr::unc-40
F
wild-type
G
myr::unc-40
H
rhgf-1(gk217); myr::unc-40

Figure 4.8. MYR::UNC-40 and MYR::UNC-5 require RHGF-1 to limit EBP-2 accumulation in the VD growth cone.

(A) Quantification of the number of EBP-2::GFP puncta in wild-type and mutant animals as described in Figure 4.2A. Asterisks (*) indicate the significant difference between *myr::unc-40*, single mutants and double mutants (**$p < 0.001$), determined by two-sided *t*-test with unequal variance. **(B-E)** Fluorescence micrographs of EBP-2 distribution in the VD growth cones; (B) wild-type VD growth cone (C) *myr::unc-40* growth cone and (D) *rhgf-1(ok880); myr::unc-40 g*rowth cones with an increase in *ebp-2* puncta. Arrows indicate representative EBP-2::GFP puncta. Dashed lines indicate the growth cone periphery. Dorsal is up and anterior is left. Scale bar: 5 μm. **(E)** The average dorsal-to-ventral ratio of GFP/mCherry from multiple growth cones in wild-type, single and double mutant animals. **(F-H)** Representative images of VD growth cones with cytoplasmic mCherry in red (a volumetric marker) and the VAB-10ABD::GFP in green. Areas of overlap are yellow (arrows). Error bars represent 2x standard error of the mean. Asterisks (*) indicate the significant difference between *myr::unc-40*, single mutants and double mutants (*$p < 0.05$) determined by two-sided *t*-test with unequal variance. Scale bar: 5 μm. (F) wild-type growth cone, (G) *myr::unc-40* growth cone, (H) *rhgf-1(gk217); myr::unc-40* double mutant VD growth cones with cytoplasmic mCherry and VAB-10ABD::GFP expression. Dashed lines indicate the growth cone periphery. Dorsal is up and anterior is left. Scale bar: 5 μm.

Figure 4.9.

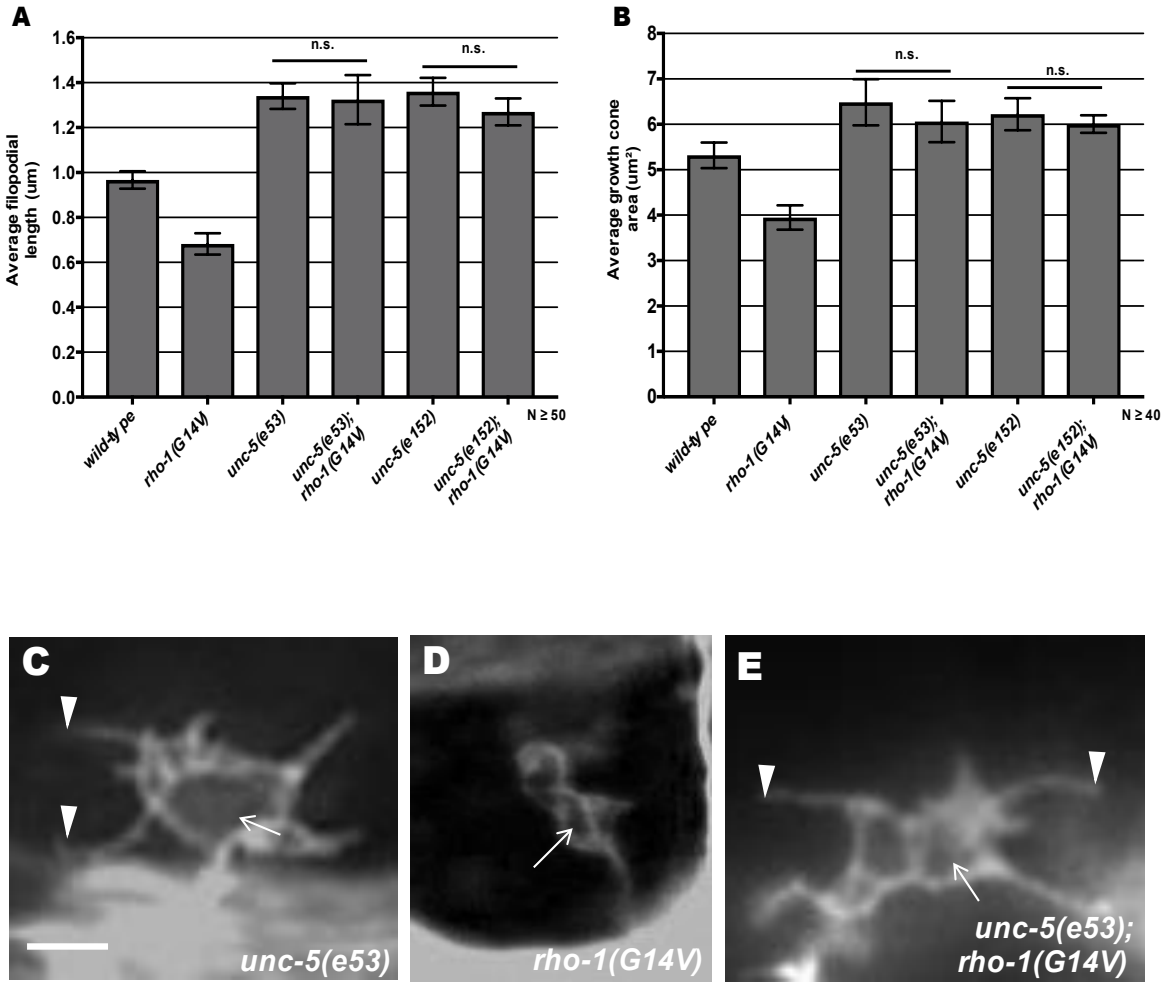
A
Average filopodial length (um)
1.6
1.4
1.2
1.0
0.8
0.6
0.4
0.2
0.0
n.s.
n.s.
N ≥ 50
wild-type
rho-1(G14V)
unc-5(e53)
unc-5(e53); rho-1(G14V)
unc-5(e152)
unc-5(e152); rho-1(G14V)
B
Average growth cone area (um²)
8
7
6
5
4
3
2
1
0
n.s.
n.s.
N ≥ 40
wild-type
rho-1(G14V)
unc-5(e53)
unc-5(e53); rho-1(G14V)
unc-5(e152)
unc-5(e152); rho-1(G14V)
C
unc-5(e53)
D
rho-1(G14V)
E
unc-5(e53); rho-1(G14V)

Figure 4.9. *rho-1(G14V)* does not rescue the excess growth cone filopodial protrusions seen in *unc-5* growth cones (A,B) Quantification of VD growth cone filopodial length and growth cone area in single and double mutant animals. (A) Average filopodial length, in μm. (B) Growth cone area in μm^2. Error bars represent 2x standard error of the mean; n.s., not significant determined by two-sided *t*-test with unequal variance. **(C-E)** Fluorescence micrographs of mutant VD growth cones; (C) *unc-5(e53)* VD growth cone (D) *rho-1(G14V)* and (E) *unc-5(e53); rho-1(G14V) g*rowth cone. Arrows point to the growth cone and arrow heads indicate representative filopodia. Scale bar: 5μm.

Figure 4.10.

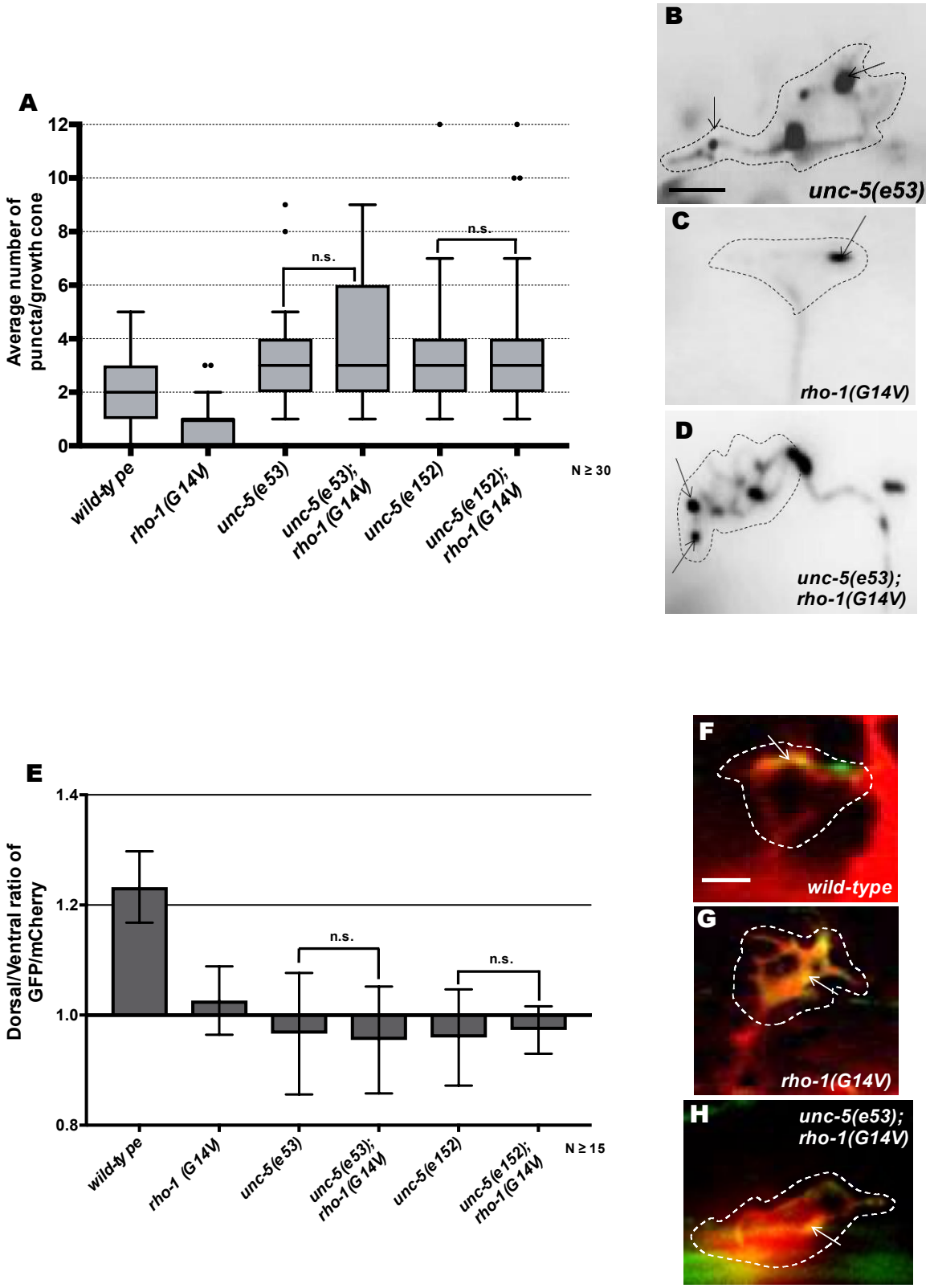
A
Average number of puncta/growth cone
12
10
8
6
4
2
0
n.s.
n.s.
N ≥ 30
wild-type
rho-1(G14V)
unc-5(e53)
unc-5(e53); rho-1(G14V)
unc-5(e152)
unc-5(e152); rho-1(G14V)
B
unc-5(e53)
C
rho-1(G14V)
D
unc-5(e53); rho-1(G14V)
E
Dorsal/Ventral ratio of GFP/mCherry
1.4
1.2
1.0
0.8
n.s.
n.s.
N ≥ 15
wild-type
rho-1 (G14V)
unc-5(e53)
unc-5(e53); rho-1(G14V)
unc-5(e152)
unc-5(e152); rho-1(G14V)
F
wild-type
G
rho-1(G14V)
H
unc-5(e53); rho-1(G14V)

Figure 4.10. *rho-1(G14V)* does not suppress the excess MT+ -ends seen in *unc-5* mutant growth cones (A) Quantification of the number of EBP-2::GFP puncta in wild-type and mutant animals as described in Figure 4.2A. n.s., not significant, determined by two-sided *t*-test with unequal variance. **(B-D)** Fluorescence micrographs of EBP-2 distribution in the VD growth cones; (B) *unc-5(e53)* showing increased *ebp-2* puncta (C) *rho-1(G14V)* showing small and inhibited growth cone with significantly lower *ebp-2* puncta and (D) *unc-5(e53); rho-1(G14V) g*rowth cones with an increase in *ebp-2* puncta. Arrows indicate representative EBP-2::GFP puncta. Dashed lines indicate the growth cone periphery. Dorsal is up and anterior is left. Scale bar: 5 μm. **(E)** The average dorsal-to-ventral ratio of GFP/mCherry from multiple growth cones in wild-type, single and double mutant animals. **(F-H)** Representative images of VD growth cones with cytoplasmic mCherry in red (a volumetric marker) and the VAB-10ABD::GFP in green. Areas of overlap are yellow (arrows). Error bars represent 2x standard error of the mean; n.s. indicates no significant difference between *unc-5* single mutants and double mutants determined by two-sided *t*-test with unequal variance. Scale bar: 5 μm. (F) wild-type growth cone, (G) *rho-1(G14V)* growth cone, (H) *unc-5(e53); rho-1(G14V)* double mutant VD growth cones with cytoplasmic mCherry and VAB-10ABD::GFP expression. Dashed lines indicate the growth cone periphery. Dorsal is up and anterior is left. Scale bar: 5 μm.

Figure 4.11.

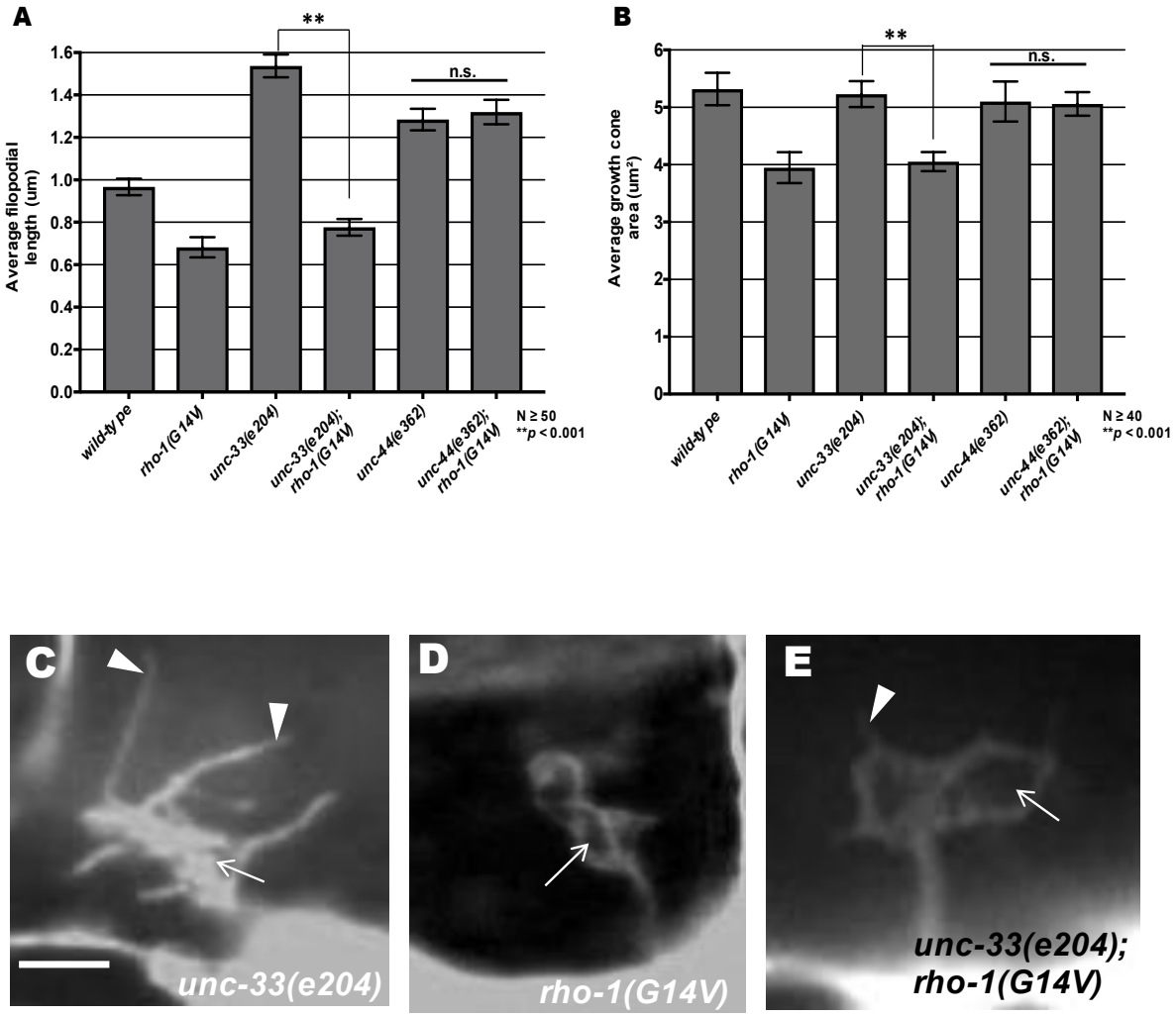
A
**
n.s.
Average filopodial length (um)
1.6
1.4
1.2
1.0
0.8
0.6
0.4
0.2
0.0
wild-ty pe
rho-1(G14V)
unc-33(e204)
unc-33(e204); rho-1(G14V)
unc-44(e362)
unc-44(e362); rho-1(G14V)
N ≥ 50
**p < 0.001
B
**
n.s.
Average growth cone area (um²)
6
5
4
3
2
1
0
wild-ty pe
rho-1(G14V)
unc-33(e204)
unc-33(e204); rho-1(G14V)
unc-44(e362)
unc-44(e362); rho-1(G14V)
N ≥ 40
**p < 0.001
C
unc-33(e204)
D
rho-1(G14V)
E
unc-33(e204); rho-1(G14V)

Figure 4.11. *unc-33* but not *unc-44* is epistatic to *rho-1(G14V)*. (A,B) Quantification of VD growth cone filopodial length and growth cone area in single and double mutant animals. (A) Average filopodial length, in μm. (B) Growth cone area in μm^2. Error bars represent 2x standard error of the mean; asterisks indicate the significant difference between the single mutant and the double mutant phenotype (**$p < 0.001$) determined by two-sided *t*-test with unequal variance. n.s., not significant. **(C-E)** Fluorescence micrographs of mutant VD growth cones; (C) *unc-33(e204)* growth cone (D) *rho-1(G14V)* growth cone (E) *unc-33(e204); rho-1(G14V) g*rowth cone. Arrows point to the growth cone and arrow heads indicate representative filopodia. Scale bar: 5μm.

Figure 4.12.

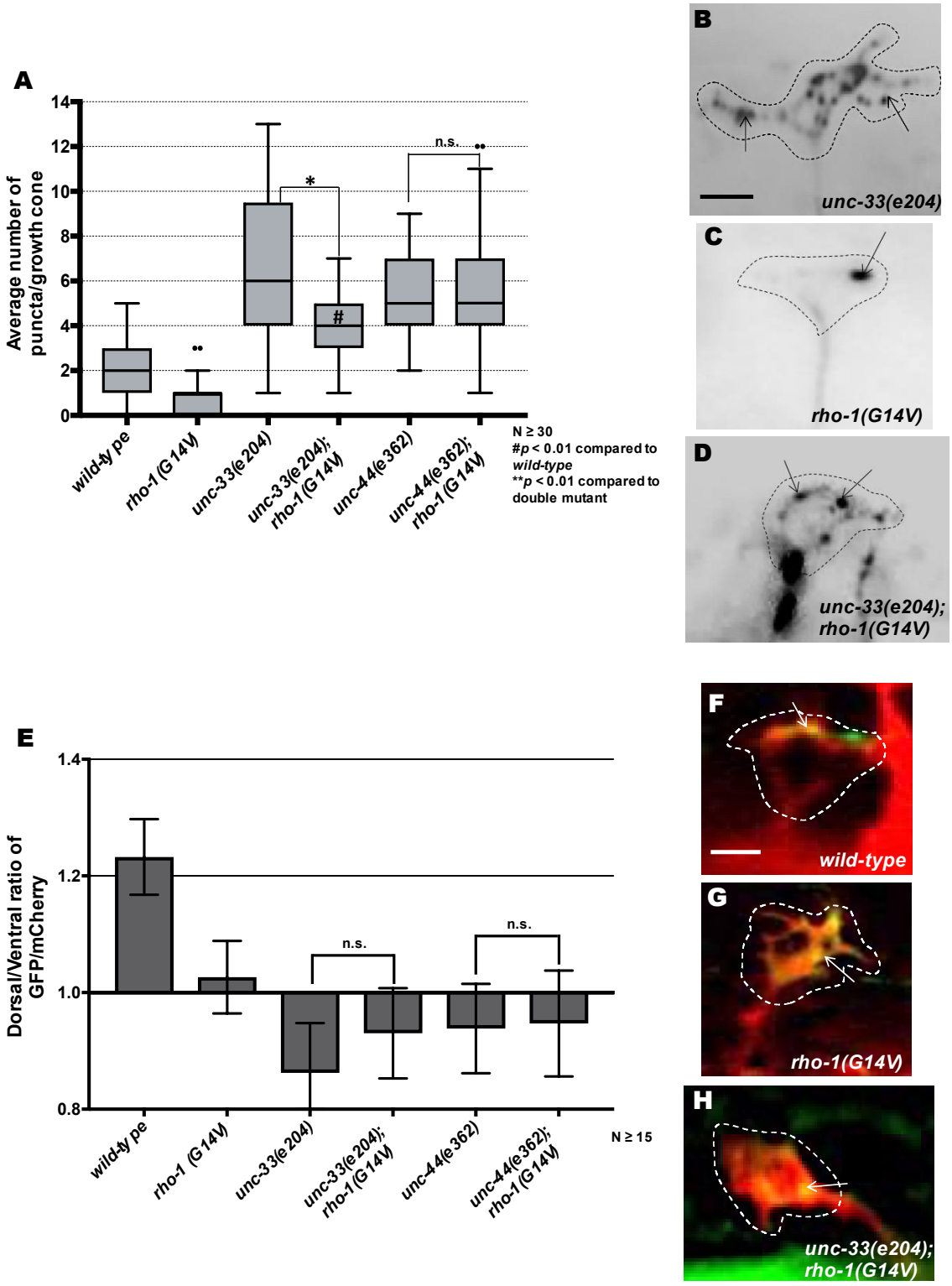
A
Average number of puncta/growth cone
14
12
10
8
6
4
2
0
n.s.
*
#
wild-ty pe
rho-1(G14V)
unc-33(e204)
unc-33(e204); rho-1(G14V)
unc-44(e362)
unc-44(e362); rho-1(G14V)
N ≥ 30
#p < 0.01 compared to wild-type
**p < 0.01 compared to double mutant
B
unc-33(e204)
C
rho-1(G14V)
D
unc-33(e204); rho-1(G14V)
E
Dorsal/Ventral ratio of GFP/mCherry
1.4
1.2
1.0
0.8
n.s.
n.s.
wild-ty pe
rho-1 (G14V)
unc-33(e204)
unc-33(e204); rho-1(G14V)
unc-44(e362)
unc-44(e362); rho-1(G14V)
N ≥ 15
F
wild-type
G
rho-1(G14V)
H
unc-33(e204); rho-1(G14V)

Figure 4.12. RHO-1 is required for UNC-33 to limit EBP-2 accumulation in the growth cone (A) Quantification of the number of EBP-2::GFP puncta in wild-type and mutant animals as described in Figure 4.2A. Asterisks (*) indicate the significant difference between single mutants and the double mutant (*$p < 0.01$). Pound (#) indicates significant difference between wild-type and double mutant (#$p < 0.01$) determined by two-sided *t*-test with unequal variance. **(B-D)** Fluorescence micrographs of EBP-2 distribution in the VD growth cones; (G) *unc-33(e204)* showing increased *ebp-2* puncta (D) *rho-1(G14V)* showing small and inhibited growth cone with significantly lower *ebp-2* puncta and (E) *unc-33(e204); rho-1(G14V)* inhibited *g*rowth cones with an increase in *ebp-2* puncta. Arrows indicate representative EBP-2::GFP puncta. Dashed lines indicate the growth cone periphery. Dorsal is up and anterior is left. Scale bar: 5 µm. **(E)** The average dorsal-to-ventral ratio of GFP/mCherry from multiple growth cones in wild-type, single and double mutant animals. **(F-H)** Representative images of VD growth cones with cytoplasmic mCherry in red (a volumetric marker) and the VAB-10ABD::GFP in green. Areas of overlap are yellow (arrows). Error bars represent 2x standard error of the mean; n.s. indicates no significant difference between *unc-33* and *unc-44* single mutants and their respective double mutants determined by two-sided *t*-test with unequal variance. Scale bar: 5 µm. (F) wild-type growth cone, (G) *rho-1(G14V)* growth cone, (H) *unc-33(e204); rho-1(G14V)* double mutant VD growth cones with cytoplasmic mCherry and VAB-10ABD::GFP expression. Dashed lines indicate the growth cone periphery. Dorsal is up and anterior is left. Scale bar: 5 µm.

Chapter V

Effects of tubulin mutations on VD growth cone morphology in *C. elegans*

5.1 Abstract

Microtubules play important roles in many aspects of neuronal development including, cell migration, axon guidance, synapse growth and maintaining synaptic structure. The building blocks of microtubules (MTs), alpha- and beta-tubulin play a critical role in regulating MT structure, organization and stability during axon outgrowth. In humans, a range of neurodevelopmental defects have been associated with missense mutations in several tubulin isotypes. While many of these mutations have been identified, little is known about how these mutations affect axon outgrowth and growth cone morphology *invivo*. Here we show that, missense mutations in the *C. elegans tba-1* and *tbb-1* showed VD/DD axon guidance and branching defects. in antimorphic *tba-1* and *tbb-1* mutants, developing growth cones *invivo*, showed decreased protrusion, whereas, neomorphic mutations displayed excessive filopodial protrusions. We also find that the gain-of-function *tba-1(ju89)* mutants show an inhibited growth cone phenotype and is also required to control MT+- end distribution in the VD growth cone. In summary, our results suggest TBA-1 and TBB-1 are required for proper axon guidance by maintaining growth cone morphology possibly through MT organization with in the growth cone.

5.2 Introduction

Growth cones are highly dynamic actin and microtubule-based structures present at the tip of growing axons. Growth cones guide axons by responding to extracellular guidance cues towards their appropriate synaptic target resulting in the establishment of functional neural circuits (Mortimer et al., 2008; Tessier-Lavigne and Goodman, 1996).

Growth cone motility that causes the growing axon to extend, turn or retract is dependent on the actin and microtubule cytoskeleton (Dent and Gertler, 2003). The axon shaft and the central region of the growth cone is composed of bundled microtubules with their plus (+) ends (MT+) oriented towards the growth cone. The peripheral region of the growth cone contains highly dynamic actin that is relatively free of microtubules. Although many stable microtubules remain in the central domain, it has been shown that a small population of dynamic microtubules constantly explore the growth cone periphery until they are captured by stable actin filaments or guidance receptors enriched on the growth cone responding to a guidance cue (Challacombe et al., 1996; Qu et al., 2013; Schaefer et al., 2008; Tanaka et al., 1995). This capture stabilizes MTs and allows for MT elongation in the direction of growth cone turning, suggesting an instructive role for MTs in neurite guidance. Furthermore, *invitro* studies using MT stabilizing and destabilizing drugs to alter MT stability and structure have shown to directly affect growth cone turning (Buck and Zheng, 2002), indicating the importance of MT stability in axon outgrowth and guidance.

Microtubules are composed of alpha- and beta-tubulin subunits that form heterodimers which are incorporated into microtubule polymers through interactions with other tubulin heterodimers (Desai and Mitchison, 1997). The assembly and disassembly of MT polymers is highly regulated and the building blocks of MTs; the alpha- and beta subunits are crucial determinants of MT stability.

Mutations in the tubulin genes have been shown to be associated with several neurological disorders such as microcephaly, lissencephaly and other cortical malformations as well as a variety of axon guidance defects (Tischfield et al., 2011). Several point mutations in the alpha- and beta-tubulin genes that cause neurological disorders in heterozygous carriers have been identified (Bahi-Buisson et al., 2014; Chakraborti et al., 2016; Liu and Dwyer, 2014). These mutated residues have been found in regions predicted to mediate GTP binding, inter- and intradimeric interactions, heterodimeric stability or association with motor proteins and act mostly as dominant-negative mutations (Tischfield et al., 2010). Though a few invitro studies have shown how these tubulin mutations affect tubulin folding, heterodimer formation and MT growth (Jaglin et al., 2009; Tian et al., 2010; Tischfield et al., 2010), very little is known about how these mutations affect axon outgrowth and growth cone morphology *invivo*.

The *C. elegans* genome contains 9 alpha-tubulin genes (*mec-12, tba-1, tba-2* and *tba-4* through *tba-9*) and 6 beta-tubulin genes (*ben-1, mec-7, tbb-1, tbb-2, tbb-4* and *tbb-6*). Previous studies have shown that the tubulin missense mutations seen in humans when introduced in the *mec-7* and *mec-12* genes

affected the MT structure, neurite growth and neuronal function of the *C. elegans* mechanosensory touch receptor neurons (Zheng et al., 2017), suggesting a conserved role for the amino acid residues affected in these mutations. Furthermore, mutations in other tubulin genes such as, *tba-1* and *tbb-2* have also been shown to affect number and size of motor neuron synapses and axon extension (Baran et al., 2010). This suggests that alterations in tubulin proteins can lead to changes in MT stability thus affecting neurite formation, guidance and extension.

In this work, we tested the effects of different missense mutations in *tba-1* and *tbb-1* in axon guidance and growth cone protrusion. We find that *tba-1* and *tbb-1* mutants display pathfinding defects in dorsally-directed VD/DD motor neuron axons. We also find that VD growth cone morphology was affected differently in one type of mutation versus the other (antimorphic mutations showed inhibited growth cone protrusion, whereas, neomorphic mutants did not) in *tba-1* and *tbb-1*. We also show that the previously described *tba-1* gain of function mutation (*tba-1(ju89)*) acts in a dominant-negative manner and inhibits growth cone protrusion Lastly, we find that the tubulin mutations affected the distribution of MT+ -ends (EBP-2::GFP) in the VD growth cone. Together, our results suggest an important role for tubulin subunits in growth cone morphology and axon pathfinding.

5.3 Materials and methods

Genetic methods

Experiments were performed at 20°C using standard *C. elegans* technique (Brenner, 1974). Mutations used were LGI: *tba-1(ju89)*; LGII: *juIs76[Punc-25::gfp]*. Chromosomal locations not determined: *lqIs279[Punc-25::ebp-2::gfp]*. Extrachromosomal arrays were generated using standard gonadal injection (Mello and Fire, 1995) and include: *lqEx1192, lqEx1193* and *lqEx1194[Punc-25::tba-1, Pgcy-32::yfp]; lqEx1195, lqEx1196, lqEx1197* and *lqEx1198[Punc-25::tbb-1, Pgcy-32::yfp]; lqEx1199, lqEx1200, lqEx1201* and *lqEx1202[Punc-25::tba-1(V323I), Pgcy-32::yfp]; lqEx1203, lqEx1204, lqEx1205* and *lqEx1206[Punc-25::tba-1(E97K), Pgcy-32::yfp]; lqEx1207, lqEx1208* and *lqEx1209[Punc-25::tbb-1(P220S), Pgcy-32::yfp]; lqEx1210, lqEx1211* and *lqEx1212[Punc-25::tbb-1(P243L), Pgcy-32::yfp]*. Multiple (≥3) extrachromosomal transgenic lines for each *tba-1* and *tbb-1* mutation were analyzed.

Transgene construction

Punc-25::tba-1 and *Punc-25::tbb-1* were made by amplifying the entire genomic regions of *tba-1* and *tbb-1* respectively . Site-directed mutagenesis was used to generate constructs expressing the TBA-1 and TBB-1 variants.

Analysis of axon guidance defects

VD neurons were visualized with a *Punc-25::gfp* transgene, *juIs76* (Jin et al., 1999), which is expressed in GABAergic neurons including the six DDs and

13 VDs, 18 of which extend commissures on the right side of the animal. The commissure on the left side (VD1) was not scored. In *wild-type*, an average of 16 of these 18 VD/DD commissures are apparent on the right side, due to fasciculation of some of the commissural processes. In some mutant backgrounds, fewer than 16 commissures were observe. In these cases, only observable axons emanating from the ventral nerve cord were scored for axon guidance defects. VD/DD axon defects scored include axon guidance (termination before reaching the dorsal nerve cord or wandering at an angle greater than 45° before reaching the dorsal nerve cord) and ectopic branching (ectopic neurite branches present on the commissural processes).

Growth cone imaging

VD growth cones were imaged and quantified as previously described (Norris and Lundquist, 2011). Briefly, animals at ~16 h post-hatching at 20°C were placed on a 2% agarose pad and paralyzed with 5mM sodium azide in M9 buffer, which was allowed to evaporate for 4 min before placing a coverslip over the sample. Some genotypes were slower to develop than others, so the 16 h time point was adjusted for each genotype. Growth cones were imaged with a Qimaging Rolera mGi camera on a Leica DM5500 microscope. Images were analyzed in ImageJ, and statistical analyses done with Graphpad Prism software. As described in (Norris and Lundquist, 2011; Norris et al., 2014), growth cone area was determined by tracing the perimeter of the growth cone body, not including filopodia. Average filopodial length was determined using a line tool to

trace the length of the filopodium. These data were gathered in ImageJ and entered into Graphpad Prism for analysis. A two-sided *t*-test with unequal variance was used to determine significance of difference between genotypes.

EBP-2::GFP imaging

EBP-2::GFP has previously been used to monitor microtubule plus ends in other *C. elegans* cells including neurons (Kozlowski et al., 2007; Srayko et al., 2005; Yan et al., 2013). We constructed a transgene consisting of the *unc-25* promoter driving expression of *ebp-2::gfp* in the VD/DD neurons. In growth cones, a faint fluorescence was observed throughout the growth cone, resembling a soluble GFP and allowing for the growth cone perimeter to be defined. In addition to this faint, uniform fluorescence, brighter puncta of EBP-2::GFP were observed that resembled the EBP-1::GFP puncta described in other cells and neurons. For each growth cone, the perimeter and filopodia were defined, and the EBP-2::GFP puncta in the growth cone were counted. For each genotype, the puncta number for many growth cones (≥25 unless otherwise noted) was determined. Puncta number displayed high variability within and between genotypes, so box-and-whiskers plots (Graphpad Prism) were used to accurately depict this variation. The grey boxes represent the upper and lower quartiles of the data set, and the “whiskers” represent the high and low values. Dots represent major outliers. Significance of difference was determined by a two-sided *t*-test with unequal variance.

5.4 Results

Mutations in *tba-1* and *tbb-1* affect VD/DD axon pathfinding

To examine the role of TBA-1 and TBB-1 in VD/DD axon guidance we introduced point mutations in the coding regions of *tba-1* and *tbb-1* through site directed mutagenesis. The two *tba-1* mutations generated were: *tba-1(E97K)* which has previously been described as an antimorphic mutation. The conserved Glutamic acid residue is required for the intradimeric interactions between the alpha and beta- tubulin subunits (Zheng et al., 2017). *tba-1(V323I)* is a neomorphic mutation and the conserved Valine residue is required for the longitudinal interactions between one tubulin heterodimer and its neighboring one (Zheng et al., 2017). Both the *tba-1* mutations are recessive (Zheng et al., 2017). The antimorphic *tbb-1* mutation generated was a proline residue to serine change *(P243L)* and is also important for the intradimeric interaction between tubulin subunits. The neomorphic *tbb-1(P220S)* mutation and is thought to affect tubulin folding. *(P243L)* is a dominant mutation whereas *(P220S)* is semi-dominant (Zheng et al., 2017). These mutations along with wild-type *tba-1* and *tbb-1* were then expressed specifically in the VD neurons using the *unc-25* promoter. Several transgenic lines for each mutation were obtained and ≥ 3 lines for each mutation were scored for effects (see materials and methods and Figure 5.1A and F). We find that all three: over-expression, antimorphic and neomorphic mutations in *tba-1* and *tbb-1* caused significant defects in VD/DD axon pathfinding including ectopic axon branching and wandering (Figure 5.1). This

data suggests that alpha and beta- tubulin are required for proper axon outgrowth and guidance in the VD/DD motor axons.

Antimorphic mutations in *tba-1* and *tbb-1* inhibit growth cone protrusion

Mutations in tubulin genes have been associated with axon guidance defects (Tischfield et al., 2010), however, the effects of these genes on the growth cone during axon outgrowth *invivo* have not been studied. We find that over-expression of tba-1 and tbb-1 in the VD/DD neurons had no significant effect on VD growth cone protrusion as compared to wild-type growth cones (Figure 5.2A,B and Figure 5.2 F,G). Interestingly, we find that the in *tba-1(E97K)* and *tbb-1(P243L)* antimorphic mutations showed a significant decrease in VD growth cone protrusiveness. *tba-1(E97K)* and *tbb-1(P243L)* growth cones were small with few or no filopodial protrusions (Figure 5.2). These results suggest that antimorphic mutations in tubulin genes have an anti-protrusive effect on the VD growth cone, possibly by blocking MT polymerization.

Neomorphic mutations in *tba-1* and *tbb-1* increased growth cone filopodial protrusion

In contrast to the antimorphic mutations that caused decreased VD growth cone protrusions, we find that neomorphic mutations in *tba-1* and *tbb-1* affected growth cone morphology in a different manner. Though *tba-1(V323I)* mutants has no significant effect on VD growth cone morphology (Figure 5.3A-D), *tbb-1(P220S)* mutant growth cones displayed significantly longer filopodial protrusions as compared to wild-type (Figure 5.3E-H). Growth cone area,

however, was not significantly different in *tbb-1(P220S)* mutants. This data suggests that the amino acid residue mutated in the antimorphic versus neomorphic mutations have different roles in MT structure and function, thus leading to different VD growth cone morphological defects.

Gain-of-function *tba-1* mutants inhibit growth cone protrusion

Previous studies have identified the tba-1(ju89) allele as a gain-of-function mutation that converts a glycine residue to arginine (G414R) in the C-terminal H11-H12 loop of the alpha-tubulin TBA-1. This mutation causes a mild disruption of synapse morphology and a reduction in synapse number and affects DD motor axon guidance (Baran et al., 2010). We find that *tba-1(ju89)* mutants showed significant defects in VD/DD motor axon guidance (Figure 5.4A-D) as previously reported (Baran et al., 2010). We also found that *tba-1(ju89)* significantly reduced the growth cone area and filopodial protrusions of VD growth cones as compared to wild-type (Figure 5.4E-H). This phenotype was similar to the one observed in *tba-1* antimorphic mutants. These data confirm that mutations in *tba-1* affect VD/DD neurons in axon guidance and growth cone morphology.

TBA-1 and TBB-1 can affect MT+ -end distribution in the VD growth cone.

To test whether mutations in the tubulin genes affected MT distribution in the VD growth cone, we examined the MT+-end binding protein EBP-2 fused to GFP which was expressed in the VD/DD neurons using the *unc-25* promoter (see materials and methods). In wild-type VD growth cones, an average of about

2 EBP-2::GFP puncta are observed in the growth cone itself, suggesting that MT+-ends are relatively rare in the growth cone. Interestingly, we found no significant change in the EBP-2::GFP distribution in *tba-1* and *tbb-1* over-expression transgenic lines, antimorphic mutations in *tba-1* and *tbb-1* or even in the neomorphic *tba-1* mutant as compared to wild-type (Figure 5.6A-J). However, *tbb-1(P220S)* mutants showed a significant increase in the number of EBP-2 puncta in the VD growth cones. The fact that *tbb-1(P220S)* mutants showed increased filopodial protrusions and increased EBP-2 numbers in the growth cone suggests that the neo mutations may increase the length of filopodial protrusions by possibly forming hyperstable MTs. In contrast, we also find that the *tba-1(ju89)* also caused a significant increase in the number of MT+-ends entering the growth cone periphery. This phenotype was interesting as *tba-1(ju89)* growth cones were smaller with shorter filopodial protrusions. Taken together, these findings suggest that TBA-1 and TBB-1 control MT+-end distribution in the growth cones.

5.5 Discussion

TBA-1 and TBB-1 regulate axon guidance and growth cone protrusion.

A recent study examined the effect of disease-associated tubulin missense mutations in the *C. elegans* tubulin genes *(mec-7, mec-12 and tba-7)* and their impact on neuronal development and neurite outgrowth in Touch Receptor Neurons (TRNs) (Zheng et al., 2017). Based on the phenotypes observed these mutations were categorized into three classes; loss of function *(lf)* mutants caused only mild neurite growth defects. The antimorphic *(anti)* mutations are thought to block MT polymerization and cause severe neurite growth defects and lastly, the neomorphic *(neo)* mutations caused ectopic neurite growth by inducing hyperstable MTs (Zheng et al., 2017). This correlation between MT stability and the amount of neurite growth observed suggests the importance of MT structure and organization in neurite growth.

We analyzed one antimorphic and one neomorphic mutation in *C. elegans* alpha-tubulin isotype TBA-1 and beta-tubulin isotype TBB-1. Expression of these mutants was driven by the *unc-25* promoter specific for GABAergic neuron expression (including the VD/DD neurons). Both *neo* and *anti*-mutations in *tba-1* and *tbb-1* caused defects in the dorsal guidance of the VD/DD motor axons suggesting the importance of these genes in axon outgrowth (Figure 5.1). Antimorphic mutations in *tba-1* and *tbb-1* resulted in VD growth cones with a marked decrease in growth cone protrusion, with smaller growth cone area and shorter filopodial protrusions (Figure 5.2). The *anti* mutants have been shown to possibly act in a dominant-negative manner by forming poisonous alpha/beta

dimers that causes the termination of MT polymerization and thus induce MT instability (Zheng et al., 2017). These changes in TBA-1 and TBB-1 could affect MT polymerization in the growth cone thus causing the anti-protrusive phenotype we observe.

In contrast, neomorphic mutation in *tbb-1* resulted in longer filopodial protrusions in the VD motor neurons (Figure 5.3), consistent with the idea that *neo* mutations induce the growth of ectopic neurites by forming hyperstable MTs (Zheng et al., 2017). Growth cone morphology, however, was unaffected in *tba-1* neomorphic mutants (Figure 5.3), even though axon guidance in these mutants as evidenced by end-point analysis was affected. One possible explanation for this result is that the effects of the mutations depend on the residues that are mutated as well as their physical location on the alpha/beta-tubulin heterodimer structure. Furthermore, the *neo tba-1(V323I)* mutation is recessive in nature, and possibly may not have a phenotype strong enough to be detected through our assays. In sum, these results suggest TBA-1 and TBB-1 are required for proper axon outgrowth and growth cone morphology. That different mutated residues in *tba-1* and *tbb-1* caused distinct effects on growth cone morphology suggests a correlation between the position of the altered residue and its function in affecting MT stability and polymerization.

tba-1 gain-of-function affects VD growth cone morphology

The gain-of-function *tba-1(ju89)* mutation converts a glycine residue to arginine (G414R) and is located near the beginning of helix 12 of the TBA-1 C-

terminus near the alpha-beta tubulin heterodimer boundary and is thought to alter the external architecture of the MT polymer which affects the binding of motor proteins and other MT-associated proteins. Furthermore, *ju89* mutants have been shown to cause DD motor axon defects and decreased number of GABAergic synapses suggesting that the mutation could alter microtubule dynamics or function (Baran et al., 2010). Here we show that *ju89* caused significant defects in the VD/DD motor axons, consistent with previous findings (Baran et al., 2010). We also find that *tba-1(gf)* mutants caused an inhibited growth cone phenotype similar to those observed in *tba-1* and *tbb-1* anti mutations (Figure 5.4). Previous studies have shown that the *ju89* mutation dominantly alters *tba-1* function (Baran et al., 2010), suggesting that *ju89* may function as an antimorphic mutation and possibly alters VD growth cone morphology by inducing MT instability.

TBA-1 and TBB-1 regulate MT+-end distribution in the VD growth cone

Our findings suggest that TBA-1 and TBB-1 regulate MT+- end distribution to facilitate proper axon outgrowth and growth cone protrusion. *tbb-1(P220S)* mutants showed a significant increase in MT+ -end accumulation in then the growth cone periphery consistent with the idea that *neo* mutants cause ectopic neurites by forming highly stable MT bundles. Anti and neo mutations in *tba-1 (E97K and V323I)* did not affect MT+- end distribution in the VD growth cone, suggesting discrete roles of the amino acid residues mutated. It is also possible that these mutations affect MT organization in a different way (not only plus end

distribution) that was not identified through this study. Future studies will be directed in answering this question as well as analyzing other missense mutations to observe their effects on growth cone morphology and MT organization.

In sum, we have shown that TBA-1 and TBB-1 can regulate VD growth cone morphology and axon outgrowth, providing a link between the importance of MT stability and proper neuronal morphogenesis.

Figure 5.1.

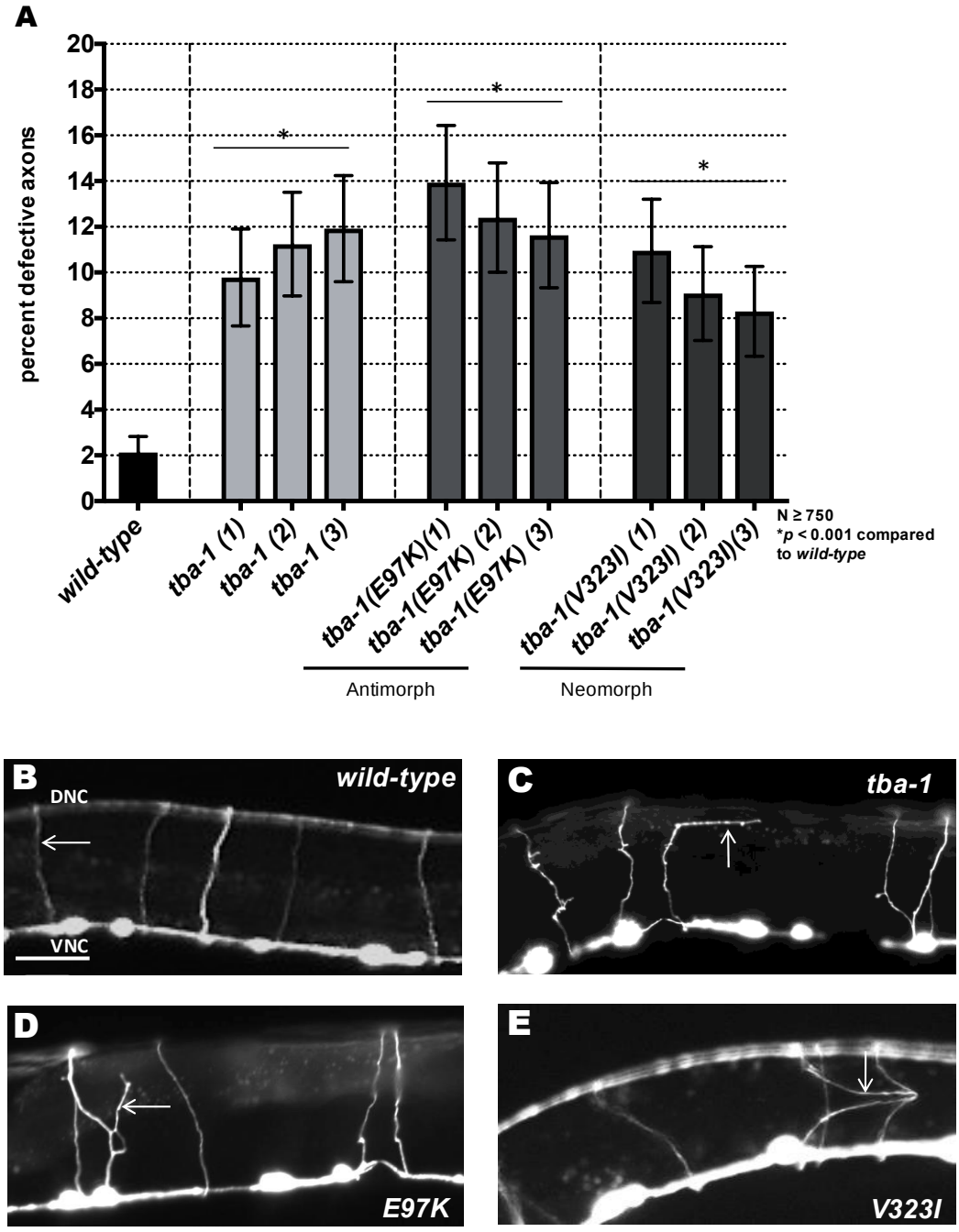
A
percent defective axons
20
18
16
14
12
10
8
6
4
2
0
*
*
*
wild-type
tba-1 (1)
tba-1 (2)
tba-1 (3)
tba-1(E97K)(1)
tba-1(E97K) (2)
tba-1(E97K) (3)
tba-1(V323I) (1)
tba-1(V323I) (2)
tba-1(V323I)(3)
N ≥ 750
*p < 0.001 compared to wild-type
Antimorph
Neomorph
B
wild-type
DNC
VNC
C
tba-1
D
E97K
E
V323I

Figure 5.1

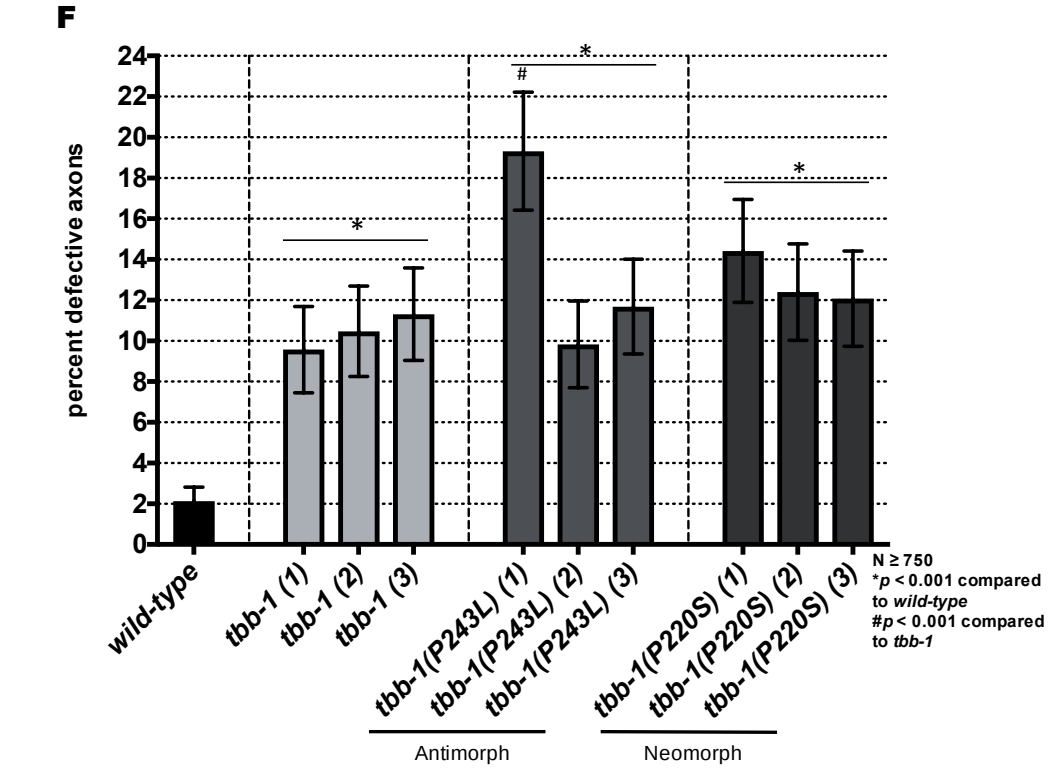
F
percent defective axons
24
22
20
18
16
14
12
10
8
6
4
2
0
*
#
*
wild-type
tbb-1 (1)
tbb-1 (2)
tbb-1 (3)
tbb-1(P243L) (1)
tbb-1(P243L) (2)
tbb-1(P243L) (3)
tbb-1(P220S) (1)
tbb-1(P220S) (2)
tbb-1(P220S) (3)
N ≥ 750
*p < 0.001 compared to wild-type
#p < 0.001 compared to tbb-1
Antimorph
Neomorph

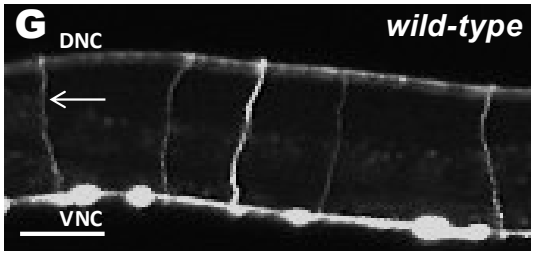
G
DNC
wild-type
VNC

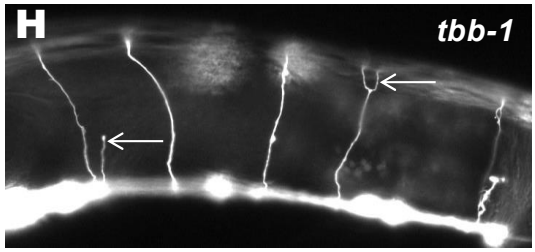
H
tbb-1

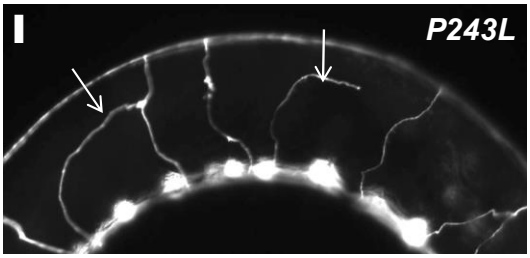
I
P243L

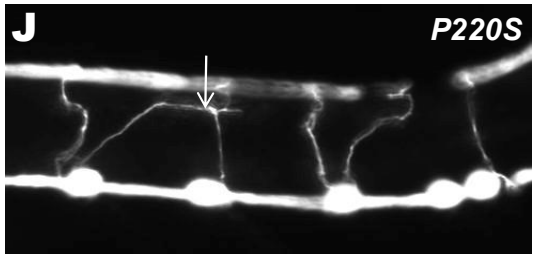
J
P220S

Figure 5.1. Axon outgrowth defects in tubulin mutants. (A) Percentage of VD/DD axons with pathfinding defects (see Materials and Methods) in wild-type, *tba-1* over-expression and *tba-1* (antimorphic and neomorphic) mutants harboring the *juIs76[Punc-25::gfp]* transgene. Single asterisks (*) indicate the significant difference between wild-type and the mutant phenotype ($p < 0.001$) determined by Fischer's exact test. Error bars represent 2x standard error of proportion. **(B-E)** Representative fluorescent micrograph of L4 VD/DD axons. Anterior is to the left, and dorsal is up. The scale bar represents 5µm. DNC, dorsal nerve cord; and VNC, ventral nerve cord. (B) A *wild-type* commissure is indicated by an arrow. (C) *tba-1* over-expression, (D) *tba-1(E97K)* and (E) *tba-1(V323I)* VD/DD axons show guidance defects (arrows). (F) Percentage of VD/DD axons with pathfinding defects (see Materials and Methods) in wild-type, *tbb-1* over-expression and *tbb-1* (antimorphic and neomorphic) mutants harboring the *juIs76[Punc-25::gfp]* transgene. Single asterisks (*) indicate the significant difference between wild-type and the mutant phenotype ($p < 0.001$) determined by Fischer's exact test. Error bars represent 2x standard error of proportion. **(G-J)** Representative fluorescent micrograph of L4 VD/DD axons. Anterior is to the left, and dorsal is up. The scale bar represents 5µm. DNC, dorsal nerve cord; and VNC, ventral nerve cord. (G) A *wild-type* commissure is indicated by an arrow. (H) *tbb-1* over-expression, (I) *tbb-1(P243L)* and (J) *tbb-1(P220S)* VD/DD axons show guidance defects (arrows). At least 750 axons were scored per genotype.

Figure 5.2

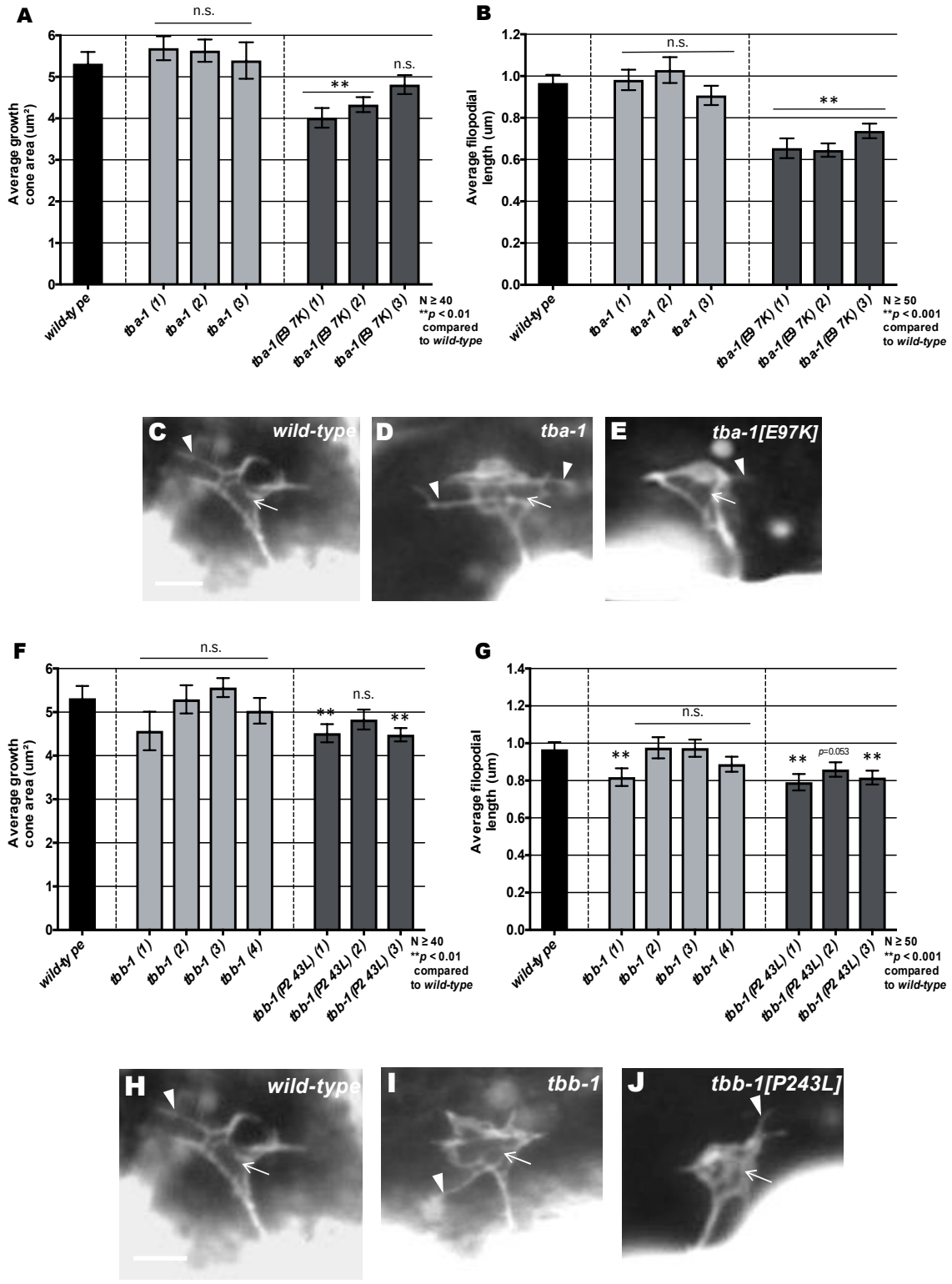
A
n.s.
n.s.
**
Average growth cone area (um²)
wild-type
tba-1 (1)
tba-1 (2)
tba-1 (3)
tba-1(E9 7K) (1)
tba-1(E9 7K) (2)
tba-1(E9 7K) (3)
N ≥ 40
**p < 0.01 compared to wild-type
B
n.s.
**
Average filopodial length (um)
N ≥ 50
**p < 0.001 compared to wild-type
C wild-type
D tba-1
E tba-1[E97K]
F
n.s.
n.s.
**
Average growth cone area (um²)
tbb-1 (1)
tbb-1 (2)
tbb-1 (3)
tbb-1 (4)
tbb-1(P2 43L) (1)
tbb-1(P2 43L) (2)
tbb-1(P2 43L) (3)
N ≥ 40
**p < 0.01 compared to wild-type
G
n.s.
**
p=0.053
Average filopodial length (um)
N ≥ 50
**p < 0.001 compared to wild-type
H wild-type
I tbb-1
J tbb-1[P243L]

Figure 5.2.

Antimorphic *tba-1 and tbb-1* mutations inhibit VD growth cone protrusion

(A,B) Quantification of VD growth cone filopodial length and growth cone area in wild-type and mutant animals. (A) Average filopodial length, in μm. (B) Growth cone area in μm^2. Error bars represent 2x standard error of the mean. Double asterisks (**) indicate the significant difference between wild-type and the mutant phenotype ($p < 0.001$); n.s., not significant determined by two-sided *t*-test with unequal variance. **(C-E)** Fluorescence micrographs of VD growth cones; (C) A wild-type VD growth cone. (D) *tba-1* over-expression and (E) *tba-1(E97K)* growth cones. Arrows indicate representative filopodia. Scale bar: 5μm. **(F,G)** Quantification of VD growth cone filopodial length and growth cone area in wild-type and mutant animals as described above. Error bars represent 2x standard error of the mean. Double asterisks (**) indicate the significant difference between wild-type and the mutant phenotype ($p < 0.001$); n.s., not significant determined by two-sided *t*-test with unequal variance. **(H-J)** Fluorescence micrographs of VD growth cones; (H) A wild-type VD growth cone. (I) *tbb-1* over-expression and (J) *tbb-1(P243L)* growth cones. Arrows indicate representative filopodia. Scale bar: 5μm.

Figure 5.3

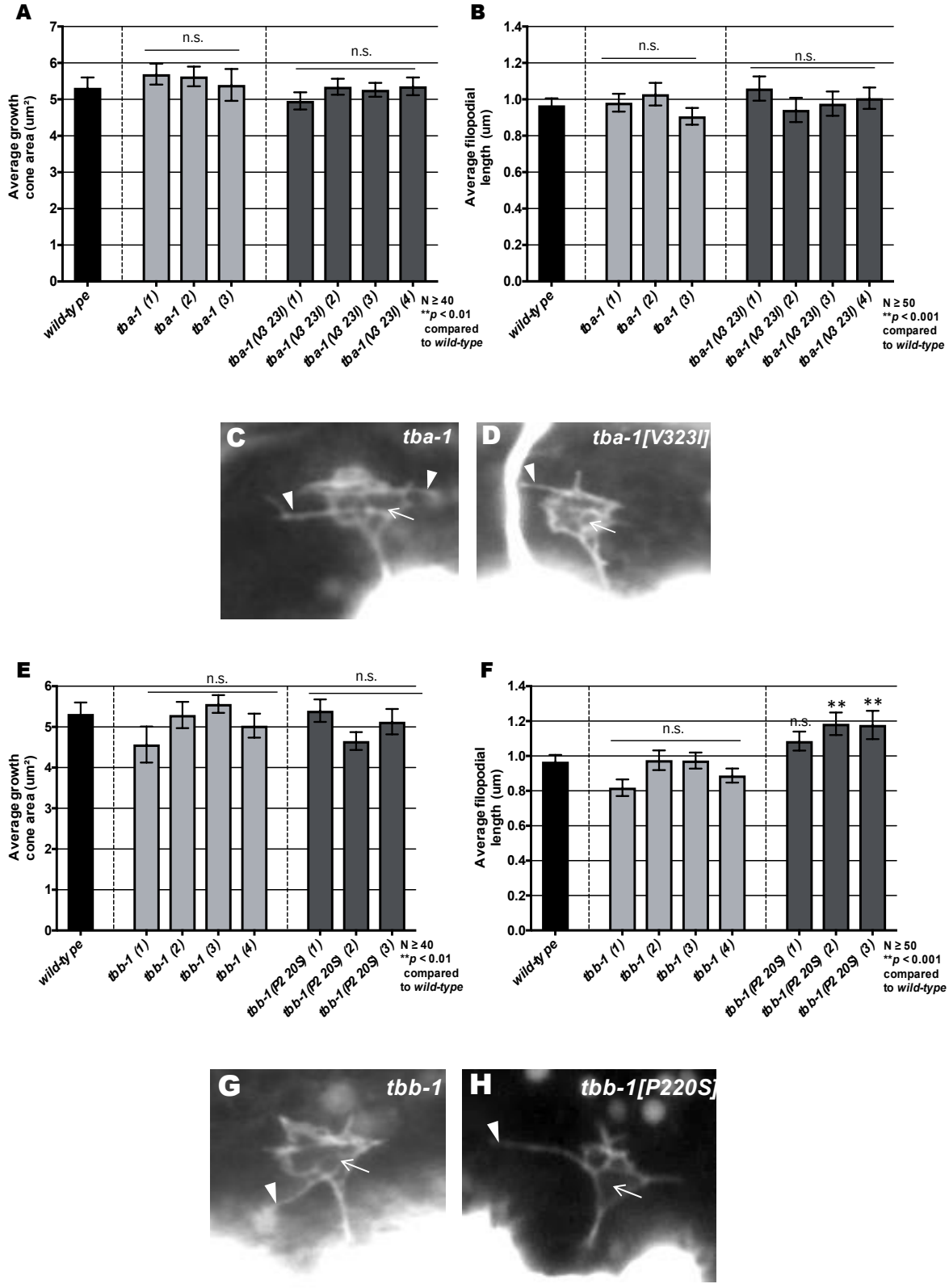
A
Average growth cone area (um²)
n.s.
n.s.
wild-type
tba-1 (1)
tba-1 (2)
tba-1 (3)
tba-1(Nβ 23I) (1)
tba-1(Nβ 23I) (2)
tba-1(Nβ 23I) (3)
tba-1(Nβ 23I) (4)
N ≥ 40
**p < 0.01
compared to wild-type
B
Average filopodial length (um)
n.s.
n.s.
N ≥ 50
**p < 0.001
compared to wild-type
C
tba-1
D
tba-1[V323I]
E
Average growth cone area (um²)
n.s.
n.s.
tbb-1 (1)
tbb-1 (2)
tbb-1 (3)
tbb-1 (4)
tbb-1(P2 20S) (1)
tbb-1(P2 20S) (2)
tbb-1(P2 20S) (3)
F
Average filopodial length (um)
n.s.
n.s.
**
**
G
tbb-1
H
tbb-1[P220S]

Figure 5.3. Neomorphic *tbb-1* increase VD growth cone filopodial length

(A,B) Quantification of VD growth cone filopodial length and growth cone area in wild-type and mutant animals. (A) Average filopodial length, in μm. (B) Growth cone area in μm^2. Error bars represent 2x standard error of the mean; n.s., not significant determined by two-sided *t*-test with unequal variance. **(C-D)** Fluorescence micrographs of VD growth cones; (C) *tba-1* over-expression and (D) *tba-1(V323I)* growth cones. Arrows indicate representative filopodia. Scale bar: 5μm. **(E,F)** Quantification of VD growth cone filopodial length and growth cone area in wild-type and mutant animals as described above. Error bars represent 2x standard error of the mean. Double asterisks (**) indicate the significant difference between wild-type and the mutant phenotype ($p < 0.001$); n.s., not significant determined by two-sided *t*-test with unequal variance. **(G-H)** Fluorescence micrographs of VD growth cones; (G) *tbb-1* over-expression and (H) *tbb-1(P220S)* growth cones. Arrows indicate representative filopodia. Scale bar: 5μm.

Figure 5.4

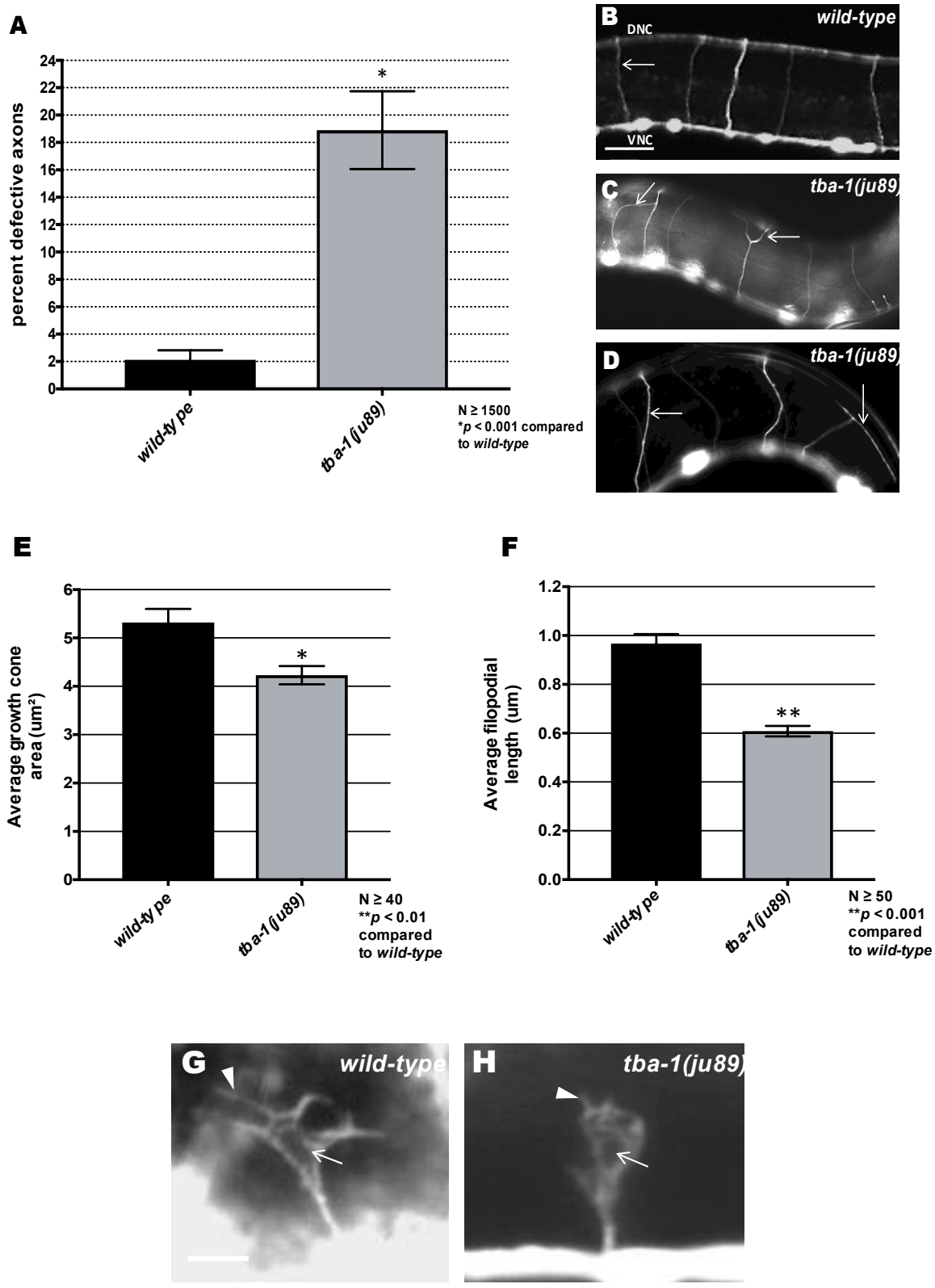
A
percent defective axons
24
22
20
18
16
14
12
10
8
6
4
2
0
*
wild-type
tba-1(ju89)
N ≥ 1500
*p < 0.001 compared to wild-type
B
wild-type
DNC
VNC
C
tba-1(ju89)
D
tba-1(ju89)
E
Average growth cone area (um²)
6
5
4
3
2
1
0
*
wild-type
tba-1(ju89)
N ≥ 40
**p < 0.01 compared to wild-type
F
Average filopodial length (um)
1.2
1.0
0.8
0.6
0.4
0.2
0.0
**
wild-type
tba-1(ju89)
N ≥ 50
**p < 0.001 compared to wild-type
G
wild-type
H
tba-1(ju89)

Figure 5.4. *tba-1* gain of function mutants affect motor axon guidance and VD growth cone morphology. (A) Percentage of VD/DD axons with pathfinding defects (see Materials and Methods) in wild-type and mutant harboring the *juIs76[Punc-25::gfp]* transgene. Single asterisks (*) indicate the significant difference between wild-type and the mutant phenotype ($p < 0.001$) determined by Fischer's exact test. Error bars represent 2x standard error of proportion. **(B-D)** Representative fluorescent micrograph of L4 VD/DD axons. Anterior is to the left, and dorsal is up. The scale bar represents 5μm. DNC, dorsal nerve cord; and VNC, ventral nerve cord. (B) A *wild-type* commissure is indicated by an arrow. (C) and (D) *tba-1(ju89)* VD/DD axons show guidance defects (arrows). At least 1500 axons were scored per genotype. **(E,F)** Quantification of VD growth cone filopodial length and growth cone area in wild-type and mutant animals. (E) Average filopodial length, in μm. (F) Growth cone area in μm^2. Error bars represent 2x standard error of the mean. Double asterisks (**) indicate the significant difference between wild-type and the mutant phenotype ($p < 0.001$) determined by two-sided *t*-test with unequal variance. **(G-H)** Fluorescence micrographs of VD growth cones; (G) A wild-type VD growth cone. (H) *tba-1(ju89)* inhibited growth cones. Arrows indicate representative filopodia. Scale bar: 5μm.

Figure 5.5

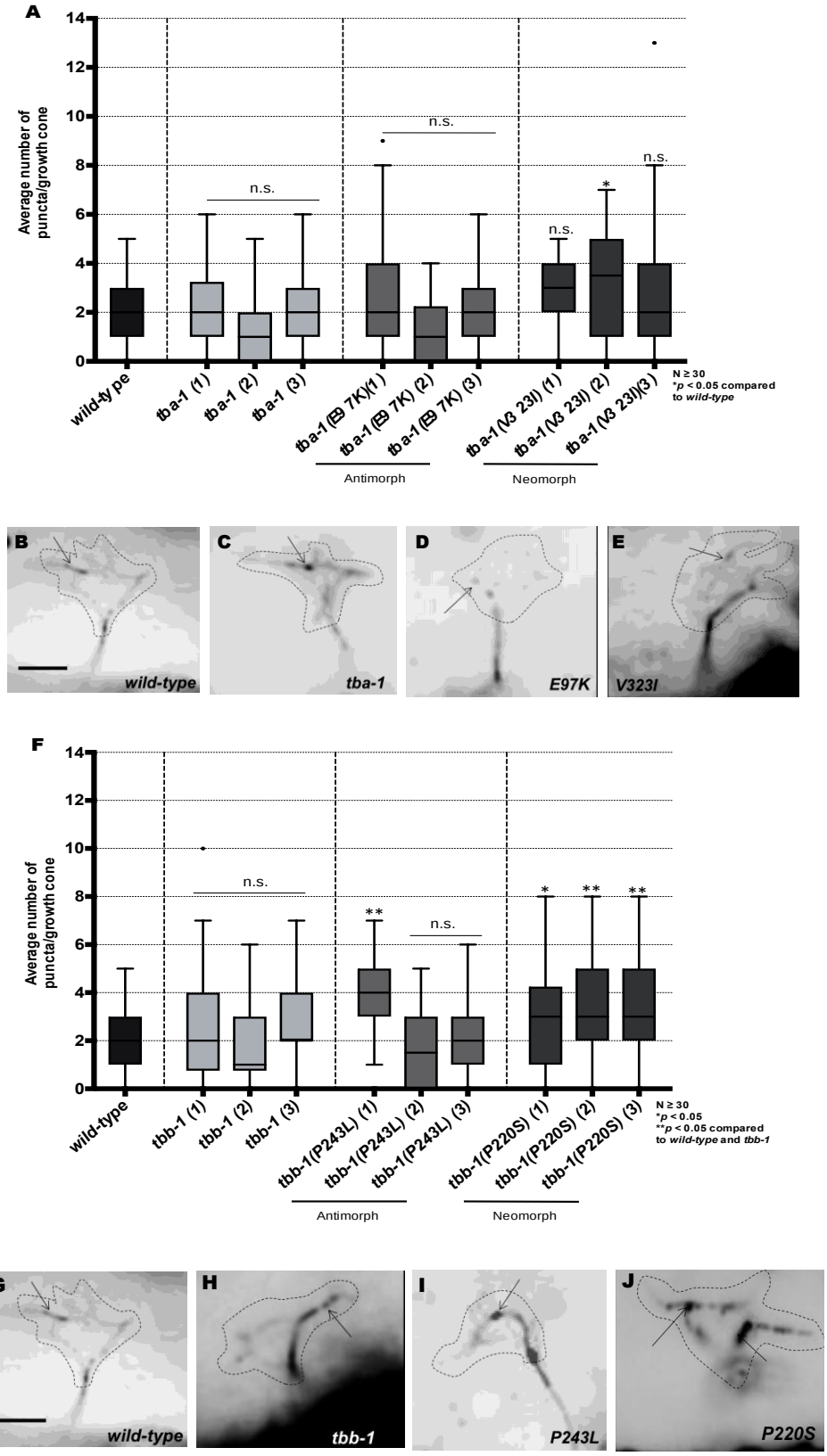
A
Average number of puncta/growth cone
n.s.
n.s.
n.s.
*
wild-type
tba-1 (1)
tba-1 (2)
tba-1 (3)
tba-1(E97K)(1)
tba-1(E97K) (2)
tba-1(E97K) (3)
tba-1(V323I) (1)
tba-1(V323I) (2)
tba-1(V323I)(3)
Antimorph
Neomorph
N ≥ 30
*p < 0.05 compared to wild-type
B
wild-type
C
tba-1
D
E97K
E
V323I
F
Average number of puncta/growth cone
n.s.
**
n.s.
*
**
**
wild-type
tbb-1 (1)
tbb-1 (2)
tbb-1 (3)
tbb-1(P243L) (1)
tbb-1(P243L) (2)
tbb-1(P243L) (3)
tbb-1(P220S) (1)
tbb-1(P220S) (2)
tbb-1(P220S) (3)
Antimorph
Neomorph
N ≥ 30
*p < 0.05
**p < 0.05 compared to wild-type and tbb-1
G
wild-type
H
tbb-1
I
P243L
J
P220S

Figure 5.5

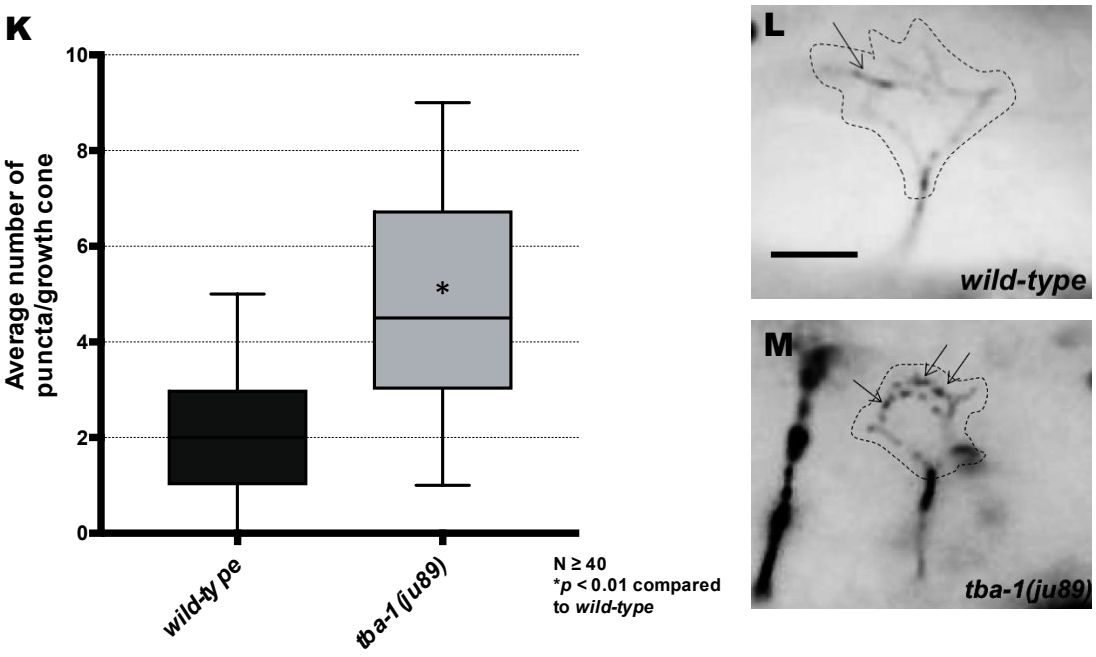
K
Average number of puncta/growth cone
10
8
6
4
2
0
*
wild-type
tba-1(ju89)
N ≥ 40
*p < 0.01 compared to wild-type
L
wild-type
M
tba-1(ju89)

Figure 5.5. *tba-1(ju89)* mutants VD growth cones display increased numbers of EBP-2::GFP puncta. (A) Box-and-whiskers plot of the number of EBP-2::GFP puncta in the growth cones of wild-type and *tba-1* mutants (≥30 growth cones for each genotype). The grey boxes represent the upper and lower quartiles, and error bars represent the upper and lower extreme values. Dots represent outliers. *p* values were assigned using the two-sided *t*-test with unequal variance. **(B-E)** Growth cones of different genotypes, with EBP-2::GFP puncta indicated with arrows. Dashed lines indicate the growth cone perimeter. Dorsal is up and anterior is left. Scale bar: 5μm. **(F)** Box-and-whiskers plot of the number of EBP-2::GFP puncta in the growth cones of wild-type and different *tbb-1* mutants as described in 5.6A. **(G-J)** Growth cones of different genotypes, with EBP-2::GFP puncta indicated with arrows. Dashed lines indicate the growth cone perimeter. **(K)** Box-and-whiskers plot of the number of EBP-2::GFP puncta in the growth cones of wild-type and *tba-1(ju89)* mutants as described in 5.6A. **(G-J)** Growth cones of different genotypes, with EBP-2::GFP puncta indicated with arrows. Dashed lines indicate the growth cone perimeter. Dorsal is up and anterior is left. Scale bar: 5μm.

Chapter VI

SAX-3/Robo regulates *Caenorhabditis elegans* dorsal axon guidance and growth cone protrusion

6.1 Abstract

Neural circuit development involves the coordinated growth and guidance of axons to their target destination. Guidance receptors present on the growth cone sense and respond to environmental guidance cues that attract or repel axons, thus enabling them to reach their target destination. The guidance cue SLT-1/Slit and its receptor SAX-3/Robo have important roles in repulsive axon guidance. In *C. elegans* SAX-3/ Robo acts in anterior-posterior, dorsal-ventral and midline guidance decisions. Though the role of SAX-3 in ventral axon guidance has been extensively studied, less is known about SAX-3 mediated dorsal axon guidance and its effect on growth cone morphology. In contrast to previous studies, our work suggests that SAX-3 is required for the dorsal guidance of motor axons in a SLT-1 independent manner. We also find that in repelled VD growth cones *sax-3* mutants displayed filopodial protrusions that are no longer dorsally biased. Furthermore, constitutive activation of SAX-3 lead to a decrease in growth cone protrusiveness, suggesting that SAX-3 is normally required for dorsal axon guidance and to inhibit growth cone protrusion. UNC-40 and UNC-5 are not required for SAX-3 mediated growth cone inhibition. *unc-73* suppressed the inhibited growth cone phenotype of activated *myr::sax-3*, indicating that the rac GEF UNC-73/Trio likely functions downstream of SAX-3. These studies suggest a new role of SAX-3/Robo in dorsal guidance and inhibition of growth cone protrusion.

6.2 Introduction

During development, the formation of neural circuits depends on the guidance of growing axons to their appropriate targets to establish functional synaptic connections. The growth cone, a highly dynamic, actin-based structure located at the distal tip of a developing axon, senses and responds to various extracellular guidance cues through different receptors, thus directing the axon to its target destination (Mortimer et al., 2008; Tessier-Lavigne and Goodman, 1996). The growth cone consists of a dynamic lamellipodial body ringed by spike-like protrusions known as filopodia (Pak et al., 2008; Zhou and Cohan, 2004), both of which are important in the navigation of a growing axon (Gallo and Letourneau, 2004). Several conserved families of ligands and their receptors are involved in axon guidance, including UNC-6/Netrin and its receptors UNC-40/DCC/Frazzled and UNC-5, as well as, Slit and its receptor SAX-3/Robo (Brose and Tessier-Lavigne, 2000; Culotti and Merz, 1998; Flanagan and Van Vactor, 1998).

The secreted guidance cue UNC-6/Netrin mediates both axon attraction and axon repulsion and along with its receptors UNC-40/DCC and UNC-5 is required for axon guidance along the dorsal-ventral axis in *C. elegans, Drosophila* and vertebrates (Culotti and Merz, 1998; Tessier-Lavigne and Goodman, 1996). The netrin receptor UNC-40/DCC mediates attraction and the UNC-40-UNC-5 heterodimeric receptor mediates repulsion along the dorsal ventral axis (Chan et al., 1996; Hong et al., 1999; Leonardo et al., 1997; MacNeil et al., 2009; Montell, 1999; Moore et al., 2007).

In *C. elegans* UNC-6/ Netrin is secreted from the ventral cells and along with and its receptors UNC-40 and UNC-5 are required for the circumferential migrations of growth cones and axons (Chan et al., 1996; Hedgecock et al., 1990a; Ishii et al., 1992; Leung-Hagesteijn et al., 1992). Previous work from our lab has shown that UNC-6/Netrin can mediate stimulation of growth cone protrusion through its receptor UNC-40/DCC and downstream signaling molecules including the Rac-like GTPases CED-10 and MIG-2, CDC-42, the GTP exchange factor TIAM-1, as well as several cytoskeletal modulatory proteins; Arp2/3, UNC-34/Enabled and UNC-115/abLIM (Demarco et al., 2012; Gitai et al., 2003; Norris et al., 2009; Shakir et al., 2008; Struckhoff and Lundquist, 2003). We have also found that UNC-5-UNC-40 heterodimers are required for their inhibitory effects on growth cone protrusion and this involves the Rac GTPases CED-10 and MIG-2, the Rac GEF UNC-73/Trio and the cytoskeletal interacting molecule UNC-33/CRMP (Norris et al., 2014).

The large secreted protein Slt-1/Slit and its receptor SAX-3/Robo are another important ligand-receptor pairing in axon guidance. Disruption of Robo function in *Drosophila* and *C. elegans* leads to inappropriate axon crossing of the ventral midline (Kidd et al., 1998; Zallen et al., 1998). In *C. elegans*, SLT-1/Slit is expressed predominantly by dorsal body-wall muscles and repels SAX-3/Robo expressing axons towards the VNC (Hao et al., 2001). Mutations in *sax-3* lead to axon abnormal midline crossing, long-range cell migration defects, ventral axon guidance failure, and nerve ring formation defects (Zallen et al., 1999; Zallen et al., 1998).

While much is known about the requirement of SAX-3 in ventral axon guidance, little is known about its role in dorsally-directed axon guidance and its effects on the developing growth cone. In this work, we show that SAX-3 is required for the guidance of dorsally-directed VD/DD motor neuron axons in *C.elegans,* and that this role of SAX-3 maybe independent of SLT-1. We also find that the polarity of protrusion in VD growth cones are affected by loss of *sax-3*, and that constitutive activation SAX-3 (MYR::SAX-3) inhibits growth cone protrusion. We also show that UNC-40 and UNC-5 are not required for the inhibitory effects of activated SAX-3. We also provide evidence that the Rac GEF UNC-73/Trio may function downstream of Sax-3 to restrict growth cone protrusion.

6.3 Materials and methods

Genetic methods

Experiments were performed at 20°C using standard *C. elegans* technique (Brenner, 1974). Mutations used were LGI: *unc-40(n324)*, *unc-73(rh40)*; LGII: *juIs76[Punc-25::gfp]*; LGIV: *unc-5(e53* and *e152)*; LGX: *sax-3(ky123 and ky200)*. Chromosomal locations not determined: *lqIs238, lqIs239 and lqIs240[Punc-25::myr::sax-3]*.

Analysis of axon guidance defects

VD neurons were visualized with a *Punc-25::gfp* transgene, *juIs76* (Jin et al., 1999), which is expressed in GABAergic neurons including the six DDs and 13 VDs, 18 of which extend commissures on the right side of the animal. The commissure on the left side (VD1) was not scored. In *wild-type*, an average of 16 of these 18 VD/DD commissures are apparent on the right side, due to fasciculation of some of the commissural processes. In some mutant backgrounds, fewer than 16 commissures were observed (e.g. *unc-5*). In these cases, only observable axons emanating from the ventral nerve cord were scored for axon guidance defects. VD/DD axon defects scored include axon guidance (termination before reaching the dorsal nerve cord or wandering at an angle greater than 45° before reaching the dorsal nerve cord) and ectopic branching (ectopic neurite branches present on the commissural processes).

Growth cone imaging

VD growth cones were imaged and quantified as previously described (Norris and Lundquist, 2011). Briefly, animals at ~16 h post-hatching at 20°C were placed on a 2% agarose pad and paralyzed with 5mM sodium azide in M9 buffer, which was allowed to evaporate for 4 min before placing a coverslip over the sample. Some genotypes were slower to develop than others, so the 16 h time point was adjusted for each genotype. Growth cones were imaged with a Qimaging Rolera mGi camera on a Leica DM5500 microscope. Images were analyzed in ImageJ, and statistical analyses done with Graphpad Prism software. As described in (Norris and Lundquist, 2011; Norris et al., 2014), growth cone area was determined by tracing the perimeter of the growth cone body, not including filopodia. Average filopodial length was determined using a line tool to trace the length of the filopodium. These data were gathered in ImageJ and entered into Graphpad Prism for analysis. A two-sided *t*-test with unequal variance was used to determine significance of difference between genotypes.

Polarity of filopodia protrusion was determined as previously described (Norris and Lundquist, 2011). Using the ImageJ software to analyze images, the growth cone was divided into roughly four equally sized quadrants (dorsal-anterior, dorsal-posterior, ventral-anterior and ventral-posterior) and then the quadrant from where each filopodium emanated was determined. Statistical analyses were done with Graphpad Prism software. Significance of difference was determined in all cases by a two-sided *t*-test with unequal variance.

6.4 Results

Mutations in sax-3 cause axon pathfinding defects in dorsally directed axons.

The *C. elegans* guidance cue SLT-1/Slit is expressed dorsally and mediates ventral guidance by repulsion via the SAX-3/Robo receptor. SAX-3 has been shown to be important in anterior–posterior, dorsal–ventral, and midline guidance decisions (Killeen and Sybingco, 2008; Zallen et al., 1998). Most work till date has focused on the role of SAX-3 in ventral axon guidance in multiple types of neurons (Li et al., 2013; Yu et al., 2002; Zallen et al., 1998). However, not much is known on how SAX-3 may affect dorsal axon guidance. To probe the role of SAX-3 in dorsal axon guidance we used the *C. elegans* VD/DD motor neurons and axons. The 19 D-class motor neuron cell bodies reside in the ventral nerve cord and extend axons anteriorly and then straight dorsally to the dorsal nerve cord to form commissures. We analyzed two mutations of *sax-3* for VD/DD axon guidance defects. The *sax-3(ky123)* allele results in a deletion of the signal peptide sequence and first exon of the gene, whereas *sax-3(ky200)* is a missense mutation at a conserved proline residue (P37S) in the first immunoglobin-like domain (Zallen et al., 1998). The *sax-3(ky200)* mutation is temperature sensitive and previous work suggests that the SAX-3 protein in this mutation is misfolded and mislocalized at the restrictive temperature which is 25°C (Wang et al., 2013). *sax-3* mutants showed significant defects in VD/DD axon pathfinding, including ectopic axon branching and prematurely terminated axons. We also find that *slt-1* mutants do not (Figure 6.1). This result suggests

that SAX-3 maybe required for the proper guidance of dorsally directed axons, possibly through UNC-6/Netrin mediated axon repulsion.

SAX-3 affects polarity of growth cone filopodial protrusion.

To further understand how these axon guidance defects seen in *sax-3* mutants would relate to growth morphology during growth cone outgrowth, we analyzed VD growth cones in *sax-3* mutants. Interestingly, loss of *sax-3* had no significant effect on growth cone morphology as indicated by growth cone area and filopodia length (Figure 6.2A-E). Instead, we find that the polarity of filopodia protrusion was significantly altered in *sax-3* mutant growth cones (Figure 6.2F-I). Wild-type VD growth cones display highly polarized filopodial protrusions, where in majority of filopodia (70%) protrude dorsally away from the source of UNC-6/Netrin towards their target in the dorsal nerve cord (Norris and Lundquist, 2009) (Figure 6.2A and B). This polarity was abolished in *sax-3* mutants such that filopodia protruded more in ventral directions rather than dorsal (60% of filopodia directed ventrally in *sax-3(ky123)*) (Figure 6.2). These results indicate that SAX-3 controls the polarity of filopodial protrusion from growth cones that are repelled from UNC-6/Netrin.

Constitutively-active MYR::SAX-3 inhibits VD growth cone protrusion.

Mutations in *sax-3* had no significant effect on VD growth cone morphology as compared to wild-type as indicated by average growth cone area and filopodia length but affected polarity of growth cone filopodia protrusion

(Figure 6.2). To further investigate the role of SAX-3 in growth cone morphology, we constructed a constitutively active version of SAX-3, by adding an N-terminal myristoylation signal to the cytoplasmic domain of SAX-3 (Gitai et al., 2003). MYR::SAX-3 lacks the transmembrane domain and the extracellular domains similar to that seen in activated MYR:UNC-40 and MYR::UNC-5 (Norris and Lundquist, 2011; Norris et al., 2014).

Expression of *myr::sax-3* in the VD neurons using the *unc-25* promoter caused a marked decrease in VD growth cone protrusiveness, with small growth cone area and few if any filopodial protrusions (Figure 6.3A-E). Consistent with these defects in growth cone morphology, *myr::sax-3* caused severe defects in VD/DD dorsal axon pathfinding, as determined by end-point analysis (95% defective axons in *lqIs240[myr::sax-3]*) (Figure 6.3F-I). These data suggest that SAX-3 may have a role in inhibition of growth cone protrusion.

Constitutively-active MYR::SAX-3 does not require UNC-40 and UNC-5 to inhibit VD growth cone protrusion.

Previous work has shown that SAX-3 can interact with UNC-40/DCC by forming an heteromeric receptor complex to control repulsive axon guidance (Yu et al., 2002). We tested whether the MYR::SAX-3-mediated inhibition of VD growth cone protrusion was dependent on the presence of UNC-6/Netrin guidance receptors, UNC-40/DCC and UNC-5. We found that the MYR::SAX-3 inhibited growth cone phenotype was not dependent on UNC-40 or UNC-5 as *unc-40; myr::sax-3* and *unc-5; myr::sax-3* double mutant VD growth cones

resembled *myr::sax-3* alone (Figure 6.4A-E). These results suggest that MYR::SAX-3 does not require UNC-40 or UNC-5 to inhibit growth cone protrusion.

Over-protrusive growth cone phenotype of *unc-5* does not require SAX-3.

Previous studies have shown that a functional UNC-40 was required for the over protrusive growth cone phenotype observed in *unc-5* loss of function mutants alone (Norris and Lundquist, 2011). *unc-5* mutants display increased VD growth cone protrusiveness with larger growth cone area and longer filopodial protrusions as compared to wild-type (Norris and Lundquist, 2011). However, *unc-5; unc-40* double mutants were found to have near wild-type levels of VD growth cone protrusion (Norris and Lundquist, 2011). To examine the relationship between SAX-3 and UNC-5 we constructed *unc-5(e152); sax-3(ky123)* double mutants and found that *sax-3(ky123)* did not suppress the over-protrusive phenotype seen in the *unc-5* single mutants : growth cone size and filopodia protrusions in the double mutant resembled *unc-5* alone (Figure 6.5A-F). This result along with the MYR::SAX-3 data suggests that SAX-3 and UNC-5 function independently in inhibition of growth cone protrusion.

SAX-3 requires UNC-73/Rac GEF to inhibit VD growth cone protrusion.

The Rac GEF UNC-73/Trio has been shown to work downstream of SAX-3 to stimulate axon outgrowth in PDE neurons (Li et al., 2013). Furthermore, the Rac GTP exchange factor activity of UNC-73 is required to inhibit growth cone

protrusion downstream of UNC-5 (Norris and Lundquist, 2011; Norris et al., 2014). The *unc-73(rh40)* mutation is a Ser-1216 to Phe substitution that eliminates only the Rac-GEF domain activity of UNC-73 but does not affect other activities (Lundquist et al. 2001; Steven et al. 1998). *unc-73(rh40)* mutants display excessive growth cone protrusion(Norris and Lundquist, 2011; Norris et al., 2014) (Figure 6.6B and D). We determined whether UNC-73 is required for filopodial inhibition mediated by MYR::SAX-3. Loss of *unc-73* completely suppressed inhibition of filopodial protrusion and growth cone size of *myr::sax-3* (Figure 6.6). This data indicates that UNC-73 is required for SAX-3 to inhibit growth cone protrusion and suggests that it may act downstream of SAX-3 in the process.

6.5 Discussion

SAX-3 regulates polarity and inhibition of growth cone protrusion

The guidance cue SLT-1/Slit is expressed dorsally and mediates a ventral guidance by repulsion via the SAX-3/Robo receptor (Hao et al., 2001). We find that *sax-3/Robo* mutants display defects in dorsally-directed VD/DD motor axons, but *slt-1* mutants do not (Figure 6.1). This result suggests a SLT-1 independent or a second ligand dependent function of SAX-3 in dorsal axon guidance, consistent SLT-1 independent SAX-3 signaling in several different processes (Hao et al., 2001; Li et al., 2008; Xu et al., 2015; Zallen et al., 1999). Most known roles of Slit/Robo signaling are repulsive (Pappu and Zipursky, 2010), but evidence from Drosophila indicates that Robo2 can stimulate midline crossing, suggesting a role in attractive guidance (Evans and Bashaw, 2010; Spitzweck et al., 2010). Thus, it is possible that SAX-3 mediates attractive dorsal guidance using a cue distinct from SLT-1. However, previous work has shown that SAX-3 can act with UNC-40/DCC possibly as a co-receptor in repulsion independent of UNC-6/Netrin (Yu et al., 2002). Hence, it is also possible that SAX-3 may participate in UNC-40-mediated repulsion of VD growth cones.

Though we find that loss of *sax-3* had no significant effect on VD growth cone area or length of filopodia protrusion, loss of *sax-3* abolished the dorsal polarity of filopodia protrusions in the VD growth cones (Figure 6.2), suggesting extent versus polarity of protrusion may be in part two separate mechanisms. Furthermore, we find that constitutive activation of MYR::SAX-3 lead to a significant reduction in growth cone protrusiveness (Figure 6.3) similar to those

seen in MYR::UNC-40 and MYR::UNC-5, suggesting a role of SAX-3 in inhibition of protrusion in repelled VD growth cones possibly in an UNC-6/Netrin dependent manner.

SAX-3 inhibition of growth cone protrusion may not require UNC-5 or UNC-40

We demonstrate that mutations in *unc-5 and unc-40* were unable to suppress the effects of *myr::sax-3*, suggesting that MYR::SAX-3 does not require UNC-5 or UNC-40 to inhibit growth cone protrusion (Figure 6.4). This is interesting as SAX-3 has been shown to act with UNC-40 in repulsion possibly as co-receptors (Xu et al., 2015; Yu et al., 2002). In contrast to *unc-5* mutants, mutations in *unc-40* display a significant reduction in filopodia length but a relatively normal growth cone size as compared to wild-type (Figure 6.4A). This is likely due to the dual role of UNC-40 in stimulation of protrusion as a homodimer and inhibition of protrusion as an heterodimer with UNC-5. We find that this reduction in filopodia length in *unc-40* is almost comparable to those seen in *myr::sax-3* single mutants. Hence, though we see a reduction in growth cone area in *unc-40; myr::sax-3* double mutants as compared to *unc-40* alone, we could not observe any significant differences in length of filopodial protrusions making the result difficult to interpret. It is probable that SAX-3 may not require UNC-40 in this process, however, we cannot rule out the possibility of them interacting with one another to inhibit growth cone protrusion.

SAX-3 signals through the Rac GEF UNC-73/Trio in inhibition of growth cone protrusion.

UNC-73/Trio is required for proper neuronal migration and axon guidance (Steven et al. 1998; Bateman et al, 2000). Previous studies have shown that UNC-73/Trio affected the accumulation and distribution of SAX-3/Robo and UNC-40 receptors in neurons (Levy-Strumpf 2007; Watari-Goshima et al. 2007) suggesting that UNC-73 acts upstream of guidance receptors and affects their localization. We have previously found that UNC-73 did not affect the localization of UNC-40 and UNC-5 to the VD growth cone and that it functions downstream of the UNC-40-UNC-5 receptors to inhibit growth cone protrusion. Our findings here suggest that UNC-73 is required for filopodial inhibition driven by MYR::SAX-3. The *unc-73(rh40)* mutation significantly suppressed the effects of activated MYR::SAX-3 on inhibition of growth cone protrusion. In this case, both filopodial protrusion and growth cone area resembled *unc-73* alone. That UNC-73 was required for the effects of the constitutively active MYR::SAX-3 suggests that it acts downstream of SAX-3 in inhibition of growth cone protrusion. Future studies will include understanding whether UNC-73 affects the localization of SAX-3 in the VD growth cone.

6.6 Future Directions

There remain several interesting questions to be asked in this project. Since the *unc-40; myr::sax-3* data was hard to interpret one of the most direct questions is whether s*ax-3* suppresses the *myr::unc-40* construct. If it does, it would confirm that SAX-3 requires UNC-40 to mediate inhibition of growth cone protrusion possibly as co-receptor.

Furthermore, it would be interesting to know if SAX-3 acts in an UNC-6/Netrin dependent manner in repulsion of VD growth cones. If *sax-3* could suppress the *unc-6* over-expression phenotype, this would confirm the role of SAX-3 in UNC-6- mediated repulsion.

We have already implicated *unc-73* as being downstream of the MYR::SAX-3 inhibition-of-protrusion phenotype, it would be interesting to know whether or not the Rac GTPases CED-10 and MIG-2 as well as the cytoskeletal interacting protein UNC-33/CRMP act downstream of SAX-3 to limit filopodial protrusion. It would also be interesting to see whether the potential downstream signaling components would affect the localization of SAX-3 in the growth cone.

Finally, it would be useful to observe if *sax-3* affects the cytoskeletal organization of the VD growth cone (F-actin polarity and MT distribution).

Figure 6.1

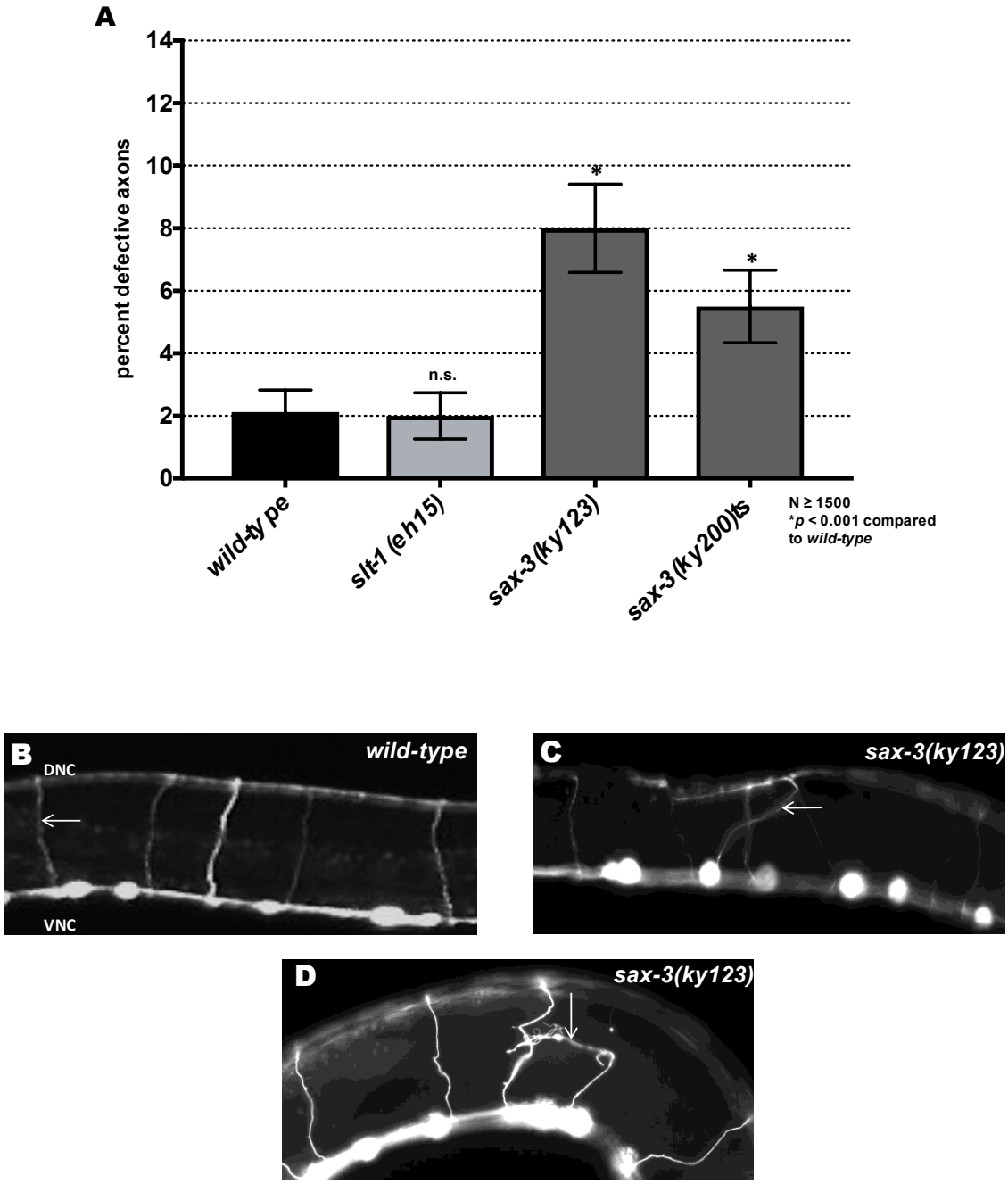
A
percent defective axons
14
12
10
8
6
4
2
0
n.s.
*
*
wild-type
slt-1 (eh15)
sax-3(ky123)
sax-3(ky200)ts
N ≥ 1500
*p < 0.001 compared to wild-type
B
wild-type
DNC
VNC
C
sax-3(ky123)
D
sax-3(ky123)

Figure 6.1. Mutations in *sax-3* cause axon pathfinding defects in dorsally guided VD/DD axons. (A) Percentage of VD/DD axons with pathfinding defects (see Materials and Methods) in wild-type and *sax-3* mutants harboring the *juIs76[Punc-25::gfp]* transgene. Single asterisks (*) indicate the significant difference between wild-type and the mutant phenotype ($p < 0.001$) determined by Fischer's exact test. Error bars represent 2x standard error of proportion. **(B-D)** Representative fluorescent micrograph of L4 VD/DD axons. Anterior is to the left, and dorsal is up. The scale bar represents 5μm. DNC, dorsal nerve cord; and VNC, ventral nerve cord. (B) A *wild-type* commissure is indicated by an arrow. (C) *sax-3(ky123)* VD/DD axons branched and wandered (arrows). (D) *sax-3(ky123)* commissure branched and failed to reach to dorsal nerve cord (arrow). At least 1500 axons were scored per genotype.

Figure 6.2

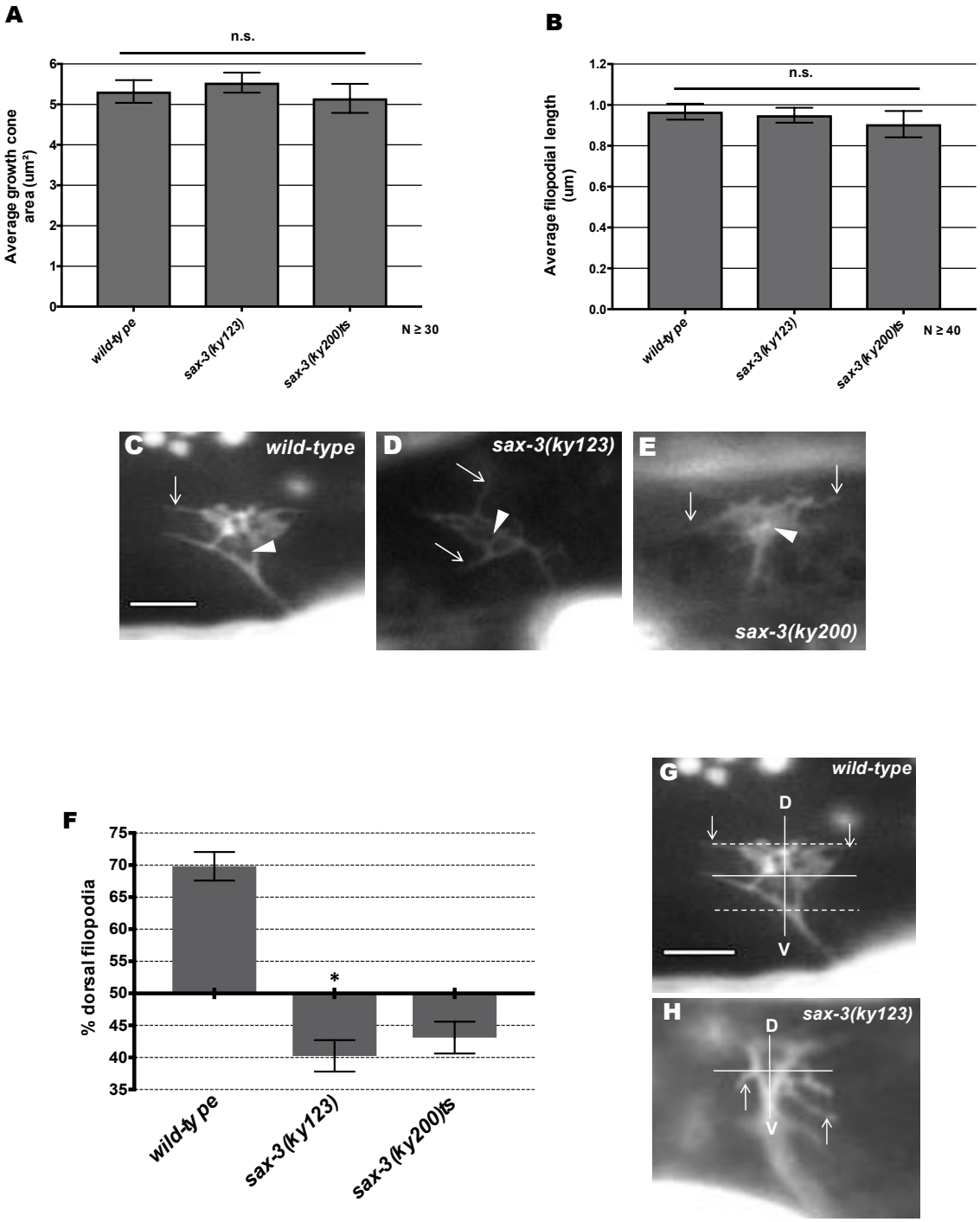
A
n.s.
Average growth cone area (um²)
wild-type
sax-3(ky123)
sax-3(ky200)ts
N ≥ 30
B
n.s.
Average filopodial length (um)
wild-type
sax-3(ky123)
sax-3(ky200)ts
N ≥ 40
C
wild-type
D
sax-3(ky123)
E
sax-3(ky200)
F
% dorsal filopodia
*
wild-type
sax-3(ky123)
sax-3(ky200)ts
G
wild-type
D
V
H
sax-3(ky123)
D
V

Figure 6.2. *sax-3* mutants cause growth cone polarity defects. (A,B) Quantification of VD growth cone filopodial length and growth cone area in wild-type and mutant animals. (A) Average filopodial length, in μm. (B) Growth cone area in μm^2. Error bars represent 2x standard error of the mean; n.s., not significant determined by two-sided *t*-test with unequal variance. **(C-E)** Fluorescence micrographs of VD growth cones; (C) A wild-type VD growth cone. (D) *sax-3(ky123)* and (E) *sax-3(ky200)* growth cones. Arrows indicate representative filopodia. Scale bar: 5μm. (**F**) Percentage of filopodia protruding dorsally from VD growth cones. The *x*-axis is set at 50%, such that bars extending above the *x*-axis represent percentages above 50%, and bars that extend below the axis represent percentages below 50%. Asterisks indicate a significant difference between wild type and the mutant ($p<0.01$) determined by two-sided *t*-test with unequal variance. (**G-H**) Representative images of VD growth cones, Scale bar: 5 μm. Dashed gray lines in G delineate dorsal and ventral boundaries of the growth cone; solid lines in G and H indicate the dorsal-ventral and anterior-posterior boundaries used for scoring filopodia polarity.

Figure 6.3

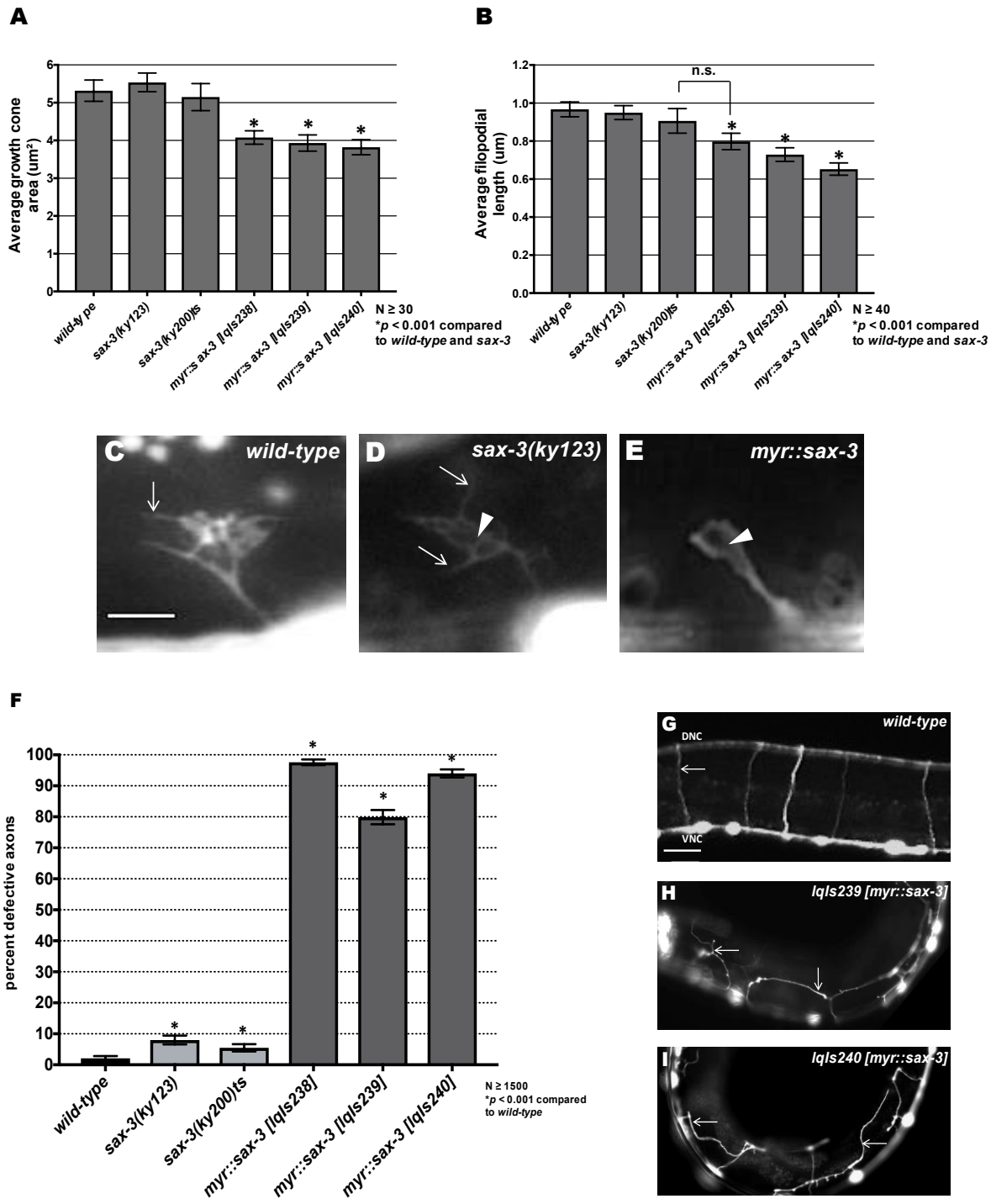
A
Average growth cone area (um²)
wild-type
sax-3(ky123)
sax-3(ky200)ts
myr::sax-3 [lqls238]
myr::sax-3 [lqls239]
myr::sax-3 [lqls240]
N ≥ 30
*p < 0.001 compared to wild-type and sax-3
B
Average filopodial length (um)
n.s.
N ≥ 40
*p < 0.001 compared to wild-type and sax-3
C wild-type
D sax-3(ky123)
E myr::sax-3
F
percent defective axons
N ≥ 1500
*p < 0.001 compared to wild-type
G wild-type
DNC
VNC
H lqls239 [myr::sax-3]
I lqls240 [myr::sax-3]

Figure 6.3. Expressing constitutively active MYR::SAX-3 in the VD growth cones causes a reduction in extent of filopodia protrusion. (A,B) Quantification of VD growth cone filopodial length and growth cone area in wild-type and mutant animals. (A) Average filopodial length, in μm. (B) Growth cone area in μm^2. Error bars represent 2x standard error of the mean. Single asterisks (*) indicate the significant difference between wild-type and the mutant phenotype ($p < 0.001$) determined by two-sided *t*-test with unequal variance. **(C-E)** Fluorescence micrographs of VD growth cones; (C) A wild-type VD growth cone. (D) *sax-3(ky123)* and (E) *myr::sax-3* growth cones. Arrows indicate representative filopodia. Scale bar: 5μm. (F) Percentage of VD/DD axons with pathfinding defects (see Materials and Methods) in wild-type and mutant animals. Single asterisks (*) indicate the significant difference between wild-type and the mutant phenotype ($p < 0.001$) determined by Fischer's exact test. Error bars represent 2x standard error of proportion. **(G-I)** Representative fluorescent micrograph of L4 VD/DD axons. Anterior is to the left, and dorsal is up. The scale bar represents 5μm. DNC, dorsal nerve cord; and VNC, ventral nerve cord. (G) A *wild-type* commissure is indicated by an arrow. (H) *lqIs239[myr::sax-3]* and (I) *lqIs240[myr::sax-3]* commissures branched and failed to reach to dorsal nerve cord (arrows). At least 1500 axons were scored per genotype.

Figure 6.4

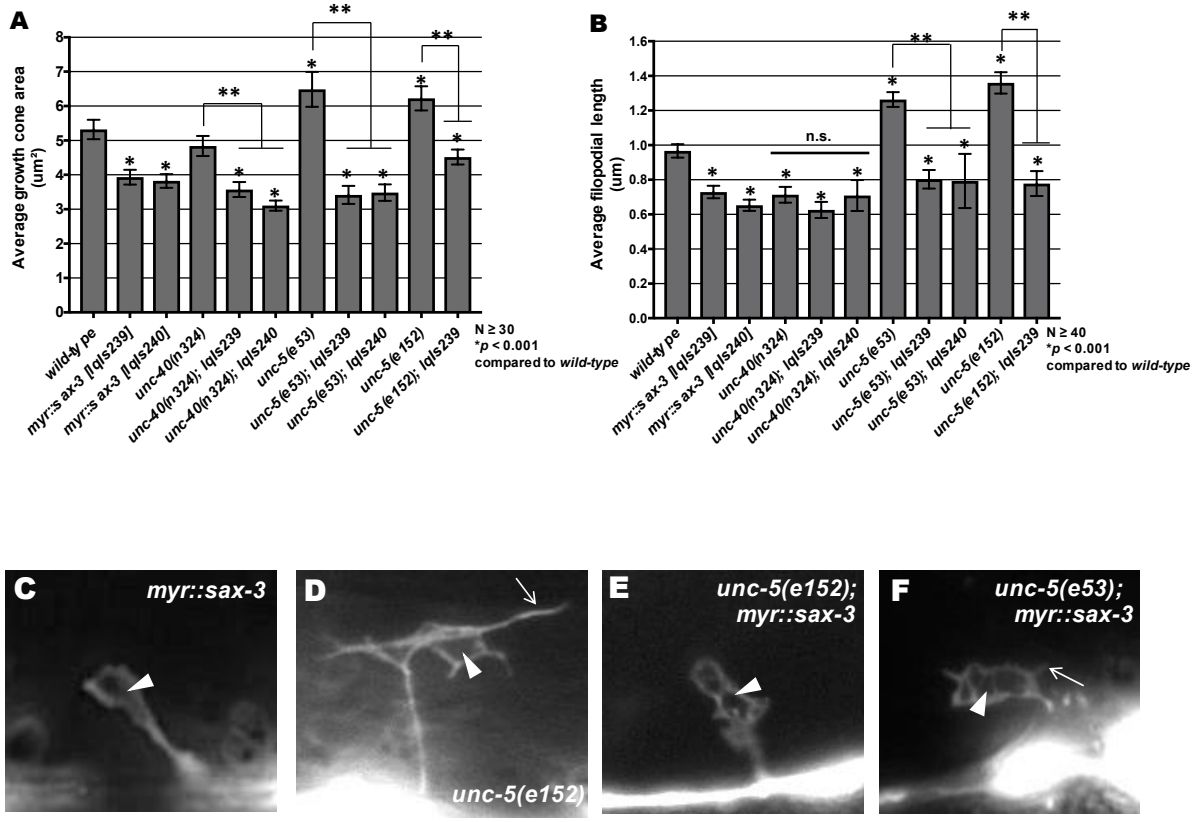
A
Average growth cone area (um²)
wild-type
myr::sax-3 I[qIs239]
myr::sax-3 I[qIs240]
unc-40(n324)
unc-40(n324); lqIs239
unc-40(n324); lqIs240
unc-5(e53)
unc-5(e53); lqIs239
unc-5(e53); lqIs240
unc-5(e152)
unc-5(e152); lqIs239
N ≥ 30
*p < 0.001
compared to wild-type
B
Average filopodial length (um)
n.s.
N ≥ 40
*p < 0.001
compared to wild-type
C
myr::sax-3
D
unc-5(e152)
E
unc-5(e152); myr::sax-3
F
unc-5(e53); myr::sax-3

Figure 6.4. MYR::SAX-3 mediated inhibition of VD growth cone protrusion does not require UNC-40 and UNC-5. (A,B) Quantification of VD growth cone filopodial length and growth cone area in wild-type and mutant animals. (A) Average filopodial length, in μm. (B) Growth cone area in μm^2. Error bars represent 2x standard error of the mean. Single asterisks (*) indicate the significant difference between wild-type and the mutant phenotype ($p < 0.001$), Double asterisks (**) indicate the significant difference between single mutant and double mutant phenotype ($p < 0.001$) determined by two-sided *t*-test with unequal variance; n.s., not significant. **(C-F)** Fluorescence micrographs of VD growth cones; (C) A *myr::sax-3* growth cone. (D) *unc-5(e152)* growth cone showing increased filopodial protrusion in the form of longer filopodia. (E) *unc-5(e152); myr::sax-3* and (F) *unc-5(e53); myr::sax-3* growth cones. Arrows indicate representative filopodia. Scale bar: 5μm.

Figure 6.5

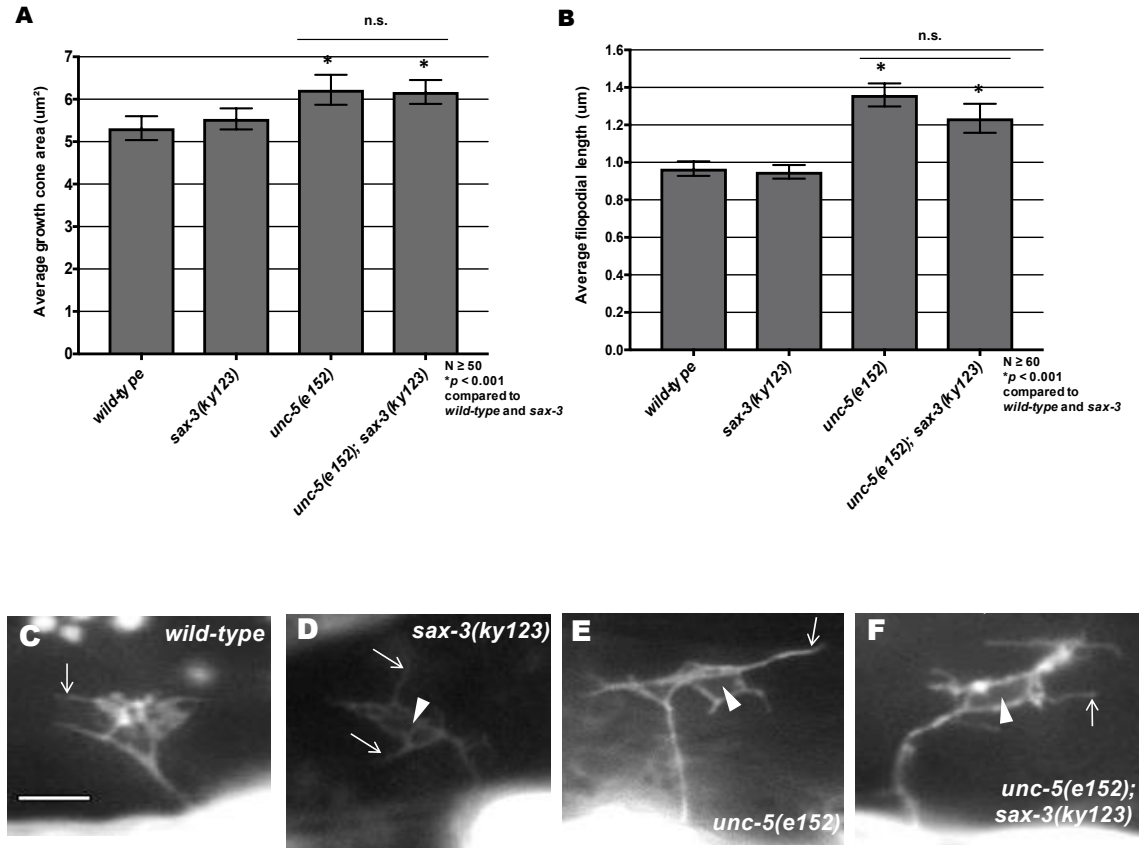
A
n.s.
Average growth cone area (um²)
wild-type
sax-3(ky123)
unc-5(e152)
unc-5(e152); sax-3(ky123)
N ≥ 50
*p < 0.001
compared to
wild-type and sax-3
B
n.s.
Average filopodial length (um)
wild-type
sax-3(ky123)
unc-5(e152)
unc-5(e152); sax-3(ky123)
N ≥ 60
*p < 0.001
compared to
wild-type and sax-3
C
wild-type
D
sax-3(ky123)
E
unc-5(e152)
F
unc-5(e152);
sax-3(ky123)

Figure 6.5 VD growth cone over-protrusive phenotype of *unc-5* are not suppressed by *sax-3* mutation. (A,B) Quantification of VD growth cone filopodial length and growth cone area in wild-type and mutant animals. (A) Average filopodial length, in µm. (B) Growth cone area in μm^2. Error bars represent 2x standard error of the mean. Single asterisks (*) indicate the significant difference between wild-type and the mutant phenotype ($p < 0.001$) determined by two-sided *t*-test with unequal variance. n.s., not significant. **(C-F)** Fluorescence micrographs of VD growth cones; (C) A wild-type VD growth cone. (D) *sax-3(ky123*) growth cone. (E) *unc-5(e152)* growth cone showing increased filopodial protrusion in the form of longer filopodia. (F) *unc-5(e152); sax-3(ky123)* growth cone. Arrows indicate representative filopodia. Scale bar: 5µm.

Figure 6.6

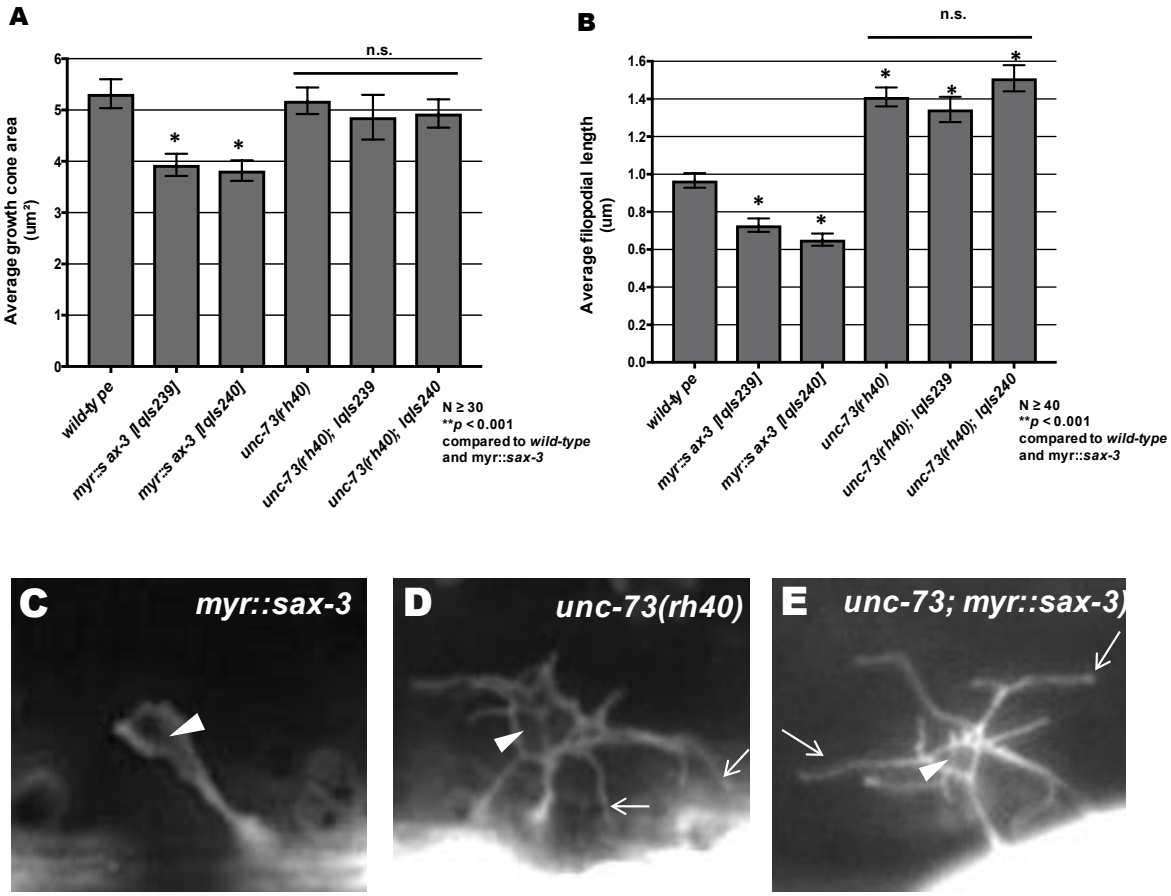
A
n.s.
Average growth cone area (um²)
wild-ty pe
myr::s ax-3 [lqls239]
myr::s ax-3 [lqls240]
unc-73(rh40)
unc-73(rh40); lqls239
unc-73(rh40); lqls240
N ≥ 30
**p < 0.001
compared to wild-type
and myr::sax-3
B
n.s.
Average filopodial length (um)
wild-ty pe
myr::s ax-3 [lqls239]
myr::s ax-3 [lqls240]
unc-73(rh40)
unc-73(rh40); lqls239
unc-73(rh40); lqls240
N ≥ 40
**p < 0.001
compared to wild-type
and myr::sax-3
C
myr::sax-3
D
unc-73(rh40)
E
unc-73; myr::sax-3)

Figure 6.6 UNC-73 is required for activated MYR::SAX-3 inhibition of growth cone protrusion (A,B) Quantification of VD growth cone filopodial length and growth cone area in wild-type and mutant animals. (A) Average filopodial length, in μm. (B) Growth cone area in μm^2. Error bars represent 2x standard error of the mean. Single asterisks (*) indicate the significant difference between wild-type and the mutant phenotype ($p < 0.001$) determined by two-sided *t*-test with unequal variance. n.s., not significant. **(C-E)** Fluorescence micrographs of VD growth cones; (C) *myr::sax-3* VD growth cone. (D) *unc-73(rh40)* growth cone and (E) *unc-73(rh40); myr::sax-3* growth cone showing increased filopodial protrusion in the form of longer filopodia. Scale bar: 5μm.

Chapter VII

Concluding remarks

7.1 Concluding remarks:

To date, the vast majority of our understanding on the roles of guidance cues, their receptors and the signalling mechanisms they employ to regulate axon pathfinding come from experiments performed post-developmentally at an end-point stage analysis, or on growth cones from cultured neurons growing *in vitro*. While *in vivo* end-point analyses have provided a great deal of information and advanced the field significantly, the understanding on how these molecules control cone behaviour and dynamics during outgrowth is not well understood. In contrast, *invitro* growth cone experiments overcome this limitation, but the possibility that this artificial environment would be significantly different than the environment that a growth cone encounters *in vivo* in an organism is evident.

To try and overcome these limitations, we used the *C. elegans* VD/DD motorneurons as an *in vivo* model system. In this dissertation we specifically examine the cytoskeletal mechanisms by which the guidance cue UNC-6/Netrin and its receptors UNC-40 and UNC-5 mediate inhibition of growth cone protrusion and how these molecules affect the cytoskeletal organization of the growth cone to promote directional axon outgrowth.

Chapter II revealed new roles for the *C. elegans* MICAL-like flavin monooxygenase (FMO) and EHBP-1genes downstream of UNC-6/Netrin signalling in growth cone protrusion and axon repulsion. We demonstrate that *fmo-1, fmo-4, fmo-5* and *ehbp-1*were cell-autonomously required for VD/DD axon guidance and that *fmo-1, fmo-4* and *fmo-5* could genetically interact with *unc-40*

and *unc-5* in VD/DD axon pathfinding. We also find that *fmo-1, fmo-4* and *fmo-5* were required to inhibit growth cone filopodial protrusions as mutations in these genes lead to longer VD growth cone filopodial protrusions and transgenic expression of wild-type FMO-5 resulted in growth cones with marked decreased in area and filopodial protrusions. In *Drosophila*, MICAL has been shown to directly oxidize cysteine residues in F-actin, leading to actin depolymerization and growth collapse (Hung et al., 2011; Hung et al., 2013; Hung and Terman, 2011). We speculate that the FMOs may act by a similar mechanism to limit growth cone protrusion.

The role of EHBP-1 in repulsive axon guidance and growth cone protrusion is rather complex. Though we find that *ehbp-1* is required for VD axon guidance, it did not affect growth cone morphology. We think that in certain instances such as in axon guidance, the FMOs might require the CH domain provided by EHBP-1 or that in some cases the CH domain is not required and the FMO domain can act alone. This differential mechanism will be interesting to tease apart in future studies. Our work has shown that the FMOs and EHBP-1 function downstream of the netrin receptors UNC-40 and UNC-5 and the Rac GTPases CED-10 and MIG-2 and can interact with UNC-33/CRMP in inhibition of growth cone protrusion. How the FMOs regulate UNC-33/CRMP and if they cause F-actin depolymerization is still unclear. Future studies may be able to decipher these mechanisms mediated by the *fmo* genes in inhibiting growth cone protrusion.

In chapter III, we describe distinct mechanisms by which UNC-6/Netrin can regulate growth cone protrusion. These roles were identified by analyzing the F-actin and MT+-end (EBP-2::GFP) distribution in mutant VD growth cones. We show that UNC-6 and UNC-5 inhibit protrusion by preventing F-actin accumulation in the ventral and lateral regions of the growth cone to restrict filopodial protrusions to the dorsal leading-edge, as well as by preventing MT+-ends from entering the growth cone periphery. This role possibly involves the cytoskeletal interacting protein UNC-33, as *unc-33* mutants also abolished dorsal F-actin polarity and increased MT+-end accumulation in the growth cone similar to *unc-5*. We speculate that UNC-33 may be involved in maintaining MT attachment to actin, thus restricting MTs from entering the growth cone to control protrusion. We further characterize a role for UNC-40 and the Rac GTPases in stimulation of protrusion at the dorsal leading-edge of the growth cone, based on the establishment of this polarity via UNC-5. Thus, we demonstrate a novel mechanism by which UNC-6/Netrin controls growth cone protrusion *in vivo* in directed axon outgrowth; by polarizing the growth cone to restrict protrusions to the leading-edge and then by regulating the extent of protrusions. Our work represents a shift from the previously proposed chemoaffinity model of Netrin-based axon guidance (Tessier-Lavigne and Goodman, 1996), where growth cones follow gradients of Netrin and are either attracted or repelled, but suggests a more contact-dependent interaction with cells expressing Netrin is important for mediating proper outgrowth of a developing axon. How UNC-6 mediates these polarized protrusive activities in the growth cone and how are they maintained as

the growth cone extends away from the source of UNC-6/Netrin is intriguing and might involve the asymmetric localization of cytoskeletal signaling and cytoskeletal interacting molecules in the growth cone or then the cooperation of other guidance systems with UNC-6/Netrin.

In chapter IV we characterize the roles of *rho-1/RhoA* and *rhgf-1/PDZRhoGEF* in inhibition of growth cone protrusion and restricting MT+-end entry into the VD growth cone in UNC-6/Netrin mediated signaling. Our analysis determined that *rho-1* was required to limit the amount of growth cone filopodial protrusions possibly by excluding MT entry in to the growth. *In vitro* cell motility studies have shown that RhoA can regulate both the microtubule and actin cytoskeleton (Wittmann and Waterman-Storer, 2001). RhoA has been shown to regulate formation of contractile actin structures such as stress fibers and promote stabilization of microtubules (Cook et al., 1998; Etienne-Manneville and Hall, 2002) through actomyosin contraction. One of the principal targets of RhoA activity is RhoA kinase, which activates contractility by phosphorylating the regulatory myosin light chain. This heightened myosin II activity may increase actin retrograde flow preventing MTs from entering the growth cone periphery, thereby reducing leading edge protrusion resulting in growth cone collapse and retraction (Gallo, 2004; Zhang et al., 2003). We speculate that loss of *rho-1* in the VD neurons prevents ROCK and non-muscle myosin activation thus leading to decreased actin retrograde flow, increased protrusion and a higher number of MTs entering the periphery of the growth cone.

We further find that RHO-1 regulates growth cone protrusion and MT entry downstream of its guanine nucleotide exchange factor RHGF-1 and possibly the UNC-40-UNC-5 Netrin receptor complex. In *C.elegans* RHGF-1 has been shown to normally be associated with microtubules (CHEN *et al.* 2014). We suspect that RHGF-1 regulates MT+ -entry and further growth cone protrusion by associating with tips of growing MTs and regulating myosin II dynamics via RHO-1 and ROCK. Our work validates the importance of these genes in affecting the MT cytoskeleton and growth cone outgrowth *in vivo.* Studies aimed at determining where RHGF-1 is localized and which domains of RHGF-1 are required for its interaction with MT+-ends are ongoing and are aimed at determining the mechanism by which RHGF-1 functions in this process.

In chapter V, we try to find a causal link between MT organization and growth cone morphology. Missense mutations in *C. elegans* tubulin genes result in altered MT stability either by destabilization of MTs or by the formation of hyperstable MTs (Zheng et al., 2017). We find that these single amino acid changes in the *tba-1* and *tbb-1* genes directly affected VD growth cone morphology and axon guidance, indicating the importance of these genes in neuronal morphogenesis. Based on the amino acids altered at specific locations such as a Pro- 243 to a Ser, Glu-97 to Lys and Gly-414 to Arg, caused shorter or no filopodial protrusions along with a smaller growth cone area. We speculate that these mutations likely act in a dominant-negative manner and terminate MT polymerization and induce instability possibly by disrupting the stacking of tubulin dimers or preventing microtubule associated proteins (MAPs) to bind to the

tubulin dimers. Mutations that are likely to form hyperstable MTs, including Pro-220 to Ser and Val-323 to Ile displayed varying phenotypes, where some growth cones produced significantly longer filopodial protrusions and some exhibited no change as compared to wild-type. One possible explanation is the recessive nature of these mutations or then possibly redundancy in the tubulin genes. Further studies involving several other mutations that could form hyperstable MTs may enable us to gain better insight into how they affect growth cone morphology. How TBA-1 and TBB-1 affect MT distribution in the growth cone is still unclear. We initially suspected that tubulin mutations that caused smaller growth cones would have fewer MT+-ends, however, our results involving the *tba-1(G414R)* mutation says otherwise. We suspect this may be due to altered interactions with MAPs and specific motor proteins such as myosin, which could further disrupt the retrograde flow of actin causing MTs to accumulate in the growth cone.

Our work so far has identified several cytoskeletal signaling mechanisms by which UNC-6/Netrin mediates growth cone inhibition in repulsive axon guidance. However, there are several other guidance cues known to be involved in axon guidance. We were interested in understanding how UNC-6/Netrin might act with other guidance cues to polarize growth cone protrusion resulting in directed migration. In chapter VI, we characterize the role of the guidance receptor SAX-3/Robo in VD/DD axon guidance and growth cone protrusion. We provide evidence that *sax-3* is required for the guidance of dorsally-directed VD/DD axons independent of the guidance cue SLT-1/Slit. Further analysis in the

VD growth cones showed that *sax-3* is normally required to inhibit growth cone filopodial protrusions possibly through the Rac GEF UNC-73/Trio, as well as maintain the polarity of filopodial protrusions towards the dorsal leading-edge of the growth cone. Previous work has implicated Slit/Robo signaling in ventral guidance of axons through repulsion (Hao et al., 2001; Pappu and Zipursky, 2010). The SLT-1 independent role of SAX-3 we describe suggests that SAX-3 mediates dorsal guidance through another guidance cue, possibly UNC-6/Netrin. Previous studies have placed the Rac GEF UNC-73 downstream of the UNC-40-UNC-5 receptor complex to inhibit growth cone protrusion (Norris et al., 2014). We think that SAX-3 may act as co-receptor for UNC-40/DCC to mediate repulsion of VD growth cones and does so upstream of UNC-73 and the Rac GTPases. How SAX-3 may interact with UNC-40 and UNC-5 or if it functions through UNC-6/Netrin or possibly another guidance cue are yet to be determined. This study should provide valuable information on how different guidance molecules cooperate with one another to sculpt the growth cone during axon outgrowth *in vivo*.

Together, the results detailed above highlight new roles and characterizes new mechanisms by which UNC-6/Netrin and its receptors UNC-40 and UNC-5 control growth cone protrusion and polarity during outgrowth. The genes that we have studied are for the most part well-characterized guidance molecules, cytoskeletal signaling or interacting molecules, but little was known about how these genes affect the development of the growth cone *in vivo*. We have thus elucidated the important growth-cone shaping roles of many genes and provide

groundwork for studying many other genes required in regulating growth cone protrusion and axon pathfinding.

References.

Alabed, Y.Z., Pool, M., Ong Tone, S., Fournier, A.E., 2007. Identification of CRMP4 as a convergent regulator of axon outgrowth inhibition. The Journal of neuroscience : the official journal of the Society for Neuroscience 27, 1702-1711.
Alam, T., Maruyama, H., Li, C., Pastuhov, S.I., Nix, P., Bastiani, M., Hisamoto, N., Matsumoto, K., 2016. Axotomy-induced HIF-serotonin signalling axis promotes axon regeneration in C. elegans. Nat Commun 7, 10388.
Arimura, N., Inagaki, N., Chihara, K., Menager, C., Nakamura, N., Amano, M., Iwamatsu, A., Goshima, Y., Kaibuchi, K., 2000. Phosphorylation of collapsin response mediator protein-2 by Rho-kinase. Evidence for two separate signaling pathways for growth cone collapse. J Biol Chem 275, 23973-23980.
Arimura, N., Kaibuchi, K., 2007. Neuronal polarity: from extracellular signals to intracellular mechanisms. Nat Rev Neurosci 8, 194-205.
Arimura, N., Menager, C., Kawano, Y., Yoshimura, T., Kawabata, S., Hattori, A., Fukata, Y., Amano, M., Goshima, Y., Inagaki, M., Morone, N., Usukura, J., Kaibuchi, K., 2005. Phosphorylation by Rho kinase regulates CRMP-2 activity in growth cones. Mol Cell Biol 25, 9973-9984.
Asakura, T., Ogura, K., Goshima, Y., 2007. UNC-6 expression by the vulval precursor cells of Caenorhabditis elegans is required for the complex axon guidance of the HSN neurons. Dev Biol 304, 800-810.
Ayoob, J.C., Terman, J.R., Kolodkin, A.L., 2006. Drosophila Plexin B is a Sema-2a receptor required for axon guidance. Development 133, 2125-2135.
Bahi-Buisson, N., Poirier, K., Fourniol, F., Saillour, Y., Valence, S., Lebrun, N., Hully, M., Bianco, C.F., Boddaert, N., Elie, C., Lascelles, K., Souville, I., Consortium, L.I.-T., Beldjord, C., Chelly, J., 2014. The wide spectrum of tubulinopathies: what are the key features for the diagnosis? Brain 137, 1676-1700.
Baran, R., Castelblanco, L., Tang, G., Shapiro, I., Goncharov, A., Jin, Y., 2010. Motor neuron synapse and axon defects in a C. elegans alpha-tubulin mutant. PLoS One 5, e9655.
Bateman, J., Shu, H., Van Vactor, D., 2000. The guanine nucleotide exchange factor trio mediates axonal development in the Drosophila embryo. Neuron 26, 93-106.
Bear, J.E., Krause, M., Gertler, F.B., 2001. Regulating cellular actin assembly. Curr Opin Cell Biol 13, 158-166.
Bernadskaya, Y.Y., Wallace, A., Nguyen, J., Mohler, W.A., Soto, M.C., 2012. UNC-40/DCC, SAX-3/Robo, and VAB-1/Eph polarize F-actin during embryonic morphogenesis by regulating the WAVE/SCAR actin nucleation complex. PLoS Genet 8, e1002863.
Beuchle, D., Schwarz, H., Langegger, M., Koch, I., Aberle, H., 2007. Drosophila MICAL regulates myofilament organization and synaptic structure. Mech Dev 124, 390-406.
Bosher, J.M., Hahn, B.S., Legouis, R., Sookhareea, S., Weimer, R.M., Gansmuller, A., Chisholm, A.D., Rose, A.M., Bessereau, J.L., Labouesse, M.,

2003. The Caenorhabditis elegans vab-10 spectraplakin isoforms protect the epidermis against internal and external forces. J Cell Biol 161, 757-768.
Brenner, S., 1974. The genetics of *Caenorhabditis elegans*. Genetics 77, 71-94.
Bringmann, H., Hyman, A.A., 2005. A cytokinesis furrow is positioned by two consecutive signals. Nature 436, 731-734.
Bron, R., Vermeren, M., Kokot, N., Andrews, W., Little, G.E., Mitchell, K.J., Cohen, J., 2007. Boundary cap cells constrain spinal motor neuron somal migration at motor exit points by a semaphorin-plexin mechanism. Neural Dev 2, 21.
Brose, K., Tessier-Lavigne, M., 2000. Slit proteins: key regulators of axon guidance, axonal branching, and cell migration. Curr Opin Neurobiol 10, 95-102.
Buck, K.B., Zheng, J.Q., 2002. Growth cone turning induced by direct local modification of microtubule dynamics. The Journal of neuroscience : the official journal of the Society for Neuroscience 22, 9358-9367.
Burnette, D.T., Schaefer, A.W., Ji, L., Danuser, G., Forscher, P., 2007. Filopodial actin bundles are not necessary for microtubule advance into the peripheral domain of Aplysia neuronal growth cones. Nat Cell Biol 9, 1360-1369.
Chakraborti, S., Natarajan, K., Curiel, J., Janke, C., Liu, J., 2016. The emerging role of the tubulin code: From the tubulin molecule to neuronal function and disease. Cytoskeleton (Hoboken) 73, 521-550.
Challacombe, J.F., Snow, D.M., Letourneau, P.C., 1996. Actin filament bundles are required for microtubule reorientation during growth cone turning to avoid an inhibitory guidance cue. J Cell Sci 109 (Pt 8), 2031-2040.
Chan, S.S., Zheng, H., Su, M.W., Wilk, R., Killeen, M.T., Hedgecock, E.M., Culotti, J.G., 1996. UNC-40, a C. elegans homolog of DCC (Deleted in Colorectal Cancer), is required in motile cells responding to UNC-6 netrin cues. Cell 87, 187-195.
Chen, C.H., Lee, A., Liao, C.P., Liu, Y.W., Pan, C.L., 2014. RHGF-1/PDZ-RhoGEF and retrograde DLK-1 signaling drive neuronal remodeling on microtubule disassembly. Proc Natl Acad Sci U S A 111, 16568-16573.
Chen, W., Lim, L., 1994. The Caenorhabditis elegans small GTP-binding protein RhoA is enriched in the nerve ring and sensory neurons during larval development. J Biol Chem 269, 32394-32404.
Coles, C.H., Bradke, F., 2015. Coordinating neuronal actin-microtubule dynamics. Curr Biol 25, R677-691.
Conde, C., Caceres, A., 2009. Microtubule assembly, organization and dynamics in axons and dendrites. Nat Rev Neurosci 10, 319-332.
Cook, T.A., Nagasaki, T., Gundersen, G.G., 1998. Rho guanosine triphosphatase mediates the selective stabilization of microtubules induced by lysophosphatidic acid. J Cell Biol 141, 175-185.
Craig, E.M., Van Goor, D., Forscher, P., Mogilner, A., 2012. Membrane tension, myosin force, and actin turnover maintain actin treadmill in the nerve growth cone. Biophys J 102, 1503-1513.
Culotti, J.G., Merz, D.C., 1998. DCC and netrins. Curr Opin Cell Biol 10, 609-613.

Davenport, R.W., Dou, P., Rehder, V., Kater, S.B., 1993. A sensory role for neuronal growth cone filopodia. Nature 361, 721-724.
deBakker, C.D., Haney, L.B., Kinchen, J.M., Grimsley, C., Lu, M., Klingele, D., Hsu, P.K., Chou, B.K., Cheng, L.C., Blangy, A., Sondek, J., Hengartner, M.O., Wu, Y.C., Ravichandran, K.S., 2004. Phagocytosis of apoptotic cells is regulated by a UNC-73/TRIO-MIG-2/RhoG signaling module and armadillo repeats of CED-12/ELMO. Curr Biol 14, 2208-2216.
Demarco, R.S., Struckhoff, E.C., Lundquist, E.A., 2012. The Rac GTP exchange factor TIAM-1 acts with CDC-42 and the guidance receptor UNC-40/DCC in neuronal protrusion and axon guidance. PLoS Genet 8, e1002665.
Dent, E.W., Gertler, F.B., 2003. Cytoskeletal dynamics and transport in growth cone motility and axon guidance. Neuron 40, 209-227.
Dent, E.W., Gupton, S.L., Gertler, F.B., 2011. The growth cone cytoskeleton in axon outgrowth and guidance. Cold Spring Harb Perspect Biol 3.
Dent, E.W., Kalil, K., 2001. Axon branching requires interactions between dynamic microtubules and actin filaments. The Journal of neuroscience : the official journal of the Society for Neuroscience 21, 9757-9769.
Desai, A., Mitchison, T.J., 1997. Microtubule polymerization dynamics. Annu Rev Cell Dev Biol 13, 83-117.
Dominici, C., Moreno-Bravo, J.A., Puiggros, S.R., Rappeneau, Q., Rama, N., Vieugue, P., Bernet, A., Mehlen, P., Chedotal, A., 2017. Floor-plate-derived netrin-1 is dispensable for commissural axon guidance. Nature 545, 350-354.
Esposito, G., Di Schiavi, E., Bergamasco, C., Bazzicalupo, P., 2007. Efficient and cell specific knock-down of gene function in targeted C. elegans neurons. Gene 395, 170-176.
Etienne-Manneville, S., Hall, A., 2002. Rho GTPases in cell biology. Nature 420, 629-635.
Evans, T.A., Bashaw, G.J., 2010. Functional diversity of Robo receptor immunoglobulin domains promotes distinct axon guidance decisions. Curr Biol 20, 567-572.
Flanagan, J.G., Van Vactor, D., 1998. Through the looking glass: axon guidance at the midline choice point. Cell 92, 429-432.
Forscher, P., Smith, S.J., 1988. Actions of cytochalasins on the organization of actin filaments and microtubules in a neuronal growth cone. J Cell Biol 107, 1505-1516.
Fox, R.M., Von Stetina, S.E., Barlow, S.J., Shaffer, C., Olszewski, K.L., Moore, J.H., Dupuy, D., Vidal, M., Miller, D.M., 3rd, 2005. A gene expression fingerprint of C. elegans embryonic motor neurons. BMC Genomics 6, 42.
Fukata, Y., Itoh, T.J., Kimura, T., Menager, C., Nishimura, T., Shiromizu, T., Watanabe, H., Inagaki, N., Iwamatsu, A., Hotani, H., Kaibuchi, K., 2002. CRMP-2 binds to tubulin heterodimers to promote microtubule assembly. Nature cell biology 4, 583-591.
Fukuhara, S., Chikumi, H., Gutkind, J.S., 2000. Leukemia-associated Rho guanine nucleotide exchange factor (LARG) links heterotrimeric G proteins of the G(12) family to Rho. FEBS Lett 485, 183-188.

Fukuhara, S., Murga, C., Zohar, M., Igishi, T., Gutkind, J.S., 1999. A novel PDZ domain containing guanine nucleotide exchange factor links heterotrimeric G proteins to Rho. J Biol Chem 274, 5868-5879.
Gallo, G., 2004. Myosin II activity is required for severing-induced axon retraction in vitro. Exp Neurol 189, 112-121.
Gallo, G., Letourneau, P.C., 2004. Regulation of growth cone actin filaments by guidance cues. J Neurobiol 58, 92-102.
Gilleard, J.S., Barry, J.D., Johnstone, I.L., 1997. cis regulatory requirements for hypodermal cell-specific expression of the Caenorhabditis elegans cuticle collagen gene dpy-7. Molecular and cellular biology 17, 2301-2311.
Giridharan, S.S., Cai, B., Vitale, N., Naslavsky, N., Caplan, S., 2013. Cooperation of MICAL-L1, syndapin2, and phosphatidic acid in tubular recycling endosome biogenesis. Molecular biology of the cell 24, 1776-1790, S1771-1715.
Giridharan, S.S., Caplan, S., 2014. MICAL-family proteins: Complex regulators of the actin cytoskeleton. Antioxid Redox Signal 20, 2059-2073.
Giridharan, S.S., Rohn, J.L., Naslavsky, N., Caplan, S., 2012. Differential regulation of actin microfilaments by human MICAL proteins. J Cell Sci 125, 614-624.
Gitai, Z., Yu, T.W., Lundquist, E.A., Tessier-Lavigne, M., Bargmann, C.I., 2003. The netrin receptor UNC-40/DCC stimulates axon attraction and outgrowth through enabled and, in parallel, Rac and UNC-115/AbLIM. Neuron 37, 53-65.
Goldberg, D.J., Burmeister, D.W., 1986. Stages in axon formation: observations of growth of Aplysia axons in culture using video-enhanced contrast-differential interference contrast microscopy. J Cell Biol 103, 1921-1931.
Goodhill, G.J., Faville, R.A., Sutherland, D.J., Bicknell, B.A., Thompson, A.W., Pujic, Z., Sun, B., Kita, E.M., Scott, E.K., 2015. The dynamics of growth cone morphology. BMC Biol 13, 10.
Goshima, Y., Nakamura, F., Strittmatter, P., Strittmatter, S.M., 1995. Collapsin-induced growth cone collapse mediated by an intracellular protein related to UNC-33. Nature 376, 509-514.
Govek, E.E., Newey, S.E., Van Aelst, L., 2005. The role of the Rho GTPases in neuronal development. Genes Dev 19, 1-49.
Guan, K.L., Rao, Y., 2003. Signalling mechanisms mediating neuronal responses to guidance cues. Nat Rev Neurosci 4, 941-956.
Gujar, M.R., Stricker, A.M., Lundquist, E.A., 2017. Flavin monooxygenases regulate Caenorhabditis elegans axon guidance and growth cone protrusion with UNC-6/Netrin signaling and Rac GTPases. PLoS Genet 13, e1006998.
Hall, A., 2005. Rho GTPases and the control of cell behaviour. Biochem Soc Trans 33, 891-895.
Hall, C., Brown, M., Jacobs, T., Ferrari, G., Cann, N., Teo, M., Monfries, C., Lim, L., 2001. Collapsin response mediator protein switches RhoA and Rac1 morphology in N1E-115 neuroblastoma cells and is regulated by Rho kinase. J Biol Chem 276, 43482-43486.
Hao, J.C., Yu, T.W., Fujisawa, K., Culotti, J.G., Gengyo-Ando, K., Mitani, S., Moulder, G., Barstead, R., Tessier-Lavigne, M., Bargmann, C.I., 2001. C.

elegans slit acts in midline, dorsal-ventral, and anterior-posterior guidance via the SAX-3/Robo receptor. Neuron 32, 25-38.
Hedgecock, E.M., Culotti, J.G., Hall, D.H., 1990a. The unc-5, unc-6, and unc-40 genes guide circumferential migrations of pioneer axons and mesodermal cells on the epidermis in C. elegans. Neuron 4, 61-85.
Hedgecock, E.M., Culotti, J.G., Hall, D.H., 1990b. The *unc-5, unc-6,* and *unc-40* genes guide circumferential migrations of pioneer axons and mesodermal cells on the epidermis in *C. elegans.* Neuron 4, 61-85.
Hedgecock, E.M., Culotti, J.G., Hall, D.H., Stern, B.D., 1987. Genetics of cell and axon migrations in Caenorhabditis elegans. Development 100, 365-382.
Higurashi, M., Iketani, M., Takei, K., Yamashita, N., Aoki, R., Kawahara, N., Goshima, Y., 2012. Localized role of CRMP1 and CRMP2 in neurite outgrowth and growth cone steering. Developmental neurobiology 72, 1528-1540.
Hiley, E., McMullan, R., Nurrish, S.J., 2006. The Galpha12-RGS RhoGEF-RhoA signalling pathway regulates neurotransmitter release in C. elegans. EMBO J 25, 5884-5895.
Hirani, N., Westenberg, M., Seed, P.T., Petalcorin, M.I., Dolphin, C.T., 2016. C. elegans flavin-containing monooxygenase-4 is essential for osmoregulation in hypotonic stress. Biol Open 5, 668.
Hong, K., Hinck, L., Nishiyama, M., Poo, M.M., Tessier-Lavigne, M., Stein, E., 1999. A ligand-gated association between cytoplasmic domains of UNC5 and DCC family receptors converts netrin-induced growth cone attraction to repulsion. Cell 97, 927-941.
Hu, S., Pawson, T., Steven, R.M., 2011. UNC-73/trio RhoGEF-2 activity modulates Caenorhabditis elegans motility through changes in neurotransmitter signaling upstream of the GSA-1/Galphas pathway. Genetics 189, 137-151.
Huang, H., Yang, T., Shao, Q., Majumder, T., Mell, K., Liu, G., 2018. Human TUBB3 Mutations Disrupt Netrin Attractive Signaling. Neuroscience 374, 155-171.
Huang, X., Cheng, H.J., Tessier-Lavigne, M., Jin, Y., 2002. MAX-1, a novel PH/MyTH4/FERM domain cytoplasmic protein implicated in netrin-mediated axon repulsion. Neuron 34, 563-576.
Hung, R.J., Pak, C.W., Terman, J.R., 2011. Direct redox regulation of F-actin assembly and disassembly by Mical. Science 334, 1710-1713.
Hung, R.J., Spaeth, C.S., Yesilyurt, H.G., Terman, J.R., 2013. SelR reverses Mical-mediated oxidation of actin to regulate F-actin dynamics. Nature cell biology 15, 1445-1454.
Hung, R.J., Terman, J.R., 2011. Extracellular inhibitors, repellents, and semaphorin/plexin/MICAL-mediated actin filament disassembly. Cytoskeleton (Hoboken) 68, 415-433.
Hung, R.J., Yazdani, U., Yoon, J., Wu, H., Yang, T., Gupta, N., Huang, Z., van Berkel, W.J., Terman, J.R., 2010. Mical links semaphorins to F-actin disassembly. Nature 463, 823-827.
Ishii, N., Wadsworth, W.G., Stern, B.D., Culotti, J.G., Hedgecock, E.M., 1992. UNC-6, a laminin-related protein, guides cell and pioneer axon migrations in C. elegans. Neuron 9, 873-881.

Jaffe, A.B., Hall, A., 2005. Rho GTPases: biochemistry and biology. Annu Rev Cell Dev Biol 21, 247-269.
Jaglin, X.H., Poirier, K., Saillour, Y., Buhler, E., Tian, G., Bahi-Buisson, N., Fallet-Bianco, C., Phan-Dinh-Tuy, F., Kong, X.P., Bomont, P., Castelnau-Ptakhine, L., Odent, S., Loget, P., Kossorotoff, M., Snoeck, I., Plessis, G., Parent, P., Beldjord, C., Cardoso, C., Represa, A., Flint, J., Keays, D.A., Cowan, N.J., Chelly, J., 2009. Mutations in the beta-tubulin gene TUBB2B result in asymmetrical polymicrogyria. Nat Genet 41, 746-752.
Jantsch-Plunger, V., Gonczy, P., Romano, A., Schnabel, H., Hamill, D., Schnabel, R., Hyman, A.A., Glotzer, M., 2000. CYK-4: A Rho family gtpase activating protein (GAP) required for central spindle formation and cytokinesis. J Cell Biol 149, 1391-1404.
Jin, Y., Jorgensen, E., Hartwieg, E., Horvitz, H.R., 1999. The Caenorhabditis elegans gene unc-25 encodes glutamic acid decarboxylase and is required for synaptic transmission but not synaptic development. J Neurosci 19, 539-548.
Kaibuchi, K., Kuroda, S., Amano, M., 1999. Regulation of the cytoskeleton and cell adhesion by the Rho family GTPases in mammalian cells. Annu Rev Biochem 68, 459-486.
Kaletsky, R., Lakhina, V., Arey, R., Williams, A., Landis, J., Ashraf, J., Murphy, C.T., 2016. The C. elegans adult neuronal IIS/FOXO transcriptome reveals adult phenotype regulators. Nature 529, 92-96.
Kalil, K., Dent, E.W., 2005. Touch and go: guidance cues signal to the growth cone cytoskeleton. Curr Opin Neurobiol 15, 521-526.
Kamath, R.S., Fraser, A.G., Dong, Y., Poulin, G., Durbin, R., Gotta, M., Kanapin, A., Le Bot, N., Moreno, S., Sohrmann, M., Welchman, D.P., Zipperlen, P., Ahringer, J., 2003. Systematic functional analysis of the Caenorhabditis elegans genome using RNAi. Nature 421, 231-237.
Kawano, Y., Yoshimura, T., Tsuboi, D., Kawabata, S., Kaneko-Kawano, T., Shirataki, H., Takenawa, T., Kaibuchi, K., 2005. CRMP-2 is involved in kinesin-1-dependent transport of the Sra-1/WAVE1 complex and axon formation. Mol Cell Biol 25, 9920-9935.
Kennedy, T.E., 2000. Cellular mechanisms of netrin function: long-range and short-range actions. Biochem Cell Biol 78, 569-575.
Khazaei, M.R., Girouard, M.P., Alchini, R., Ong Tone, S., Shimada, T., Bechstedt, S., Cowan, M., Guillet, D., Wiseman, P.W., Brouhard, G., Cloutier, J.F., Fournier, A.E., 2014. Collapsin response mediator protein 4 regulates growth cone dynamics through the actin and microtubule cytoskeleton. J Biol Chem 289, 30133-30143.
Kidd, T., Brose, K., Mitchell, K.J., Fetter, R.D., Tessier-Lavigne, M., Goodman, C.S., Tear, G., 1998. Roundabout controls axon crossing of the CNS midline and defines a novel subfamily of evolutionarily conserved guidance receptors. Cell 92, 205-215.
Killeen, M., Tong, J., Krizus, A., Steven, R., Scott, I., Pawson, T., Culotti, J., 2002. UNC-5 function requires phosphorylation of cytoplasmic tyrosine 482, but its UNC-40-independent functions also require a region between the ZU-5 and death domains. Developmental biology 251, 348-366.

Killeen, M.T., Sybingco, S.S., 2008. Netrin, Slit and Wnt receptors allow axons to choose the axis of migration. Dev Biol 323, 143-151.
Kimura, T., Watanabe, H., Iwamatsu, A., Kaibuchi, K., 2005. Tubulin and CRMP-2 complex is transported via Kinesin-1. J Neurochem 93, 1371-1382.
Kirilly, D., Gu, Y., Huang, Y., Wu, Z., Bashirullah, A., Low, B.C., Kolodkin, A.L., Wang, H., Yu, F., 2009. A genetic pathway composed of Sox14 and Mical governs severing of dendrites during pruning. Nat Neurosci 12, 1497-1505.
Knobel, K.M., Jorgensen, E.M., Bastiani, M.J., 1999. Growth cones stall and collapse during axon outgrowth in Caenorhabditis elegans. Development 126, 4489-4498.
Kozlowski, C., Srayko, M., Nedelec, F., 2007. Cortical microtubule contacts position the spindle in C. elegans embryos. Cell 129, 499-510.
Kulkarni, G., Xu, Z., Mohamed, A.M., Li, H., Tang, X., Limerick, G., Wadsworth, W.G., 2013. Experimental evidence for UNC-6 (netrin) axon guidance by stochastic fluctuations of intracellular UNC-40 (DCC) outgrowth activity. Biology open 2, 1300-1312.
Kurup, N., Yan, D., Goncharov, A., Jin, Y., 2015. Dynamic microtubules drive circuit rewiring in the absence of neurite remodeling. Curr Biol 25, 1594-1605.
Lai Wing Sun, K., Correia, J.P., Kennedy, T.E., 2011. Netrins: versatile extracellular cues with diverse functions. Development 138, 2153-2169.
Lee, A.C., Suter, D.M., 2008. Quantitative analysis of microtubule dynamics during adhesion-mediated growth cone guidance. Developmental neurobiology 68, 1363-1377.
Lee, J., Li, W., Guan, K.L., 2005. SRC-1 mediates UNC-5 signaling in Caenorhabditis elegans. Molecular and cellular biology 25, 6485-6495.
Leonardo, E.D., Hinck, L., Masu, M., Keino-Masu, K., Ackerman, S.L., Tessier-Lavigne, M., 1997. Vertebrate homologues of C. elegans UNC-5 are candidate netrin receptors. Nature 386, 833-838.
Leung-Hagesteijn, C., Spence, A.M., Stern, B.D., Zhou, Y., Su, M.W., Hedgecock, E.M., Culotti, J.G., 1992. UNC-5, a transmembrane protein with immunoglobulin and thrombospondin type 1 domains, guides cell and pioneer axon migrations in C. elegans. Cell 71, 289-299.
Leung-Hagesteijn, C., Spence, A.M., Stern, B.D., Zhou, Y., Su, M.-W., Hedgecock, E.M., Culotti, J.G., 1992. UNC-5, a transmembrane protein with immunoglobulin and thrombospondin type I domains, guides cell and pioneer axon migrations. Cell 71, 289-299.
Levy-Strumpf, N., Culotti, J.G., 2014. Netrins and Wnts function redundantly to regulate antero-posterior and dorso-ventral guidance in C. elegans. PLoS Genet 10, e1004381.
Lewis, A.K., Bridgman, P.C., 1992. Nerve growth cone lamellipodia contain two populations of actin filaments that differ in organization and polarity. J Cell Biol 119, 1219-1243.
Li, H., Kulkarni, G., Wadsworth, W.G., 2008. RPM-1, a Caenorhabditis elegans protein that functions in presynaptic differentiation, negatively regulates axon outgrowth by controlling SAX-3/robo and UNC-5/UNC5 activity. The Journal of neuroscience : the official journal of the Society for Neuroscience 28, 3595-3603.

Li, J., Pu, P., Le, W., 2013. The SAX-3 receptor stimulates axon outgrowth and the signal sequence and transmembrane domain are critical for SAX-3 membrane localization in the PDE neuron of C. elegans. PLoS One 8, e65658.
Limerick, G., Tang, X., Lee, W.S., Mohamed, A., Al-Aamiri, A., Wadsworth, W.G., 2018. A Statistically-Oriented Asymmetric Localization (SOAL) Model for Neuronal Outgrowth Patterning by Caenorhabditis elegans UNC-5 (UNC5) and UNC-40 (DCC) Netrin Receptors. Genetics 208, 245-272.
Lin, C.H., Forscher, P., 1995. Growth cone advance is inversely proportional to retrograde F-actin flow. Neuron 14, 763-771.
Lin, L., Tran, T., Hu, S., Cramer, T., Komuniecki, R., Steven, R.M., 2012. RHGF-2 is an essential Rho-1 specific RhoGEF that binds to the multi-PDZ domain scaffold protein MPZ-1 in Caenorhabditis elegans. PLoS One 7, e31499.
Liu, G., Dwyer, T., 2014. Microtubule dynamics in axon guidance. Neurosci Bull 30, 569-583.
Lowery, L.A., Van Vactor, D., 2009. The trip of the tip: understanding the growth cone machinery. Nat Rev Mol Cell Biol 10, 332-343.
Lundquist, E.A., 2003. Rac proteins and the control of axon development. Curr Opin Neurobiol 13, 384-390.
Lundquist, E.A., Reddien, P.W., Hartwieg, E., Horvitz, H.R., Bargmann, C.I., 2001. Three C. elegans Rac proteins and several alternative Rac regulators control axon guidance, cell migration and apoptotic cell phagocytosis. Development 128, 4475-4488.
Luo, L., 2002. Actin cytoskeleton regulation in neuronal morphogenesis and structural plasticity. Annu Rev Cell Dev Biol 18, 601-635.
Luo, L., Liao, Y.J., Jan, L.Y., Jan, Y.N., 1994. Distinct morphogenetic functions of similar small GTPases: Drosophila Drac1 is involved in axonal outgrowth and myoblast fusion. Genes Dev 8, 1787-1802.
MacNeil, L.T., Hardy, W.R., Pawson, T., Wrana, J.L., Culotti, J.G., 2009. UNC-129 regulates the balance between UNC-40 dependent and independent UNC-5 signaling pathways. Nat Neurosci 12, 150-155.
Maniar, T.A., Kaplan, M., Wang, G.J., Shen, K., Wei, L., Shaw, J.E., Koushika, S.P., Bargmann, C.I., 2011. UNC-33 (CRMP) and ankyrin organize microtubules and localize kinesin to polarize axon-dendrite sorting. Nat Neurosci 15, 48-56.
Maniar, T.A., Kaplan, M., Wang, G.J., Shen, K., Wei, L., Shaw, J.E., Koushika, S.P., Bargmann, C.I., 2012. UNC-33 (CRMP) and ankyrin organize microtubules and localize kinesin to polarize axon-dendrite sorting. Nat Neurosci 15, 48-56.
McKay, S.J., Johnsen, R., Khattra, J., Asano, J., Baillie, D.L., Chan, S., Dube, N., Fang, L., Goszczynski, B., Ha, E., Halfnight, E., Hollebakken, R., Huang, P., Hung, K., Jensen, V., Jones, S.J., Kai, H., Li, D., Mah, A., Marra, M., McGhee, J., Newbury, R., Pouzyrev, A., Riddle, D.L., Sonnhammer, E., Tian, H., Tu, D., Tyson, J.R., Vatcher, G., Warner, A., Wong, K., Zhao, Z., Moerman, D.G., 2003. Gene expression profiling of cells, tissues, and developmental stages of the nematode C. elegans. Cold Spring Harb Symp Quant Biol 68, 159-169.
McMullan, R., Anderson, A., Nurrish, S., 2012. Behavioral and immune responses to infection require Galphaq- RhoA signaling in C. elegans. PLoS Pathog 8, e1002530.

McMullan, R., Hiley, E., Morrison, P., Nurrish, S.J., 2006. Rho is a presynaptic activator of neurotransmitter release at pre-existing synapses in C. elegans. Genes Dev 20, 65-76.
McMullan, R., Nurrish, S.J., 2011. The RHO-1 RhoGTPase modulates fertility and multiple behaviors in adult C. elegans. PLoS One 6, e17265.
Mello, C., Fire, A., 1995. DNA transformation. Methods Cell Biol 48, 451-482.
Merz, D.C., Culotti, J.G., 2000. Genetic analysis of growth cone migrations in Caenorhabditis elegans. J Neurobiol 44, 281-288.
Merz, D.C., Zheng, H., Killeen, M.T., Krizus, A., Culotti, J.G., 2001. Multiple signaling mechanisms of the UNC-6/netrin receptors UNC-5 and UNC-40/DCC in vivo. Genetics 158, 1071-1080.
Ming, G.L., Song, H.J., Berninger, B., Holt, C.E., Tessier-Lavigne, M., Poo, M.M., 1997. cAMP-dependent growth cone guidance by netrin-1. Neuron 19, 1225-1235.
Montell, D.J., 1999. The genetics of cell migration in Drosophila melanogaster and Caenorhabditis elegans development. Development 126, 3035-3046.
Moore, S.W., Tessier-Lavigne, M., Kennedy, T.E., 2007. Netrins and their receptors. Adv Exp Med Biol 621, 17-31.
Morinaka, A., Yamada, M., Itofusa, R., Funato, Y., Yoshimura, Y., Nakamura, F., Yoshimura, T., Kaibuchi, K., Goshima, Y., Hoshino, M., Kamiguchi, H., Miki, H., 2011. Thioredoxin mediates oxidation-dependent phosphorylation of CRMP2 and growth cone collapse. Sci Signal 4, ra26.
Morita, K., Hirono, K., Han, M., 2005. The Caenorhabditis elegans ect-2 RhoGEF gene regulates cytokinesis and migration of epidermal P cells. EMBO Rep 6, 1163-1168.
Mortimer, D., Fothergill, T., Pujic, Z., Richards, L.J., Goodhill, G.J., 2008. Growth cone chemotaxis. Trends Neurosci.
Motegi, F., Sugimoto, A., 2006. Sequential functioning of the ECT-2 RhoGEF, RHO-1 and CDC-42 establishes cell polarity in Caenorhabditis elegans embryos. Nat Cell Biol 8, 978-985.
Nadella, M., Bianchet, M.A., Gabelli, S.B., Barrila, J., Amzel, L.M., 2005. Structure and activity of the axon guidance protein MICAL. Proc Natl Acad Sci U S A 102, 16830-16835.
Norris, A.D., Dyer, J.O., Lundquist, E.A., 2009. The Arp2/3 complex, UNC-115/abLIM, and UNC-34/Enabled regulate axon guidance and growth cone filopodia formation in Caenorhabditis elegans. Neural Dev 4, 38.
Norris, A.D., Lundquist, E.A., 2011. UNC-6/netrin and its receptors UNC-5 and UNC-40/DCC modulate growth cone protrusion in vivo in C. elegans. Development 138, 4433-4442.
Norris, A.D., Sundararajan, L., Morgan, D.E., Roberts, Z.J., Lundquist, E.A., 2014. The UNC-6/Netrin receptors UNC-40/DCC and UNC-5 inhibit growth cone filopodial protrusion via UNC-73/Trio, Rac-like GTPases and UNC-33/CRMP. Development 141, 4395-4405.
Omotade, O.F., Pollitt, S.L., Zheng, J.Q., 2017. Actin-based growth cone motility and guidance. Mol Cell Neurosci.

Pak, C.W., Flynn, K.C., Bamburg, J.R., 2008. Actin-binding proteins take the reins in growth cones. Nat Rev Neurosci 9, 136-147.
Pappu, K.S., Zipursky, S.L., 2010. Axon guidance: repulsion and attraction in roundabout ways. Curr Biol 20, R400-402.
Pasterkamp, R.J., Dai, H.N., Terman, J.R., Wahlin, K.J., Kim, B., Bregman, B.S., Popovich, P.G., Kolodkin, A.L., 2006. MICAL flavoprotein monooxygenases: expression during neural development and following spinal cord injuries in the rat. Mol Cell Neurosci 31, 52-69.
Patel, F.B., Bernadskaya, Y.Y., Chen, E., Jobanputra, A., Pooladi, Z., Freeman, K.L., Gally, C., Mohler, W.A., Soto, M.C., 2008. The WAVE/SCAR complex promotes polarized cell movements and actin enrichment in epithelia during C. elegans embryogenesis. Dev Biol 324, 297-309.
Petalcorin, M.I., Joshua, G.W., Agapow, P.M., Dolphin, C.T., 2005. The fmo genes of Caenorhabditis elegans and C. briggsae: characterisation, gene expression and comparative genomic analysis. Gene 346, 83-96.
Petratos, S., Li, Q.X., George, A.J., Hou, X., Kerr, M.L., Unabia, S.E., Hatzinisiriou, I., Maksel, D., Aguilar, M.I., Small, D.H., 2008. The beta-amyloid protein of Alzheimer's disease increases neuronal CRMP-2 phosphorylation by a Rho-GTP mechanism. Brain 131, 90-108.
Qu, C., Dwyer, T., Shao, Q., Yang, T., Huang, H., Liu, G., 2013. Direct binding of TUBB3 with DCC couples netrin-1 signaling to intracellular microtubule dynamics in axon outgrowth and guidance. J Cell Sci 126, 3070-3081.
Rahajeng, J., Giridharan, S.S., Cai, B., Naslavsky, N., Caplan, S., 2012. MICAL-L1 is a tubular endosomal membrane hub that connects Rab35 and Arf6 with Rab8a. Traffic 13, 82-93.
Reiner, D.J., Lundquist, E.A., 2016. Small GTPases. WormBook, 1-99.
Ren, Y., Suter, D.M., 2016. Increase in Growth Cone Size Correlates with Decrease in Neurite Growth Rate. Neural Plast 2016, 3497901.
Rogers, S.L., Wiedemann, U., Hacker, U., Turck, C., Vale, R.D., 2004. Drosophila RhoGEF2 associates with microtubule plus ends in an EB1-dependent manner. Curr Biol 14, 1827-1833.
Rosslenbroich, V., Dai, L., Baader, S.L., Noegel, A.A., Gieselmann, V., Kappler, J., 2005. Collapsin response mediator protein-4 regulates F-actin bundling. Experimental cell research 310, 434-444.
Sabry, J.H., O'Connor, T.P., Evans, L., Toroian-Raymond, A., Kirschner, M., Bentley, D., 1991. Microtubule behavior during guidance of pioneer neuron growth cones in situ. J Cell Biol 115, 381-395.
Schaefer, A.W., Schoonderwoert, V.T., Ji, L., Mederios, N., Danuser, G., Forscher, P., 2008. Coordination of actin filament and microtubule dynamics during neurite outgrowth. Developmental cell 15, 146-162.
Schmidt, A., Hall, A., 2002. Guanine nucleotide exchange factors for Rho GTPases: turning on the switch. Genes Dev 16, 1587-1609.
Schmidt, E.F., Shim, S.O., Strittmatter, S.M., 2008. Release of MICAL autoinhibition by semaphorin-plexin signaling promotes interaction with collapsin response mediator protein. J Neurosci 28, 2287-2297.

Schonegg, S., Hyman, A.A., 2006. CDC-42 and RHO-1 coordinate acto-myosin contractility and PAR protein localization during polarity establishment in C. elegans embryos. Development 133, 3507-3516.
Serafini, T., Kennedy, T.E., Galko, M.J., Mirzayan, C., Jessell, T.M., Tessier-Lavigne, M., 1994. The netrins define a family of axon outgrowth-promoting proteins homologous to C. elegans UNC-6. Cell 78, 409-424.
Shakir, M.A., Gill, J.S., Lundquist, E.A., 2006. Interactions of UNC-34 Enabled with Rac GTPases and the NIK kinase MIG-15 in Caenorhabditis elegans axon pathfinding and neuronal migration. Genetics 172, 893-913.
Shakir, M.A., Jiang, K., Struckhoff, E.C., Demarco, R.S., Patel, F.B., Soto, M.C., Lundquist, E.A., 2008. The Arp2/3 Activators WAVE and WASP Have Distinct Genetic Interactions With Rac GTPases in Caenorhabditis elegans Axon Guidance. Genetics 179, 1957-1971.
Shao, Q., Yang, T., Huang, H., Alarmanazi, F., Liu, G., 2017. Uncoupling of UNC5C with Polymerized TUBB3 in Microtubules Mediates Netrin-1 Repulsion. The Journal of neuroscience : the official journal of the Society for Neuroscience 37, 5620-5633.
Sharma, M., Giridharan, S.S., Rahajeng, J., Naslavsky, N., Caplan, S., 2009. MICAL-L1 links EHD1 to tubular recycling endosomes and regulates receptor recycling. Molecular biology of the cell 20, 5181-5194.
Shekarabi, M., Kennedy, T.E., 2002. The netrin-1 receptor DCC promotes filopodia formation and cell spreading by activating Cdc42 and Rac1. Mol Cell Neurosci 19, 1-17.
Shi, A., Chen, C.C., Banerjee, R., Glodowski, D., Audhya, A., Rongo, C., Grant, B.D., 2010. EHBP-1 functions with RAB-10 during endocytic recycling in Caenorhabditis elegans. Molecular biology of the cell 21, 2930-2943.
Short, C.A., Suarez-Zayas, E.A., Gomez, T.M., 2016. Cell adhesion and invasion mechanisms that guide developing axons. Curr Opin Neurobiol 39, 77-85.
Spencer, A.G., Orita, S., Malone, C.J., Han, M., 2001. A RHO GTPase-mediated pathway is required during P cell migration in Caenorhabditis elegans. Proc Natl Acad Sci U S A 98, 13132-13137.
Spitzweck, B., Brankatschk, M., Dickson, B.J., 2010. Distinct protein domains and expression patterns confer divergent axon guidance functions for Drosophila Robo receptors. Cell 140, 409-420.
Srayko, M., Kaya, A., Stamford, J., Hyman, A.A., 2005. Identification and characterization of factors required for microtubule growth and nucleation in the early C. elegans embryo. Developmental cell 9, 223-236.
Steven, R., Kubiseski, T.J., Zheng, H., Kulkarni, S., Mancillas, J., Ruiz Morales, A., Hogue, C.W., Pawson, T., Culotti, J., 1998. UNC-73 activates the Rac GTPase and is required for cell and growth cone migrations in C. elegans. Cell 92, 785-795.
Steven, R., Zhang, L., Culotti, J., Pawson, T., 2005. The UNC-73/Trio RhoGEF-2 domain is required in separate isoforms for the regulation of pharynx pumping and normal neurotransmission in C. elegans. Genes Dev 19, 2016-2029.

Struckhoff, E.C., Lundquist, E.A., 2003. The actin-binding protein UNC-115 is an effector of Rac signaling during axon pathfinding in C. elegans. Development 130, 693-704.
Strutt, D.I., Weber, U., Mlodzik, M., 1997. The role of RhoA in tissue polarity and Frizzled signalling. Nature 387, 292-295.
Suzuki, N., Nakamura, S., Mano, H., Kozasa, T., 2003. Galpha 12 activates Rho GTPase through tyrosine-phosphorylated leukemia-associated RhoGEF. Proc Natl Acad Sci U S A 100, 733-738.
Suzuki, T., Nakamoto, T., Ogawa, S., Seo, S., Matsumura, T., Tachibana, K., Morimoto, C., Hirai, H., 2002. MICAL, a novel CasL interacting molecule, associates with vimentin. J Biol Chem 277, 14933-14941.
Takahashi, T., Fournier, A., Nakamura, F., Wang, L.H., Murakami, Y., Kalb, R.G., Fujisawa, H., Strittmatter, S.M., 1999. Plexin-neuropilin-1 complexes form functional semaphorin-3A receptors. Cell 99, 59-69.
Tanaka, E., Ho, T., Kirschner, M.W., 1995. The role of microtubule dynamics in growth cone motility and axonal growth. J Cell Biol 128, 139-155.
Tau, G.Z., Peterson, B.S., 2010. Normal development of brain circuits. Neuropsychopharmacology 35, 147-168.
Terman, J.R., Mao, T., Pasterkamp, R.J., Yu, H.H., Kolodkin, A.L., 2002. MICALs, a family of conserved flavoprotein oxidoreductases, function in plexin-mediated axonal repulsion. Cell 109, 887-900.
Tessier-Lavigne, M., Goodman, C.S., 1996. The molecular biology of axon guidance. Science 274, 1123-1133.
Threadgill, R., Bobb, K., Ghosh, A., 1997. Regulation of dendritic growth and remodeling by Rho, Rac, and Cdc42. Neuron 19, 625-634.
Tian, G., Jaglin, X.H., Keays, D.A., Francis, F., Chelly, J., Cowan, N.J., 2010. Disease-associated mutations in TUBA1A result in a spectrum of defects in the tubulin folding and heterodimer assembly pathway. Hum Mol Genet 19, 3599-3613.
Tischfield, M.A., Baris, H.N., Wu, C., Rudolph, G., Van Maldergem, L., He, W., Chan, W.M., Andrews, C., Demer, J.L., Robertson, R.L., Mackey, D.A., Ruddle, J.B., Bird, T.D., Gottlob, I., Pieh, C., Traboulsi, E.I., Pomeroy, S.L., Hunter, D.G., Soul, J.S., Newlin, A., Sabol, L.J., Doherty, E.J., de Uzcategui, C.E., de Uzcategui, N., Collins, M.L., Sener, E.C., Wabbels, B., Hellebrand, H., Meitinger, T., de Berardinis, T., Magli, A., Schiavi, C., Pastore-Trossello, M., Koc, F., Wong, A.M., Levin, A.V., Geraghty, M.T., Descartes, M., Flaherty, M., Jamieson, R.V., Moller, H.U., Meuthen, I., Callen, D.F., Kerwin, J., Lindsay, S., Meindl, A., Gupta, M.L., Jr., Pellman, D., Engle, E.C., 2010. Human TUBB3 mutations perturb microtubule dynamics, kinesin interactions, and axon guidance. Cell 140, 74-87.
Tischfield, M.A., Cederquist, G.Y., Gupta, M.L., Jr., Engle, E.C., 2011. Phenotypic spectrum of the tubulin-related disorders and functional implications of disease-causing mutations. Curr Opin Genet Dev 21, 286-294.
Turney, S.G., Ahmed, M., Chandrasekar, I., Wysolmerski, R.B., Goeckeler, Z.M., Rioux, R.M., Whitesides, G.M., Bridgman, P.C., 2016. Nerve growth factor stimulates axon outgrowth through negative regulation of growth cone actomyosin restraint of microtubule advance. Mol Biol Cell 27, 500-517.

Van Battum, E.Y., Gunput, R.A., Lemstra, S., Groen, E.J., Yu, K.L., Adolfs, Y., Zhou, Y., Hoogenraad, C.C., Yoshida, Y., Schachner, M., Akhmanova, A., Pasterkamp, R.J., 2014. The intracellular redox protein MICAL-1 regulates the development of hippocampal mossy fibre connections. Nat Commun 5, 4317.
Van Goor, D., Hyland, C., Schaefer, A.W., Forscher, P., 2012. The role of actin turnover in retrograde actin network flow in neuronal growth cones. PLoS One 7, e30959.
Varadarajan, S.G., Butler, S.J., 2017. Netrin1 establishes multiple boundaries for axon growth in the developing spinal cord. Dev Biol 430, 177-187.
Varadarajan, S.G., Kong, J.H., Phan, K.D., Kao, T.J., Panaitof, S.C., Cardin, J., Eltzschig, H., Kania, A., Novitch, B.G., Butler, S.J., 2017. Netrin1 Produced by Neural Progenitors, Not Floor Plate Cells, Is Required for Axon Guidance in the Spinal Cord. Neuron 94, 790-799 e793.
Vitriol, E.A., Zheng, J.Q., 2012. Growth cone travel in space and time: the cellular ensemble of cytoskeleton, adhesion, and membrane. Neuron 73, 1068-1081.
Wadsworth, W.G., Bhatt, H., Hedgecock, E.M., 1996. Neuroglia and pioneer neurons express UNC-6 to provide global and local netrin cues for guiding migrations in C. elegans. Neuron 16, 35-46.
Wang, L., Zheng, Y., 2007. Cell type-specific functions of Rho GTPases revealed by gene targeting in mice. Trends Cell Biol 17, 58-64.
Wang, P., Liu, H., Wang, Y., Liu, O., Zhang, J., Gleason, A., Yang, Z., Wang, H., Shi, A., Grant, B.D., 2016. RAB-10 Promotes EHBP-1 Bridging of Filamentous Actin and Tubular Recycling Endosomes. PLoS genetics 12, e1006093.
Wang, Z., Hou, Y., Guo, X., van der Voet, M., Boxem, M., Dixon, J.E., Chisholm, A.D., Jin, Y., 2013. The EBAX-type Cullin-RING E3 ligase and Hsp90 guard the protein quality of the SAX-3/Robo receptor in developing neurons. Neuron 79, 903-916.
Wang, Z., Linden, L.M., Naegeli, K.M., Ziel, J.W., Chi, Q., Hagedorn, E.J., Savage, N.S., Sherwood, D.R., 2014. UNC-6 (netrin) stabilizes oscillatory clustering of the UNC-40 (DCC) receptor to orient polarity. J Cell Biol 206, 619-633.
White, J.G., Southgate, E., Thomson, J.N., Brenner, S., 1986. The structure of the nervous system of the nematode Caenorhabditis elegans. Philos Trans R Soc Lond B Biol Sci 314, 1-340.
Williams, S.L., Lutz, S., Charlie, N.K., Vettel, C., Ailion, M., Coco, C., Tesmer, J.J., Jorgensen, E.M., Wieland, T., Miller, K.G., 2007. Trio's Rho-specific GEF domain is the missing Galpha q effector in C. elegans. Genes Dev 21, 2731-2746.
Wittmann, T., Waterman-Storer, C.M., 2001. Cell motility: can Rho GTPases and microtubules point the way? J Cell Sci 114, 3795-3803.
Wu, Y.C., Cheng, T.W., Lee, M.C., Weng, N.Y., 2002. Distinct rac activation pathways control Caenorhabditis elegans cell migration and axon outgrowth. Dev Biol 250, 145-155.
Xu, Y., Taru, H., Jin, Y., Quinn, C.C., 2015. SYD-1C, UNC-40 (DCC) and SAX-3 (Robo) function interdependently to promote axon guidance by regulating the MIG-2 GTPase. PLoS genetics 11, e1005185.

Yamauchi, K., Yamazaki, M., Abe, M., Sakimura, K., Lickert, H., Kawasaki, T., Murakami, F., Hirata, T., 2017. Netrin-1 Derived from the Ventricular Zone, but not the Floor Plate, Directs Hindbrain Commissural Axons to the Ventral Midline. Sci Rep 7, 11992.
Yan, J., Chao, D.L., Toba, S., Koyasako, K., Yasunaga, T., Hirotsune, S., Shen, K., 2013. Kinesin-1 regulates dendrite microtubule polarity in Caenorhabditis elegans. eLife 2, e00133.
Yang, Y., Lee, W.S., Tang, X., Wadsworth, W.G., 2014. Extracellular matrix regulates UNC-6 (netrin) axon guidance by controlling the direction of intracellular UNC-40 (DCC) outgrowth activity. PLoS One 9, e97258.
Yau, D.M., Yokoyama, N., Goshima, Y., Siddiqui, Z.K., Siddiqui, S.S., Kozasa, T., 2003. Identification and molecular characterization of the G alpha12-Rho guanine nucleotide exchange factor pathway in Caenorhabditis elegans. Proc Natl Acad Sci U S A 100, 14748-14753.
Yu, T.W., Hao, J.C., Lim, W., Tessier-Lavigne, M., Bargmann, C.I., 2002. Shared receptors in axon guidance: SAX-3/Robo signals via UNC-34/Enabled and a Netrin-independent UNC-40/DCC function. Nat Neurosci 5, 1147-1154.
Yu-Kemp, H.C., Kemp, J.P., Jr., Brieher, W.M., 2017. CRMP-1 enhances EVL-mediated actin elongation to build lamellipodia and the actin cortex. J Cell Biol 216, 2463-2479.
Zallen, J.A., Kirch, S.A., Bargmann, C.I., 1999. Genes required for axon pathfinding and extension in the C. elegans nerve ring. Development 126, 3679-3692.
Zallen, J.A., Peckol, E.L., Tobin, D.M., Bargmann, C.I., 2000. Neuronal cell shape and neurite initiation are regulated by the Ndr kinase SAX-1, a member of the Orb6/COT-1/warts serine/threonine kinase family. Mol Biol Cell 11, 3177-3190.
Zallen, J.A., Yi, B.A., Bargmann, C.I., 1998. The conserved immunoglobulin superfamily member SAX-3/Robo directs multiple aspects of axon guidance in C. elegans. Cell 92, 217-227.
Zhang, X.F., Schaefer, A.W., Burnette, D.T., Schoonderwoert, V.T., Forscher, P., 2003. Rho-dependent contractile responses in the neuronal growth cone are independent of classical peripheral retrograde actin flow. Neuron 40, 931-944.
Zheng, C., Diaz-Cuadros, M., Nguyen, K.C.Q., Hall, D.H., Chalfie, M., 2017. Distinct effects of tubulin isotype mutations on neurite growth in Caenorhabditis elegans. Mol Biol Cell 28, 2786-2801.
Zhou, F.Q., Cohan, C.S., 2004. How actin filaments and microtubules steer growth cones to their targets. J Neurobiol 58, 84-91.
Zhou, F.Q., Waterman-Storer, C.M., Cohan, C.S., 2002. Focal loss of actin bundles causes microtubule redistribution and growth cone turning. J Cell Biol 157, 839-849.
Zipkin, I.D., Kindt, R.M., Kenyon, C.J., 1997. Role of a new Rho family member in cell migration and axon guidance in C. elegans. Cell 90, 883-894.